Characterising the amplitude and mechanisms responsible for the Pushout Load and Torque for a staked, self-lubricating spherical plain bearing

Jacob Christopher Hugh Hatherell

A thesis submitted in partial fulfilment of the requirements of the University of the West of England, Bristol for the degree of Doctor of Philosophy

This research programme was carried out in collaboration with the SKF Clevedon

Faculty of Engineering, University of the West of England, Bristol

May 2024

Director of Studies

Dr Jason Matthews

Second Supervisor 1

Dr Arnaud Marmier

Second Supervisor 2

Dr Grant Dennis

Second Supervisor 3

Will Curry

Word Count

51,421

Abstract

Staking is a cold metal joining process widely used in the manufacture of self-lubricating spherical plain aerospace bearings. These are used to form components such as tie-rod links or threaded rod ends as often seen on control surfaces for rotary winged aircraft. The staking of a bearing is achieved by plastically deforming the bearing's outer race to precisely retain the bearing assembly. Traditional analysis methods of these bearings include analytical methods, computational methods, or through manufacturing trials. Each of these methods have their own strengths and weaknesses with the choice of which method to use being a trade-off between time, cost, accuracy, understanding of the influencing variables, and generalising that understanding across a wide range of bearing geometries.

The work presented in this thesis details the development of a virtual design of experiments (Virtual-DoE) methodology to model the staking of self-lubricating spherical plain bearings by combining the two disciplines of computational modelling and the applied statistical methods of a design of experiments. The Virtual-DoE methodology allows for the creation of a rigorous and thorough test programme to be rapidly analysed within a computational modelling environment. This analysis method demonstrated its capability to identify all the relevant parameters that impact the staking process and to characterise their influence on the pushout strength and post-stake torque through a series of closed-form solutions.

The accuracy of these solutions was validated against manufacturing trails data over a period of 18 months with their performance far exceeding the accuracy of the traditional bearing analysis methods. The understanding of the fundamental mechanisms that control the staking process, enabled by the Virtual-DoE methodology, has allowed for both the optimisation of new bearing designs and a "first time right" capability that significantly reduces the likelihood of scrapped bearings during manufacturing or the need for costly and time-consuming manufacturing trials. The broad applicability of a Virtual-DoE provides an inexpensive, methodical, and scalable solution that could be applied to the majority of complex cold metal joining processes.

To support the computational model developed for the Virtual-DoE, ring compression tests (RCT) were undertaken to characterise the dynamic friction behaviour of the stainless steel that aerospace bearings are made from. A fundamental flaw with RCT was observed whereby the standard RCT analysis method cannot accurately model friction behaviour that dynamically changes with contact pressure. To address this flaw, a new iterative analysis method was proposed that compared to the standard method saw a five times reduction in modelling error.

Acknowledgements

I would like to thank the following people for their help and support throughout my doctoral studies.

For the funding that made this research possible…

SKF and UWE

To the technical staff at UWE for their kind support, encouragement, sarcasm, and for reminding me to take the time to relax and sleep more…

Daniel Cole, Douglas Nash, Lucy Corfield, Mark Allonby, Nathan Townsend, Rick Adams, Tamsila Tauqir and Tom Barrington

To the engineering team at SKF for their technical expertise and for putting up with my constant emails…

Will Curry, Grant Dennis, Ian Rogers, Lester James, Michael Colton and Nick Adams

To my supervisors for helping me navigate the doctoral journey through all the ups and downs…

Arnaud Marmier, Grant Dennis, and Jason Matthews

For always being there for me, and the sacrifices you have made for me to achieve all that I have…

Vittoria Hatherell and Mark Hatherell.

And lastly, for supporting and encouraging me to pursue my passion, for keeping me going when times get tough, all my love…

Lisa Coomes

Authors Declaration

I declare that the work in this dissertation was carried out in accordance with the requirements of the university's regulations and code of practice for research degree programmes and that it has not been submitted for any other academic award. Except where states otherwise by reference or acknowledgement, the work presented is entirely the candidate's own work. Work done in collaboration with, or with the assistance of, others, is indicated as such. Any views expressed in the dissertation are those of the author.

Signed:

Date:

02/05/2024

Jacob Hatherell

University of the West of England

Dissemination of Work

Hatherell, J., Marmier, A., Dennis, G., Curry, W. and Matthews, J. (2023) Exploring the potential for a FEA-based Design of Experiments to develop design tools for bulk-metal joining processes. *International Conference on Engineering Design* (ICED), Bordeaux, France, 24-28 July 2023. (This forms the basis of Chapter 5: Pressure-Dependant Friction Analysis)

Hatherell, J., Marmier, A., Dennis, G., Curry, W. and Matthews, J. (2023) An Iterative Numerical Approach to Evaluate the Variable Friction Coefficient of Steel AMS5643 Using Ring Compression Tests. *Tribology Transactions.* 67(1), pp. 15-21. (This forms the basis of Chapter 6: Virtual Design of Experiments)

Table of contents

List of Figures

List of Tables

Nomenclature

Abbreviation	Meaning	Page
APDL	Ansys Parametric Design Language	111
CT	Computed Tomography	29
DoE	Design of Experiments	6
DSD	Definitive Screening Design	128
EMF	Electromagnetic Forming	24
EMWC	Electromagnetic Wire Crimping	24
ETI	Engineering Technical Instruction	27
FDM	Finite Difference Method	62
FEA	Finite Element Analysis	25
FEM	Finite Element Model	26
FCC	Friction Calibration Chart	49
GUI	General User Interface	140
HERF	High Energy Rate Forming	24
ISBMF	Incremental Sheet-Bulk Metal Forming	16
NDT	Non-Destructive Test	29
PEEK	Polyetheretherketone	20
PTFE	Polytetrafluoroethylene	30
VIF	Variance Influence Factor	64

Chapter

1

Introduction

1.1. Background

This research was carried out with the support of SKF, a leading global manufacturer of bearings are and are located across 100 sites within Europe, North and Latin America, Africa, and Asia (SKF, 2022a). At their Clevedon site, SKF specialises in the manufacture of self-lubricating spherical plain bearings which are found in a wide range of applications ranging from motorsport to rail, but mostly within the aerospace industry. The aerospace sector makes up 85% of total sales with a breakdown of 42% civil rotary wing, 18% military rotary wing, 22% civil fixed-wing aircraft and 5% military fixed-wing aircraft (SKF, 2019).

Self-lubricating spherical plain bearings are widely used in the aerospace industry due to their high impact resistance, load-bearing capacity, and self-lubrication properties (Kim et.al., 2006; Zhang et.al., 2018a) and are primarily seen in applications such as fixed and rotary wing pitch control links, dampers, control surfaces, cargo bay doors and undercarriages (Hoo and Green, 1998). Self-lubricating spherical plain bearings consist of three parts; an inner ring that enables the bearing to freely oscillate about 3 degrees-of-freedom; an outer race that conforms to the inner ring and acts as a mating surface for external assemblies; and a composite fabric (liner) bonded to the inside of the outer race that provides lubrication and a low friction interface against the inner ring (Figure 1).
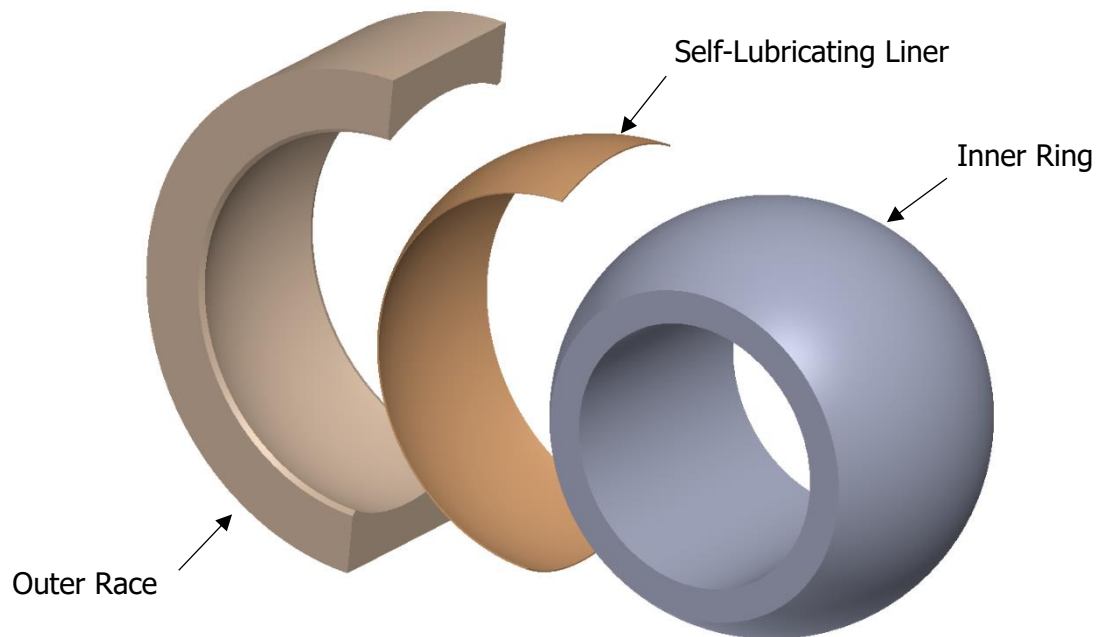
Figure 1: Deconstructed self-lubricating plain spherical bearing.

Of all bearings produced by SKF Clevedon, approximately 20% receive additional manufacturing and are joined to a housing typically in the form of a rod end/tie rod (SKF, 2019). Staking, sometimes referred to as upsetting or open-die forging, is the cold-metal joining process of choice for this. Circumferential v-grooves are machined into both parallel faces of an already manufactured spherical plain bearing (Figure 2a). These grooves form two thin lips on the outer race that when compressed (staked) between opposing anvils conform the outer race to a chamfer in the housing (Figure 2b). This process produces a lightweight and reliable mechanical joint requirement with no additional components in the assembly.
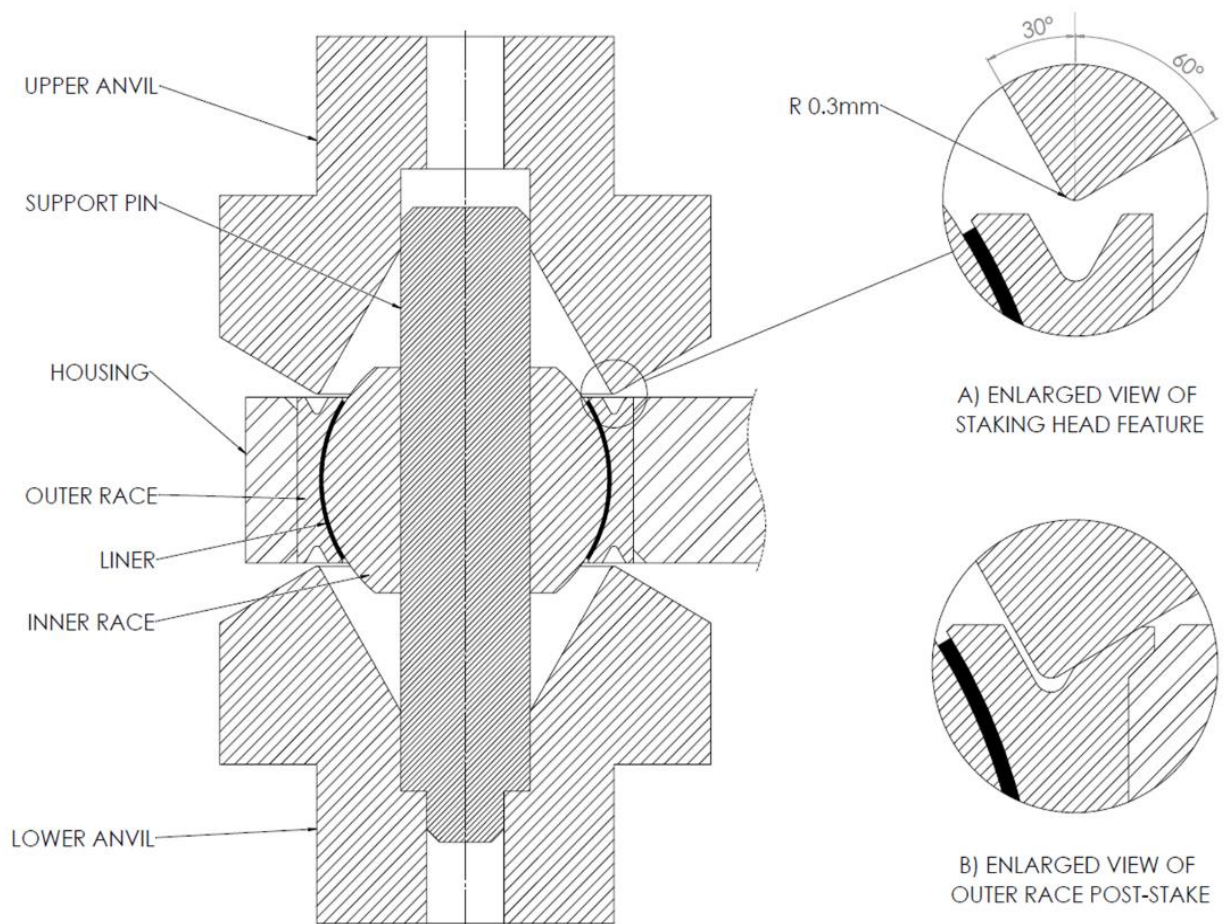
Figure 2: Cross-sectional schematic of the Staking process.

1.2.   Manufacturing Challenges

The understanding of what defines the optimal stake has historically been surrounded by ambiguity and a lack of detailed analysis. This is a problem that not only SKF, but the wider aerospace manufacturing sector has failed to resolve. The majority of the current guidelines, design rules, and understanding of bearing staking trace back to a proposed design standard produced by the Airframe Control Bearing Group (1989). Despite small changes in recent revisions of the design standard (Aerospace Industries Association, 2020), the only measure to define a successful stake that has been presented is if a 0.005-inch wire gauge cannot be fit between the staking lip and the housing chamfer (Figure 3).
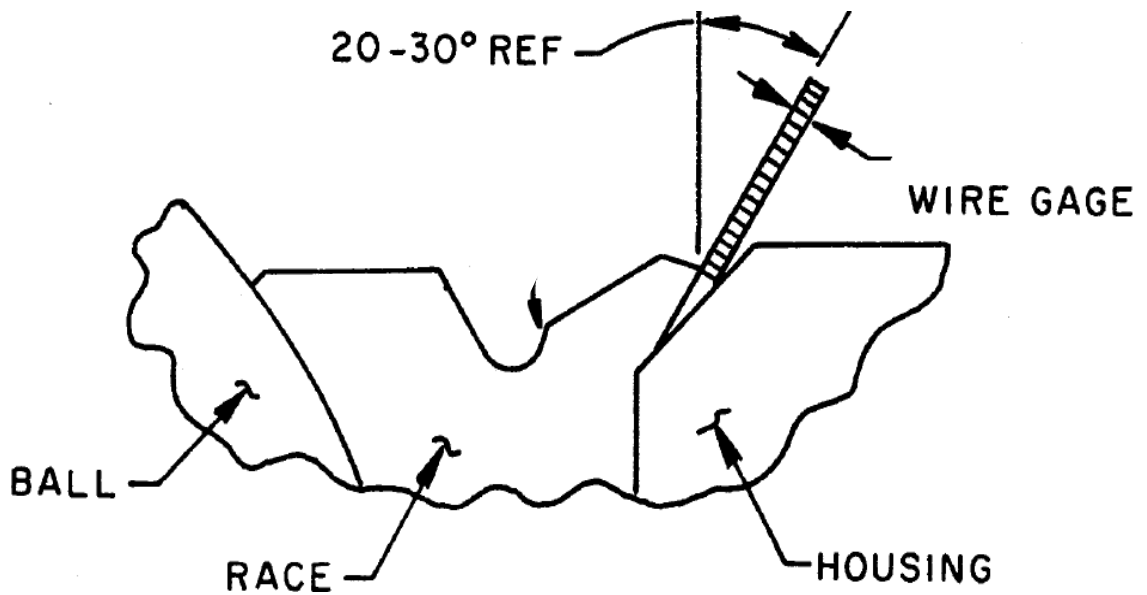
Figure 3: Test method for checking the quality of a bearing stake (Airframe Control Bearing Group. 1989).

No rationale was given as to why a 0.005 wire gauge was deemed as the appropriate measure of a successful stake, though it is thought to be one of the more convenient methods at the time to determine if the lip has been fully formed against the housing.

Derived from this basic concept of an optimal stake, lookup tables were produced to aid operators in determining the staking load (the load applied on the upper anvil) whereby the staking load scales linearly with the outer diameter of the spherical bearing. From this staking load, the lookup table then states the expected joint strength (pushout strength). The machine settings are validated by pushing the bearing out of its housing and in doing so, scrapping the assembly. If the joint strength measured is not greater than that stated in the part drawing, the staking force is increased in 5kN increments until the minimum joint strength is achieved; the final staking load is then carried forward for the rest of that batch. This process is followed to ensure the least possible stress is imparted into the housing as it is usually load bearing (such as rod ends and tie rods) and any residual stress from the staking operation reduces the maximum operating load of the housing.

Whilst it is a logical assumption that the outer race diameter should dominate the relationship between staking force and pushout strength, the lack of consideration for any other geometric feature or manufacturing tolerances could explain the large uncertainty found in predicting the pushout strength prior to staking. Some of the potential influencing parameters include: the interference fit between the bearing and rod end, groove geometry, bearing width, and inner ring diameter (SKF 2022b). This makes quantifiable trends hard to establish due to the small quantity of bearings made per batch (typically 1-80) with each batch typically being a unique design.

The second major concern is the rise in post-stake torque of the bearing. The current understanding is that the torque of a bearing would normally decrease (torque-dropout) if the staking load was sufficiently low. As the staking load increases, the bearing would then return to its original torque and eventually lock-out (torque exceeding 10 Nm) if the staking load became too large. Because bearing geometries are typically unique to each batch and the staking loads are inconsistent, there is a large uncertainty in predicting the final torque of the staked bearing. This uncertainty results in several finished parts requiring expensive and time-consuming reworking to bring the post-stake torque back within specification. This is particularly problematic for bearings which lock-out.

These two issues suggest that the fundamental mechanisms present in the staking of spherical plain bearings and the influence of the design parameters on the pushout strength and post-stake torque of the final assembly are poorly understood.

1.3. Aims and Objectives

To improve on the knowledge and understanding of the staking of self-lubricating spherical plain bearings, the original aim was to "*optimise the staking process*" and evaluate all aspects of bearing, housing, tooling, and process settings. It was identified early on that that this could be achieved through the combination of computational modelling and a Design of Experiment (DoE) methodology to form a Virtual-DoE: a novel approach within the field of cold-metal joining. However, this ambitious aim was far outside of what could be achieved within the scope of a PhD, with the main limitation being the need to validate a Virtual-DoE model against practical data. Primarily because of the limited manufacturing capacity to produce custom bearings and tooling, all practical data would have to be gathered from the first-off of each batch of staked bearings that passed through manufacturing. This constrained the investigation to the study of the parameters that can be varied within normal production. Therefore, this investigation is a case study to validate the use of Virtual-DoE as a method to understand, design, and optimise cold-metal joining processes. The aim of this investigation can be stated as the following research question:

"As a case study for the application of Virtual-DoE to a cold-metal joining process, what defines the optimal stake within the range of standard aerospace self-lubricated plane spherical bearings?"

Whereby the optimal stake is defined as:

"The combination of bearing geometry and process parameters that achieve the desired pushout strength whilst minimising the rise in post-stake torque"

Taking into consideration the research aim and the literature reviewed in Chapter 2, the objectives of this research are as follows:

- Characterise the mechanical and friction properties necessary for the computational modelling of the staking process.

- Identify the key process parameters and characterise their impact on the staking process into a series of closed-form solutions.

- Validate the closed-form solutions against experimental results.

1.4. Thesis Outline

Chapter 1: Introduction

The introductory chapter provides the reader with a background into the staking process, establishes scope of the PhD, and delineates the structure of the thesis.

Chapter 2: Literature Review

This chapter presents a review of the relevant literature to evaluate the gaps in the current scientific knowledge. This study contains an overview of the fundamental mechanisms involved in the cold joining of metallic components and a summary of the current state of the art from recently published work. The details of spherical bearing staking along with alternative staking methods are presented with a discussion on the manufacturing challenges faced in production and the factors which affect the staking process.

Chapter 3: Methodology

This chapter brings together the research from the literature review and outlines the chosen methodology that this investigation followed to satisfy the research objectives. The three areas of discussion were: how to model the staking process, determining the mechanical properties of a spherical bearing, and characterising the friction-pressure relationship between the various interface surfaces during staking.

Chapter 4: Mechanical Characterisation of High-Alloy Steels

This chapter presents the compression testing required to evaluate the compressive plastic behaviour of the two metals that are used in the manufacture of self-lubricating spherical plain bearings, AMS 5643 H1025 and H1150. This testing was carried out at strain-rates varying from $0.01s^{-1}$ to $1s^{-1}$ and characterised using a modified-Hollomon flow stress model that provides a significant improvement over the standard Hollomon model by allowing for the flow stress to be continuously evaluated at any strain rate.

Chapter 5: Pressure-Dependent Friction Analysis

Ring compression testing was used to evaluate the friction coefficient between the outer race and housing (Dry) and the outer race and staking anvil (Lubricated). It was found that the friction coefficient changes dynamically with contact pressure which the standard ring compression test analysis method cannot accurately capture. A new approach to evaluate the friction-pressure relationship is proposed using computational methods to generate iterative friction calibration charts which significantly improves the modelling accuracy over the standard analysis method.

Chapter 6: Virtual Design of Experiments

Building off of the material and friction characterisation work from Chapters 4 and 5, a computational model of the staking process is produced and integrated with a design of experiments method to create a Virtual Design of Experiments methodology. Following a systematic test programme, 216 simulations of staked bearings were conducted. A regression analysis of this dataset produced a series of closed-form solutions to define the relationship between the bearing's geometry and its impact on the Staking Force, Pushout Strength, and the Post-Stake Torque. A staking tool was produced from these closed form solutions to aid in the design and analysis of future bearings.

Chapter 7: Validation and Implementation

Staking trials were carried out over 18 months of production bearings to determine the accuracy of the staking tool developed in Chapter 6. Whilst the raw staking tool already outperformed SKFs currented design tools, analysis of the manufacturing data highlighted trends and systematic errors within the staking tool that by applying correction factors further improved the performance of the staking tool. This accuracy enables a "first-time-right" capability that reduces the likelihood of needing to re-work high torque bearings or the need for manufacturing trials for new bearing designs: both eliminating waste and reducing costs. To improve on the understanding of the regression equations that drive the staking tool, an analysis of each staking tool parameter was conducted to generate contour plots visualising how each parameter impacts the staking process.

Chapter 8: Discussion

The findings from this investigation are summarised and interpreted within the context of the wider literature and their potential impact on the field of cold metal joining, including a discussion of the limitations of this study. The findings from Figure 118 through Figure 122 challenge many of the previously perceived truths about bearing design, in particular the negative impacts of interference fit on the post-stake torque of bearings. These challenges to bearing design convention are important in changing the design principles of future bearing designs.

Chapter 9: Conclusions and Future Work

This body of work has demonstrated that the combination of the two disciplines, computational modelling, and the applied statistical methods of a design of experiments, is suitable for analysing and predicting the behaviour of complex metal joining processes which has not been done before. Additionally, this chapter details how each of the research objectives was addressed along with the key findings and conclusions to each of these objectives. Lastly, a list of the key areas that future research should pursue to build upon the work of this investigation is proposed.

1.5. Contribution to Knowledge

The outputs from this investigation have resulted in three contributions to knowledge to both the scientific and engineering community.

Major Contribution:

1) Evidence that the combination of the two disciplines, computational modelling, and the applied statistical methods of a design of experiments, is suitable for analysing and predicting the behaviour of complex metal joining processes

Minor Contributions:

2) Characterisation of the relevant geometric features and process control settings that impact the pushout strength and post-stake torque of a staked self-lubricating spherical plain bearing

3) New methodology for analysing the results from a ring compression test to better capture the non-linear behaviour of the friction coefficient during forging conditions

Contributions 1 and 3 have been composed into their own respective works and published in peer reviewed articles. These publications form the basis of Chapters 5 and 6 respectively.

Hatherell, J., Marmier, A., Dennis, G., Curry, W. and Matthews, J. (2023) Exploring the potential for a FEA-based Design of Experiments to develop design tools for bulk-metal joining processes. *International Conference on Engineering Design* (ICED), Bordeaux, France, 24-28 July 2023. (Appendix F)

Hatherell, J., Marmier, A., Dennis, G., Curry, W. and Matthews, J. (2023) An Iterative Numerical Approach to Evaluate the Variable Friction Coefficient of Steel AMS5643 Using Ring Compression Tests. *Tribology Transactions.* 67(1), pp. 15-21. (Appendix G)

Chapter

2

Literature Review

There is a substantial knowledge gap regarding the fundamental mechanisms present in the staking of self-lubricating spherical plain bearings. To address this gap in knowledge and answer the questions that arise from the project objectives, this chapter aims to summarise of the current state of the art within the field of cold metal joining and review the supporting academic literature to identify knowledge gaps within past and present research.

2.1. Cold Metal Joining Overview

The process of forming metal is classified into one of five categories: direct-compression, indirect-compression, tension, bending, and shearing. These categories define how force is applied to the workpiece as it is formed (Dieter, 1961). In direct-compression processes such as forging and rolling, the force is applied directly to the surface of the workpiece with metal flow at right angles to the compressive force. With indirect-compression processes such as wire and bar drawing, the primary force on the workpiece is tension but compressive forces are generated by the interaction of the workpiece and die. Whilst not a comprehensive list, the five metal forming categories manifest themselves into broader forming processes of; forging, rolling, wire drawing, extrusion, deep drawing, stretch forming, bending, and shearing (Valberg, 2012; Marinov, 2010; Hosford and Caddell, 2007).

Metal forming processes are carried out in a range of temperatures with cold metal forming being defined as plastic deformation below the metal's recrystallisation temperature. Work done above the recrystallisation temperature is called hot metal working (Kalpajian, S. (1997). Warm metal working can be achieved by mildly increasing the working temperature without exceeding the recrystallisation temperature. This is done to provide increased ductility and reduce the strength of the workpiece but as Black and Kohser discuss (2008, p.373) "recent advances have expanded their [cold working] capabilities, and a trend toward increased cold working appears likely to continue".

The push towards more cold working processes can be explained in part by the desire to avoid some of the complications that arise from hot working such as thermal expansion, poor tolerances, and oxidisation (Black and Kohser, 2008; Hosford and Caddell, 2007). This typically results in the workpiece requiring further processing to produce a finished product. Cold metal forming has many advantages such as the ability to produce near-net shape components (Kudo, 1990) with little to no material waste and exceptional surface finishes (Swift and Booker, 2003). However, cold working results in the work hardening of the metal which in turn generates a spring back in the metal (Figure 4). This effect is amplified when using higher-strength metals and by the extent to which the metal has been work-hardened (Bhadeshia and Honeycombe, 2017). Other considerations for the use of cold metal forming have been reviewed and investigated by Swift and Booker (2013), Valberg (2012), and Marinov (2010) and can be summarised as follows:

- Cost savings from high material utilisation

- Excellent surface detail and finishes

- Cost savings as no heating is required

- Low finishing costs (little or no post-processing); High production rates

- Fatigue, impact, and surface strength increased from work hardening

- Sharp corners can reduce tool life

- High contact pressures between die and workpiece

- Residual stresses induced from work hardening and spring back
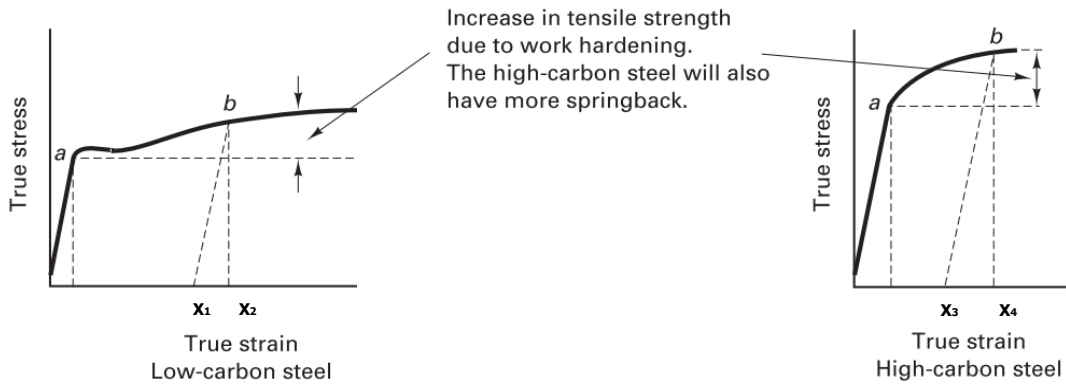
Figure 4: Spring back illustrated as the relaxation of steel after plastic deformation (b) having gone past its yield point (a). The greater work hardening of the high carbon steel increases the degree of spring back, X_4-X_3 > X_2-X_1. (Adapted from Kalpajian and Schmid, 2008).

The force required to deform a workpiece is a function of the total material strain, the material's mechanical properties, and the area being deformed. For the simplified case of a workpiece of an uniform cross-sectional being compressed, the true compressive strain ($\bar{\varepsilon}$) is calculated as

$$\bar{\varepsilon} = ln\left(H_0/H_f\right),$$ [1]

where H_0 and H_f are the initial and final height of the specimen respectively. Assuming the workpiece deforms uniformly with no barrelling, the forming area (A_f) changes proportionally with H_f and can be written as

$$A_f = V/H_f,$$ [2]

Where V represents the volume of the specimen. Lastly, the forming force (P) can be calculated as the product of the forming area and flow stress from the Hollomon strain-hardening equation (Kalpajian and Schmid, 2008) and is given as:

$$P = A_f\,K\bar{\varepsilon}^{\,n},$$ [3]

where K is the strength coefficient and n is the strain-hardening exponent. By rearranging Equations 1 and 2, the working load can be expressed as a function of the true compressive strain

$$P = \frac{Ve^{\bar{\varepsilon}}}{H_0}\,K\bar{\varepsilon}^{\,n}.$$ [4]

2.1.1. Joining Mechanisms

In general, joining by plastic deformation mechanisms can be classified into three principal categories: friction locking, positive locking, and metallurgical locking (Figure 5).
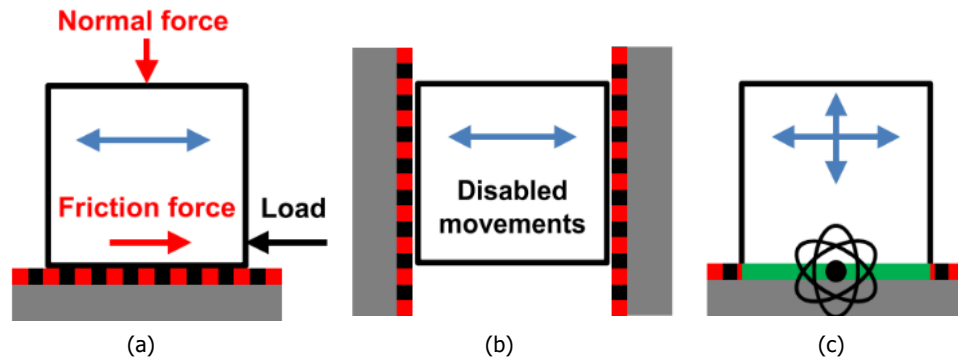
Figure 5: Joining principles (a) friction locking, (b) positive locking, (c) metallurgical locking (adapted from Groche and Turk, 2011).

Friction locking (also referred to as an interference-fit or force-fit joint) is based on the difference in the elastic recovery between two parts, leading to a normal pressure between the two parts after the deformation process. This results in the relative movement of the parts parallel to their shared interface being constrained by the induced friction force. An example of this joint type is used extensively in the joining of tubular parts which can be manufactured by a variety of processes such as die-less hydroforming (Groche and Tibari, 2006), electromagnetic forming (Weddeling et al., 2011) and rolling (Kiuchi, Shintani and Hwang, 1992).

Along with the interface pressure, the contact area and the coefficient of friction are major determinants of the final joint strength. Increasing the area of contact is typically limited by design restrictions, however, Hammers *et al.* (2009) showed that increasing the surface roughness by rough milling (and to a lesser degree by shot peening) increases the potential joint strength.

The primary mechanism for positive locking (also referred to as form-fit and form-closed) that governs joint strength is the geometric interference between parts and the magnitude of the resultant normal forces. The residual stresses caused by the manufacture of a positive locking joint often results in a degree of friction locking, however, this effect is often considered secondary when determining joint strength.

A common manufacturing approach for achieving a positive lock is to have a geometric feature in the form of an undercut on one part so that the opposing mating part can deform into. For example, this can be seen in the joining of tubes (Weddeling *et al.*, 2015a and 2011; Schäfer *et al.*, 2010) and the roller swaging of spherical bearings (Zhang *et al.*, 2017). This approach is best suited to joints where the part with the undercut is significantly more rigid than the part being deformed as seen in the crimping of couplings into hydraulic hoses (Figure 6).

In each of the previous examples, the joint strength increases with forming pressure. This can be attributed to both the work hardening of the base material and the increased area of contact as deformation increased. In instances where both parts are of similar rigidity and size, dies are used to plastically deform both parts to create a positive lock such as in wire crimping (Rajak *et al.*, 2017), mechanical clinching (Neugebauer, Kraus, and Dietrich, 2008), and the rotary swaging of tubes (Zhang *et al.*, 2014; *Cho et al.*, 2005).
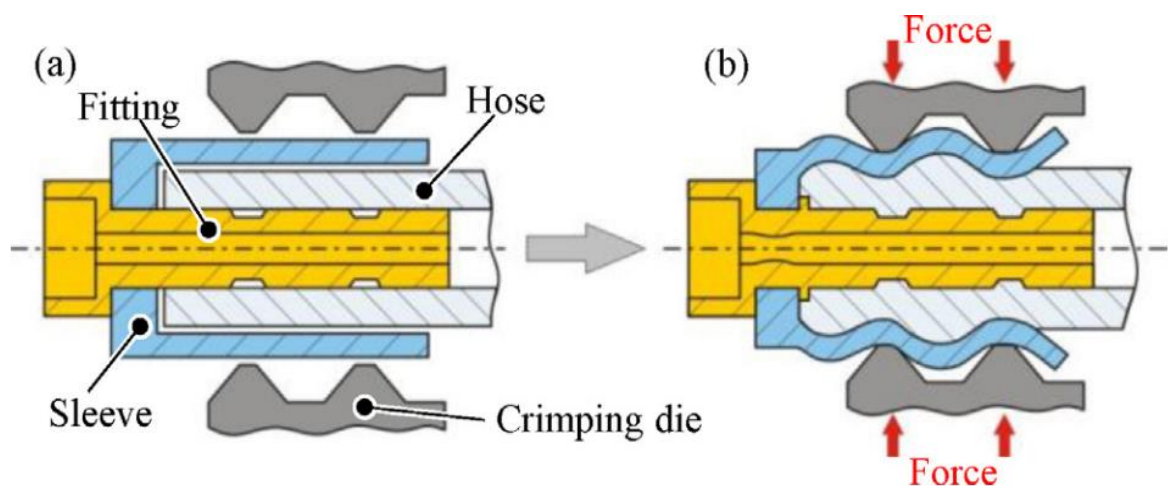
Figure 6: Process principle of mechanical crimping. (a) Positioning and (b) crimping (*Cho et al.*, 2005).

Lastly, metallurgical locking (also referred to as solid-state welding) creates a joint by fusing two mating parts without the need for an external heat supply. As seen in Figure 7, severe plastic deformation breaks down the surface oxides and contaminants, exposing clean surfaces that can bond together under high interfacial pressure. Due to the large plastic deformations required for metallurgical locking, significant internal heating is generated which aids in softening the workpieces and accelerating the deformation (Kalpajian and Schmid, 2008; Bay, 1983).
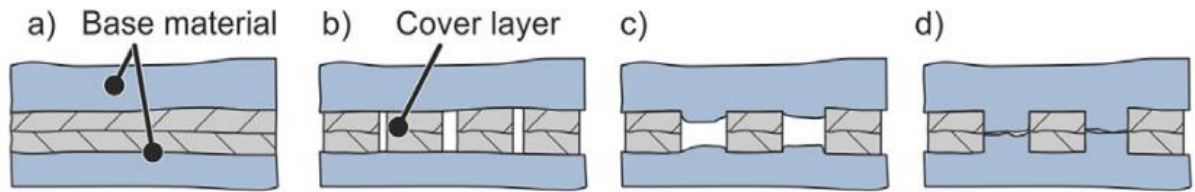
Figure 7: Material bond by cold forming: (a) Contact of the cover layer, (b) Breaking of the cover layer, (c) Extrusion of the base material and d) Contact of the base material. (Bay, 1979).

For a joint to be established, at least one of the three joining principles is required but in practice, most manufacturing processes use more than one of these principles simultaneously. Table 1 gives an overview of the common metal joining process and their respective joining mechanism. A pattern emerges where both positive and friction locking frequently occur together and could be classified under a broader category of a "mechanical joint". To create a mechanical lock with no backlash, inevitably, a friction lock will also be created due to the elastic recovery of the workpieces.

Table 1: Joint classification by joining principle and manufacturing process. Key; ● = Primarily utilised, ○ = Secondarily utilised, Blank = Not generally utilised. (Adapted from Groche *et al.,* 2014)

Process	Positive locking	Friction locking	Metallurgical locking
clinching	●	○	
Electromagnetic forming	●	●	○
Hemming	●	●	
Rolling	●	●	●
Rotary swaging	●	●	
Spinning	●	●	
Hydroforming	●	●	
Friction Stir Welding			●
Cold forging	●	○	●
Bar Extrusion	●	○	●

Groche et al. (2014) and Mori et al. (2013) present a comprehensive overview and summary of the state of the art for the cold metal joining operations listed in Table 1. At the time it was written, it was surmised that the basic knowledge of mechanical joining is widely spread throughout industrial applications. In the context of laboratory scale experiments, all processes were able to show promising potential for new technical utilisations, especially for both the joint's mechanical and fatigue strength. However, across the academic literature surveyed there was limited knowledge about the relevant influences on joint properties, nor the process limitations, because the specific mechanisms of their particular process were not sufficiently understood. When it comes to the predictability of the joint's properties, primarily regarding the joint's strength, accurate prognoses are challenging and, in most cases, nearly impossible.

The following sections are a summary of the research and current state of the art within the field of cold metal joining from recently published work.

2.1.2.   Incremental Sheet-bulk Metal Forming

Incremental forming encompasses several sheet, bulk, and hybrid forming processes that incrementally deform a workpiece until the final shape is achieved. At the time of writing, incremental sheet-forming processes have not been adopted for the joining of components and are still limited to single-part manufacturing. In the early 2010s, developments in incremental sheet forming along with the demand for sheet metal components with heavily loaded elements brought about a new class of manufacturing processes called Incremental Sheet-Bulk Metal Forming (ISBMF). One characteristic of bulk-forming processes is their ability to produce load-adapted parts by controlling the material distribution of the workpiece (Tekkaya *et al.*, 2014). However, this typically has the drawback of requiring the use of metal cutting processes for material removal instead of the highly efficient sheet-forming blanking process. By applying bulk-forming to sheet-like parts, the manufacture of load-adapted, near-net-shape components without the need for inefficient metal cutting processes is possible as shown in Figure 8.
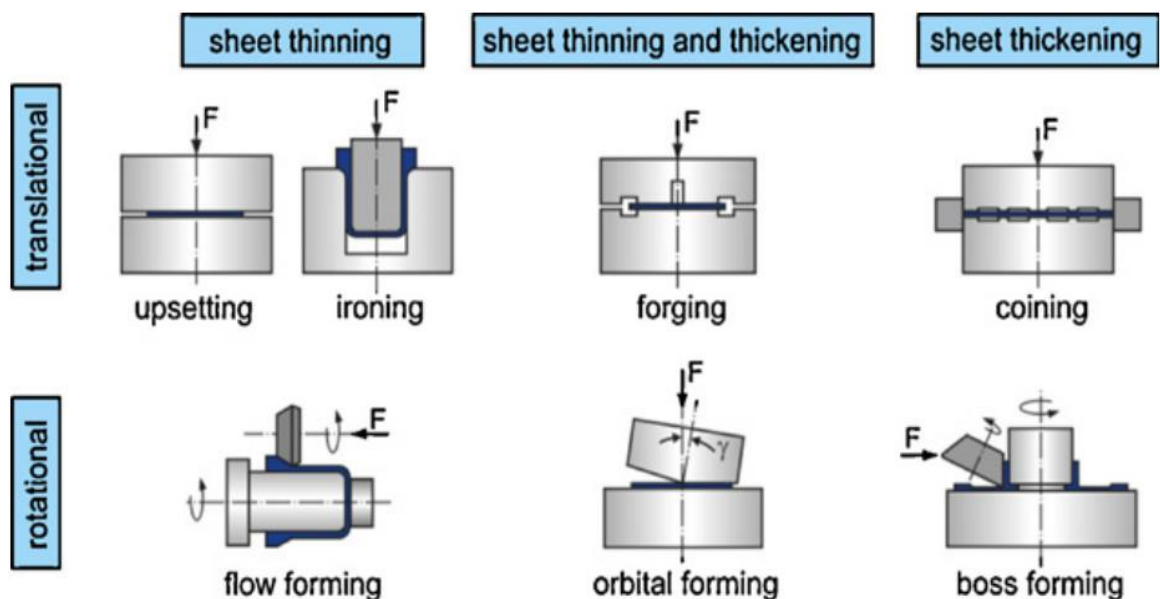
Figure 8: Classification of sheet-bulk metal forming processes. F notates the direction of the applied forming load. (Merklein et al., 2011).

The ISBMF of gears from a single homogenous material (Figure 9) has received a large amount of attention best summarised by Sieczkarek *et al.* (2017), Mori and Nakano (2016), and Merklein *et al.* (2015 and 2012). Despite the benefits of ISBMF, it has been shown to have two primary challenges. First is the difficulty in grading the mechanical properties of the gear teeth because of strain hardening and void growth (Wernicke *et al.*, 2020), second is the high loads experienced by the forming tools and their reduction in tool life (Sieczkarek *et al.*, 2016).
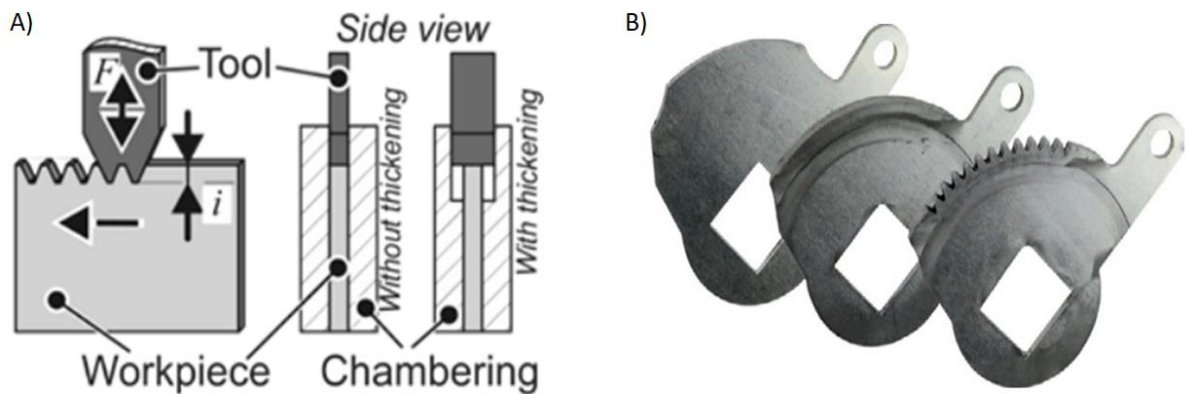
Figure 9: A) ISBMF-gearing process with and without thickening of the forming area, B) thickening and gearing of a seat adjuster (Sieczkarek et al., 2017).

At a similar time, the hybridisation of gears was being investigated to tackle these challenges and reduce the weight from rotary transmissions through the combination of dissimilar materials. LaBerge *et al.* (2016) achieved this by bonding a composite core to a pre-milled bull gear whilst Chavdar *et al.* (2016 and 2015) used hot hydroforging of steel/aluminium hybrid billets.

The culmination of this research led to the work by Wernicke *et al.* (2019) and Wernicke, Hahn, and Tekkaya (2021) in which a novel approach to achieve a hybrid gear through the joining of aluminium and steel plates using ISBMF was presented (Figure 10). The process starts with a high-strength steel sheet (DC04) that is sandwiched and protruded out between two aluminium blanks (AlMg3). The assembly is first rotated, whilst the steel sheet is radially compressed by a thickening tool, until it covers the surrounding blanks across the thickness of the assembly. The second step involves the radial indentation of the gear profile by either a continuous or discontinuous form tool.
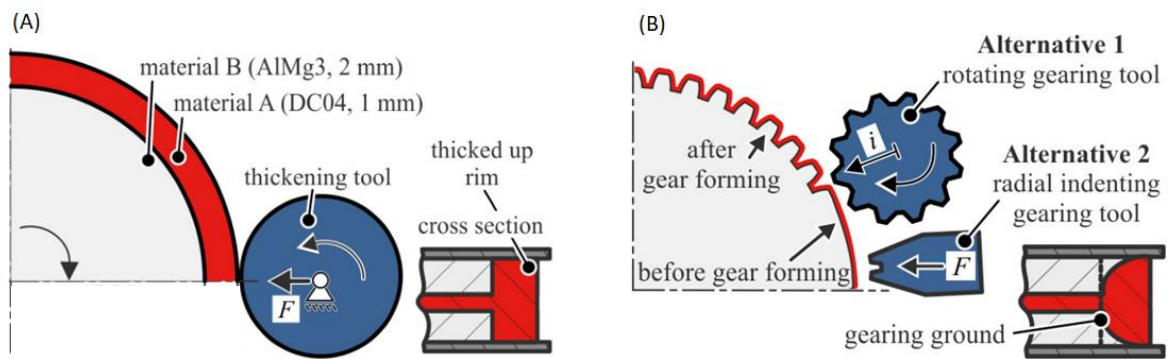
Figure 10: Hybrid gear forming. Schematic of the a) thickening process, b) gear forming process with two proposed gear tooth forming tools (Adapted from Wernicke et al., 2019).

The two gear forming methods produced drastically different results concerning the distribution of material on the teeth flanks. As seen in Figure 11a, the discontinuous form tool produced a symmetric distribution of material across the gear teeth, whereas the continuous rotating form tool (Figure 11b) biased the flow of steel onto the leading face of the gear teeth. Whilst not useful for most gearbox applications, the bias of steel to the leading face may lend itself to applications where there is a preferred loading direction or to asymmetric gears (Kapelevich, 2009 and 2011).
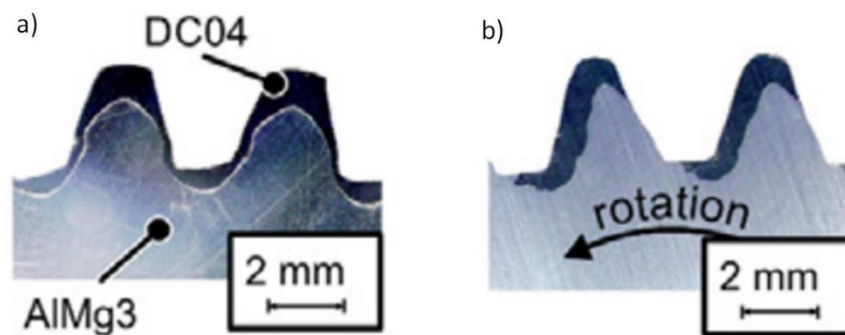
Figure 11: Cross sectional view of the gear teeth after a) discontinuous radial forming, b) continuous (rotating) radial forming (Wernicke et al., 2019).

Regarding the primary challenges faced by the forming of gears via iSBMF, hybrid gears have shown the potential in reducing the force required to form the gear teeth. The zone of material that forms the gear teeth is not entirely made of steel and therefore a reduction in peak forming load of up to 30% was observed relative to a solid steel gear. However, defining the material properties and strength of the gear teeth was not investigated for hybrid gears. Further research by Wernicke *et al*. (2020) did investigate the void growth at the root of the gear teeth but only for the ISBMF of homogenous gears.

2.1.3.   Composite Cold Forging

Cold extrusion is a forging process that is characterised by high material utilisation and low cycle times which has seen its use in industry for the mass production of automotive parts (Lange *et al.*, 2008). Gumm (1964) was one of the first to attempt to join two dissimilar metals (copper and aluminium) by forward rod and backward can extrusion (Figure 12) to produce a composite cold forging. Providing the right forming conditions, metallurgical bonding has been achieved using backward can extrusion with titanium-steel (Wagener and Haats, 1994) and steel-aluminium (Wohletz *et al.*, 2013; Matsubara *et al.*, 2010) with the potential to form composite components with a lightweight core and a high strength, wear-resistant outer sheath.
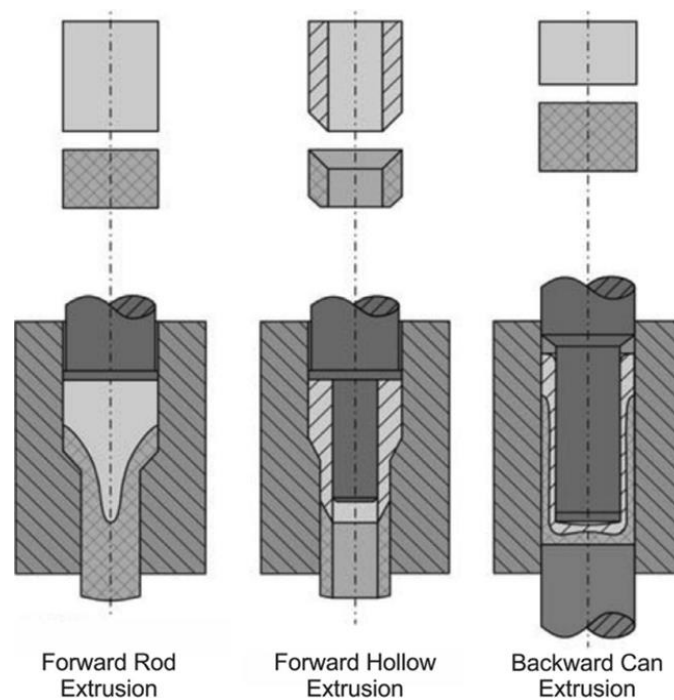
Figure 12: Variations on the cold forming process (Weber et al., 2021).

A composite gear shaft is a desirable component to be made by cold forging as most of the load bearing capacity would be carried by the outer sheathing. To achieve this design, Ossenkemper, Dahnke, and Tekkaya (2018b) first created a steel cup by backward cup extrusion into which an aluminium core was placed. The final part was then formed by forward rod extrusion as shown in Figure 13. By treating the steel cup as a thin-walled tube, a good correlation between theoretical and experiment pushout tests was found with the thickness threshold at approximately 5mm. Beyond this point, the deviation rapidly increases.

It was assumed Ossenkemper (2018b) that the joint mechanism was a force-fit and that no metallurgical bonding would be present. The maximum recorded bond strength was 5.5 MPa which compared to a theoretical bond strength of 113 MPa for metallurgical bonding. This result validated a prior numerical investigation by Ossenkemper *et al.* (2017) in which their simulations suggested that neither the surface expansion nor the contact pressure would be sufficient during composite forward rod extrusion to produce metallurgical bonding. By sandblasting the steel cups (increasing the surface roughness from 0.1 μm to 84.4 μm) prior to inserting the aluminium core, the resulting joint strength increased over 40 times with an average joint strength of 165.3 MPa: exceeding the initial shear limit of the aluminium core.
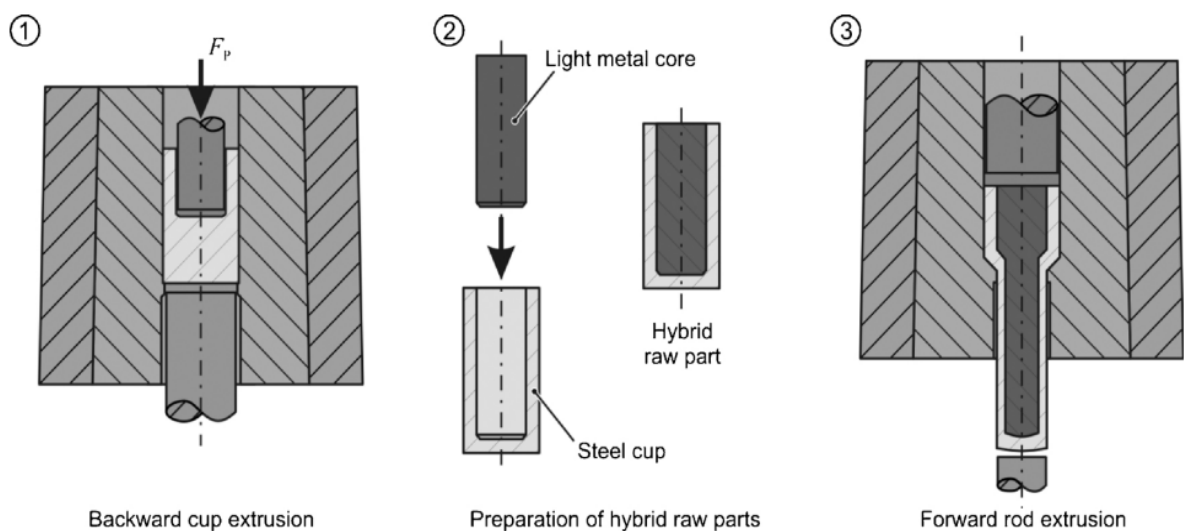
Figure 13: Process sequence of composite cold forging (Ossenkemper Dahnke and Tekkaya, 2018).

Whilst steel remains the preferred choice for the outer sheathing for composite cold forging, the core material is not limited to just aluminium. Magnesium and polyetheretherketone (PEEK) were successfully manufactured by Gitschel *et al.* (2021) and Ossenkemper (2018a) respectively. It was found that the micro form-fit joints achieved with aluminium cores could not be replicated with magnesium due to its low formability. The maximum joint strength that was achieved was only 55% of the initial magnesium shear stress. However, the superior damping properties of magnesium could benefit ultra-high cycle fatigue applications where loading exceed 10^8 cycles but small stresses are still present (Wang, Khan, and Bathias, 2012).

2.1.4.   Draw Forging

Draw forging was first patented by Jäger *et al.* (2012) and is a sheet-bulk forming process that simultaneously combines the two processes of deep drawing and cold forging. As demonstrated in Figure 14, a lightweight core acts as a drawing punch to initially form the blank around it. Once contact is made with the die shoulder, joining begins and the process can be characterised as the simultaneous redrawing of the blank and cold forging of the core. This produces a composite shaft similar to that formed by composite cold forging but is not limited to the minimum wall thickness of the outer joining partner (Weber *et al.*, 2021).
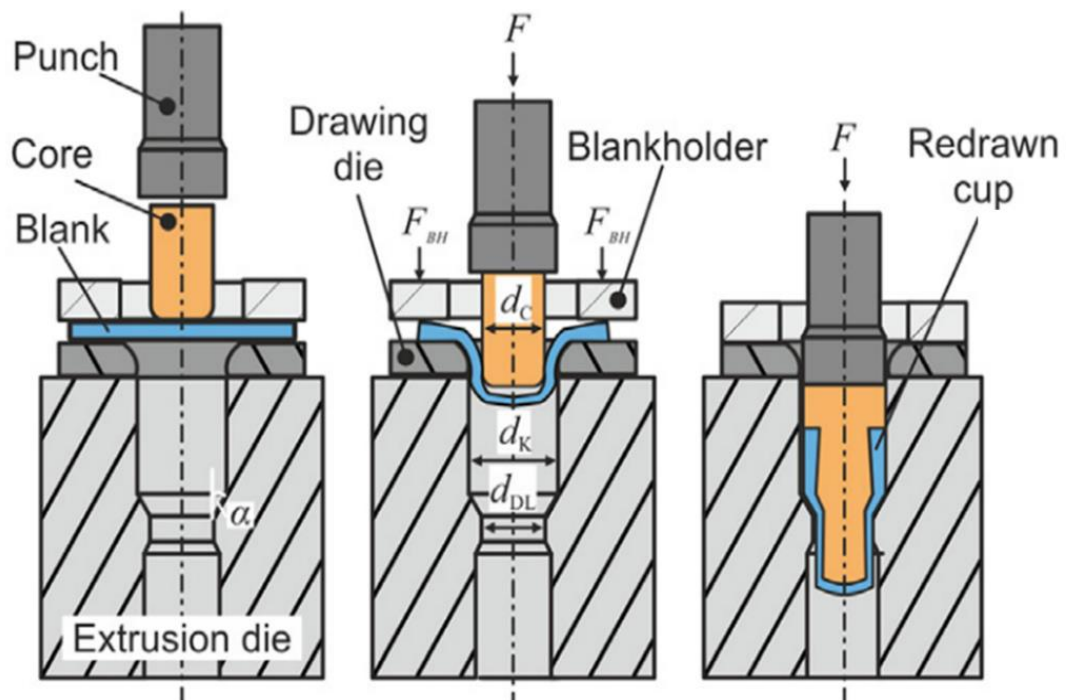
Figure 14: Process of draw forging. Symbol key: F = Direction of forming load, d_C = Core Diameter, d_K = container diameter, d_{DL} = Die land diameter, α = Die shoulder angle (Napierala et al, 2019).

Draw forging shares several process failure modes with conventional deep drawing such as wrinkling, earing, and fracture of the blank (Wu *et al.*, 2013). Unique to draw forging is the potential development of a gap between the redrawn blank and the core as the last part of the blank is pushed through the extrusion die (Figure 15). Friction at the die shoulder results in a reduced material flow velocity at the shoulder compared to the centre of the core: effectively pushing the blank away from the core and creating a gap at the interface. This difference in flow velocity increases with the angle of the die shoulder (Napierala et al., 2019) and can expose the joint to potential crevice corrosion.
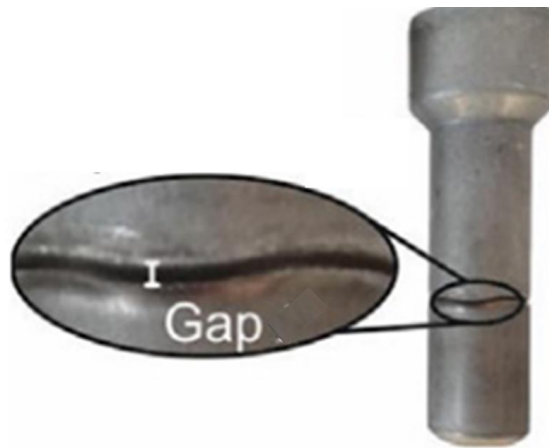
Figure 15: Process failure caused by a gap developing between the outer joining partner and the core during draw forging (Napierala et al, 2019).

Napierala et al. (2019) experimentally determined a process window and failure limits for draw forging (Figure 16) by using the same control parameters as would be typically used by forward rod extrusion: die shoulder angle and extrusion strain. Their results showed a relatively large parameter space for the new process, helped considerably by the 35% increase in the redrawing ratio relative to conventional sheet metal redrawing. This increase was attributed to the compressive stresses acting on the cup rim during redrawing and forging.
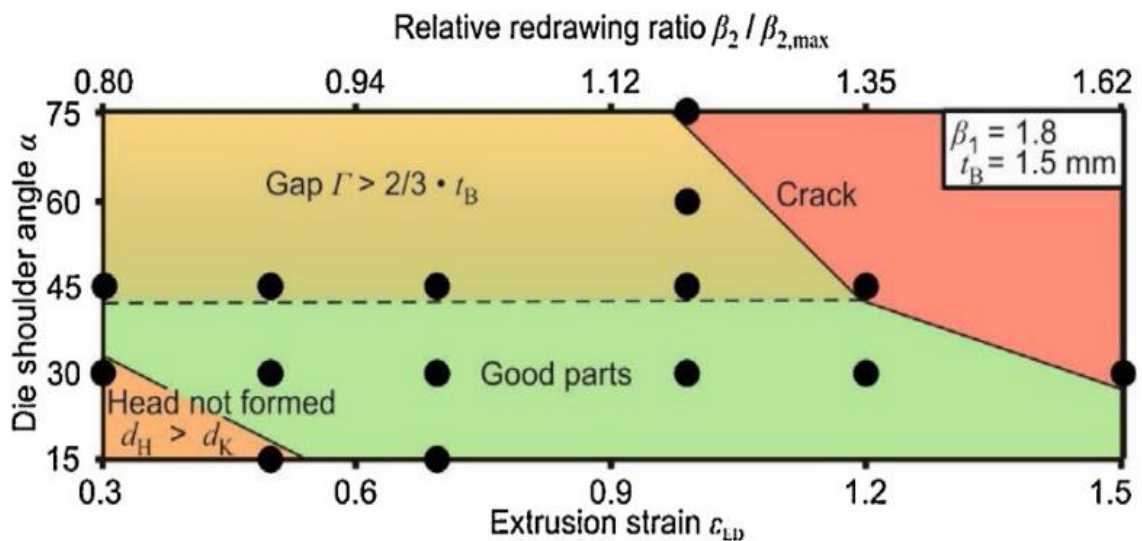
Figure 16: Experimental process window for draw forging. Symbol key: t_B = Blank thickness, d_K = container diameter, d_H = Blank height, $\beta 1$ = Drawing ratio (Napierala et al, 2019).

The minimum joint strength measured by Napierala *et al.* across all successful forgings was 40% of the shear yield strength of the aluminium core. Finite element modelling eliminated metallurgical bonding as a potential joint mechanism due to insufficient contact pressure. Instead, the axial joint strength was deemed to be formed by 1) the flow of aluminium into the rough, sandblasted surface of the steel blank forming a micro form-fit joint, 2) a macro form-fit joint caused by the non-uniform thickness of the steel shell (Figure 17) and 3) a force-fit between the blank and core caused by a difference in the elastic recovery of the two metals. The strength of the joint relative to the parent material is lower than that seen in composite cold forging, but this is most likely due to the significantly lower forming loads required in this process.
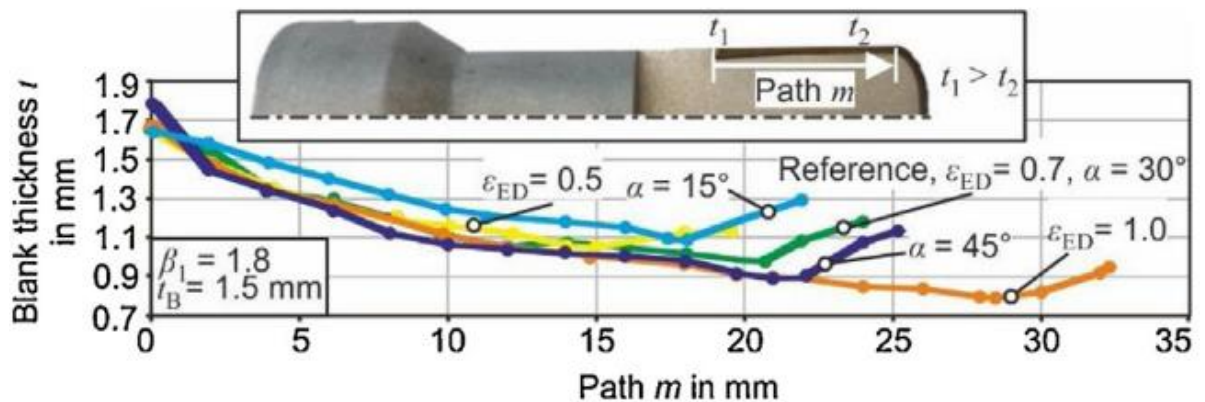
Figure 17: Blank thickness after draw-forging. Symbol key: t_B = Blank thickness, $\beta 1$ = Drawing ratio, α = Die shoulder angle, εED = Extrusion Strain (Napierala et al, 2019).

No analytical model for joint strength was proposed by Napierala *et al.* but the model developed by Ossenkemper, Dahnke and Tekkaya (2018b) could serve as a good starting point to develop from. The accuracy of their pushout model for composite cold forging was biased towards thinner wall thicknesses and could translate well to draw forging.

2.1.5.   Electromagnetic Forming

Within the family of High Energy Rate Forming methods (HERF), Electromagnetic Forming (EMF) uses Lorentz body forces to fabricate metallic parts through high-strain rate deformation. Compared to quasi-static forming operations, EMF has many desirable properties such as: being able to reach extremely high ductility of a workpiece through high strain rates, low spring back after forming, and the simplicity to form parts and joints with either a one-sided die or entirely die-less operations (Haratmeh *et al.*, 2017; Noh *et al.*, 2005).

The deformation of a workpiece can reach velocities exceeding 100m/s in less than 0.1ms (El-Azab *et al.,* 2003) with the subsequent high-speed impact against a die or mating component thought to be responsible for the low spring-back characteristics of EMF, though it wasn't until Cui, Yu and Wang (2018) that the mechanism for this was fully understood. It was found that the sudden deceleration resulted in a series of tension and compression waves through the material that converted elastic potential into plastic deformation. This significantly reduces residual stress and spring back is nearly eliminated. This phenomenon has been further studied by Cui *et al*. (2020) and Du *et al*. (2021).

EMF was identified by Rajak and Kore (2017) as a potential replacement for the conventional mechanical crimping of lightweight aluminium terminals to copper cables. Mechanical crimping creates a non-uniform pressure distribution that raises the critical notch stress that reduces the strength of the joint. By contrast, die-less electromagnetic wire crimping (EMWC) was found to create a uniform pressure distribution without the need for moulds or lubrication. They found that EMWC produced a joint with a pull-out strength of 200% that of mechanical crimping whilst also reducing the electrical resistance by 34%. The improved electrical connection was attributed to the higher compression of the wire strands and the reduced gap between the wire and terminal due to the reduced spring back associated with EMF.

The efficiency of EMF can be improved by using field shapers to concentrate the magnetic field in the forming area (Chu and Lee, 2013; Bahmani, Niayesh and Karimi, 2009). Rajak *et al*. (2018) investigated the use of field-shapers (Figure 18) to improve the efficiency of EMWC. By using Finite Element Analysis (FEA), they found that a single stepped field-shaper produced the strongest magnetic field and greatest compression of the wire and adjoining terminal. This result was validated with experimental testing with the single-stepped field-shaper producing a crimp with the greatest pull-out strength. This result was consistent across the entire discharge voltage range tested.
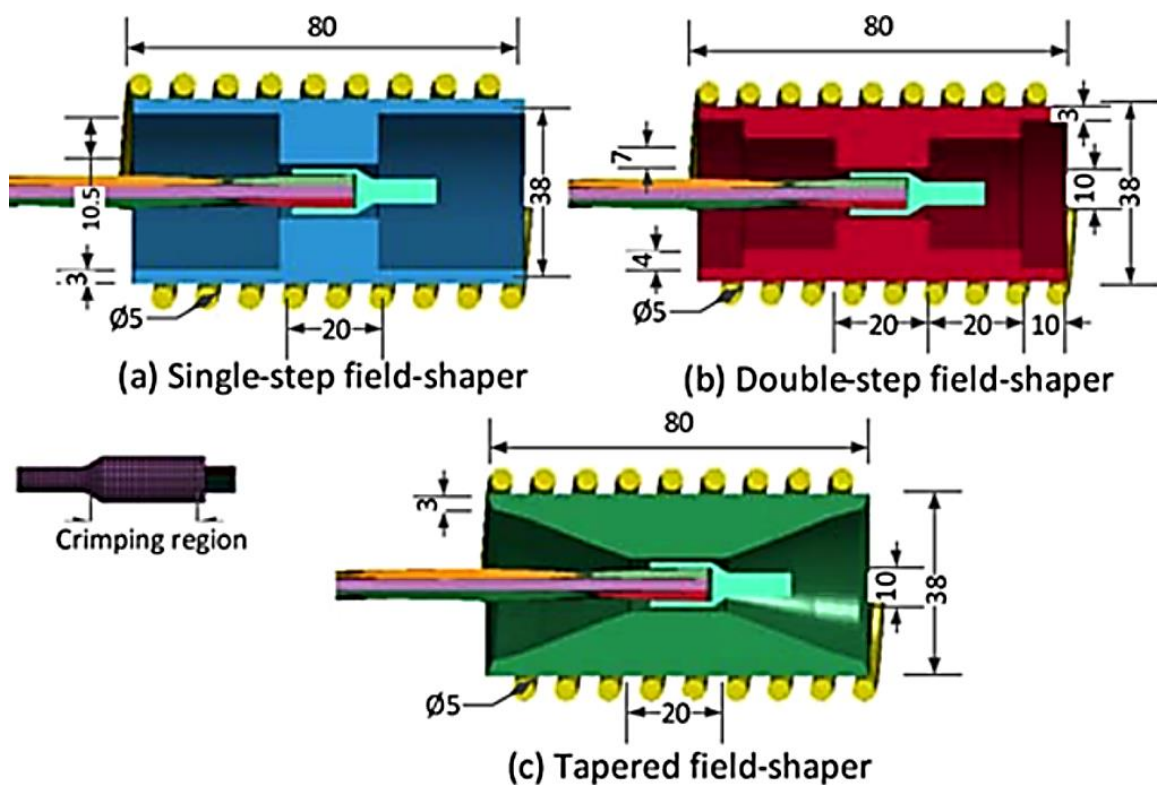
Figure 18: Cross section view of magnetic field shapers (Rajak et al., 2018).

2.1.6. Summary of Current Research

To summarise, current research within the field of cold metal joining has been dominated by the desire to create lightweight composite components typically in the form of a steel exterior and lightweight core. Across all joining processes, there has been an increase in the depth of understanding regarding their respective joining mechanisms, driven primarily by the increasing use of computer simulation tools. However, just as Groche et al. (2014) and Mori et al. (2013) had previously identified, there still remains the severe challenge in accurately predicting a joint's mechanical properties even with the use of computer simulations. This is due in part to the number of complex interactions that must be accounted for and the variation of joining conditions such as surface roughness and lubrication dynamics. It is not surprising then that closed-form analytical solutions derived from geometric interactions are rarely presented in cold metal joining research because of how many variables need to be considered for such complex 3D problems.

Figure 19 shows the most frequently occurring variables, that were considered to be critical factors for cold metal Finite Element Models (FEM). Despite this survey being conducted in 2015, its findings are still relevant to the current challenges in cold-metal joining simulations with the top identified variable as "friction conditions, coefficient and variability".
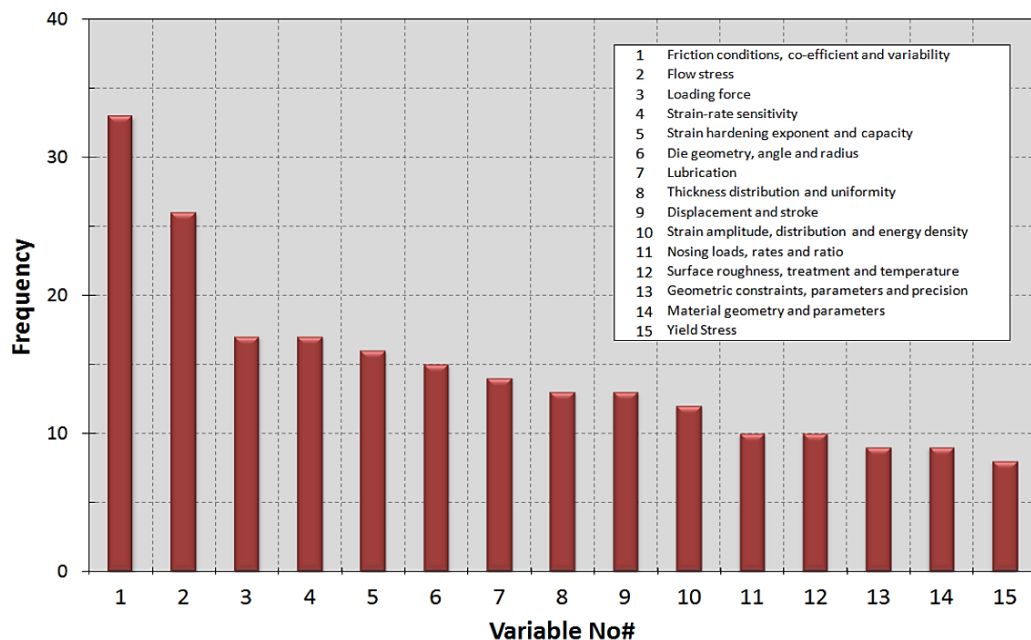
Figure 19: Frequency chart of the 15 most frequently-occurring variables, in cold-metal forming literature, considered to be critical factors identified by researchers in their work (Woodhead, 2015).

2.2.   Staking of Self-Lubricating Spherical Plain Bearings

Staking, sometimes referred to as upsetting (Kalpajian and Schmid, 2008), is part of a group of cold metal working processes that fall under the broader category of open die forging. Staking shares many of the same features and process limitations as tube flaring (Hazawi *et al.,* 2017; Fischer, Rammerstorfer and Daxner, 2006), orbital forging (Samołyk, 2013; Moon, Lee and Joun, 2007), clinching (Mucha, 2011; Borsellino, Bella and Ruisi, 2007) and heading (Cora *et al.*, 2008).

The staking of self-lubricating spherical plain bearings follows a 12-step process as outlined by the Engineering and Technical Instruction [REDACTED] (SKF, 2002). Summarised below are the critical steps in this process.

- Clean both bearing and housing by flash vapour degreasing or wiping surfaces with an approved fluid and clean cloth.

- Fit and position bearing in housing using the insertion tool (Figure 20). Do not press on the end face of the ball.

- Insert both staking anvils into the press and align the bearing and housing assembly as detailed in (Figure 2) the bearing assembly into the press.

- From the graph (Figure 21) determine the theoretical staking load and adjust the press accordingly. In the case of larger bearings with scatter loads, start with the lowest figure. When considerable operating experience has been obtained the actual staking force can be added to the drawing.

- Remove assembly from the press, carefully remove any surplus jointing compound and check breakout torque, this should be at least as high as it was prior to staking. If this is too low, increase the staking load by 5 kN (½ ton) increments and repeat until the correct torque level is obtained. Maximum staking force not to exceed 5 kN/mm (13 T/in) of staking groove diameter.

- To check the retaining strength of the swaged lip, the installed bearing is axially loaded until failure. Loads must be applied through the outer race of the bearing and not through the ball face.
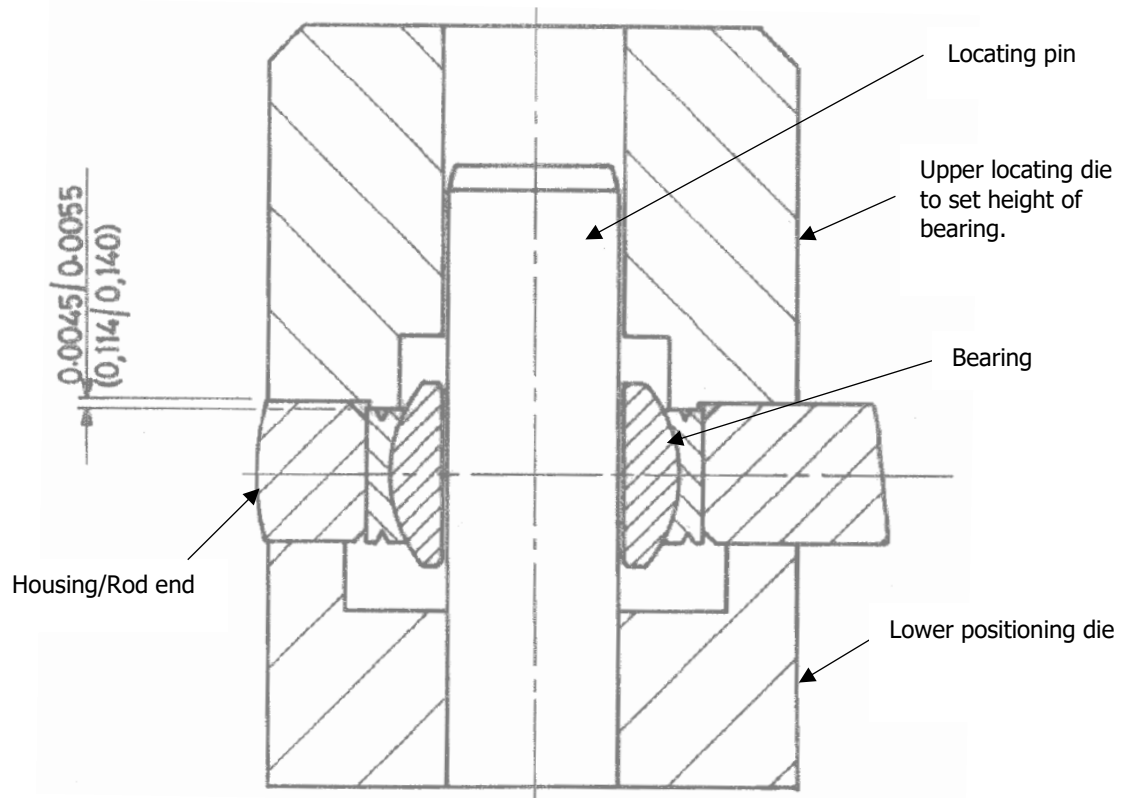
Figure 20: Fit and positioning tool used to set the bearing symmetrically within the mating housing.

Figure Redacted

Figure 21: Staking force and expected resulting pushout load.

2.2.1.   Liner Conformity

As inferred from the [REDACTED] staking procedure, the breakout torque of the final bearing is controlled by varying the applied staking force. This is because as the bearing is staked and metal is driven into the chamfer in the rod end, the rod end begins to expand and upon relaxation compresses the outer race and liner into the inner ring. The compression of the liner is referred to internally as "liner conformity" and is measured by splitting the bearing in half and taking five equally spaced measurements across the outer race width using an optical microscope as seen in Figure 22. As per AS81820 (SAE International, 2014), conformity of the bearing should be 0.28mm ± 0.03mm and is checked for the first bearing of each batch prior to staking. Therefore, it is not currently known how the staking process impacts the conformity of the bearing.
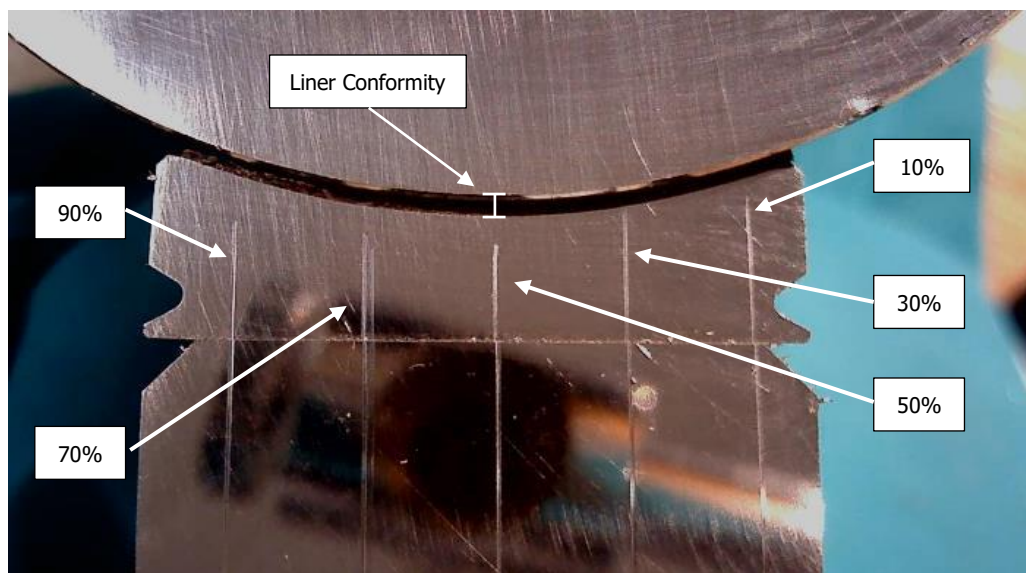
Figure 22: Measurement method for bearing conformity. Scratched lines represent 10%, 30%, 50%, 70% and 90% of the outer race width.

An alternate means of measuring bearing conformity could be to use a Non-Destructive Test (NDT) such as X-ray Computed Tomography (CT). X-ray CT has been used in industrial applications since the early 1990s (Bossi and Georgeson, 1992) in roles such as identifying porosities and defects in metal castings (Simon and Sauerwein, 2000; Wells, 2007). Maire and Withers (2014) detail the current state of the art of X-ray CT as a quantitative tool with current techniques able to produce special resolutions as small as 0.1 microns.

2.2.2. Self-Lubricating Liner, Mechanical Properties

Polytetrafluoroethylene (PTFE) has often been seen as a desirable material for a wide range of low-friction and non-stick applications such as bearings liners, composite release films and kitchenware. As PTFE wears it produces third-body debris creating a third-body film (Play, 1985; Godet *et al.,* 1980) greatly reducing its wear rate. This allows for PTFE to be used as a dry, self-lubricating wear surface. PTFE excels in high-load or slow-sliding-speed environments, but its performance diminishes at higher sliding speeds and low loads. (Santner & Czichos, 1989). In these unfavourable conditions, PTFE can exhibit friction coefficients as high as 0.3, which does not differentiate itself from many other polymers. For use in aerospace plain bearings, PTFE alone was unable to support the higher load requirements (Lancaster, 1982) which necessitated the introduction of a reinforcement.

Ampep Ltd. was founded in 1963 and produced plain bearings for the aerospace industry. In the early 1960's they introduced a self-lubricating liner called "Fiberslip", which went on to become the standard self-lubricating liner used for aerospace spherical plain bearings. Ampep Ltd was acquired by SKF in 1988 with SKF's current liner technology a derivative of the original Fiberslip product. The self-lubricating liner in use today is an orthotropic composite composed of a woven PTFE yarn and glass fibres bonded with a phenolic resin as shown in Figure 23.
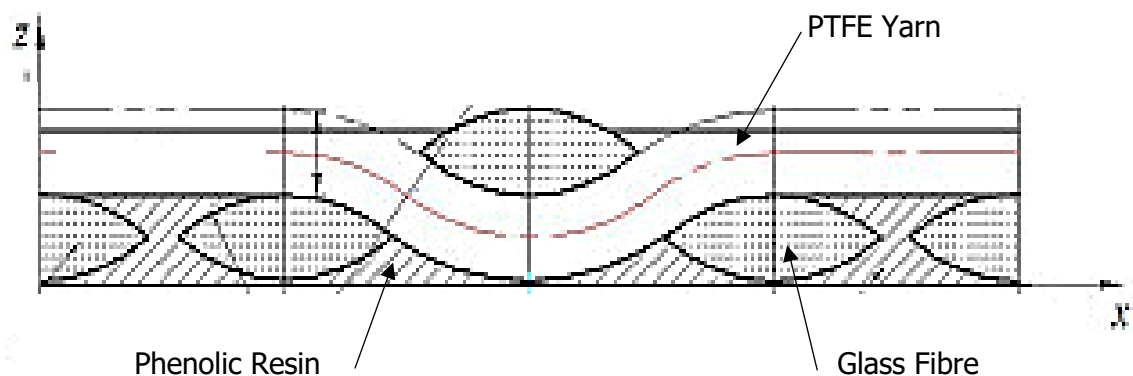
Figure 23: Section view of the fabric liner composite (Lu, Qiu and Li, 2016).

The mechanism that drives the change in torque of a bearing during staking is the inward flow of metal compressing the liner against the inner ring. The stiffness of the liner is therefore a critical parameter that influences the contact pressure on the inner ring and the subsequent torque of the bearing.

PTFE Self-lubricated liners have been extensively studied for their mechanical and wear properties (Gong *et al.*, 2018; Qi *et al.*, 2014; Shen *et al.,* 2014; Gay. 2013). Despite the anisotropic and non-homogenous nature of a woven composite, the common consensus has been to model the liner as an isotropic, homogenous solid with a compressive modulus ranging between 1.95 GPa and 12.5 GPa. By contrast, researchers who are not concerned by the torque of the bearing and instead focus on the manufacture of the bearing have found success by choosing to exclude the liner from their models entirely (Zhang *et al.,* 2017 and 2018a; Woodhead, 2015a; Orsolini and Booker, 2012). Woodhead argued that because the liner is approximately 20x less stiff than the steel of the bearing, it should have relatively little impact on the metal working process in forming a bearing.

Ampep Ltd. (Ampep, 1993) stated compressive modulus for their X1 liner of between [REDACTED] and [REDACTED] in their design manual. At the request of [REDACTED], SKF investigated the compressive modulus in more detail after it had been suspected that both X1 and X31 technologies may exhibit non-linear behaviour. The tests consisted of flat liner samples bonded and cured to a hardened steel coupon and then compressed at a range of pressures up to their maximum design limits [REDACTED]. An inductive sensor recessed into the upper anvil was used to record the compression of the liner. X1 and X31 coupons both showed a non-linear relationship between the compressive modulus and the contact pressure (Figure 24) and their relationships are defined in Equation 5 and Equation 6.
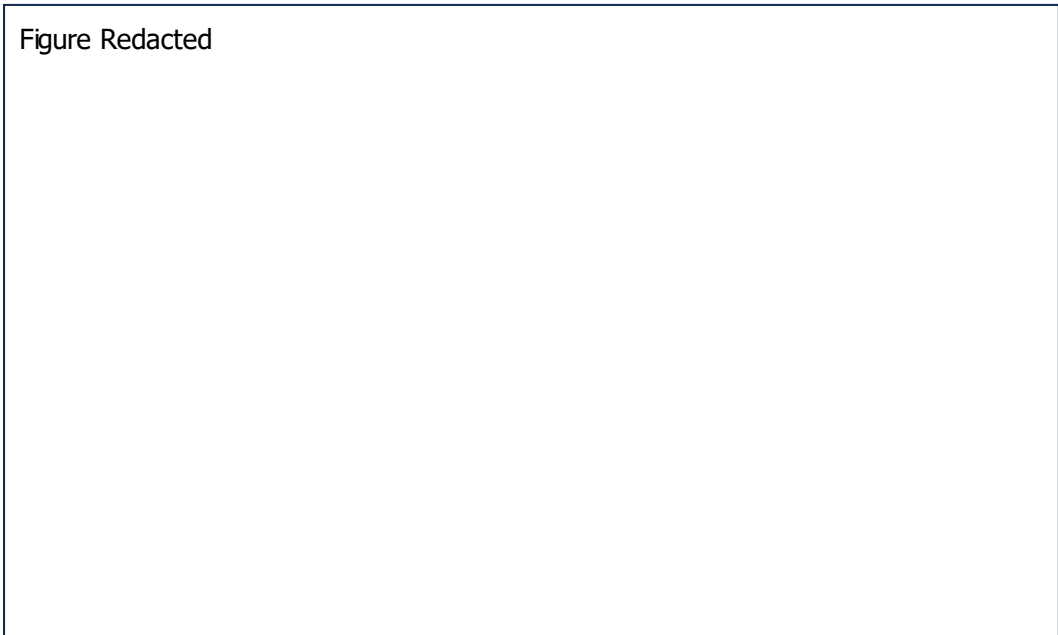
Figure Redacted

Figure 24: Graph of Young's modulus versus contact pressure for X1 liner (SKF 2008).

The compressive modulus relationship for X1 and X31 are given as

$$[REDACTED] \qquad\qquad [\,5\,]$$

$$[REDACTED] \qquad\qquad [\,6\,]$$

where P represents the contact pressure in MPa. A summary of all the compressive moduli cited in this chapter is given in Table 2.

Table 2: Summary of previous research for fabric liner stiffness.

Author(s)	Material	Modelling Approach	Compressive Modulus (MPa)
Gay, R. (2013)	PTFE fabric liner X1-40	Isotropic, Constant Stiffness	10,000
Gong, L., Yang, X., Kong, K and Zhong, S. (2018)	PTFE fabric liner	Isotropic, Constant Stiffness	2800
Shen, X., Gao, P., Liu, Z. and Chen, X. (2014)	Plain liner	Isotropic, Constant Stiffness	1,950
	Stain liner	Isotropic, Constant Stiffness	3,290
Woodhead, J. (2015a)	PTFE fabric liner X1-40	Liner Not Modelled	Assumed 6,000
Zhang, Q., Hu, Z., Su, W., Zhou, H., Qi, X. and Yang, Y. (2018a)	Liner Not Modelled		
Zhang, Q., Hu, Z., Ma, J., Qi, X. and Yang, Y. (2017)	Liner Not Modelled		
SKF (2008)	PTFE fabric liner X1-40	Isotropic, Variable Stiffness	[REDACTED]
Ampep (1993) Design Manual Suggested Value	Fibre Slip X1	Isotropic, Constant Stiffness	[REDACTED]

2.2.3. Breakout Torque

SKF measures the breakout torque by using desk-mounted torque dial gauges and the operator must manually rotate the bearing about the central axis. Care must be taken to maintain a consistent rotational speed and not to misalign the outer race by pitching it off-axis. As with any manual process, there will always be an element of human error and individual operator judgement. To reduce the influence of the operator, SKF is currently developing an automated torque measurement rig similar to the design of Öztürk *et al.* (2018). Öztürk *et al.* design consisted of a cantilever connected to the test bearing where weights could be hung off until the bearing rotates (Figure 25). In addition, a second cantilever was suspended under the bearing case for weights to be added so that a relationship between the friction coefficient and liner contact force could be investigated.

Component No	Components
1	Hook and hung weights
2	Measurement cantilever
3	Component for shaft fixing
4	Bearing case
5	Counter balance
6	Setup plate
7	Weights
8	Loading cantilever
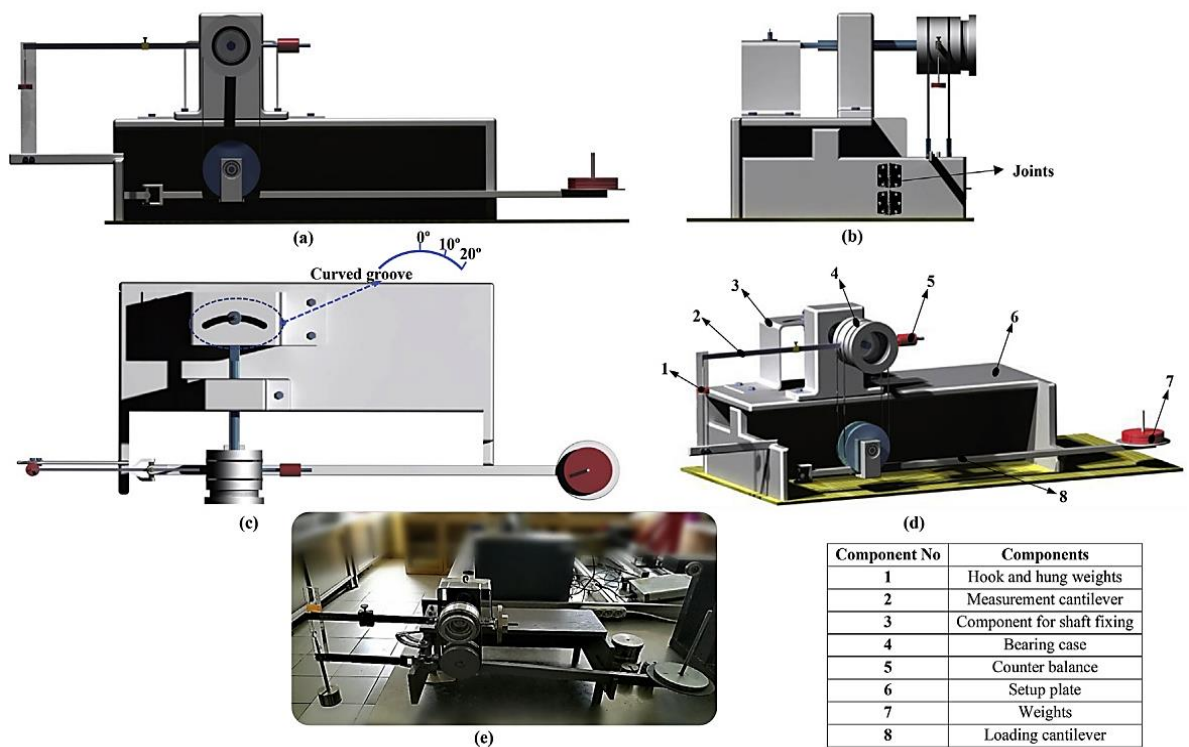
Figure 25: Front (a), side (b), top (c) and assembly (d) views of the designed experimental setup. Manufactured experimental setup (e) (Öztürk *et al.,* 2018).

As shown in Figure 26, a decrease in the friction coefficient was found as the applied load increased from 100N (0.81) to 800N (0.20). Despite the difference in liner technology (polyoxymethylene against a steel inner ring compared to PTFE/steel) a similar trend can be seen with SKF's bearings and with Play and Pruvost's research (1984) where the coefficient of friction decreases with an increase in contact pressure (Figure 27). The friction coefficient for SKF's liners was derived from data gathered from their bearing fatigue and wear test benches (Karras, 2018).
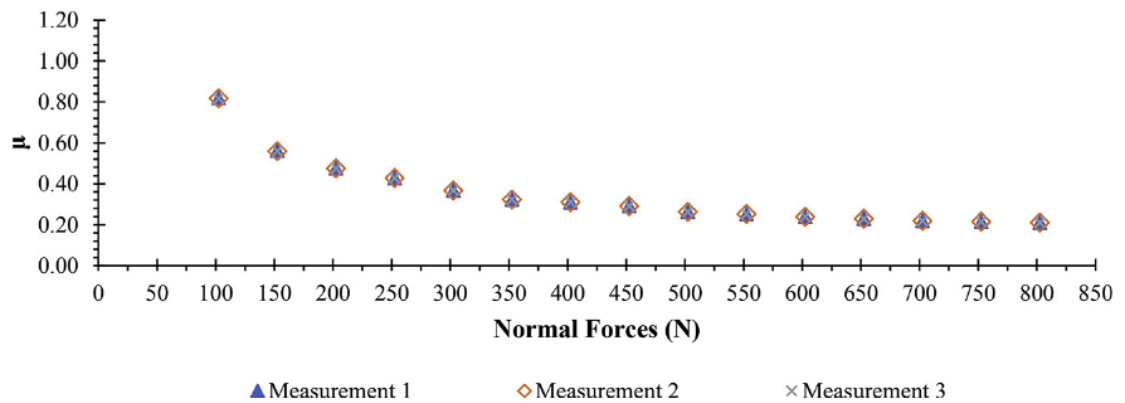
Figure 26: The friction coefficient of a spherical bearing compared to an applied load (Öztürk et al., 2018)

Figure 27: Friction coefficient of various SKF liner technologies (Karras, 2018).

For both SKF's and Öztürk *et al.* methodologies, no measurement or consideration was given to the torque of the bearing when no radial load was applied to the bearing. Due to a combination of the residual stresses in the outer race and the compression of the liner (an intentional feature of the manufacturing process), all bearings have a small degree of contact pressure at the liner-inner ring interface in their rest state (Woodhead, 2015). The complete expression to calculate the coefficient of friction is expressed as

$$COF = \frac{T}{r(F_R+F_L)}$$
[7]

where T is the torque applied to the bearing required to initiate rotation, r is the radius of the inner race and liner contact surface, F_R is the applied radial test load to the bearing (which Öztürk *et al.* referrers to as the Normal Force in Figure 26), and lastly F_L represents the resultant force induced by the outer race residual stresses and compression of the liner that act normal to the inner race and liner contact surface. Due to the presence of F_L every bearing will have a no-load breakout torque that must be overcome to initiate rotation. If F_L is ignored (as done by both SKF's and Öztürk *et al.*) then the calculated coefficient of friction becomes asymptotic and tends toward infinite as F_R approaches zero. This is an unrealist result to describe the coefficient of friction of the liner at small radial loads and is driven by discrepancy between the assumed normal force (F_R) and the total normal force (F_R+F_L) at the liner contact surface. This discrepancy would diminish however at large radial loads ($F_R \gg F_L$) and explains the plateauing of the coefficient of friction at larger applied loads and pressures as seen both SKF's and Öztürk *et al.* findings (Figure 26 and Figure 27).

2.2.4. Manufacturing Challenges

From an internal process report of the staking manufacturing channel (SKF, 2021), a common concern was raised regarding the torque change of the bearing post-staking. As of the introduction of [REDACTED], the proof load is determined by pushing out the bearing via the outer race instead of applying the load through the ball face. The reason for this change is unknown to the current staff at SKF but it is believed to be an attempt to apply the force more directly onto the staked lip. This change has had a detrimental effect on the proof load of the bearing as the operators have had to consistently use a higher staking force (than that derived from Figure 21) to achieve the same proof load when pushing out on the ball face. This observation was later confirmed as part of a separate investigation into the staking process (Appendix A).

According to the operators, the increased staking load is leading to a higher frequency of staked bearings exceeding their maximum permissible breakout torque resulting in time-consuming and costly reworking.

The pushout strength plot from Figure 21 was derived from the slab method and by approximating the cross-sectional of the staked lips after final forming. Whilst this has proven over time to give a reasonable estimate of the expected joint strength, it has no consideration for any other geometric feature of the bearing nor the influence of manufacturing tolerances. As an example, in November 2022 (SKF, 2022b) two identical batches of bearings were due to be staked: one batch into a rod end produced by SKF (54 bearings) and the second into a customer provided rod-end (38 bearings). The staking chamfer cut into the rod end produced by SKF measured 0.59mm x 45° and the customer provided rod-end measured 0.56mm x 45°.

Despite the customer's rod-end chamfer being within the tolerance band that SKF stipulated, to achieve the same pushout load the customer rod-end required approximately 10% greater staking force on average when compared to the SKF produced rod-ends. The resulting breakout torque of the customer rod-ends was significantly increased, typically ranging between two to three times that of the SKF produced rod ends. This was a unique case where only a single parameter was different between two batches; however, this is not normally the case as each batch of bearings and rod-ends are unique to every customer. This makes identifying quantifiable trends and patterns hard to establish.

2.2.5. Alternative Spherical Bearing Retention Methods

Whilst anvil staking is the most common method for the installation of spherical bearings, four alternative methods are also used.

Roller Swaging

The roller swaging process consists of two to three rollers that rotate around the outer race groove and forms the staking lip into the housing chamfer (Figure 28). Instead of staking the entire staking lip at once, roller swaging is an incremental forming technique that requires a lower maximum force to generate the desired shape at the cost of requiring multiple passes to form (Samołyk, 2013). Roller swaging is the preferred assembly method for in situ applications such as installation into bulkheads or aircraft maintenance due to the lower forming loads and the possibility to use hand tools instead of industrial presses (Drgon, 2020). This method can permit bearing replacement without damaging the housing.
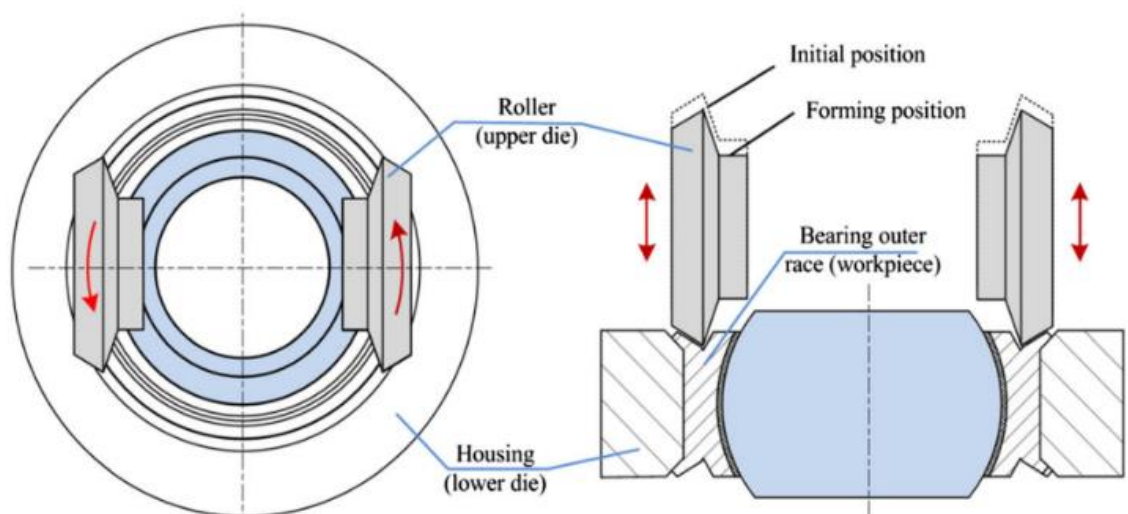
Figure 28: Roller swaging process (Zhang *et al.*, 2018a).

Segmented Stake

This is a common method for installing bearings (both spherical and rolling elements) with hardened races into ductile housings. The housing is designed slightly thicker than the width of the bearing outer race and is staked in one step but only partially around its circumference in 4-8 segments. Examples of segmented stake ball impression die tools are shown in Figure 29.

Ball Impression/Point Stake

This method is used where ease of installation is required with non-grooved spherical bearings. An anvil containing 3-8 ball bearings (or done manually with a die punch) deforms the housing into the outer chamfer of a bearing (Figure 29). Because of the minimal contact between the die and housing, this method can only sustain minimal axial loads but can be easily performed in the field due to the low staking forces required.

Figure 29: Ball Impression dies (Lower middle) and Segmented staking die tools (Upper right). Impression patterns for these two tools can be seen in the upper left block (Carter, 2020).

Swaged Sleeve

This method is most often used for retaining bearings in magnesium housings when both outer race and housing are made of hardened materials. A ductile intermediate sleeve is staked into chamfers in both the bearing and housing, providing limited axial load capacity but replaceable without damaging the housing.
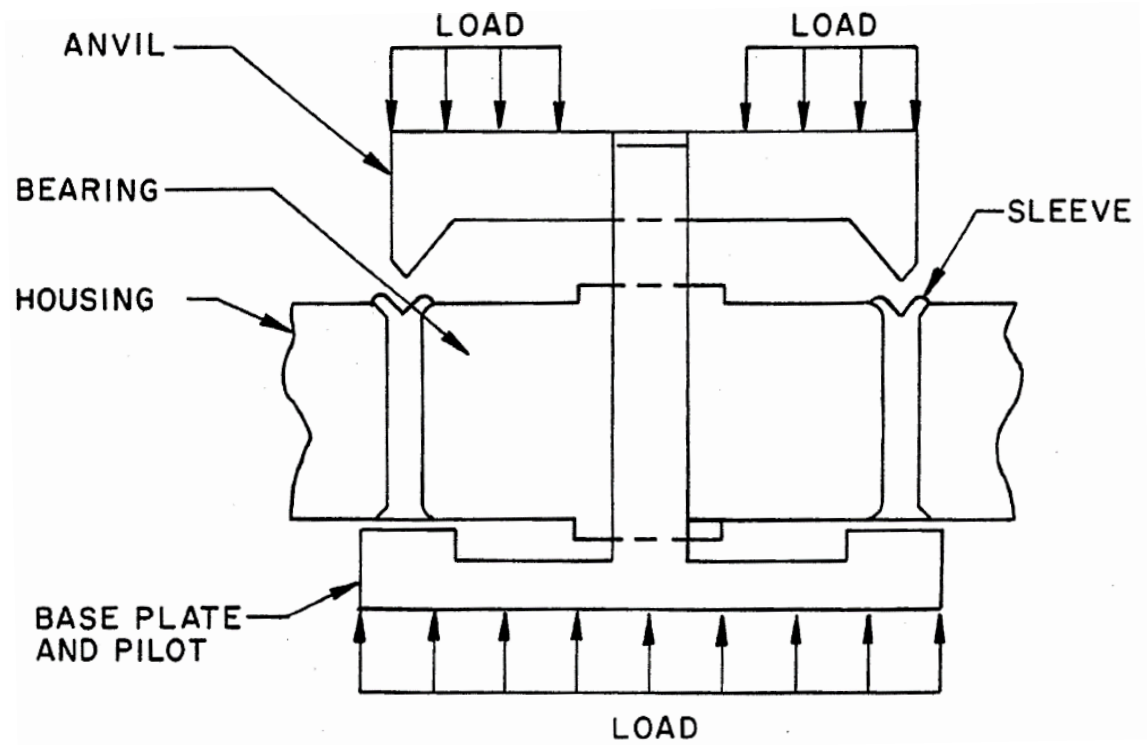
Figure 30: Swaged Sleeve retention method (Aerospace Industries Association, 2020)

Swaged Sleeve

2.2.6. Roller Swaging Modelling

To the author's best knowledge, no published work explicitly focuses on the modelling of anvil staking, ball impression, segmented staking, or swaged sleeve retention methods. By contrast, numerous recent publications investigate the process parameters of roller swaging using computational models (Wang *et al.,* 2021 and 2022, Zhang *et al.,* 2017 and 2018a). In Zhang *et al.* 2017, an analytical plane-strain model was proposed to calculate the forming load as a function of roller depth (Figure 31). This model is representative of a near fully formed bearing to bias the accuracy of the model towards the most critical and high-load phase of the assembly process.
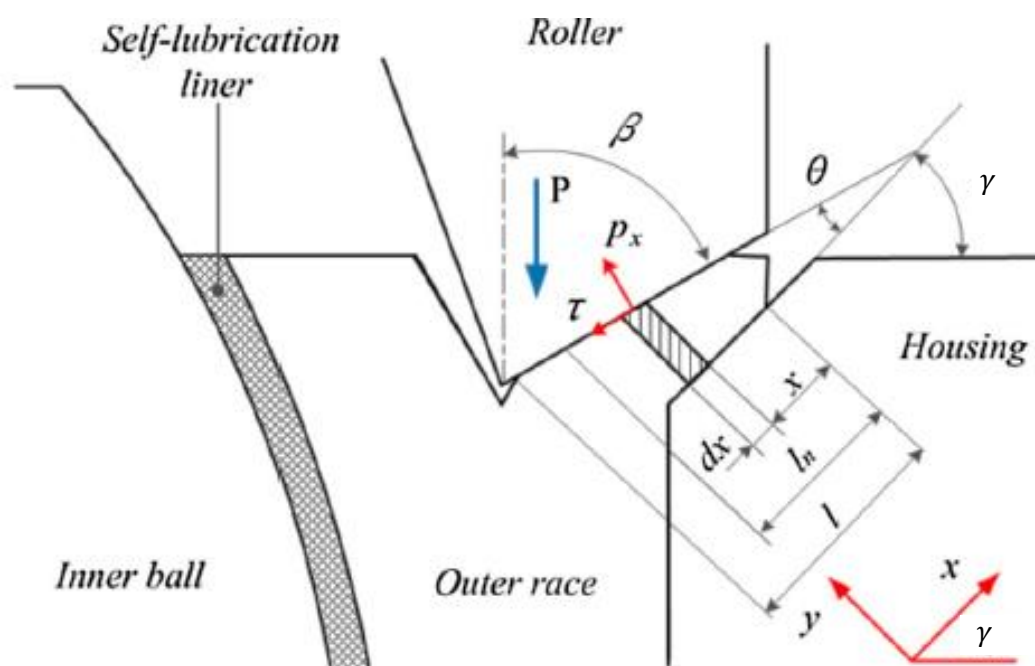
Figure 31: The forming load in roller swaging (Zhang *et al.,* 2017). The Forming load is represented as the variable *P.*

In developing their plane strain model, Zhang *et al.* made five assumptions to simplify the problem when creating their analytical solution:

- Deformation is homogeneous and volume invariable.

- A constant friction coefficient can be applied and is negligible sometimes.

- The circumferential metal flow is negligible in cross-section.

- The housing and roller are regarded as rigid.

- The elastic deformation is negligible.

Similar assumptions were used by Moon, Lee and Joun (2007) and Samołyk (2013) to create analytical models for rotary forming processes. The forming load from Zhang's *et al.* (2017) model was defined as the product of the contact pressure between the roller and swaging lip and the surface area of that contact area. By assuming the forming load is uniformly distributed in the contact area, the forming load is represented as

$$P = \bar{b} \int_0^{L_f} \sigma_y \; dL_f \, ,$$
[8]

where $\bar{b}$ is the average width of contact area between roller and flanging lip, L_f is the length of the contact area on the flanging lip and σ_y is the contact pressure in the vertical direction. Figure 32 is a detailed view of the contact zone and σ_y can be expressed as

$$\sigma_y = P_x \sin(\beta) \pm \tau \cos(\beta) \, ,$$
[9]

where P_x is the normal contact pressure between the roller and swaging lip.
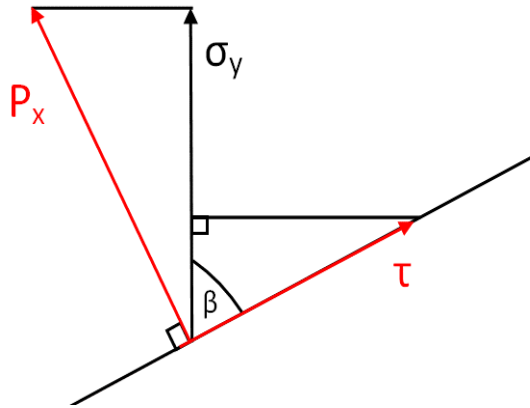
Figure 32: Normal and shear stress at the contact zone between roller and swaging lip.

By substituting Equation 9 into Equation 8, the forming load can be expressed as

$$P = \bar{b} \left[\int_0^{L_f} P_x \sin(\beta) \, dL_f + \int_0^{L_{fn}} \tau \cos(\beta) \, dL - \int_{L_{fn}}^{L_f} \tau \cos(\beta) \, dL_f \right] ,$$
[10]

where L_{fn} represents the position of the neutral axis.

In their derivation, Zhang (2017) eliminates the positive and negative shear components from Equation 10 as it is assumed that the sum of their components to be negligible when compared to the normal contact pressure. Similar simplifications were taken in forming force studies for other rotary forging processes with a plane strain analysis where the effect of friction was ignored on rolling force. (Zhang, 2009; Kazeminezhad and Karimi Taheri, 2006; Cao, 1987; Ma, 1980).

The coordinate system established in Figure 31 aligns the x-axis with the chamfer angle of the bearing housing. Using this local coordinate system, The x-axis projection of roller contact face (L_f) becomes L, and small changes in the length of the roller contact face (dL_f) can be expressed in the local coordinate system as $dx/\cos\theta$. Equation 10 can now be simplified and written as

$$P = \bar{b}\left[\int_0^L P_x \sin(\beta)\frac{dx}{\cos(\theta)}\right]. \qquad [\,11\,]$$

Translating from the local coordinate system from Figure 31, the global horizontal projected length of L is equal to $L\cos(\gamma)$. Multiplying Equation 11 by $\frac{L\cos(\gamma)}{L\cos(\gamma)}$ gives

$$P = \bar{b}L\cos(\gamma)\frac{1}{L\cos(\gamma)}\left[\int_0^L P_x \sin(\beta)\frac{dx}{\cos(\theta)}\right] = S\bar{p} \qquad [\,12\,]$$

$$\text{and} \quad \begin{cases} S = \bar{b}L\cos(\gamma) \\ \\ \bar{p} = \dfrac{1}{L\cos(\gamma)}\left[\displaystyle\int_0^L P_x \sin(\beta)\frac{dx}{\cos(\theta)}\right] \end{cases} \qquad [\,13\,]$$

where S is the horizontal projected area of the flanging lip and $\bar{p}$ is the average contact pressure in the vertical direction. To enable the mechanical analysis, the flanging lip is divided into two zones ($S_1\ and\ S_2$) as shown in Figure 33 and therefore Equation 12 is instead written as

$$P = S_1\bar{p}_1 + S_2\bar{p}_2. \qquad [\,14\,]$$
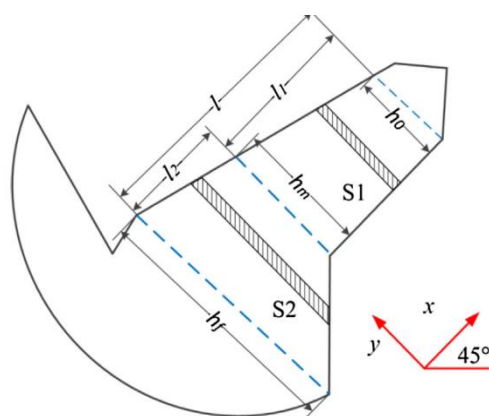
Figure 33: Sections S1 and S2 in the deformation zone in the flange/staking lip (Zhang *et al.,* 2017).

From a competitor analysis carried out by SKF (2017), it was found that the final geometry of a roller swaged bearing was almost indistinguishable from an anvil staked bearing with regards to the geometry of the final formed staking lip. Therefore, Equation 13 could be modified to create a plane strain model for Anvil Staking by substituting the horizontal projected area (S) of the rollers for a staking anvil.

2.3. Tribology

Tribology is a broad field that covers the study of friction, wear, and lubrication and how these influence the interactions between surfaces (Grote and Antonsson, 2009). Compared to hot metal working, the stresses in the dies for cold forming processes are quite high and, consequently, predicting the forming load and stresses in the dies is an important part of die geometry, energy consumption and surface finishes (Kobayashi, Altan and Oh, 1989). The applied forming load, component geometry and the stresses imparted onto the component are all heavily affected by the friction between the component and the die interface (Cora *et al.*, 2008).

2.3.1. Friction-Pressure Relationship

Friction is the measure of the resistance to relative motion between two or more surfaces in contact with one another. This impedance to motion affects the flow of material during cold working processes. A number of factors can influence the coefficient of friction and it is inherently difficult to precisely quantify even within a simple static problem (Kobayashi, Altan and Oh, 1989). Some of these factors include but are not limited to, surface roughness, use of lubricates, workpiece and die material combinations, temperature, contact pressure, surface contaminates, third-body debris and corrosion. With respect to cold bulk-metal forming, one of the largest factors leading to a loss in production is excessive die wear or failure where friction is the leading contributing factor (Buschhausen *et al.*, 1992), highlighting the importance of understanding this phenomenon. Table 3 lists the typical coefficient of friction associated with common metal-forming processes.

Table 3: Typical range of friction coefficients for metal working processes (Kalpajian and Schmid, 2008).

Process	Cold Working (μ)	Hot Working (μ)
Rolling	$0.05 - 0.1$	$0.2 - 0.7$
Forging	$0.05 - 0.1$	$0.1 - 0.2$
Drawing	$0.03 - 0.1$	-
Sheet-Metal Forming	$0.05 - 0.1$	$0.1 - 0.2$
Machining	0.5 - 2	-

Friction coefficient evaluations and simulations are further complicated by the frictional force not being linearly related to the normal force imparted to the workpiece during metal forming processes (Kalpajian and Schmid, 2008). This has resulted in the common practice of a single 'global' value to be set for the friction coefficient for each computational simulation (Cora *et al.*, 2008; Orsolini and Booker, 2012). Given the costly and time-consuming nature to obtain friction coefficient data, it is therefore normal practice that this data is often taken directly from reference texts.

The most accepted theory of friction is the *adhesion theory of friction* and is formed from the observation that two clean, dry, and seemingly smooth surfaces do not contact each other over the apparent area that can be seen (A). Instead, the real contact area (A_r) is significantly smaller and is formed via the contacts between the surface asperities. These contact points are referred to as junctions and under small normal forces the normal stress remains within the elastic limit of the material. The mechanical interaction at these junctions produces the commonly observed result of a linear relationship between the tangential frictional stress and the applied normal stress. This relationship is defined in Coulomb's law as

$$\tau_f = \mu\sigma_N, \qquad\qquad [\,15\,]$$

where τ_f is the tangential frictional stress, σ_N is the normal contact pressure and μ is the coefficient of friction. As the normal force increases, localised plastic deformation begins to occur at the junctions which increases their size until the real contact area approaches the apparent contact area (Figure 34). The interface at the junctions can develop an adhesive bond involving atomic interactions, mutual solubility and diffusion often referred to as micro-welding (Kalpajian and Schmid, 2008).
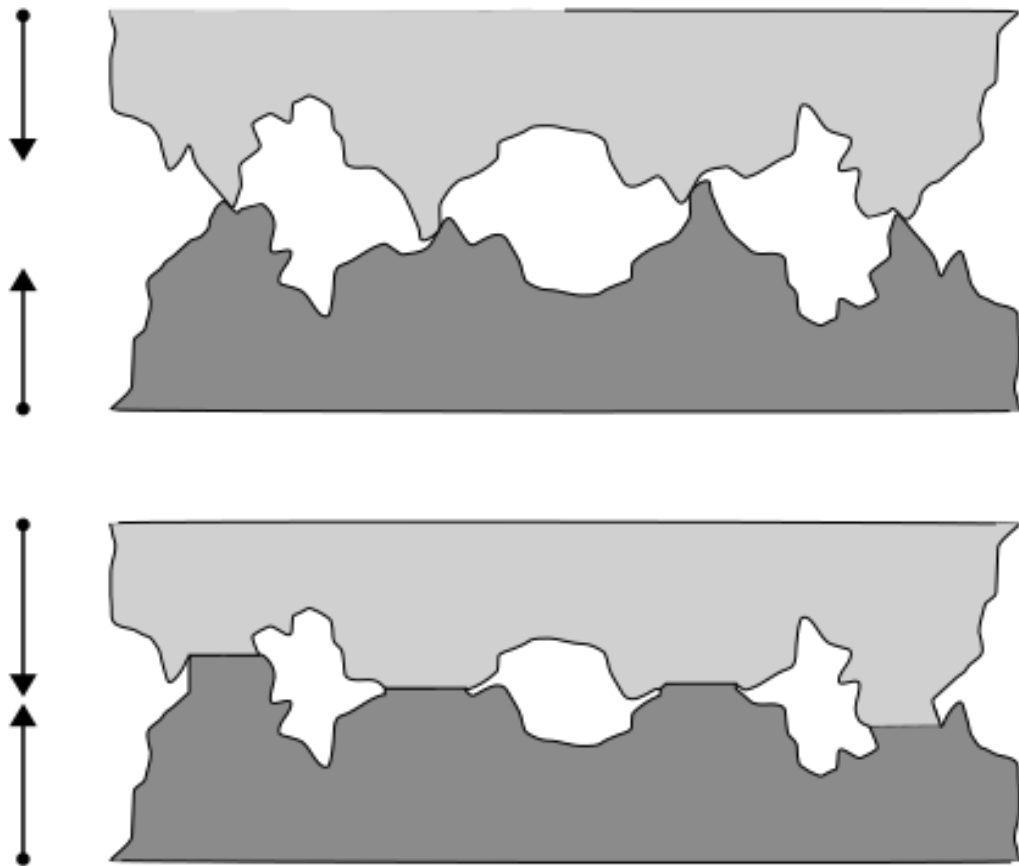
Figure 34: The junction area as the normal force increases and localised plastic deformation begins to occur (Shaun, 2007).

If the shear strength remains constant during this process, then for a fixed friction coefficient there is a point at which a sufficiently large normal force will generate a frictional stress greater than the material shear strength: a condition known as sticking (Altan, Ngaile, and Shen, 2005). Under this condition, the two bodies behave as one and any relative movement will occur via shearing of the bulk material as appose to sliding at the junction. This creates an upper bound to the frictional force that is equal to the material's shear strength (Figure 35). If the normal load continues to increase beyond the yield strength of the material, then because of the frictional shear stress remaining constant, the coefficient of friction must decrease as defined by Equation 15.
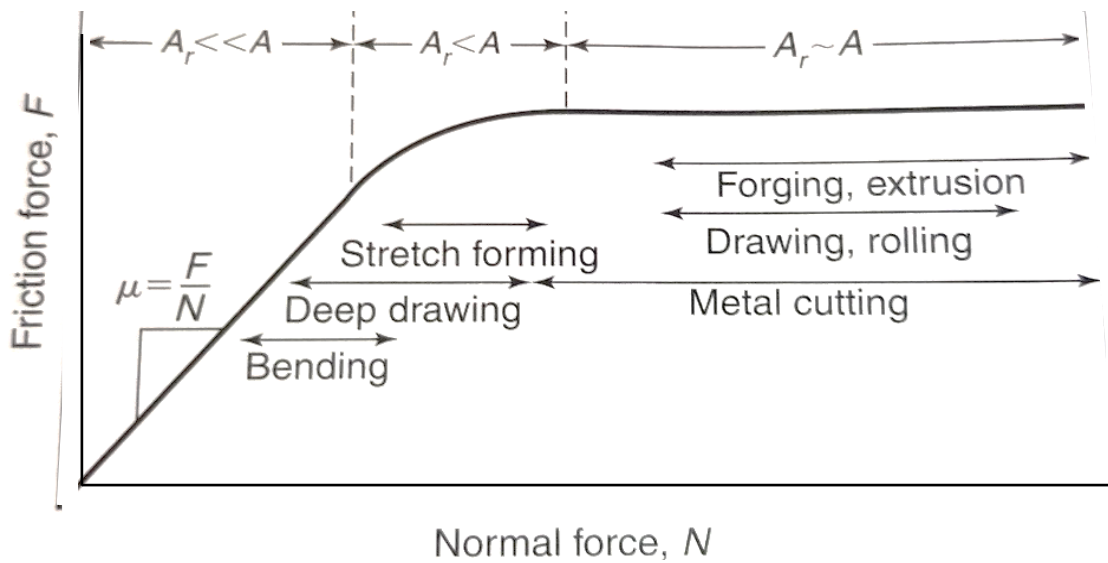
Figure 35: Relationship between the friction force and the normal force (Kalpajian and Schmid, 2008). A_r is the real contact area and A is the apparent contact area.

From Figure 35, it is clear that the elastic region ($A_r \ll A$) is sufficiently described by Coulomb's law but cannot simultaneously describe the sticking region ($A_r \approx A$). This region is better described by the Tresca friction model (Kobayashi *et al.*, 1989) in which the tangential frictional stress is assumed to be constant and is expressed as

$$\tau_f = mk, \qquad\qquad [\ 16\ ]$$

where m is the friction factor and k the materials shear strength. This model is also referred to as the Constant Friction model (Orsolini and Booker, 2012).

The concept of a friction-pressure relationship that varies with pressure has been proven in multiple works such as those by Woodhead, Truman and Booker (2015b), Orsolini and Booker (2012), Cora et al. (2008), and Tang and Kobayashi (1982) and in their conclusions, they all corroborate that neither Coulomb's law nor Tresca's friction model can accurately model friction across the entirety of a bulk metal forming processes because the contact pressure does not remain constant throughout the process.

This problem can be seen in the analytical models that have been created to describe the cold forming of metal in a variety of open-die upsetting processes (Fischer *et al.*, 2006; Foster *et al.*, 2009; Gisbert *et al.*, 2015) including the roller swaging of spherical bearings (Zhang *et al.*, 2017 and 2018a). All of these models take the form of a closed-form solution which cannot accommodate dynamic variables and therefore "fail to accurately predict the shape of the flow curve and magnitude of the forming load" (Woodhead, 2015a, p.63).

Alongside a coefficient of friction, these dynamic variables can also include boundary conditions and material flow stress. Both Foster and Gisbert did find some improvements by incorporating correction factors to the end of their equations, but this only produced satisfactory results across a narrow range of their respective forming models.

Incorporating dynamic variables into a model requires an iterative feedback loop to continuously update those variables as the solution evolves. This functionality is built into FEM software packages and provides the best method to predict the load history during a forming operation.

2.3.2. Ring Compression Test

Based on the original work of Kunogi (1956), Male and Cockcroft (1966) published a standard methodology for determining the coefficient of friction through the use of ring compression tests. This test method has been proven successful in determining both the coefficient of friction and friction factor for steels (Sofuoglu *et al.*, 2001; Martin *et al.*, 2015; Woodhead, Truman and Booker, 2015b) and has gained wide acceptance "particularly for bulk deformations processes such as forging" (Kalpajian and Schmid, 2008, p.141).

The ring compression test consists of a ring specimen compressed axially between two flat and parallel platens such that the specimen undergoes plastic deformation. If the interface between the specimen and dies is of sufficiently low friction (assuming isotropic material properties, perfect-plastic behaviour, and homogenous deformation), then the inner diameter of the ring will expand together with the outer diameter. As friction increases, sticking will occur at the interface which resists the outward flow of the material. Once the friction coefficient reaches a critical value it becomes favourable for material to flow inwards, resulting in the reduction of the inner diameter which is shown in Figure 36.
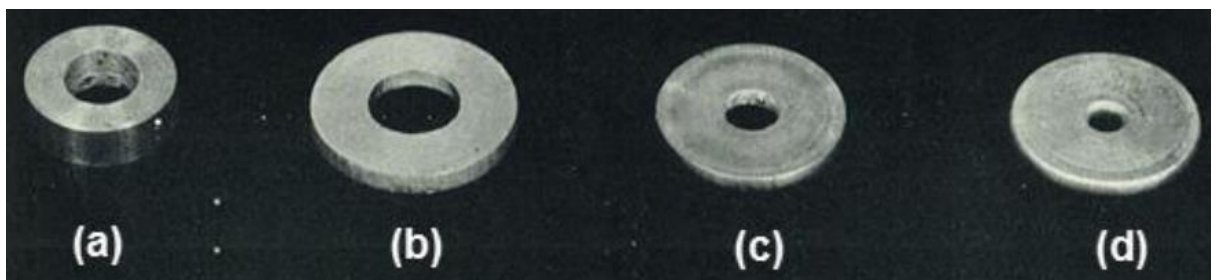
Figure 36: Test specimens from a ring compression test reduced to 30% of the original height. (a) Original undeformed specimen (b) Low friction (c) Medium friction (d) High friction. (Kalpajian and Schmid, 2008).

Using this relationship, Friction Calibration Curves (FCC) were generated by Male and Cockcroft to relate the percentage reduction of the internal diameter to the percentage reduction in height of the specimen for a range of friction coefficients (Figure 37). Friction coefficients are only defined at pressures beyond the yield strength of the material because measurements can only be taken once plastic deformation has begun.
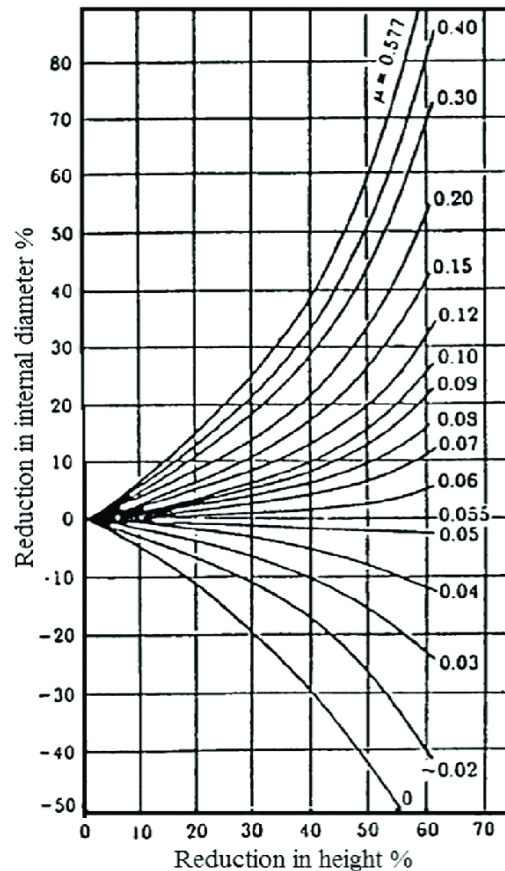
Figure 37: Typical friction calibration curve in terms of the coefficient of friction (Male and DePierre, 1970).

At pressures greater than the yield strength, the maximum coefficient of friction that can be defined is 0.577. By using Coulomb's law (Equation 16), if the coefficient of friction exceeds 0.577 then for normal contact pressures greater than the yield strength, the resulting frictional stress would be greater than the shear strength of the material (0.577 for the Von-mises criterion and 0.5 for the Tresca criterion). Therefore, if the friction coefficient was to exceed 0.577 then it would be impossible to distinguish between the surfaces relatively sliding or if the surfaces remain locked and instead the bulk of the material is beginning to deform in shear.

One of the main challenges with the ring compression test is the difficulty in accurately measuring the inside diameter at large compressions. Recent work by Hu *et* al. (2023) Dwivedi, *et al.* (2021), and Kaviti and Thakur (2021) have sought to mitigate this problem by machining a step or boss into the outer diameter (Figure 38) and using the outer diameter to determine the friction coefficient. Their results have shown promise for this technique, but work is still ongoing to determine the optimal geometry for the external steps.
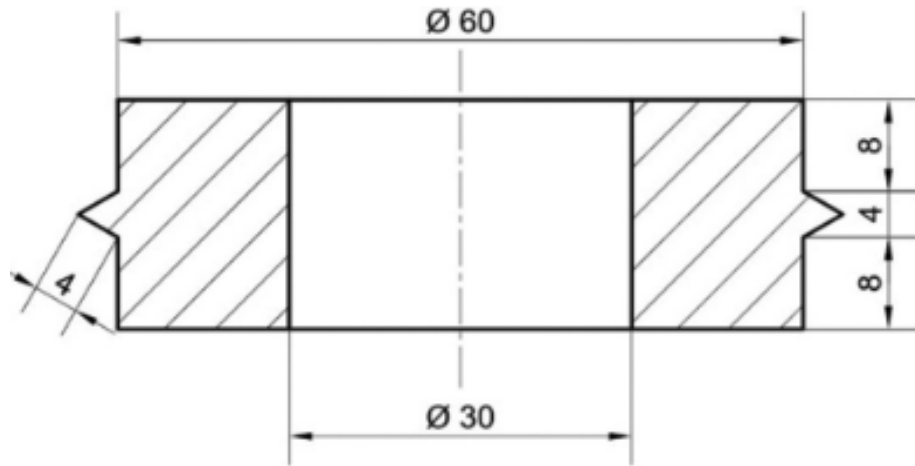
Figure 38: The geometry of ring with isosceles triangular boss (Kaviti and Thakur, 2021).

2.3.2.1. Friction Calibration Curve

The friction calibration curves from Figure 37 were generated from the friction factor m by Male and Depierre, where

$$
m = \left[\frac{-1}{2\frac{R_o}{h}\left(1 + \frac{R_i}{R_o} - 2\frac{R_{avg}}{R_o}\right)} \right] * \ln\left[\left(\frac{R_i}{R_o}\right)^2 \frac{\left(\frac{R_{avg}}{R_o}\right)^2 + \sqrt{3 + \left(\frac{R_{avg}}{R_o}\right)^4}}{\left(\frac{R_{avg}}{R_o}\right)^2 + \sqrt{3 + \left(\frac{R_i}{R_o}\right)^2 + \left(\frac{R_{avg}}{R_o}\right)^4}} \right], \qquad [\,17\,]
$$

and R_i is the inner radius, R_o is the outer radius and h is the height of the specimen. R_{avg} is the mean radius of the ring and is defined as

$$
R_{avg} = R_o \sqrt{\frac{\left(\frac{R_i}{R_o}\right) + \left(\frac{\Delta R_i}{\Delta R_o}\right)}{\left(\frac{R_o}{R_i}\right) + \left(\frac{\Delta R_i}{\Delta R_o}\right)}}, \qquad [\,18\,]
$$

where ΔR_o and ΔR_i is the change in outer and inner radius of the ring respectively. The friction factor from Equation 17 was empirically linked by Male and DePierre (1970) to the coefficient of friction as

$$
\mu = \frac{m}{\sqrt{3}}. \qquad [\,19\,]
$$

The ring compression test method separates the displacement caused by plastic deformation from the mechanical properties of the material, therefore eliminating the need to know the flow stress of the material or record the force during the test. With only the measurements of the initial and final dimensions of the specimen required, the ring compression test is a relatively simple test. This simplicity also makes it suitable for strain-rate sensitivity and high temperature tests.

However, the earlier made assumption (perfect-plastic/non-strain hardening material) and other real-world effects (such as barrelling) result in errors in the FCCs generated by Equation 17. This is not a concern when determining the relative frictional differences between tests (such as assessing the performance of different lubricants) but to quantify the absolute friction of a specimen, another method of calibrating the FCCs is required such as generating FCCs using computational modelling (Kahhal et al., 2021; Martin et al., 2015; Woodhead, 2015a; Horwatitsch, Merstallinger and Steinhoff, 2012).

As part of Woodhead's doctoral thesis (2015a), a variable friction model was developed using ring compression tests after it was shown that a constant friction coefficient was not suitable to predict the load history of the forming of the outer race during spherical bearing manufacture (Figure 39). FCCs for Woodhead's ring compression specimens were generated via computational models with friction coefficients varying from 0–0.5 (Figure 40) and compared against the experimental results.
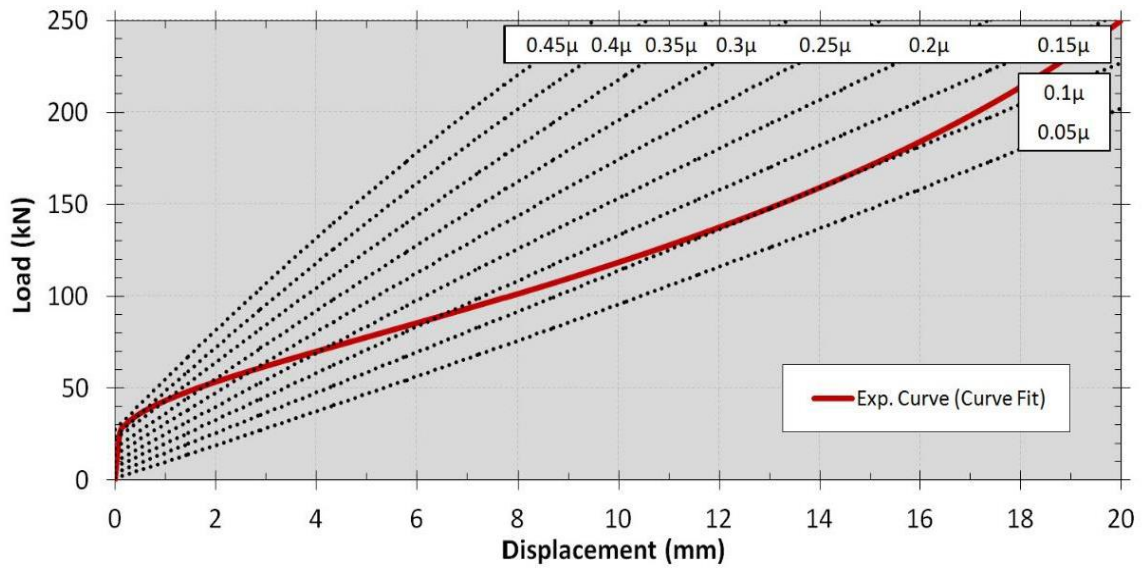
Figure 39: Load history of finite element simulations of the nosing operation with varying friction coefficients compared to experimental data (Woodhead, 2015).
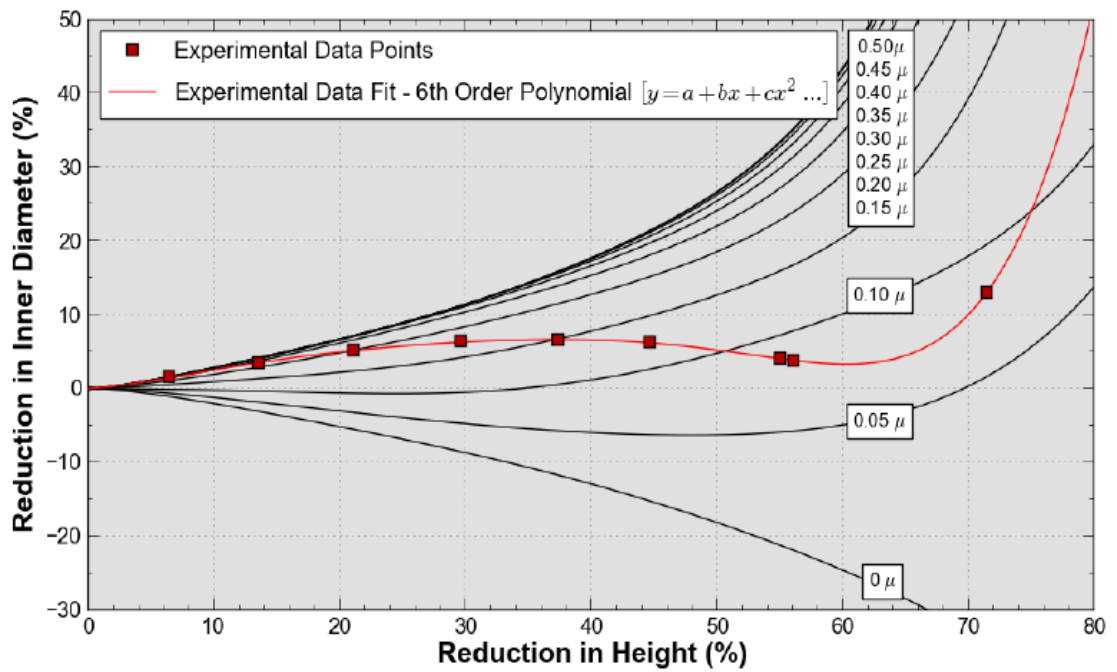
Figure 40: Friction calibration cure for AMS 5643 with experimental data set (Woodhead, 2015).

The friction coefficient at each experimental data point was determined by interpolation between each contour line and a plot of the friction coefficient against its respective contact pressure was generated (Figure 41).
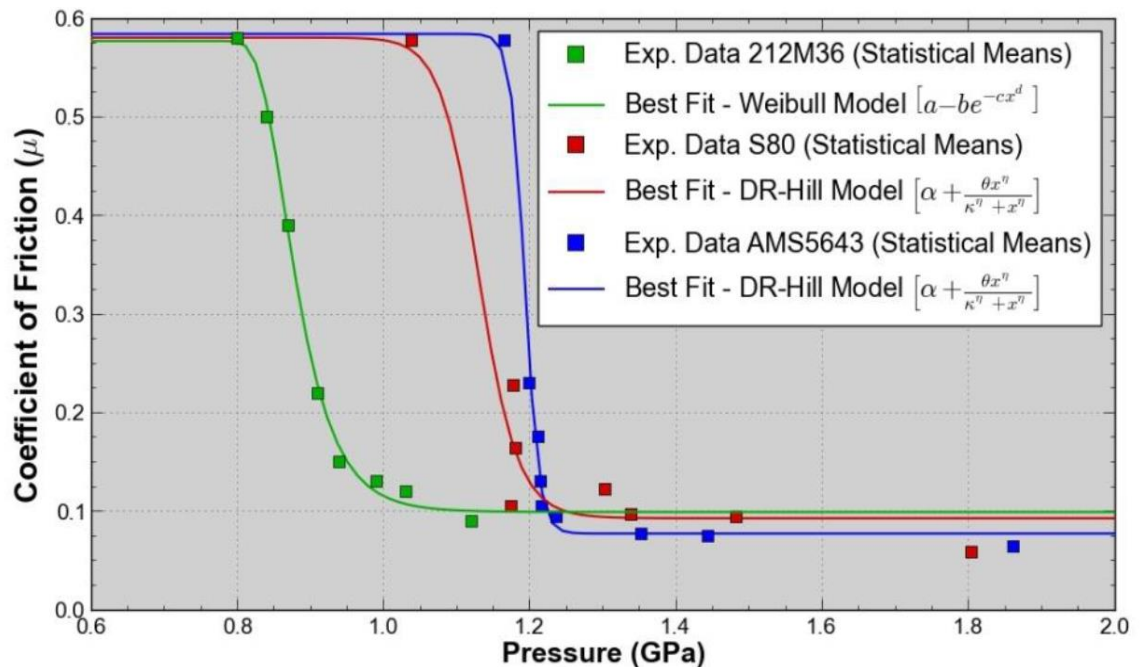
Figure 41: Variation in the coefficient of friction against the change in pressure for 212M36, S80 and AMS 5643 (Woodhead, 2015).

When this friction-pressure relationship for AMS 5643 was programmed into the nosing computational model, it was found that the accuracy of the simulation was not significantly improved compared to a constant friction coefficient of 0.1 (Figure 42). Whilst Woodhead assumed that this error could be attributed to other parts of the computation model (such as the plastic material data or contact behaviour between die and workpiece), it could instead be a result of the interpretation of the FCCs.
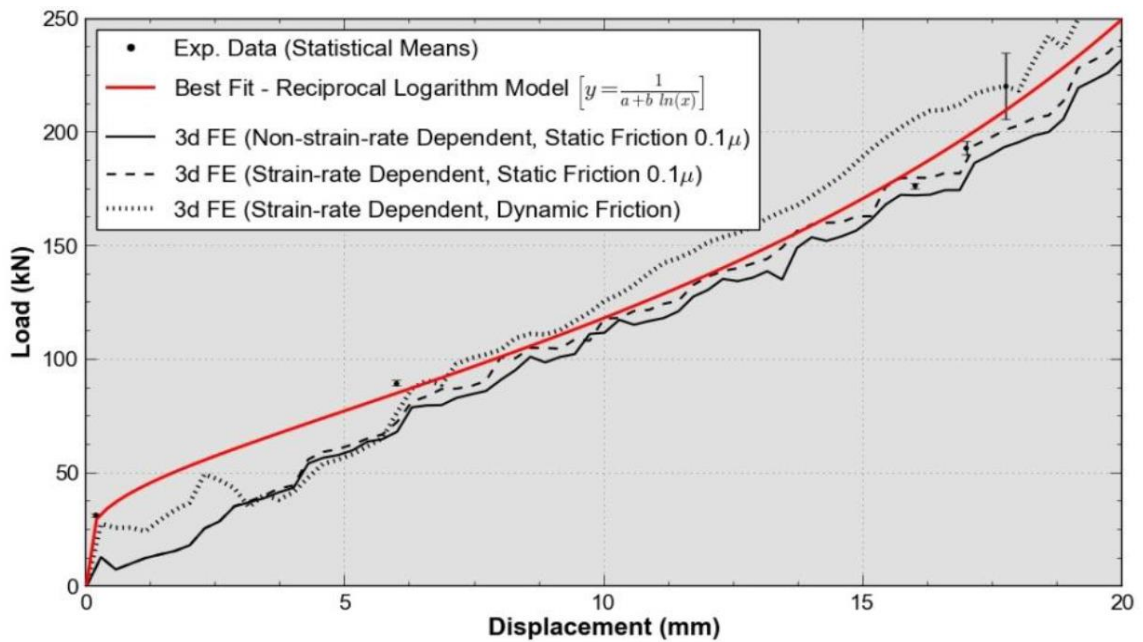
Figure 42: Steady-state load history for the nosing of a production bearing (Woodhead, 2015).

The conventional approach for ring compression testing is to compress the test samples to the same state of deformation and then interpolate their friction coefficient value from between the FCC contour lines. However, for this to be accurate it must assume that the friction coefficient remains constant and is invariant to contact pressure.

From Figure 40, at a reduction in height of 37% (equivalent to 1.21 GPa) the experimental data intersects the 0.15 contour and was therefore determined to be the friction coefficient at this pressure. A closer inspection of this data point shows that the gradient of the experimental data fit is negative and therefore the inner diameter should be expanding. By contrast, the gradient of the 0.15 contour is positive implying a reduction of the inner diameter. It appears for a material with a changing friction coefficient interpolating between contour lines does not give an accurate reflection of its deformation history or future trajectory.

2.3.2.2. Geometry

FCCs are unique to the geometries of each ring specimen and therefore cannot be compared when there is a change in specimen geometry (Alves, Martins, and Rodrigues, 2003; Woodhead, Truman, and Booker, 2015b). Both Narayanan *et al.* (2008) and Sofuoglu *et al.* (2001) demonstrated that when the ring thickness is increased, or the ratio for the outer diameter to inner diameter to height (OD:ID:H) is increased, the calculated coefficient of friction would appear to increase when using the original FCCs (where the OD is the outer diameter, ID is the inner diameter and H is the height).

There is no consensus in the literature for the best OD:ID:H ratio for ring compression testing as highlighted in Table 4. However, most research carried out in the 21st century has converged around a ratio of approximately 6:3:2. Male and Cockcroft (1966) made the following observations that must be considered when choosing a ring geometry. 1) If the OD:ID is too large and the coefficient of friction is high, then the ID will close during deformation making measurements of the coefficient of friction impossible. 2) if the OD:ID ratio is too small then the ring may become unstable and buckle. This can be mitigated by reducing the starting height of the sample. 3) A small sample height may cause issues when testing at elevated temperatures as the reduced mass of the sample will suffer from greater heat loss to the surrounding dies.

Table 4: Summary of reviewed literature for ring compression test geometries and conditions.

Author(s)	Material	Lubrication	Metal Working Temperature	OD:ID:H	Strain Rate (s^{-1})
Narayanan *et al.*, 2008	Pure Aluminium	Grease, Teflon	Cold	6:3:1	0.1
Alves, Martins and Rodrigues, 2003	Aluminium AA6082	Mineral oil, Teflon	Cold	6:3:2	Unknown
Woodhead, Truman and Booker, 2015b	Steels AMS5643 H1000, 212M36, and S80	Molybdenum Disulphide	Cold	6:3:2	1
Sofuoglu and Rasty, 1999	Plasticine	Talcum powder, Teflon, Vaseline	N/a	4:2:1	0.085
Male and Cockcroft, 1966	Steel, Copper, Brass, Aluminium	Graphite	Hot	3:2:1	0.001-10,000
Martin *et al.*, 2015	Aluminium EN AW-2030	Dry	Cold	6:3:2 and 6:3:1	0.08
Horwatitsch, Merstallinger and Steinhoff, 2012	Aluminium AA1050	Dry	Cold	6:4:2	1
Kahhal *et al.*, 2021	Steel A105	Dry	Cold	6:3:2	0.1

2.3.2.3. Barrelling

The influence of friction between the dies and a cylindrical workpiece means the contact surfaces are restricted from radial expansion. This results in a greater radial expansion at the centre of the workpiece and produces the barrelling effect (Figure 43). Under these conditions the stress and strains are not uniform.
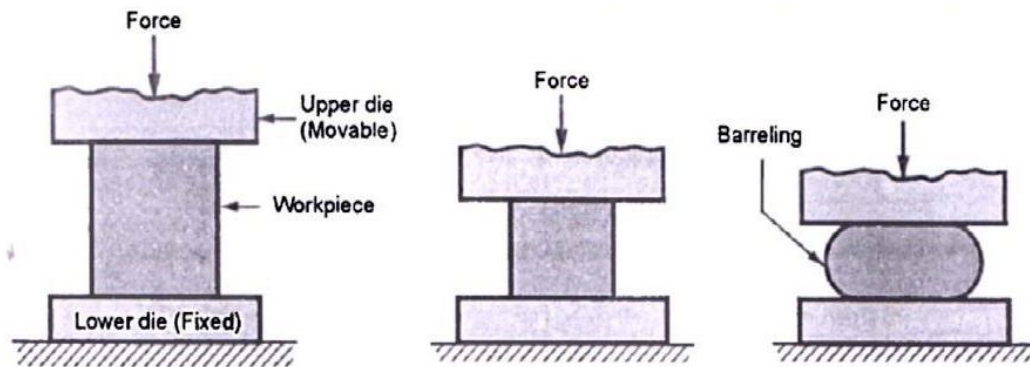
Figure 43: Left to right, the geometric shape caused by friction between the die and workpiece (Badrossamay, 2016).

For a disc of material, however, the direction of the barrelling changes with the magnitude of the friction coefficient. Whilst the outside diameter will always bulge radially outwards, Sofuoglu and Rasty (1999) demonstrated that below a friction of 0.05 the middle of the inside diameter will increase at a greater rate than at the interface. This is the inverse of the classical barrelling effect and is often referred to as "mushrooming". Above a friction coefficient of 0.05, the frictional forces are sufficient to cause the middle of the inside diameter to flow inwards (Figure 44). The effects of barrelling can skew the results of the ring compression test as it can introduce discrepancies depending on whether the internal diameter is measured at the interface or in the middle of the specimen (Figure 44). Therefore, care must be taken to ensure consistency in the measurement method.

Low friction (good lubrication)

High friction (poor lubrication)
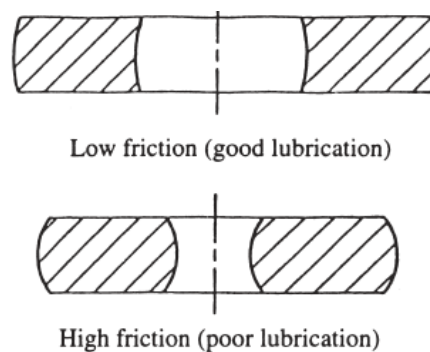
Figure 44: Effect of friction on metal flow during the ring compression test (Sofuoglu and Rasty, 1999).

2.4. Modelling of Cold Forming

Modelling of a cold-forming process can usually be categorised into one of three types: analytical, computational, and empirical. Analytical models are mathematical models derived from fundamental mechanics and geometry which produce a closed-form solution. Numerical models are discrete computational simulations designed to predict complex interactions which within the field of cold forming typically take the form of a FEA. Lastly, empirical models are mathematical models that have been derived from experimental data.

2.4.1. Analytical Methods

2.4.1.1. Slab Method

The Slab method is a relatively simple analytical method where a free-body diagram (FBD) of an infinitesimal slab is constructed to represent the forming area. Included in the FBD are any relevant boundary conditions such as die faces or open edges. The forces that act on the slab (F) are proportional to the materials flow stress ($\bar{\sigma}$) and take the form $F = \mu\bar{\sigma}A$ where μ is the friction coefficient. By balancing the forces of the FBD a series of differential equations are generated that can be solved either analytically or numerically to find the forming force. This method usually involves making a number of simplifying assumptions such as rigid dies, simplified friction laws, and rigid-perfectly plastic material behaviour and therefore can be difficult to apply to complex forming processes such as impression die forming (Chandramouli, 2014; Foster *et al.*, 2009) However, it is still being used for metal forming processes because it is a quick form of analysis and under the right conditions can produce reasonable accuracies as seen with wire drawing (Rubio *et al.,* 2005 and 2006), sheet rolling (Razani, Dariani, and Soltanpour, 2018; Salimi and Kadkhodaei, 2004; Salimi and Sassani, 2002) and hot forging (Kamble and Nandedkar, 2011).

2.4.1.2. Slip-line Field Analysis

Slip-line field analysis is used to model plastic deformation in plane strain by assuming homogenous, rigid-perfectly plastic material behaviour. At any point, a pair of orthogonal lines can be drawn that represent the lines of maximum shear stress (slip-lines) that material is assumed to flow along. The slip-line field analysis aims to solve the following equations (Dixit, 2020):

- yield criterion for plane strain.

- equilibrium equations along two orthogonal directions in the plane

- continuity equation (volume conservation as the density remains practically unchanged during metal forming for most of the metals).

- an equation indicating that directions of principal stress and corresponding principal strains coincide.

Dixit argues that the construction of slip-line fields is a nontrivial exercise, and most users are disinclined to use this method because it can only be applied to plane-strain models for rigid-perfectly plastic metals. Nevertheless, it has seen some limited use in axisymmetric metal forming applications with strain-hardening metals (Chitkara and Butt 1992. Collins and Williams, 1985, Farmer and Oxley, 1971).

2.4.1.3. Upper Bound Method

The upper bound method is used to provide an upper estimate of the force required to plastically deform a component and is particularly useful for the study of metalworking processes. The approach taken to estimate the upper bound is to estimate the likely lines along which shear slip would be expected to occur. The rate of energy dissipated by shear slip along these lines can be calculated and equated to the work done by an external force. Frictional forces can be accommodated through Hodogaphs (University of Cambridge, 2021) in which a velocity boundary condition is assumed. This is referred to as a kinematically admissible velocity field. Based on the assumed velocity field, the total energy for deformation is calculated as the energy for plastic deformation as well as the energy to overcome friction.

The upper bound theorem has been used for estimating the forming load in processes such as forging (Krishna and Jena, 2019; Wu *et al.,* 2015; Ghaei *et al.,* 2006), extrusion (Parghazeh and Haghighat, 2016; Hartley, 1973), and rolling (Zhang *et al., 2018b; Sun et al., 2016; Liu et al., 2015).* Attempts have been made to include the effect of strain-hardening into the upper bound method by using Hollomon's flow stress relationship (Equation 3) and approximating the equivalent plastic strain (Sinha, Deb, and Dixit, 2009; Avitzur, 1967). This method has generally provided mixed results and is better suited to simpler metal-forming geometries as seen in some extrusion processes.

2.4.2. Empirical Methods

2.4.2.1. *Design of Experiments*

The trend towards lightweight designs and assemblies is perpetual and requires an ever-increasing need for design optimisation and a deeper understanding of the respective manufacturing process. The Design of Experiments method, also referred to as Robust design, is a systematic and efficient method that aims to study the relationship between multiple input and output variables (Taguchi, Chowdhury, and Wu, 2007) instead of relying on the costly use of design margins, overengineering or excessive quality control (Eckert, Isaksson and Earl, 2019). The aim of a DoE model is to either optimise the value for each process variable in order to achieve a desired response or to predict the output from a series of fixed inputs. To achieve this, the DoE process is as follows:

- The most likely process variables that could affect the desired output are identified.

- The upper and lower bound for each process variable is determined, typically 80% and 20% respectively. These values are referred to as "levels".

- For a full factorial design, an experiment is run for every possible combination of process variables. The total number of experiments is thus the number of levels raised to the power of the number of process variables.

- A regression analysis is carried out on the experimental results that evaluate the impact of each process variable.

- The final output is a closed-form solution able to predict the response of the output based on the chosen input parameter values.

The regression analysis step plays a key role in the DoE process as not only does quantify the relationship between any input variable (or combination of variables) to the response, but it must also eliminate any insignificant variables from the analysis. More is not always better, and the inclusion of insignificant factors can negatively impact a model's overall performance, particularly at the extreme points within a design space (Minitab, 2020a). This process is achieved by a stepwise regression analysis by either forward selection of backward elimination methods. The forward selection method starts with a blank model, evaluates each individual term, and then adds the term with the most significance to the model. This step is repeated until there are no remaining terms the meet the acceptance criteria. Backward elimination by contrast starts with all possible terms in the model but eliminates the term with the least significance to the model. This step is repeated until all remaining terms in the model are above to acceptance criteria. Significance is typically determined by a terms P-value which is a test for the null hypothesis. A low P-value (<0.05) indicates a high probability that the term

is strongly related to the model's response and that the null hypothesis can be rejected. Backwards elimination is generally considered favourable to Forward selection because by starting with the full model the effects of all variables can be assessed simultaneously. This is especially important in the case of collinearity when there are strong interactions between terms but not necessarily in isolation which may be missed during forward selection (Joseph et al., 2019; Woodhead, 2015a).

Even if low P-values were chosen for the acceptance criteria there is always a risk of overfitting to a particular and dataset. This is likely to occur if the training dataset is too small to accurately represent all possible permutations of a design space. To reduce this risk there are multiple statistical tests can be carried out to identify potential overfit.

R-Squared Adjusted

R-Squared is a prediction of how well the model fits the data with 1 being perfect correlation and 0 no correlation. R-Squared Adjusted compensates for the number of terms in the model because as R-Squared increases with an increasing number of terms. R-Squared Adjusted is used to compare correlations between models with different numbers of terms.

R-Squared Predicted

R-Squared Predicted determines how well a model predicts the response to new observations. It is equivalent to systematically removing observations from the raw dataset and comparing the change in the resulting regression model correlation. If a large difference is found between R-Squared Adjusted and R-Squared Predicted, then it indicates a model that is over-fit and contains terms that are not important.

T-Value

T-value is a measure of the ratio between the coefficient within a model and its standard error. Magnitudes greater than 2 are considered sufficient to reject the null hypothesis.

Variance Inflation factor

The Variance Influence Factor (VIF) describes how much multicollinearity (correlation between predictors) exists in the regression analysis. Multicollinearity can cause an increase in the variance of regression coefficients and make it difficult to evaluate the individual impact of each predictor. A VIF value greater than 5 suggests that the coefficient is poorly estimated due to severe multicollinearity and caution should be taken with its inclusion in a model.

In general, DoE is a well-researched field, and its fundamental ideas are widely accepted among researchers (Sarema, et al., 2022; Joseph et al., 2019; Oudjene and Ben-Ayed, 2008; Lehman, Santner, and Notz, 2004; Jin, Chen, and Sudjianto, 2003). When paired with commercially available FEA software, a virtual DoE can be undertaken that can achieve a higher level of verification and eliminate experimental effort and cost (Kim, 2010; Al-Momani and Rawabdeh, 2008). Despite these opportunities, there remains a gap in most engineering industries when it comes to the application of virtual DoE to evaluate the effect of geometrical, material, and load variations (Nerenst et al., 2021; Will, 2015; Coleman, 2012). The main critique of DoE has been that as the number of input parameters and levels increases to model increasingly complex systems, the number of experiments needed to run grows exponentially. The practical implications of this increasing scale can make DoE time and cost-prohibitive (Box, Bisgaard, & Fung 1988).

Although beyond the scope of this thesis, it is important to highlight the similarities that a DoE and its regression analysis shares with machine learning, in particular the algorithms of Supervised Learning (regression) and Neural Networks (reinforcement learning) (MathWorks, 2024; Sarker 2021). The general workflow for a neural network regression implementation is as follows:

- Collecting and preprocessing the dataset including categorising input features.

- Defining the architecture of the neural network layers. Input layers have nodes corresponding to the input features. Hidden layers contain one or more layers of nodes that apply transformations to the data. Lastly the output layer has a single node which provides the regression prediction. Each node in one layer connects to each node in the following layer with a certain weight.

- Select a loss function to evaluate the difference between predicted and actual values. Mean Squared Error is a common choice.

- Train the model by updating the network weights to minimise the loss function until an acceptable convergence is achieved.

- With a baseline established, hyperparameter tuning can optimise the model's performance. These parameters include: the number of layers, number of nodes in each layer, learning rate, and activation functions which can change how a node responds depending on the input value (Figure 45)
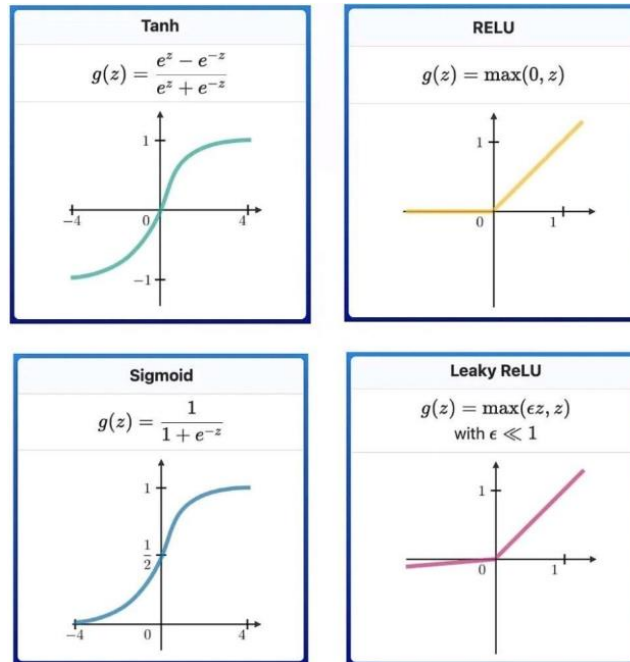
Figure 45: Examples of various activation functions for nodes in a neural network (Baheti, 2021)

Machine learning regression models are very flexible and can handle complex relationships especially when dealing with large unstructured datasets (Sarker 2021). However, they require careful tuning to achieve good model accuracy without overfitting and can require more user intervention compared to the very structured and automatic stepwise regressions used in a DoE. Whilst the overall output from both can be quite similar, one of the largest differentiating factors between them is the activation functions that allow for a nonlinear response of the nodes. This can allow for the behaviour of the output to change depending on the magnitude of the input nodes unlike a DoE regression analysis where the output behaviour remains constant regardless of input magnitude.

2.4.2.2. Visioplasticity

The Visioplasticity method was introduced by Thomsen *et al.* (1954) whereby the velocity field is obtained from a series of photographs of the instantaneous grid pattern during a forming process. Once the deformation field is visually obtained the true strain, strain-rate, and stress field can be calculated. This method has often been used only to study flow patterns because the calculations involved are considered too cumbersome to be practical (Thomson and Brown, 1982). Moreover, with the advent of finite element the prominence of this type of experimental technique has diminished.

2.4.3. Numerical Methods

Numerical methods within the domain of metalworking analysis can be summarised as computer-based methods for solving partial differential equations to describe a range of possible field parameters such as displacement or temperature.

The Finite Element Method (FEM) is the dominant numerical method for simulation of bulk-metal forming whereby the domain is subdivided into a number of well-defined elements that are joined at nodes, a process known as discretization. The nodal values are determined by the solution of an array of simultaneous equations using computational matrix methods and the accuracy of the results are dependent on the discretisation of the mesh, the accuracy of the assumed interpolation form, and the accuracy of the computation solution method used (Ashcroft and Mubashar, 2011). The continuous field parameter being solved is characterised by its value at these nodes, with the values between the nodes determined by polynomial interpolation (Larson and Bengzon, 2013).

An alternative to the FEM is the Finite Difference Method (FDM) which discretises the domain using a structures mesh with a uniform grid. The governing differential equations that define the field parameters are converted to difference equations (using the basic definitions of derivatives) and approximates of the value at the cell centre are found using finite difference approximation of the derivative (Dixit, 2020). FDM has some advantages over FEM, particularly for its simplicity and low computation cost and has been used some simple metal forming problems where heat transfer is the primary consideration of the analysis (Khan *et al.*, 2004). However, for the vast majority of metal forming problems FEM is considered the default numerical method because of the accuracy it can maintain when modelling complex geometries and boundary conditions (Larson and Bengzon, 2013).

The current popularity of FEM is its ability to model many classes of problem regardless of the complexity of the geometry, boundary, or load conditions, and is a powerful tool that can provide deeper understanding of bulk-metal forming processes (Groche *et al.*, 2014; Mori *et al.*, 2013). FEM studies have been conducted using a variety of commercial FEA programs with a summary of the reviewed literature from this thesis given in Table 5.

Table 5: Examples of computational modelling software used for metal forming processes.

Software Package	Metal Forming/Joining Process
ABAQUS	Electromagnetic Forming (Haratmeh et al., 2017; Vanhulsel et al., 2011)
	Incremental Sheet-Bulk Forming (Sieczkarek et al., 2017)
	Tube Swaging (Cho et al., 2005)
	Nosing (Luan, Hu, and Chen, 2015; Woodhead, 2015b)
	Drawing (Wu et al., 2013)
ANSYS	Electromagnetic Forming (Rajak et al., 2018 and 2017; Weddeling et al., 2015a and 2015b; Chunfeng et al., 2002)
	Drawing (Isik et al., 2021)
	Incremental Sheet-Bulk Forming (Wernicke, Hahn, and Tekkaya, 2021)
	Hydroforging (Chavdar et al., 2016 and 2015)
	Roller Swaging (Zhang et al., 2018a and 2017)
	Cold Forging (Kahhal et al., 2021)
	Nosing (Kwan et al., 2004)
SuperForm	Cold Forging (Cora et al., 2008)
Altair HyperForm	Sheet Metal Forming (Billade and Dahake, 2018; Bajaj et al., 2014)

From this reviewed literature, the reasoning behind the choice of FEA programme was never explicated stated and it appears to simply come down to the availability of software and or the personal preference or prior experience of the individual researcher or research group. The major software vendors all have very similar feature sets suited to the modelling of cold metal forming with the can be seen in Table 5 by the crossover of forming processes between the various software packages. Whilst there are no direct examples from literature, the staking of spherical bearings shares many of the same characteristics as with nosing (Kwan et al., 2004) and it most similar to roller swaging (Zhang et al., 2018a and 2017). Both of these processes have been successfully modelled using ANSYS in prior research and therefore, would likely be a suitable choice for this thesis.

2.4.3.1. Plasticity Models

Several empirical models correlating stress and strain have been widely used to describe the flow stress and strain hardening behaviour of metals undergoing plastic deformation. The most commonly used equations are Hollomon, Ludwik and Swift (Equations 20-22) which all follow a power law relationship. All three demonstrate similar performance with only small difference in fit performance depending on the particular metal, temperature, degree of strain, and the strain-rate being tested (Kweon *et al.*, 2021; Sener and Yurci, 2017).

Whilst these simple models are convenient to fit to experimental data, they lack any provision to accommodate any variability in strain-rate and can only express stress strain behaviour at a fixed strain-rate. Extended Hollomon, Johnson-Cook and modified Zerilli-Armstrong (Equations 23-25) incorporate strain-rate as a variable in their models to capture a materials sensitivity to strain-rate (Khraisat, 2023; Samuel, 2006). Extended Hollomon and Johnson-Cook are the most classical constitute models because of their ability to accurately model the plastic flow stress of metals across a wide range of forming conditions with only the need for three and four material constants respectively (Li *et al.,* 2019). Therefore, they can be obtained with only a few experimental data points. Due to its high precision, simple form, and wide applicability, these models are widely applied nowadays, especially in the FEA (Deng *et al.*, 2014; He *et al.,* 2014; Shrot and Baker, 2012). By contrast, modified Zerilli-Armstrong has seen relatively fewer uses due to its requirement for an additional material constant to be derived and adding to the minimum testing volume needed without providing any additional performance over extended Hollomon or Johnson-Cook for the majority material applications (Li *et al.,* 2019). Modified Zerilli-Armstrong is most suitable is the prediction of flow behaviour in the presence of both large strain-rates and at temperatures near the recrystallisation point (Baghani *et al.*, 2016; Lee and Liu, 2006).

$$\sigma = H\varepsilon^{n} \tag{20}$$

$$\sigma = H(\varepsilon + \varepsilon_{0})^{n} \tag{21}$$

$$\sigma = \sigma_{0} + H\varepsilon^{n} \tag{22}$$

$$\sigma = H\varepsilon^{n}\dot{\varepsilon}^{m} \tag{23}$$

$$\sigma = (A + B\varepsilon^{n})\left(1 + C\ln\frac{\dot{\varepsilon}}{\dot{\varepsilon_{0}}}\right) \tag{24}$$

$$\sigma = (A + B\varepsilon^{n})exp\{(C - D\dot{\varepsilon})\Delta T\} \qquad\qquad [\,25\,]$$

where H, n, m, ε_0, σ_0, A, B, C, $\dot{\varepsilon}_0$ and D are all properties to be determined depending on the nature of the material.

Depending on the users chosen material model, there are multiple methods by which plasticity can be implemented into a FE model. For the vast majority of computational modelling software's, they directly support the most popular constitutive material models of Hollomon and Johnson-Cook (along with their derivatives) and the model's material constants can be entered directly into the programme (Woodhead, 2015b; He *et al.,* 2014). If a material model is not directly supported by the software, then the most common implementation of stress-strain relationships is through bilinear or multilinear approximations (Figure 46).

In a bilinear model the stress-strain relationship is approximated by two linear slopes. From the rest state to the onset of plastic deformation, material stiffness is characterised by the Young's modulus after which the plastic phase is defined by a second tangent modulus ranging from a maximum value equal to the elastic Young's modulus to a minimum of zero (the zero condition defines a perfectly-plastic material). Whilst computationally efficient, bilinear hardening can only provide a reasonable approximation for metals with a very low strain-hardening exponent or for simulations where strain is typically less than 5% (Ashcroft and Mubashar, 2011). To capture the behavioural history of the stress-strain relationship more accurately, multiple linear regions can be defined in the plastic phase in a multilinear model. Therefore, providing a closer match to the actual stress-strain relationship especially for large plastic strains and metals with large strain-hardening exponents.
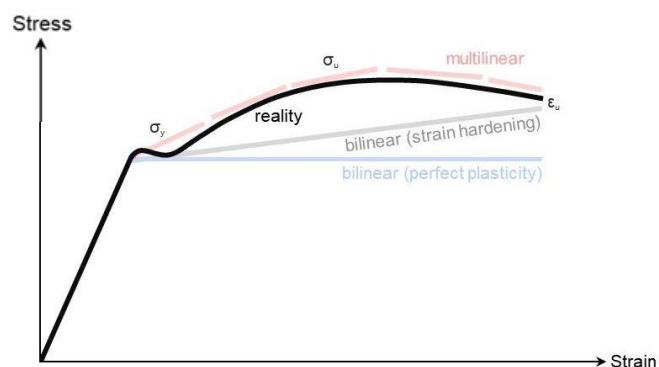
Figure 46: Visual Comparison between different elastic-plastic material models and the real material curve. Adapted from SimScale, 2024.

2.4.3.2.   *Time-Dependent and Time-independent Analysis*

The dynamics of any physical system can be represented in terms of the equation of motion which takes the general form

$$f(t) = M\ddot{x} + C\dot{x} + Kx \qquad [\,26\,]$$

where the terms $\ddot{x}$ is acceleration, $\dot{x}$ is velocity, and x is displacement and each of these term terms varying with respect to time. Acceleration and velocity also be expressed as differentials in terms of position.

$$\ddot{x} = \frac{d^2x}{dt^2} \qquad \dot{x} = \frac{dx}{dt} \qquad [\,27\,]$$

The equation of motion can now be expressed as a second order ordinary differential equation.

$$f(t) = M\frac{d^2x}{dt^2} + C\frac{dx}{dt} + Kx \qquad [\,28\,]$$

To solve this differential equation. the time domain is split into a series of discrete time-steps and then solved at each of these specific time points. This technique is called the time integration method with the unknown terms in each time-step calculated based on the value of the terms in previous time step. Depending on the nature of the problem being solved, there are two types of time integration techniques: implicit (time-independent) and explicit (time-dependent).

For the implicit time integration method, variables at an unknown time-step are calculated using the slopes (velocity and acceleration) from the same time-step. Because the displacement, velocity, and acceleration all unknow variables at that time-step, the equations of motion cannot be directly solved. This is demonstrated in Equation 29 for the displacement at time-step t_{n+1}.

$$x(t_{n+1}) \;=\; x(t_n) \;+\; \Delta t \dot{x}(t_{n+1}) \qquad [\,29\,]$$

Known   Unknow

This method generates a series of equations which must be solved simultaneously using numerical methods until satisfactory convergence is achieved (Kosaraju, 2020). Despite being

computationally expensive, the implicit method produces a stable solution irrespective of the size of the time step which is why it is referred to as time-independent.

By contrast, the explicit time integration method solves the variables at an unknown time-step using the slopes from the previous time-step which contains known values and can therefore be solved directly. The displacement at time-step t_{n+1} can be expressed as

$$x(t_{n+1}) \; = \; x(t_n) \; + \; \Delta t \dot{x}(t_n) \qquad\qquad [\; 30\;]$$

Known	known

The explicit time integration can solve time-steps very fast and efficiently compared to the implicit method, however, small time increments must be used to avoid violating the assumption that velocity and acceleration remain relatively constant throughout the entire time-step. If too large a time-step is used, then it can severely impact the model's accuracy. The maximum size of the time-step is governed by the Courant–Friedrichs–Lewy (CFL) condition which seeks to maintain model stability. The CFL condition enforces stable results by limiting the time-step size so that a stress wave cannot travel further than the distance between the smallest elements within the FE model (SimScale, 2022). The maximum allowed time-step (Δt) is calculated by

$$\Delta t = f * \left[\frac{h}{c}\right]_{min}, \qquad\qquad [\; 31\;]$$

where h is the characteristic length of the smallest element in the model, c is the speed of sound of the material and f is a safety factor which is usually equal to or smaller than 1. In practice, the explicit method should be limited to simulating time periods in the order of microseconds or less which makes it suitable for modelling drop tests and impacts were strain rates typically exceeding $10S^{-1}$ (Figure 47) summary of the key differences between implicit and explicit time integration techniques is shown in Table 6.
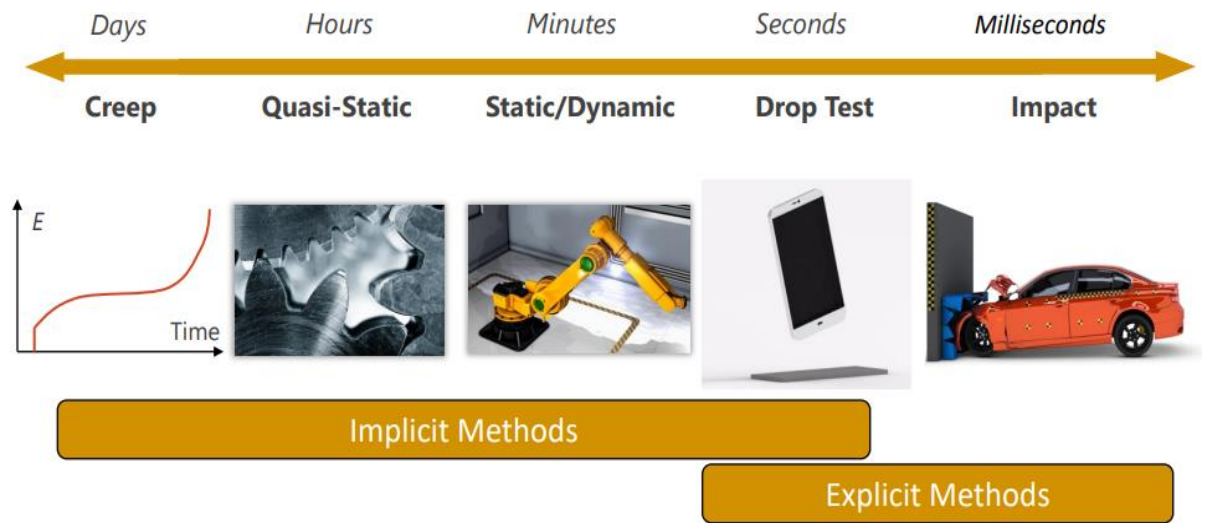
Figure 47: Guidance for choice of implicit and explicit time integration methods (ANSYS 2021b).

Table 6: Key difference between implicit and explicit time integration methods.

Implicit	Explicit
Independent of time-step size and unconditionally stable	Model accuracy and stability is dependent on time-step
Each time-step requires multiple iterations using numerical methods to achieve convergence	Solves in a single step for each time-step
Solving speed for each increment is slow	Solving speed for each increment is fast
Used for solving static, creep, and quasi static problems	Used for solving dynamic, impact, and drop test problems

2.5. Gap Analysis

After a review of the relevant literature surrounding the fields of cold-metal forming and spherical bearing staking, gaps in the knowledge were identified and the following conclusions were reached.

The current direction for research within the field of cold-metal joining has been dominated by the desire to create lightweight composite components typically in the form of a steel exterior and lightweight core (Sections 2.1.2 through 2.1.5).

Computational modelling has become the default analysis method for nearly all metalworking processes as traditional analytical methods are becoming steadily less desirable. This has been attributed to the ubiquity and ease of use of computational modelling and the inherent limitations of analytical methods to incorporate phenomena such as strain-hardening, non-rigid boundary conditions, and complex die and part geometry. As such, it is rare to see any closed-form analytical solutions presented in current research (Section 2.1.6).

Even with the widespread adoption of computational modelling, there remains the severe challenge of accurately predicting a joint's mechanical properties; with the most commonly cited parameter that impacts the modelling of cold forming processes being "friction conditions, coefficient and variability" (Woodhead, 2015. Figure 19).

The frictional behaviour of a system is an important parameter to define because it influences nearly all aspects of cold-metal forming such as material flow, forming load, surface quality, tool life, and joint strength. The ability to accurately account for the coefficient of friction is clearly regarded as the most important variable when modelling this type of process, especially if the effect of lubrication is also considered (Section 2.3.1)

Researchers in the field of cold-metal forming typically adopt Coulomb's law and assume a constant coefficient of friction throughout the entire modelling process. This is often done as an act of convenience because Coulomb's law is the standard implementation of friction in most popular computational modelling software packages (Section 2.3.1).

Given the costly and time-consuming nature of obtaining friction coefficient data, it is normal practice that friction coefficients are often taken directly from reference texts and typically vary from 0.05 to 0.15 for dry steel-steel contact regimes (Kalpajian and Schmid, 2008. Table 3)

There is sufficient research to indicate that the coefficient of friction reduces with contact pressure and that a variable or non-linear coefficient of friction is required to accurately predict

the load history during the operation. Incorporating dynamic variables into a model requires an iterative feedback loop to continuously update those variables as the solution evolves. This functionality is built into FEM software packages and provides the best method to predict the load history during a forming operation (Section 2.3.2.1)

The study of manufacturing processes using Design of Experiments is a well-researched field, and its fundamental ideas are widely accepted among researchers. There is significant potential to combine this methodology with computational modelling to create a powerful design and analytical tool without the large experimental effort and cost associated with a tradition Design of Experiments study (Section 2.4.2.1).

There is no clear choice for the best computational modelling software all of the major software packages have proven to very capable for a wide variety of cold metal forming processes. Whilst there are no direct examples from literature, staking shares many of the same characteristics as with nosing and it most similar to roller swaging. Both of these processes have been successfully modelled using ANSYS in prior research and therefore, would likely be a suitable choice for this thesis (2.4.3).

Chapter

3

Methodology

This chapter brings together the research from the literature review to determine the appropriate strategy to satisfy the objectives outlined in Section 1.3. The four broad research methodologies are: how the disciplines of computational modelling and statistical methods can be combined to form a virtual design of experiments to overcome the limitations of geometrically derived analytical solutions, how to validate the regression equations from the virtual design of experiments, the mechanical properties of the materials that constitute a spherical plain bearing, and lastly the frictional behaviour of those materials under bulk forming conditions. The background and technical details of these methods are discussed at the start of the relevant chapters (4 to 7).

3.1. Modelling Methods: FEA

Analytical models for metal forming processes are desirable because they are a simplified representation of the process and create an exact solution which typically is fairly trivial to compute. However as shown by multiple researchers (Dixit, 2020; Ossenkemper *et al.*, 2017; Gisbert *et al.*, 2015; Foster *et al.*, 2009; Moon, Lee, and Joun, 2007; Fischer *et al.*, 2006), simplified analytical models for joining processes are rarely able to accurately model or compensate for the effects of strain hardening or residual stress and are not easily applied to complex, multi-stage processes. The anvil staking process would likely exacerbate these limitations due to the presence of large plastic deformation and residual stresses in the staking

lips, therefore creating a complex stress state at the start of the second stage of the process (pushing out of the bearing).

The nearest analytical-based methodology that could be used to model the anvil staking process would be the plane-strain model developed by Zhang *et al.* (2017). Preliminary research into adapting Zhang *et al.* model for anvil staking ultimately proved to be unsuccessful in predicting the staking force during the first stage stake (Appendix B). The two reasons for this unsuccessful modelling approach were summarised to be the inability to compensate for the effects of strain-hardening in the staking lip, and the assumed rigid behaviour of the housing. Similar limitations with analytical models were found by Woodhead (2015a) for the modelling of the nosing process of spherical bearings. Nosing is a tube-end forming process whereby the outer race is formed around the inner ring; from an analytical perspective it is relatively simple to model. While some limited success was found with analytical models at higher forming loads, no analytical model could produce a reasonable estimate of the forming load range. Given the challenges presented across all the reviewed literature and the preliminary research into adapting Zhang's *et al.* roller swaging model, it was decided that analytical modelling would not be suitable for this investigation and no further attempts were made to follow this approach.

The limitations of analytical models pushed this investigation towards the same conclusions as most modern researchers which was to use the numerical modelling methods. FEA has increasingly become the default choice for the modelling of metal forming process and would be a suitable choice for modelling the staking process and understanding the mechanisms present during staking. The critical limitation of using FEA is that it does not provide an exact solution and does not provide the closed-form solutions linking the interactions between the staking force, pushout load, and post-stake torque required by the research objectives. These closed-form solutions can be created however by pairing together the numerical methodology of FEA with the statistical methods of Design of Experiments to form a Virtual-DoE.

This hybrid approach allows for the two methodologies to complement each other (Kim, 2010; Al-Momani and Rawabdeh, 2008). For example, one of the frequently cited challenges with DoE is the magnitude of testing that is required as more design variables are considered at higher resolutions which quickly becomes time and cost prohibitive. By replacing physical experiments with FEA simulations, it is possible to nearly eliminate all experimental cost and effort from the DoE method with the exception of the validation experiments required to validate the performance of the Virtual-DoE model.

3.2. Validation: Quasi-Randomised Sampling

The results and findings from the Virtual-DoE will only be of any significance if they have been validated against practical testing. The Virtual-DoE process contains three primary sources of error. The first is from the underlying FEA model, second is from the fitting of the regression model to the DoE tests, and third is ability of the regression model to predict the response to continuous input parameter values (instead of the discrete values for the DoE tests). Therefore, it is best to combine the effect of all sources of error and validate just the final Virtual-DoE model.

As previously discussed in Chapter 1, there would be limited manufacturing capacity to produce custom bearings resulting in the Virtual-DoE to be constrained to investigate parameters only able to be varied within normal production. This focus on standard manufactured bearings allows for test data to be collected directly from the SKF production at a relatively low cost.

The first bearing of each batch is staked and pushed out of its housing to validate that 1) the bearing meets the drawing specifications and 2) to set the machine parameters for the remainder of the batch. By requesting the assistance of machine operators, all of the necessary pre- and post-stake torque and all relevant geometry of that first bearing could be recorded. Therefore, at a production rate of approximately two batches of staked bearings per week, over the period of this thesis a sufficiently large dataset of approximately 150 quasi-randomised staked bearings could be gathered that would cover the majority of design space of the Virtual-DoE models to validation against. Whilst this sampling method will almost certainly leave gaps with respect to the model's design space, the data that is gathered will be representative of real-world production variation and any gaps that remain would represent unrealistic bearing geometries that do not appear in actual production.

3.3. Mechanical Characterisation: Compression Testing

A critical part of any model is the accurate characterisation of the material's mechanical properties. The most commonly used materials for the production of plane spherical bearings are as follows:

- Inner ring, 440C steel

- Outer race, AMS5643 H1150 steel

- Housing, AMS5643 H1025 steel

- Self-Lubricating Liner, X1-40 woven PTFE-glass fibre composite.

Periodically a finished staked bearing is cast in resin and split in half to measure various geometric properties including inner ring spherical conformity as per AS81820 (SAE International, 2014). No evidence has ever been found of the inner ring deforming as a result of the staking process (SKF, 2021). Therefore, for the purpose of the computational model, the inner ring's mechanical properties are simplified and assumed to be perfectly elastic with a Young's modulus of 200GPa and Poisson's ratio of 0.3 (Atlas Steels, 2008).

By contrast, the outer race and the housing plastically deform during the staking process and therefore requires plastic stress-strain data to model. To the author's best knowledge, this data is not available and therefore require material testing. Staking is an open die process with plastic deformation dominated by compression; therefore, a uniaxial compression test is the most comparable, standard material test method to acquire this data. In order to ensure the validity of this test data, standard test methodologies such as ASTM International E9-09 (2018) must be adhered to.

Lastly, whilst some researchers have opted to omit the liner from their FE models as a simplification (Zhang *et al.,* 2018a and 2017; Woodhead, 2015a; Orsolini and Booker, 2012), this is not possible for this research as modelling the contact pressure between the liner and inner ring is critical in determining the post-stake torque. As SKF has already investigated and determined the mechanical properties of its liner, it is not necessary to re-evaluate its mechanical properties.

3.4. Friction-Pressure Relationship: Ring Compression Testing

Three critical contact regions were identified where the friction-pressure relationship could have an impact on the staking force, pushout load, or the post-stake torque; these regions are (1) the staking anvils to outer race, (2) outer race to housing, and (3) the inner ring to the self-lubricating liner (Figure 48).
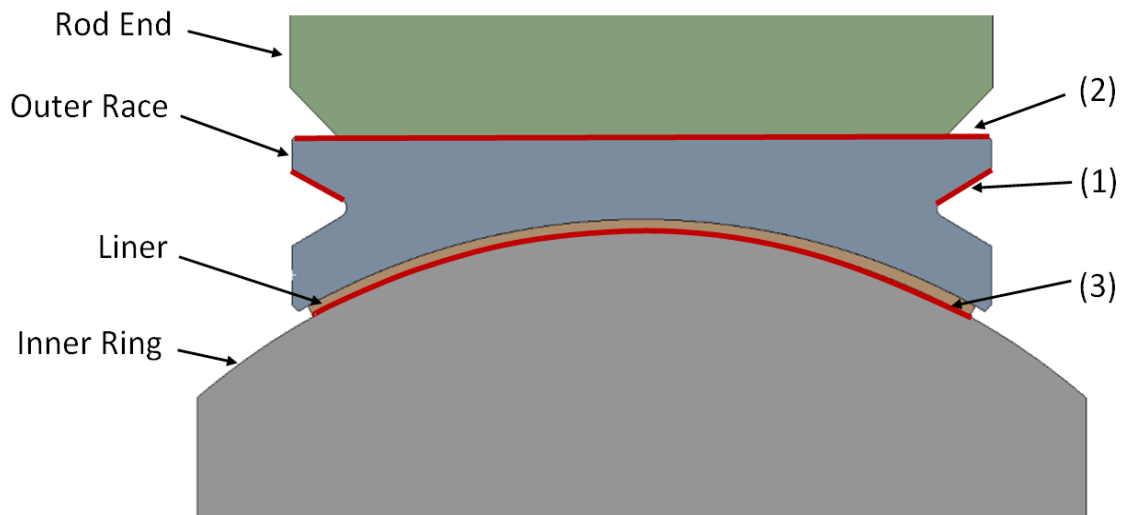
Figure 48: Location of critical contact regions (1) staking anvils to outer race, (2) outer race to housing, and (3) inner ring to self-lubricating liner.

For both regions (1) and (2), the contact pressures are expected to be in excess of the material's yield strength, and from literature there is sufficient evidence to suspect that the friction coefficient may not remain invariant with respect to contact pressure (Woodhead, Truman and Booker, 2015b; Orsolini and Booker, 2012; Cora et al., 2008; Tang and Kobayashi, 1982). The ring compression test has proven to be the most efficient and simplest method by which to measure the coefficient of friction for the cold forming of metals and will therefore form the basic methodology for determining the friction-pressure relationship for regions one and two. This will include using ring test samples with no boss or eternal features with the most widely accepted geometric ratios for the outer diameter, inner diameter, and height of 6:3:2. Despite recent research into new geometries for the ring compression test samples, there is no consensus yet as to the ideal geometry of the outer diameter boss and unlike the standard ring compression test, these test rings are much more complex and time-consuming to manufacture.

Where this research deviates from the standard ring compression test methodology is in the evaluation of the friction coefficient from the friction calibration curves. From section 2.3.2 it was shown that the conventional approach for interpreting the friction calibration charts is not suitable for evaluating the friction coefficient if the friction coefficient varies with contact pressure. Therefore, a new iterative methodology is proposed to better evaluate the dynamic friction coefficient:

- The test samples are compressed and measured at even intervals of height reduction

- Friction calibration curves are created using FEA and simulate the test from the initial geometry up to the first experimental data point. The friction coefficient is then interpolated between these curves similar to the standard ring compression test method

- New friction calibration curves are then generated starting from the first data point to the second data point where the friction coefficient is interpolated for this second section

- This process is repeated across all data points to generate a friction-pressure relationship. A schematic overview of this process is depicted Figure 49.
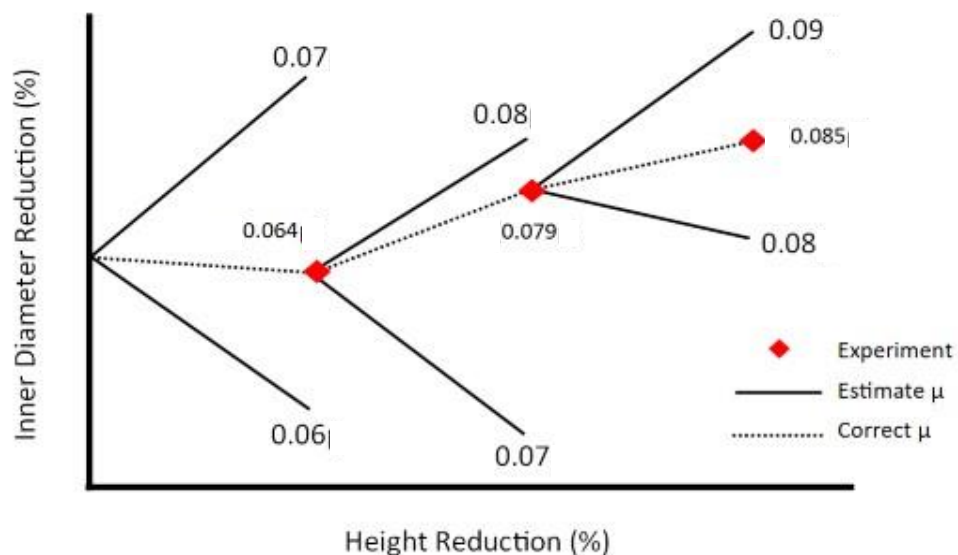
Figure 49: Schematic for the Iterative FCC method.

For region three, the self-lubricating liner's coefficient of friction has already been measured by SKF (Figure 27). However, there is concern about how this data was measured as no consideration was given to the no-load breakout torque of the bearings. The no-load breakout torque exists due to the compression of the liner from when the outer race is formed around the inner ring during the manufacture of the bearing (Woodhead, 2015a). Therefore, at very low external loads the contact pressure being applied to the liner is larger than expected and would result in an overestimate of the stated friction coefficient. This effect diminishes as the external load increases and begins to dominate the apparent liner contact pressure. The expected impact of this effect was determined to be minimal with further research into this concern falling outside the scope of this investigation.

3.5. Summary of Methodology

In summary, the methodology of this thesis will be as follows:

- Modelling of the staking process and the development of closed-form solutions to the staking force, pushout strength, and post-stake torque will be developed utilising a virtual design of experiments methodology. Finite element analysis tools will be used to compute each of the required designed experiments.

- The inner ring will be modelled as perfectly-elastic steel within the finite element analysis. The self-lubricating liner will be modelled with a non-linear compressive modulus and the material data will be provided by SKF.

- For the outer race and housing, their plastic strain data will be measured using uniaxial compressive testing and will follow the test methodology outlined in ASTM International E9-09 (2018).

- The friction-pressure relationship at the interface between the staking anvil/outer race and outer race/housing will be evaluated using ring compression tests. The test samples will use the widely accepted geometric ratios for the outer diameter, inner diameter, and height of 6:3:2.

- An iterative method to interpolating the friction calibration curves will be used whereby the coefficient of friction is evaluated between each data point from the ring compression test.

- Machine operators will measure the pre- and post-stake torque and all relevant geometry of the first bearing from each batch to create a large dataset of staked bearings to validate the Virtual-DoE against.

4

Mechanical Characterisation of High-Alloy Steels

Presented in this chapter is the characterisation of the behaviour of the steels used for the outer race and housing (AMS-5643 H1025 and H1150 respectively) and to understand how their behaviour changes with respect to strain-rate. This material data was then later used in a computational modelling environment to model the staking process.

4.1. Background

The steel predominantly used by SKF in the manufacture of spherical bearings and rod ends is AMS-5643 (Dynamic Metals, 2022). This steel is commonly referred to as 17/4PH and is used in two different heat treatment conditions: H1150 for the outer race of the bearing and H1025 for the housing. A critical component for the numerical models developed in this thesis is the accurate characterisation of the mechanical properties for AMS-5643. Its relevant mechanical properties are the Poisson's ratio, Young's modulus, yield stress, and lastly the flow stress which is defined as the pressure required to plastically deform a material as a function of its instantaneous strain. For most metals, this can be accurately described by a power-law relationship such as Hollomon's strain-hardening equation (Hollomon, 1945) as

$$\sigma = K\bar{\varepsilon}^n \,, \qquad\qquad [\,32\,]$$

where σ is the flow stress, $\bar{\varepsilon}$ is the instantaneous true strain, and K is the strength coefficient. The strain-hardening exponent, n, is a measure of a materials resistance to plastic deformation ranging from 0 to 1 with 0 representing a perfectly plastic material and 1 a perfectly elastic material.

Whilst these properties are normally determined through quasi-static testing at a constant strain rate, anvil velocities during staking vary due to how the operator applies the staking load via a hydraulic press. Strain rates have been estimated to be between $0.08s^{-1}$ and $0.5s^{-1}$ which lie within the transition phase between typical static and dynamic material behaviour (Bayraktar *et al.*, 1993; Kalpajian, S. and Schmid, 2008; Orsolini, 2010). Previous research by Woodhead (2015a) investigating the material properties of AMS-5643 (at a different heat treatment of H1000) at strain rates from $0.001s^{-1}$ to $1s^{-1}$, found that whilst Poisson's ratio and Young's modulus were invariant with respect to strain rate (0.3 and 200GPa respectively), the yield and flow stress varied significantly with strain rate.

Therefore, the following experiments were designed to measure the yield and flow stress across a range of strain-rates for AMS-5643 H1150 and H1025 to determine their behaviour with respect to strain-rate.

4.2. Uniaxial Compression Test Methodology

Staking is characterised as an open-die forging operation that predominantly generates compressive stresses in both the outer race lip and rod end, at strains typically exceeding 0.25. The process is carried out at room temperature and is reasonably assumed to be adiabatic. Therefore, uniaxial compression testing is the most suitable experiment to ascertain the required material properties as it both replicates the stress state and large strains seen in staking. ASTM International E9-09 (2018) outlines the methodology for uniaxial compression testing for metallic materials with the key criteria that must be followed summarised below:

- Both ends of the compression platens must have flat surfaces and be parallel within 0.0002 in./in (m/m).

- Platens shall be faced or made of a hard material. Tungsten carbide is recommended as die material for hardened steels 55 HRC or greater.

- It is necessary to use an alignment device unless the testing machine has been designed specifically for axial alignment.

- For high-strength metals and/or for determining plastic deformation characteristics, short, cylindrical specimens should be used with a length-diameter ratio less than 2.

- For cylindrical specimens, the parallel faces should be flat and parallel within 0.0005 in./in (mm/mm) and perpendicular to the central axis to within 3' of arc.

- Test speeds should be set to a strain rate of 0.005 strain per minute ($8.3 \times 10^{-5}\,s^{-1}$), or 0.003 strain per minute ($5 \times 10^{-5}\,s^{-1}$) if the material is strain-rate sensitive.

The only deviation from the ASTM E9-09 standard was the selection of strain rates greater than $5 \times 10^{-5}\,s^{-1}$ as discussed later in section 4.2.3. The strain rates defined in E9-09 eliminate any unwanted effects caused by strain-rate, whereas the objective of this experiment was to determine the effects of strain-rate on the material properties.

4.2.1. Test Equipment

An Instron 8802 servo-hydraulic press was used for the uniaxial compression tests in conjunction with a 2620 strain gauge extensometer to record the strain of the compressed samples. The extensometer and the press's internal 250KN load cell were both connected to an Instron 8800 controller which allowed for the two data streams to be brought together and time-synced, greatly simplifying the data logging process and post-processing of the data. The original steel compression platens that were fitted to the press were not suitable for the compression of steel specimens, therefore two 440C stainless steel anvils were made and through-hardened to 57 HRC to act as the bearing surface to meet the E9-09 test standard. Concentric rings marked on the platens aided in the alignment of the anvils and the specimen to the central axis of the press (Figure 50).
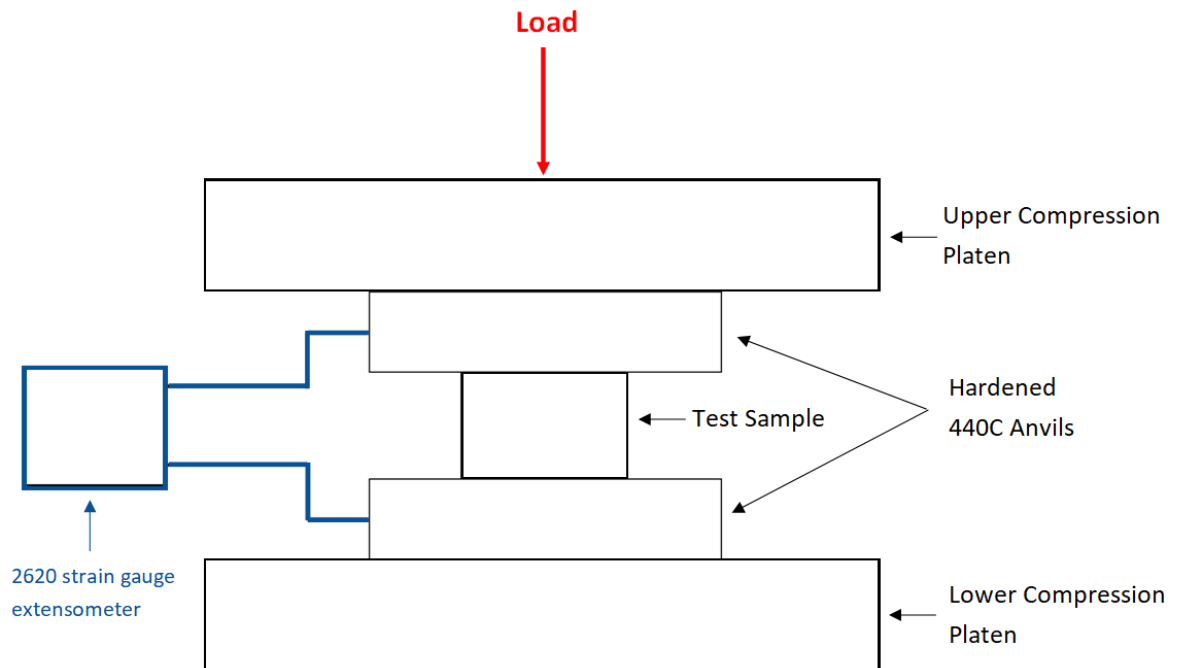
Figure 50: Uniaxial compression test setup with the specimen held between two heat-treated 440C anvils and a strain gauge extensometer to measure the compressive strain of the sample.

As can be seen in Figure 50, the extensometer arms were mounted to the hardened platens. This results in an indirect measurement of the specimen's strain because the strain gauge includes the elastic deformation of the test setup. This reduces the measured stiffness of the sample and therefore needs to be compensated for in the post-processing of the data. This is discussed in more detail in section 4.3.1.

4.2.2. Sample Preparation

Careful consideration was given when choosing the dimensions for the test samples as larger samples would reduce the relative error from manufacturing tolerances but small enough to allow for sufficient compressive strain to be generated within the press's 250 kN limit. The only guidance given by E9-09 for the size of specimens is that the length-diameter ratio should be approximately 0.8 as to avoid buckling in the unsupported region. The following calculations were made to estimate the maximum strain achievable for a 250kN working load with an initial specimen size of 10 x ⌀12.7mm (H1025) and material data from Woodhead's (2015a) research on AMS-5643 H1000. Because H1000 has a higher yield and ultimate strength than H1025, this would provide a lower bound estimate for the strain at 250kN. Using the work Equations 1 - 3 and values for K (1750 MPa) and n (0.13) from Woodhead's research allows for Equation 4 to be solved graphically to give a lower bound estimate of ≈ 0.28 true compressive strain which exceeds the expected maximum plastic strain of the housing of ≈ 0.1. This calculation is repeated for H1150 using a smaller specimen size of 8 x ⌀10mm. The lower bound estimate was evaluated to be ≈ 0.71 true compressive strain which exceeds the expected maximum plastic strain of the outer race of ≈ 0.6.

4.2.3. Test Setup

The servo-hydraulic press is controlled through user-defined waveform profiles by either position, load, or velocity. The desired strain-rate ($\dot{\varepsilon}$) was attained by calculating the equivalent velocity (v) using Equation 33. However, if the velocity profile is constant, the effective strain-rate will increase as the height of the specimen (H) reduces. For a 10mm tall specimen at a projected strain of 0.28, as previously calculated for H1025, the strain-rate would increase by 32%.

$$v = H * \dot{\varepsilon} \qquad\qquad [\,33\,]$$

To correct for this change in strain-rate, velocity compensation was enabled in the controller, to gradually reduce the test speed to ensure a constant strain-rate was maintained. For both materials being tested (AMS-5643 H1150 and H1025) strain-rates of $0.01s^{-1}$, $0.1s^{-1}$ and $1s^{-1}$ were chosen to fully encompass the estimated range of strain-rates seen during staking.

Ten specimens were tested at each strain rate for both materials to give a total test plan of 60 specimens which follows the same testing methodology and volume as Woodhead (2015a). They also used axial compression tests for the same material, AMS 5643, but at a slightly lower heat treatment (H1000 compared to H1150 and H1025) Their results found the material behaviour of AMS 5643 H1000 to be very consistent between tests and it was also expected that H1150 and H1025 would also show similar variance. Therefore, given the variance expected between test specimens, Ten specimens per material per strain rate was deemed sufficient and would keep the total number of tests to be run at a feasible limit given the time and quantity of material available.

Friction between the anvils and test specimens caused the unsupported walls of the specimen to barrel outwards as the expansion of the contact surfaces begin to stick at the anvil-specimen interface. Molykote G-n plus lubricant (Dupont, 2022) was applied to all surfaces to reduce friction and promote uniform deformation throughout the specimen.

When specimens are first brought into contact with the anvils, there is a settling period which gave a non-linear stress-strain response at the start of each test. To eliminate this, the specimens were pre-loaded to 50% of their expected yield stress before attaching the extensometer and zeroing. In post-processing, the displacement measurement was then offset to account for the initial pre-load. The 50% load was determined in preliminary testing to be 45kN for H1150 and 80kN for H1025.

4.2.4. Summary of Methodology

The methodology used for this experiment is summarised as follows:

- ASTM International E9-09 were followed for uniaxial testing except for the desired test strain-rates.

- Materials to be tested were AMS-5643 H1025 and H1150 at strain rates $0.01s^{-1}$, $0.1s^{-1}$ and $1s^{-1}$.

- A total of 60 specimens were tested with 10 specimens at each strain rate.

- Cylindrical test specimens measuring 10 x $\varnothing$12.7mm (H1025) and 8 x $\varnothing$10mm (H1150)

- Samples to be pre-loaded to 50% of their expected yield strength: 45kN and 80kN for H1150 and H1025 respectively.

- Sampling rate of 2000Hz.

Equipment used:

- Instron 8802 servo-hydraulic press, maximum working load of 250kN.

- Heat treated 440C anvils at 57 HRC.

- Instron 2620 strain gauge extensometer.

4.3. Measurement of the Material Properties

The process for determining the yield strength and flow stress with respect to strain-rate begins with the measurement of each material property at multiple strain rates, then model their evolution across those strain rates. Due to the nature of this experiment, an additional preliminary step is required to correct the elastic deformation of the test setup.

4.3.1. Displacement Compensation

The location of the extensometer (Figure 50) resulted in the total measured displacement (ΔL_T) being the sum of both the deformation of the specimen (ΔH_S) and the compression of the anvils (ΔL_A). This has the net effect of test specimens appearing to deform more than they should be and needs to be corrected for. The stiffness of the test specimens (in the elastic region) is already known to be 200GPa (Dynamic Metals, 2022) and therefore provides a reference point to ensure that the compensation applied to the measured displacement is correct.

If the compression of the test fixture responds linearly with pressure, then the change in length is calculated as

$$\Delta L_A = \frac{\sigma\,L_A}{E}, \qquad\qquad [\,34\,]$$

where σ is the contact pressure between the specimen and anvils and E is the Young's modulus of the anvils which is 200GPa (Atlas Steels, 2008). L_A is defined as the combined vertical height from the interface between the test specimen and anvil to the attachment point of the extensometer arms (for both the upper and lower anvil). The contact pressure (which is equivalent to the true stress experienced by the specimen) does not increase linearly with an increase in the applied load, due to the contact area increasing as the specimen deforms. To account for this, the contact pressure can be expressed as a function of the total measured displacement (ΔL_T) and compression of the anvils (ΔL_A) in Equation 35 as

$$\sigma = \frac{F}{A} = \frac{F\,(H_0 - \Delta H_S)}{V} = \frac{F\,(H_0 + \Delta L_A - \Delta L_T)}{V}, \qquad\qquad [\,35\,]$$

where V is the volume of the specimen, H_0 is the initial height of the specimen and ΔH_S is the change in height of the test specimen.

Substituting Equation 35 into Equation 34 allows for the compression of the anvils to be expressed as

$$\Delta L_A = \frac{FL_A\,(H_0 + \Delta L_A - \Delta L_T)}{EV} = \frac{\alpha\,(H_0 - \Delta L_T)}{1 - \alpha}, \qquad [\,36\,]$$

where α is defined as

$$\alpha = \frac{FL_A}{EV}. \qquad [\,37\,]$$

With the change in length of the test fixture calculated, the measurement from the extensometer can be corrected to give the true change in height of the specimen ΔL_S as

$$\Delta L_S = \Delta L_T - \Delta L_A. \qquad [\,38\,]$$

Circumferential v-grooves were machined into the two anvils so that for each test the extensometer would locate in the same position. These grooves were set to give a value of L_A as 25mm and resulted in the correction of all the test specimens to an elastic stiffness within 200±2GPa. To validate this method, the corrected displacement data was compared against the final measured height of each test specimen (Figure 51). The error in the correct data was found to be +0.2% ± 0.5%.

Figure 51: Predicted displacement compared to physical samples (in test order). Red lines denote the error bound in the measurement of the physical samples.

These correction equations assume that the stress throughout the anvil is constant and equal to the true stress in the test specimen. However, this is not correct as the larger cross-sectional area of the anvil results in a lower average stress than seen in the specimen. The average error was calculated to be +0.2% which was likely the result of the over-correction for the elastic compression of the anvil. However, it is still within the ±0.5% measurement error bound with a maximum error of only +1.2%.

4.3.2. Yield Stress

The yield stress defines the limit of elastic behaviour, after which plastic deformation will occur. During the compression test the specimens will become shorter and the surface area between the sample and compression anvil will increase. To determine the true yield stress of the samples the increase in contact area must be compensated for. By assuming that the volume of the test samples remains constant during compression, the corrected contact area (A_c) at each sampled data point was calculated to be

$$A_c = \frac{V}{H_0 - \Delta L_S}$$

[39]

where V is the volume of the sample, H_0 is the initial height of the undeformed test sample, and ΔL_S is the change in height of the specimen (as previously defined in 4.3.1). For test sample 21, plotting true stress against true strain (Figure 53) shows that the yield stress is approximately 850 ± 30MPa. The yield slope was defined using a linear fit over the elastic region of the stress strain plot. The exact point where the elastic region ends is difficult to determine accurately and therefore it is standard practice to use a 0.2% strain offset when defining the yield point. By visual inspection, the intersection of the 0.2% strain offset and the true stress-strain curve is 1060 ± 5 MPa. The 0.2% yield strength for both materials at all strain rates is summarised in Table 7.
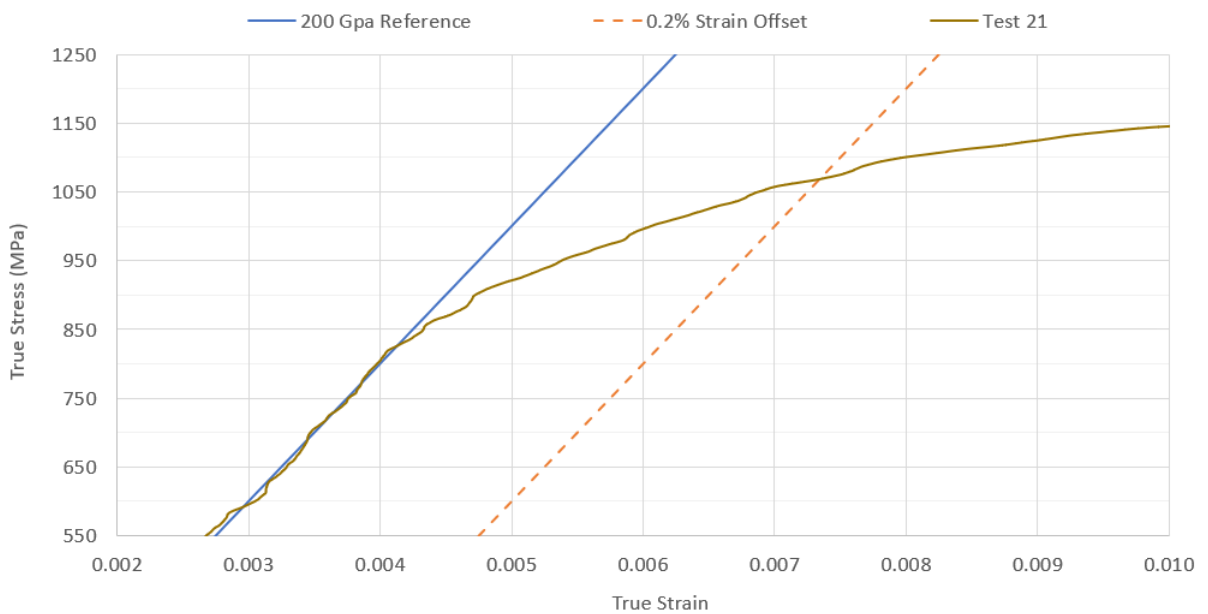
Figure 52: Magnified view of the true Stress-Strain chart for test specimen 21 with the intersection with the 0.2% strain offset at 1060MPa.

Table 7: 0.2% Yield Strength for AMS-5643 H1025 and H1150. Error bounds represent 1 standard deviation.

Material	Strain Rate		
	$0.01s^{-1}$	$0.1s^{-1}$	$1s^{-1}$
AMS-5643 H1025	1024 ± 12 MPa	1086 ± 17 MPa	1173 ± 20 MPa
AMS-5643 H1150	902 ± 10 MPa	940 ± 8 MPa	976 ± 12 MPa

For both materials, it was found that the yield stress increased with an increase in strain-rate. By plotting these results on a graph of log yield stress versus log strain-rate, a linear relationship could be fitted with a high degree of confidence: R^2 values of 0.96 for H1025 and 0.99 for H1150.
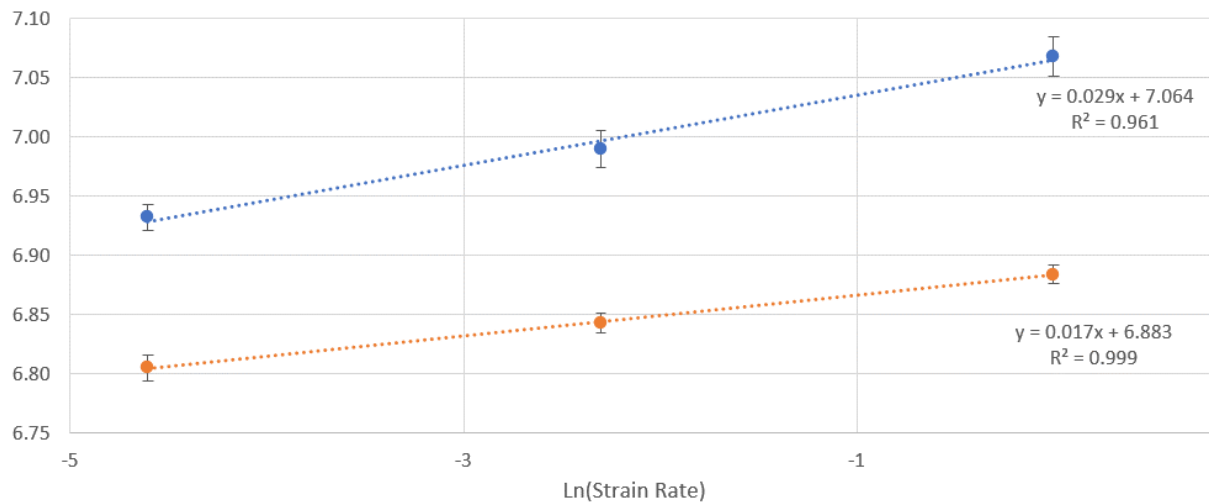
Figure 53: log yield stress versus log strain rate for materials AMS-5643 H1025 and H1150.

Assuming a linear fit, then a power-law relationship between strain-rate and yield stress follows the general form

$$\sigma_y = K_y \dot{\varepsilon}^{\,m}, \qquad\qquad [\,40\,]$$

where σ_y is the yield strength, K_y is the yield strength coefficient, $\dot{\varepsilon}$ is the strain-rate and m is the strain-rate sensitivity exponent. By rearranging Equation 40 into the general form $y = mx + c$ (Equation 41), the linear best-fit from Figure 53 can be used to calculate the yield strength coefficient and the strain-rate sensitivity exponent. These parameters have been summarised for both materials in Table 8.

$$\ln(\sigma_y) = \ln(K_y) + m\ln(\dot{\varepsilon}). \qquad\qquad [\,41\,]$$

Table 8: Yield Strength coefficient (Ky), Strain-rate sensitivity exponent (m) and coefficient of determination (R^2).

Material	K_y (MPa)	m	R^2
AMS-5643 H1025	1169	0.0295	0.96
AMS-5643 H1150	976	0.0171	0.99

4.3.3. Flow Stress

Flow stress is the pressure required to continue to deform a material as a function of its instantaneous strain-state. As discussed in Chapter 2.4.3, Hollomon (Equation 20) and Johnson-Cook (Equation 24) are two of the most common constitutive material models used to describe the flow stress for metals undergoing plastic deformation. The Hollomon model has been demonstrated to provide the best fit for austenitic steels (Sener and Yurci, 2017) and AMS5643-H1000 (Woodhead, 2015b) which are both very similar in mechanical properties and chemical composition to the tested steels in this thesis, AMS5643 H1025 and H1150. Therefore, Hollomon was chosen as the preferred material model. To determine the flow stress parameters for the Hollomon model, the true stress-strain material data was plotted onto a chart of log true stress-log true strain. In the plastic region of the stress-strain curve (from ≈0.03 true strain) the log true stress-strain plot produces a linear relationship as seen in Figure 54. Using Equation 32, the strength coefficient (K) and the strain hardening coefficient (n) can be calculated as

$$\ln(\sigma) = n\ln(\varepsilon) + \ln(K). \qquad [\,42\,]$$

This was repeated for each test specimen and the averaged results are summarised in Table 9.

Table 9: Strength coefficient and strain hardening coefficients for H1025 and H1150. The error bounds represent 1 standard deviation of variance.

Material	Mechanical Properties	Strain Rate		
		$0.01s^{-1}$	$0.1s^{-1}$	$1s^{-1}$
AMS-5643 H1025	Strength Coefficient, K (MPa)	1676 ± 11	1597 ± 9	1530 ± 10
	Strain Hardening Coefficient, n	0.0991 ± 0.0024	0.0742 ± 0.0022	0.0521 ± 0.0038
AMS-5643 H1150	Strength Coefficient, K (MPa)	1409 ± 7	1389 ± 5	1367 ± 9
	Strain Hardening Coefficient, n	0.0904 ± 0.0025	0.0806 ± 0.0017	0.0701 ± 0.0019
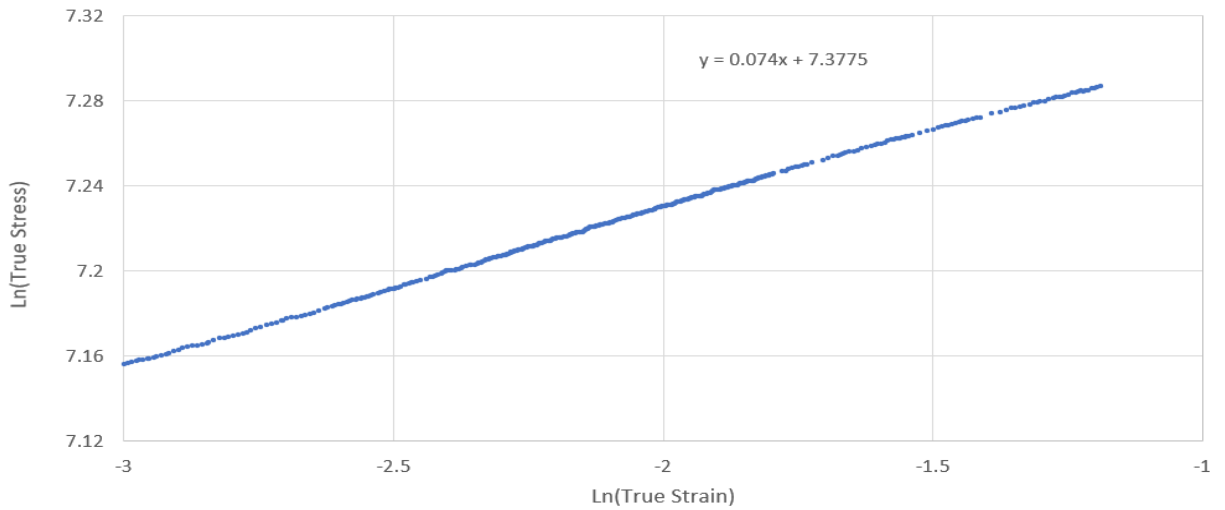
Figure 54: The linear region from the Log true stress-log true strain plot for test sample 21 (H1025) representing a true strain of 0.05-0.3.

Both H1025 and H1150 exhibit the same behaviour with respect to strain-rate: as strain-rate increases, the 0.2% yield stress increases whilst the strength coefficient and strain hardening exponent decreases. This has the effect that, at large plastic strains the true stress-strain curves cross over as shown in Figure 55. This effect, whilst uncommon, is the same as what was found by Woodhead for a different heat treatment of AMS-5643 (H1000).
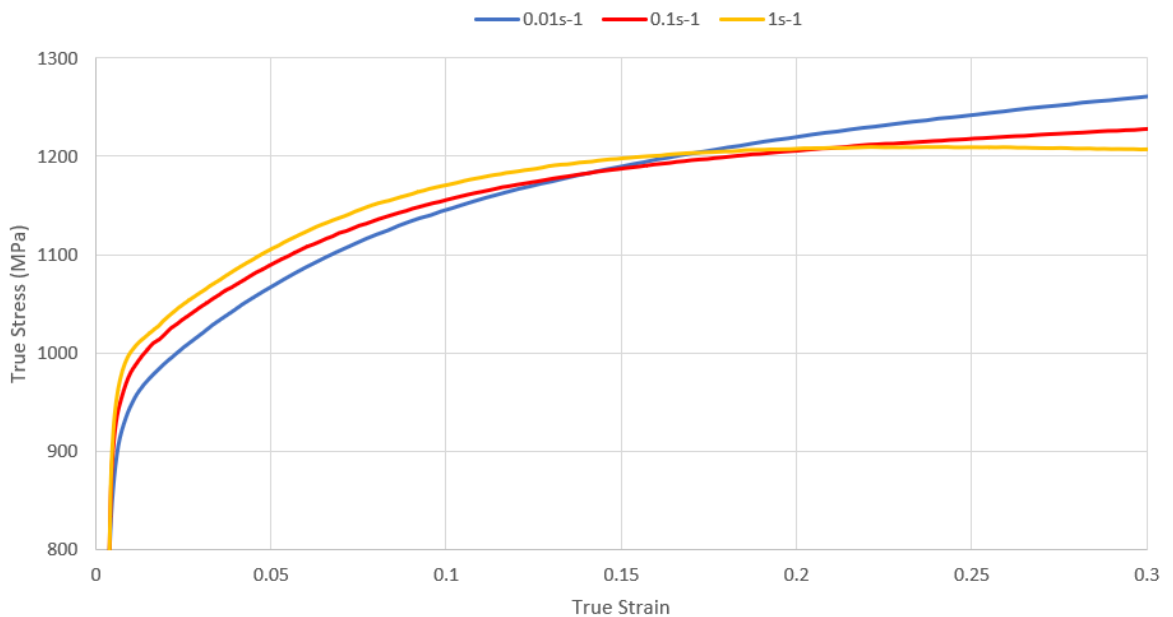
Figure 55: True stress-strain chart for AMS-5643 H1025 at strain rates 0.01, 0.1 and 1^{s-1} up to a true strain of 0.3

To account for the increase in the strength coefficient with respect to strain-rate, the standard approach is to introduce an additional term ($\dot{\varepsilon}^A$) to form the extended Hollomon model (Equation 23) where A denotes the strength sensitivity exponent and $\dot{\varepsilon}$ represents strain-rate. A similar methodology was explored by Woodhead (2015a) to account for the decreasing strain hardening coefficient with respect strain-rate for AMS5643 H1000. The strain hardening coefficient was replaced with the term $n\dot{\varepsilon}^B$ where n is the reference strain hardening coefficient and B represents the strain-hardening sensitivity exponent. By combining both of these methods, a new Modified-Hollomon model is proposed in Equation 43.

$$\sigma = K\dot{\varepsilon}^A \, \bar{\varepsilon}^{\left(n\dot{\varepsilon}^B\right)}$$

[43]

To determine the values for each of the four parameters K, A, n and B, log/log graphs of the strength coefficient (Figure 56) and strain hardening exponent (Figure 57) were plotted against their respective strain-rates from results Table 9.
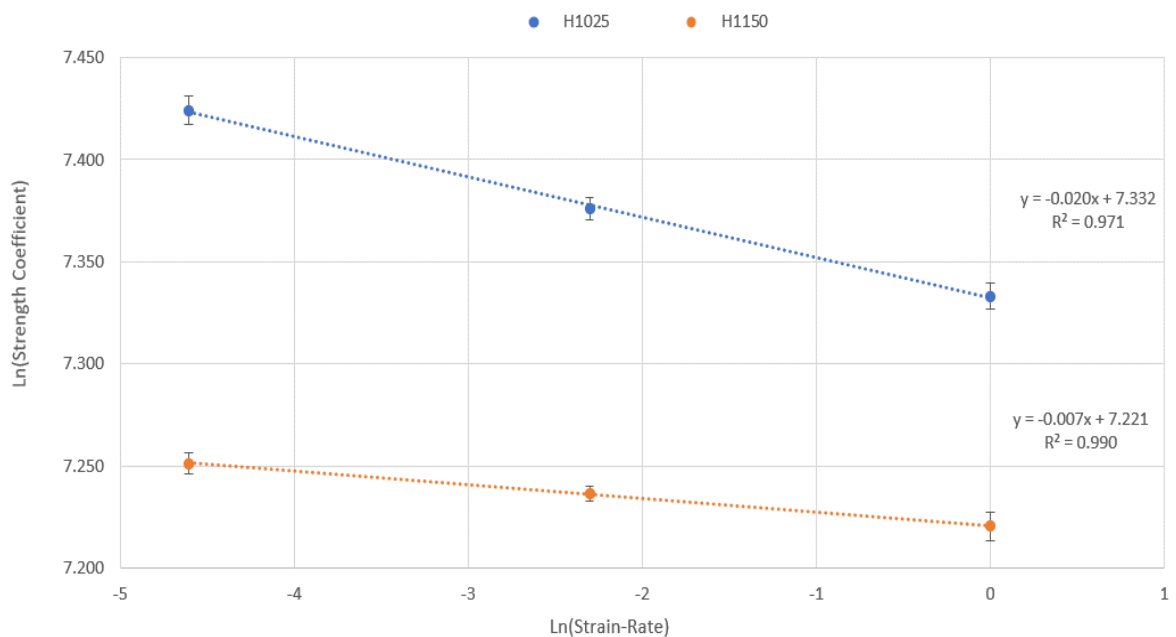
Figure 56: Log Strength Coefficient versus log strain rate for materials AMS-5643 H1025 and H1150.
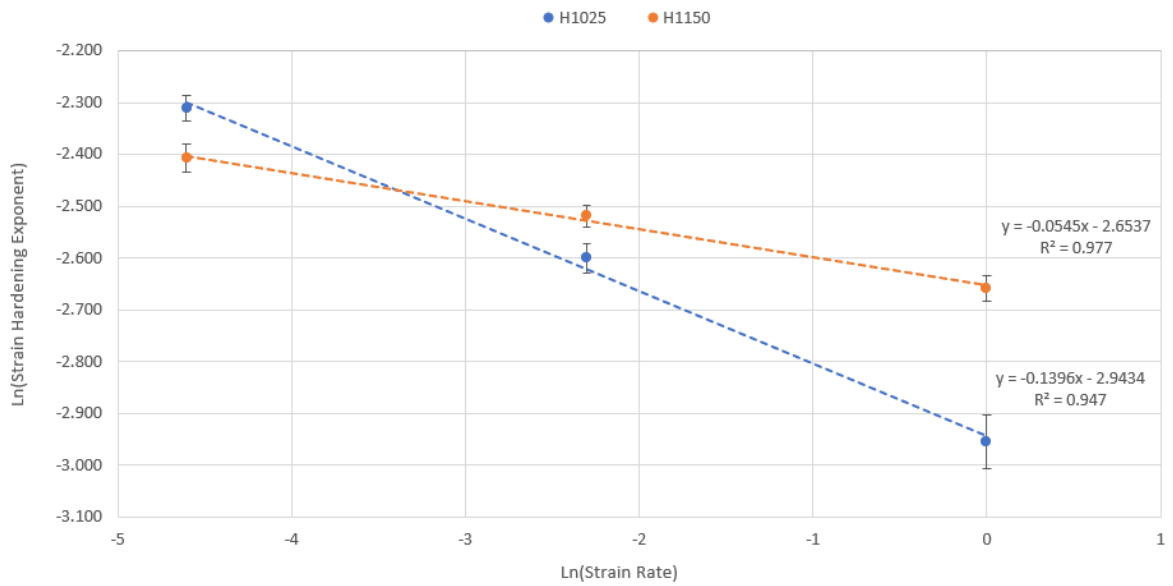
Figure 57: Log strain hardening exponent versus log strain rate for materials AMS-5643 H1025 and H1150.

The results from Figure 56 and Figure 57 indicate linear relationships with respect to strain rate with the four parameters of the Modified Hollomon model summarised in Table 10.

Table 10: Summary of terms for the modified Hollomon equation.

Material	K (MPa)	A	n	B
AMS-5643 H1025	1528	-0.0198	0.0527	-0.1396
AMS-5643 H1150	1368	-0.00662	0.0704	-0.0545

The accuracy of the Modified-Hollomon equation was tested by comparing its prediction to the averaged raw data from each of the tested strain-rates. For H1025 (Figure 58), above a true strain of 0.05 and up to the maximum measured strain of 0.32, the error did not exceed ±1%. For H1150 (Figure 59), across the same range of measure strain, the error remains within 0 to +1.5%. However, across the whole range of measured strain (0.79) the error bound increases to -3% to +2%.
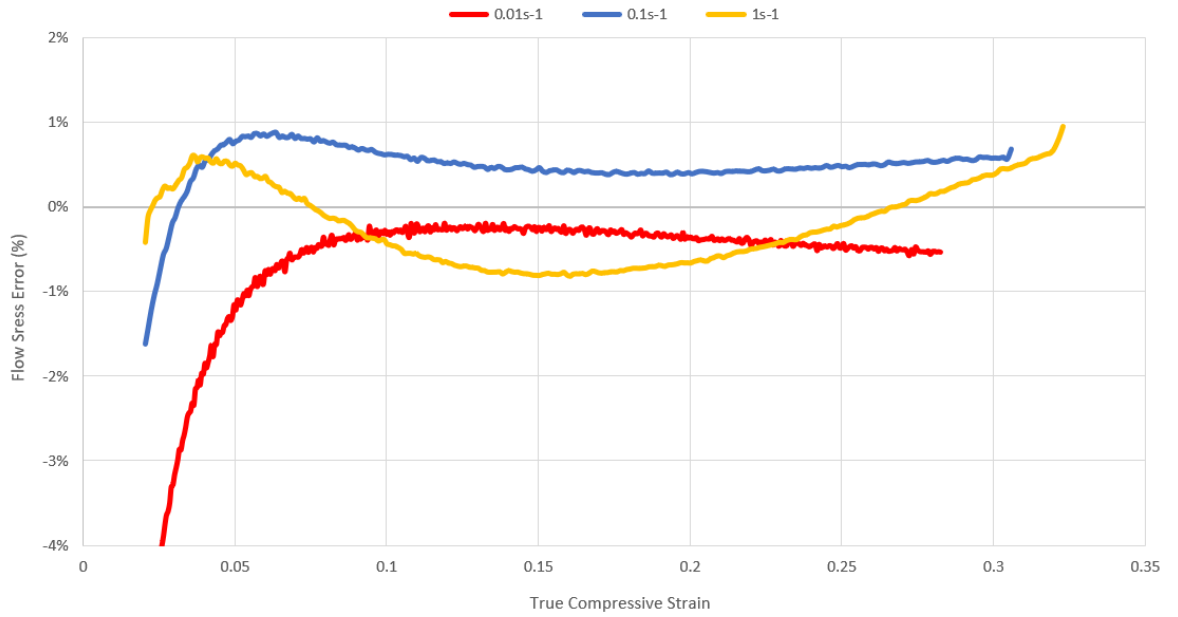
Figure 58: H1025 flow stress error using Modified-Hollomon.
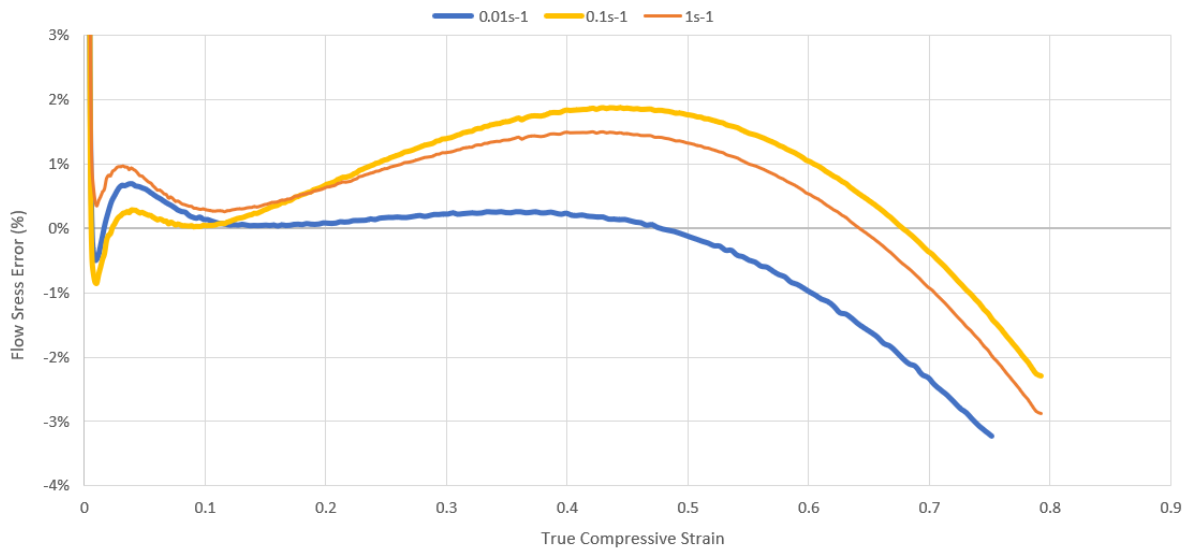
Figure 59: H1150 flow stress error using Modified-Hollomon.

4.4. Error and Uncertainty

The error analysis for the Modified-Hollomon model in Figure 58 and Figure 59 was compared against the average of all test specimens at each strain rate. The variance of the averaged flow stress (across all tested strain-rates) was a maximum of ±1.5%. This variance is due to the small uncontrollable variations in material properties and experimental setup and measurement. By combining these errors, the maximum error for the Modified-Hollomon model was evaluated to be ±2% and ±4% for H1025 and H1150 respectively. Quoting a ±2% uncertainty for the Modified-Hollomon model for H1025 is an appropriate evaluation because the error distribution from Figure 58 remains relatively consistent and balanced across the quoted range of true strain (0.03-0.32).

The same however cannot be said for H1150 as the magnitude of the error increases with true strain and swings from its upper to lower limit after 0.5 true strain. The cause of this error swing is driven by a gradient reversal in the true stress-strain curve at ≈ 0.5 true strain (Figure 60). This is likely the result of an increase in the friction between the anvil and test specimen leading to barrelling of the specimen. Methods have been developed to compensate for the effect of barrelling (Onodera and Chiba, 2009; Opela *et al.*, 2015) however, this requires the measurement of the diameter of the sample throughout the test which was not possible within this experiment setup. Despite this, a symmetric error of ±4% was still the preferred uncertainty description because it provides the simplest description of the model's uncertainty across its entire range.
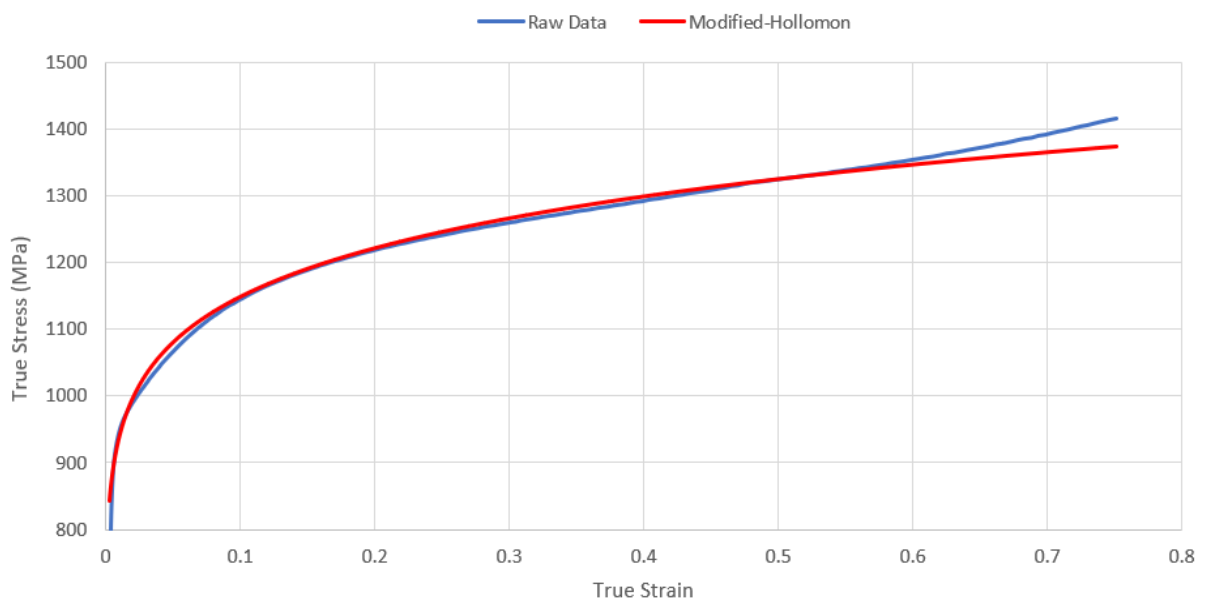
Figure 60: Comparison of the Modified-Hollomon prediction and raw data at 0.01s-1 for H1150.

4.5. Summary

The aim of this chapter is to characterise the mechanical behaviour of AMS-5643 H1025 and H1150, and to understand their behaviour with respect to strain-rate. This has been achieved through the uniaxial compression testing of 60 test specimens following the ASTM International E9-09 test standard: 30 for each material and 10 at each strain-rate of 0.01, 0.1 and $1s^{-1}$.

For both materials, whilst the yield strength increases with strain-rate, the strain-hardening rate decreases with increasing strain-rate. The yield strength follows a power-law relationship (Equation45 44) with the parameters for H1025 and H1150 summarised in Table 11.

$$\sigma_y = K_y \dot{\varepsilon}^{\,m}.$$ [44]

Table 11: Yield Strength coefficient (Ky), Strain-rate sensitivity exponent (m) and coefficient of determination (R^2).

Material	K_y (MPa)	m	R^2
AMS-5643 H1025	1169	0.0295	0.96
AMS-5643 H1150	976	0.0171	0.99

For AMS-5643 H1025, the model is validated across a range of 0.03-0.32 true strain with a maximum possible error of ±2% and is given as

$$\sigma_{(H1025)} = 1528\dot{\varepsilon}^{-0.0198}\, \bar{\varepsilon}^{\,(0.0527\dot{\varepsilon}^{-0.1396})}.$$ [45]

For AMS-5643 H1150, the model is validated across a range of 0.03-0.78 true strain with a maximum possible error of ±4% and is given as

$$\sigma_{(H1150)} = 1368\dot{\varepsilon}^{-0.00662}\, \bar{\varepsilon}^{\,(0.0704\dot{\varepsilon}^{-0.0545})}.$$ [46]

The units for flow stress are MPa, $\bar{\varepsilon}$ is the true strain and $\dot{\varepsilon}$ is the strain-rate. Through the course of this investigation, it was found that the standard Hollomon and the Modified Hollomon model both performed very similarly with regards to their fit against the experimental data across all strain rates. However, the standard Hollomon model can only produce discrete results for specific strain-rates with new coefficients required for each strain-rate. It is not possible to interpolate these coefficients between strain-rates which limits its usefulness for modelling metal forming conditions where localised strain-rate does not remain constant. The proposed Modified Hollomon model in this thesis provides a significant improvement over the standard Hollomon model by allowing for the flow stress to be continuously evaluated at any strain rate. This greater modelling flexibility can be leveraged in finite element modelling environment through either a direct implementation or by providing a greater range of datapoints to create a multilinear material model (Ashcroft and Mubashar, 2011). It is the authors opinion that the same methodology used to create the Modified Hollomon model could in principle be applied to other constitutive material models (such as Johnson-cook, modified Zerilli-Armstrong and Ludwig) to account for strain-rate sensitive material behaviours.

5

Chapter

Pressure-Dependant Friction Analysis

The coefficient of friction is an important variable that must be defined to allow the accurate prediction of the forming geometry and stresses involved in metal forming processes. Literature has shown that the coefficient of friction does not remain constant with respect to contact pressure. However, the understanding of this phenomenon varies significantly and is rarely implemented in computational models. In this chapter, a new approach to evaluate the friction-pressure relationship is outlined using friction calibration charts generated via iterative computation models and ring compression tests.

5.1. Background

The coefficient of friction is inherently difficult to quantify precisely, even within a simple static problem due to the number of factors that can influence the coefficient of friction (Kobayashi, Altan and Oh, 1989; Sofuoglu and Rasty, 1999). Some of these influencing factors include, but are not limited to, surface roughness, use of lubricants, work-piece and die material combinations, temperature, strain-hardening, third-body debris and corrosion.

Building off the work of Kunogi (1956), Male and Cockcroft (1966) published a standard methodology for determining the coefficient of friction using a ring compression test. The test consists of a ring compressed axially between two flat and parallel compression platens, so that the material undergoes plastic deformation (Figure 61). If the interface between the specimen and dies is of sufficiently low friction (assuming isotropic material properties, rigid-perfect plastic behaviour, and homogenous deformation), then the inner diameter of the ring expands together with the outer diameter. As the friction increases, sticking occurs at the interface which resists the outward flow of the material causing the specimen to bulge at the midplane (barrelling). Once the friction coefficient reaches a critical value it becomes favourable for material to flow inwards and results in the reduction of the inner diameter. The coefficient of friction is evaluated by comparing the relationship of the inner diameter and height of the specimen against analytically or numerically derived Friction Calibration Curves (FCC), at a variety of constant coefficients of friction. Ring compression tests have seen widespread adoption since the early 2000s (Sofuoglu *et al.*, 2001; Martin *et al.*, 2015; Woodhead, Truman and Booker, 2015b; Kahhal *et al.*, 2021) and have proven their suitability, particularly for the modelling of bulk deformation processes (Kalpajian and Schmid, 2008).
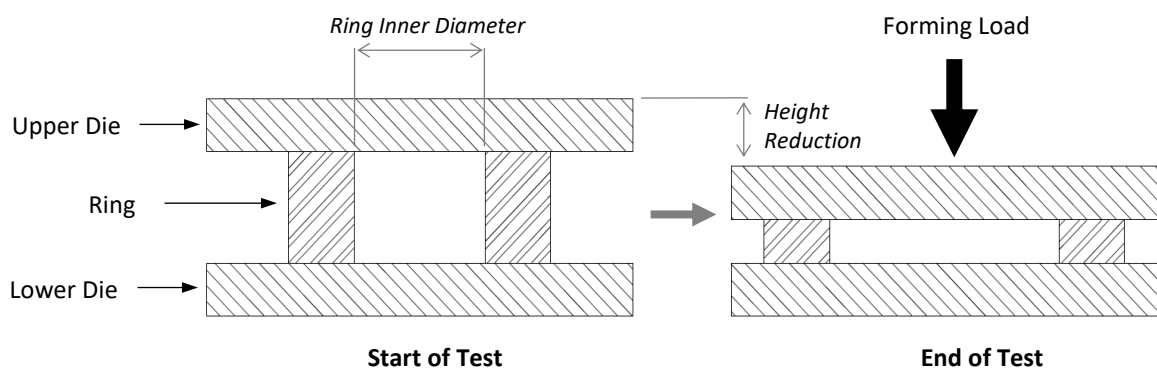
Figure 61: Ring Compression test schematic.

5.2. Ring Compression Test Methodology

As discussed in section 3.4, the two critical contact regions for a friction-pressure relationship to be determined were between 1) the staking anvil and the outer race with a molybdenum disulphide solid paste lubricant (Molykote, 2023) applied between the two contact faces and 2) the outer race and housing which is a dry contact. There is no formalised recognised test standard for ring compression tests and the consensus in previous research is to broadly follow the same methodology as uniaxial compression test standards such as those outlined in ASTM International E9-09 (2018). The key criteria that will be followed from ASTM E9-09 are as follows:

- Both ends of the compression platens must have flat surfaces and be parallel within 0.0002 in./in (m/m).

- Platens shall be faced or made of a hard material. Tungsten carbide is recommended as die material for hardened steels 55 HRC or greater.

- It is necessary to use an alignment device unless the testing machine has been designed specifically for axial alignment.

- Parallel specimen faces should be flat and parallel within 0.0005 in./in (mm/mm) and perpendicular to the central axis to within 3' of arc.

Where the ring compression test differs from the uniaxial compression standard is the requirements surrounding sample geometry, die-part lubrication, and strain-rate.

5.2.1. Specimens

For both regions, the metal undergoing plastic deformation is the outer race which is made from steel AMS5643-H1150. The most used ratio for the outer diameter to inner diameter to height (OD:ID:H) in previous research has been 6:3:2 (Kahhal *et al.*, 2021; Woodhead, Truman, and Booker, 2015b) and will be the chosen ring geometry ratio used for this experiment. However, there is no consensus on the most suitable dimensions of the rings. Whilst increasing the overall size can aid in taking measurements and reduce the relative measurement error (Sofuoglu and Gedikli, 2002), this increases the required forming load with the limiting factor becoming the capacity of the forming press. Calculations of the maximum expected forming load are made for a specimen measuring ⌀19.05mm x ⌀9.53mm x ⌀6.35mm (Figure 62) with a 50% height compression. The compressive true strain ($\bar{\varepsilon}$) of the specimen at maximum displacement is

$$\bar{\varepsilon} = ln\left(\frac{H_0}{H_f}\right) = ln\left(\frac{6.35}{3.175}\right) = 0.693, \quad\quad [\ 47\ ]$$

where H_0 and H_f is the initial and final height of the specimen respectively. The forming area (A_f) changes proportionally with H_f as

$$A_f = \frac{V}{H_f} = \frac{\pi H_0 (D^2 - d^2)}{4 H_f} = \frac{\pi * 6.35 * (19.05^2 - 6.35^2)}{4 * 3.175} = 506.71\ mm^2, \quad\quad [\ 48\ ]$$

where V represents the volume of the specimen, D and d, are the outer and inner diameters of the ring. Lastly, the forming force (P) can be calculated as the product of the forming area and flow stress from the modified Hollomon strain-hardening equation for AMS5643-H1150 (Chapter 4). Assuming a dynamic strain rate of 1 sec^{-1} the maximum forming load is

$$P = A_f * 1369\dot{\varepsilon}^{-0.00627}\ \bar{\varepsilon}^{\left(0.0712\dot{\varepsilon}^{-0.0482}\right)}, \quad\quad [\ 49\ ]$$

$$\therefore\ P = 506.71 * 1369 * 1^{-0.00627} * 0.693^{\left(0.0712*1^{-0.0482}\right)} = 666.1\ kN$$

For a 75-tonne four-column press, the calculated specimen should achieve a 50% height compression with a 10% safety margin.
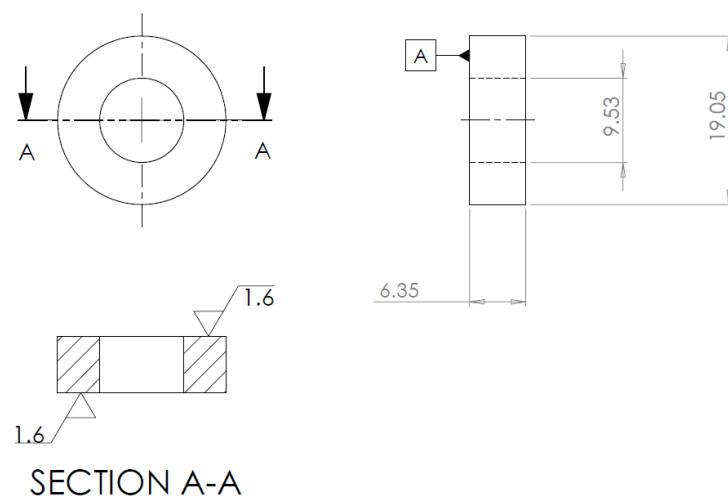
Figure 62: Ring compression test specimen drawing. All dimensions in mm.

5.2.2. Barrelling Compensation

Friction at the interface between the die and test specimen results in barrelling and an inhomogeneous strain field as the specimen is compressed (Kahhal *et al.*, 2021). This creates a condition where the uniaxial stress state principle no longer holds and needs to be compensated for. Similarly to Bridgman's correction factor (Bridgman, 1952), a bulge correction factor (C_f) was used by Ettouney and Hardt (1983) to calculate the true stress (σ) of the ring specimens undergoing compressive plastic deformation as

$$\sigma = C_f \frac{4P}{\pi(D^2 - d^2)}.$$ [50]

The bulge correction factor is derived analytically from the analysis of the stress distribution at the mid-plane (Mielnik, 1991) and is given as

$$C_f = \left[\left(1 - \frac{2R}{a}\right)\ln\left(1 - \frac{a}{2R}\right)\right]^{-1},$$ [51]

where R is the bulge radius of the sample and a is the specimen's outer radius. From geometric relations, the bulge radius was calculated as

$$R = \frac{h^2 + (D - d)}{4(D - d)},$$ [52]

where h is the instantaneous height of the test specimen.

5.2.3.   Variation in Specimen Diameter

It is normally assumed that the material used in a ring compression test is isotropic and deforms homogenously. However, Han (2002, p.13) have shown that "if an anisotropic material is assumed to be isotropic, the influence of anisotropy will be mistakenly attributed to friction because the influence of material anisotropy on ring deformation is in the same direction as friction". Both material anisotropy and changes in friction can result in the specimen becoming ovalized (Figure 63). To compensate for any anisotropic frictional behaviour that could lead to the rings becoming ovalised, a sweep of the inner diameter is taken to obtain the maximum, minimum and average dimensions (Woodhead, Truman, and Booker, 2015).

Figure 63: Influence of frictional anisotropy (dry and Teflon lubrication) on ring deformation (Han, 2002).

Across all load conditions, the variance of the average inner diameter was greater than the average variance between the maximum and minimum diameter typically by a factor no less than three. An example of the ovality of the test specimens at a load of 50 kN is shown in Figure 64. It is therefore appropriate to average the maximum and minimum inner diameter when calculating the change in inner diameter because of the small measure of anisotropic behaviour relative to the variance between test specimens.
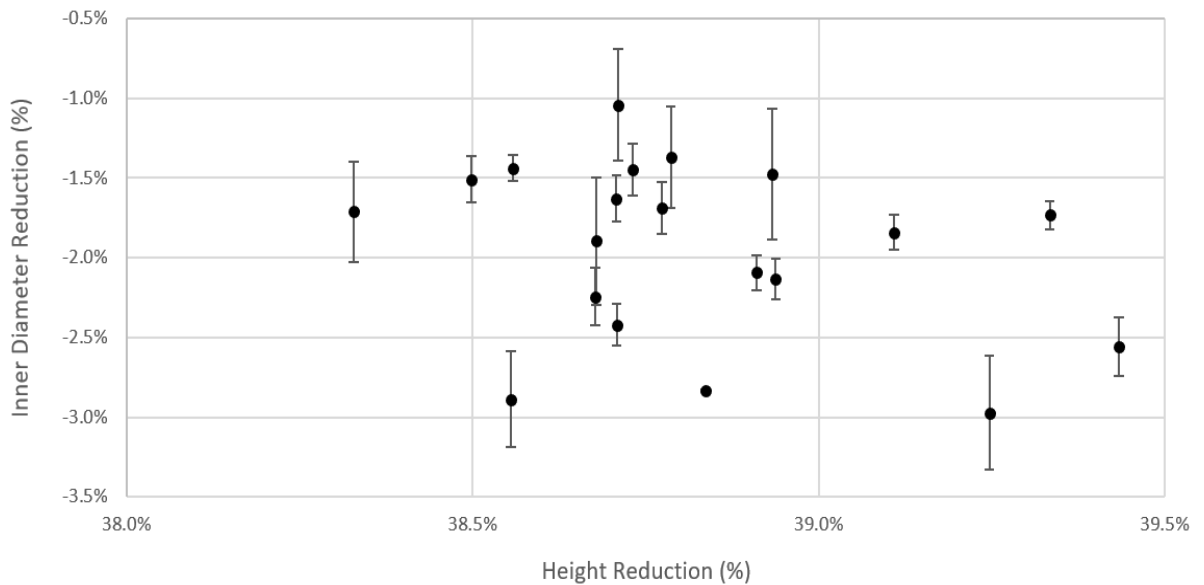
Figure 64: Variation of the inner diameter reduction percentage caused by the ovality of the test specimens for the 50 kN load condition. Larger error bars represent greater ovality.

5.2.4.   Experiment Setup

A total of 40 specimens were manufactured with 20 specimens for each friction region. Tests were carried out at SKF Clevedon's facilities using a 75-tonne, four-column press with the first load profile set to 15 tonnes and increased in increments of 5 tonnes. For the lubricated specimens, molybdenum disulphide lubricant (Molykote, 2023) was re-applied to each face of the specimens and tungsten carbide dies. Whilst the hydraulic controls were kept constant between all specimens and load steps, it was not possible to control or maintain a constant anvil speed or strain-rate during each compression. To mitigate any possible effects of variable strain-rates, the presses hydraulic flow rate was reduced to bring the loading rate to 10 tonnes per second (down from the standard manufacturing load rate of approximately 50 tonnes per second). Secondly, the dwell time was set to 5 seconds at each load step to ensure that each sample had fully settled before removing the load and taking any measurements.

5.2.5.   Finite Element Model

As discussed in Chapter 2, ANSYS (2021a) was identified as a suitable computational modelling package for simulating both the ring compression test and to generate the friction calibration curves. To increase computational efficiency, an axisymmetric analysis was used to reduce the FE model to a 2D rotationally symmetric analysis and includes a symmetry plane splitting the ring coupon about the mid-height (Figure 65). With the lower platen removed from the model due to the symmetry place, the remaining upper platen is modelled as a rigid body. This setup follows the conventional FE modelling approach for ring compression testing as detailed by Kahhal *et al.* (2021) and Woodhead, Truman, and Booker (2015b).
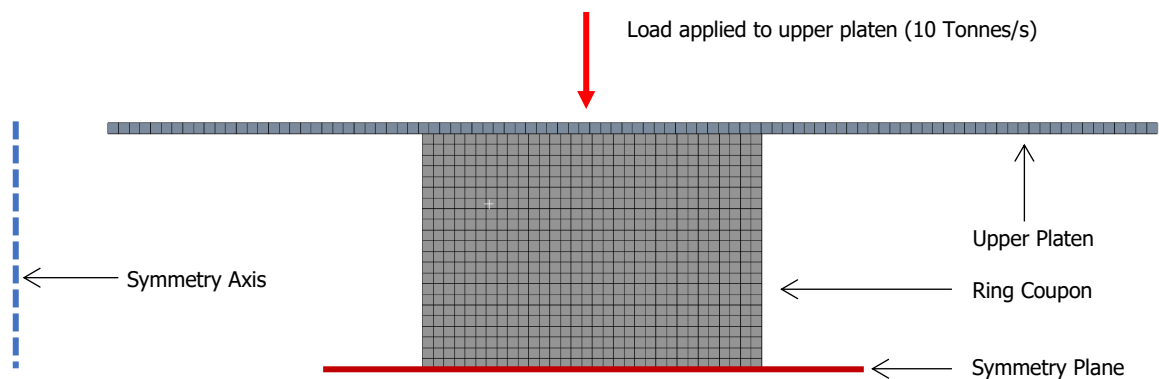
Figure 65: FE model for ring compression test with both symmetry axis and symmetry plane shown.

5.2.5.1.   *Material Model*

The material definition for the ring coupon was derived from the Modified-Hollomon flow stress model for AMS5643-H1150 as defined in Equation 46 from Chapter 4. The stress-strain profile was first generated at constant strain rates of 0.01, 0.1, 1 strain per second (the same range of tested in Chapter 4) and then tabulated as three multilinear isotropic hardening models (Figure 66). A custom command was then written using Ansys's Parametric Design Language (APDL) to interpolate between these stress-strain tables and update the stiffness of each element at the start of each time-step of the FE model (Figure 67).
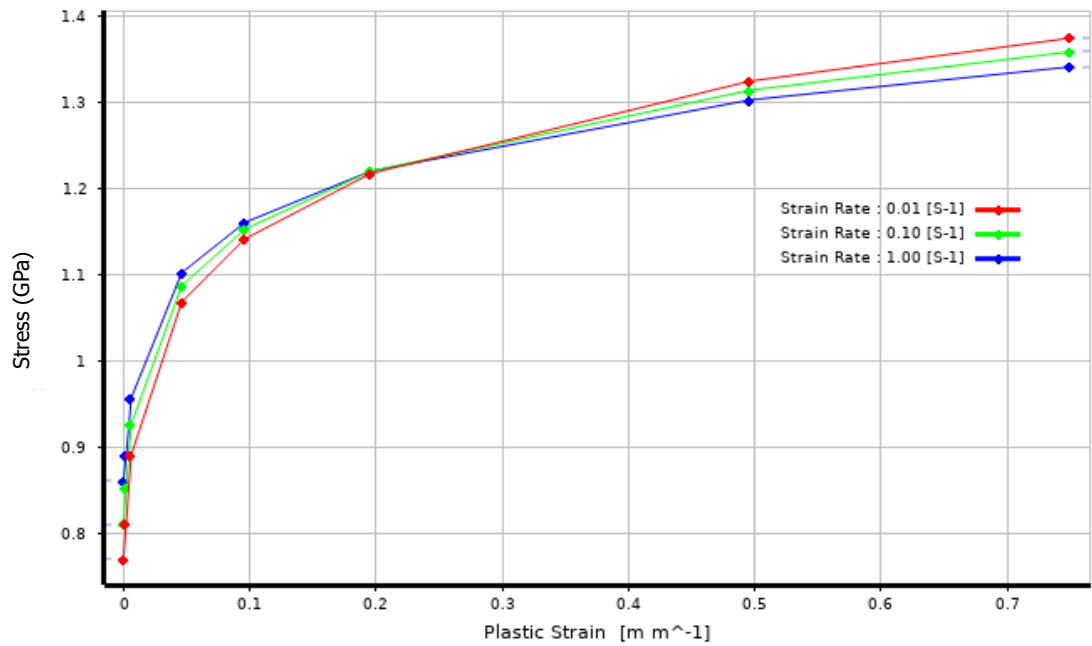
Figure 66: Stress-Strain profile for AMS5643-H1150 for strain rates varying from 0.01 to 1 s^{-1}.

```
Commands
 1  TB,PLAS,1,,,MISO       ! multilinear isotropic hardening (MISO) curves for different rates
 2
 3  TBFIELD,PLSR,0.01    ! MISO curve for a plastic strain rate (PLSR) of 0.01s-1
 4  TBPT,DEFI,0,0.005,0.01,0.05,0.1,0.2,0.5,0.75  ! Plastic Strain (0 = onset of yielding)
 5  TBDATA,,770,815,893,1067,1141,1217,1324,1374    ! Stress in MPa
 6
 7  TBFIELD,PLSR,0.1    ! MISO curve for PLSR of 0.1s-1
 8  TBPT,DEFI,0,0.005,0.01,0.05,0.1,0.2,0.5,0.75  ! Plastic Strain
 9  TBDATA,,812,852,925,1086,1152,1219,1313,1358    ! Stress in MPa
10
11  TBFIELD,PLSR,1    ! MISO curve for PLSR of 1s-1
12  TBPT,DEFI,0,0.005,0.01,0.05,0.1,0.2,0.5,0.75  ! Plastic Strain
13  TBDATA,,866,889,956,1101,1160,1219,1302,1340    ! Stress in MPa
```

Figure 67: Scripting for the implementation of strain rate dependant material properties using Ansys Parametric Desing Language (APDL). Lines 1 creates a multilinear isotropic model (MISO) to model plastic behaviour (PLAS). For lines 3-5, TBFIELD establishes the plastic strain rate to be defined. TBPT generates a table of plastic strain values with TBDATA containing the associated stress values in MPa. This is repeated for each plastic strain rate in lines 7-9, and 11-13.

5.2.5.2. Modelling Environment

This command requires strain-rates to be extracted from each element at each time-step which is not supported in the ANSYS Static Structural (Implicit) modelling environment. One of the key assumptions when working in this environment is that inertial and damping effects are negligible and thus, the acceleration and velocity terms are removed from the equations of motion (Equation 28). This greatly simplifies the solver, but it cannot provide any rate-dependant results. An explicit solver was briefly considered but as discussed in section 2.4.3, an explicit solver would also be unsuitable for this analysis as the expected test duration of (5-10 seconds) would require a prohibitively large number of time-steps to complete. The ANSYS Transient Structural modelling environment uses with an implicit solver but unlike the Static Structural environment, it uses the complete equations of motion. Therefore, it can produce rate-dependant results on an element-by-element basis which is required for the APDL command to update the stiffness of each element at the start of each time-step. Following best practices for a metal forming analysis (Zhu, 2017), time-step duration was set to "Program Controlled" allowing the solver to dynamically change the time-step duration throughout the simulation. This minimises the total number of time-steps (by increasing the duration of each time-step) without compromising the convergence at each time-step and "Force" chosen as the convergence criteria with a tolerance limit set at 0.5%.

5.2.5.3. Contact Definition

For the contact definition between the ring specimen faces and the upper platen, the contact formulation was set to "Normal Lagrange" to minimise penetration between the two bodies as they come into contact and improving geometric accuracy. The minimal penetration that comes with Normal Lagrange also helps when there is a high degree of sliding at contact surfaces making it best suited for bulk-metal deformation processes especially when compared to "Augmented Lagrange" and "Pure Penalty" formulations (Zhu, 2017; Woodhead, 2015b). The tight penetration tolerance associated with a Normal Lagrange contact can lead to model instability due complications with resolving contact forces. A phenomenon can arise whereby pairs of contact nodes between two bodies can "Jitter" between contact and non-contact states and fail to resolve within a solution sub-step. To improve the model's stability, the contact detection method was set to "Nodal-Projected Normal from Contact" which is optimised for surface-surface contacts (Zhu, 2017) and minimises localised high-pressure spikes as nodes from one body come into contact with a target surface.

5.2.5.4.   Mesh Sensitivity Analysis

It is a critical part of any FE analysis to confirm that the mesh discretisation method does not significantly influencing the results of the analysis. Following the same methodology as both Kahhal et al. (2021) and Woodhead, Truman, and Booker (2015b), the face of the ring coupon was first mapped entirely with quadrilateral elements and a course element size of 0.3mm set globally. This produced a mesh with 334 quadrilateral elements and when simulated to a height reduction of 50% (to match the maximum compression of the practical test in section 5.3.1), resulted in a forming load of 743.1 kN measured at the contact between the upper platen and the ring coupon. The density of the mesh was then increased by incrementally decreasing the global element size down to a minimum of 0.05mm. Figure 68 details response of the forming load as a function of the total element count of the ring coupon. It is clear to see that beyond approximately 3000 elements (0.1mm equivalent mesh size) the forming load plateaus at 741.7 kN. Therefore, a 0.1mm global mesh is independent of the results and that a finer mesh would not change the impact the analysis.
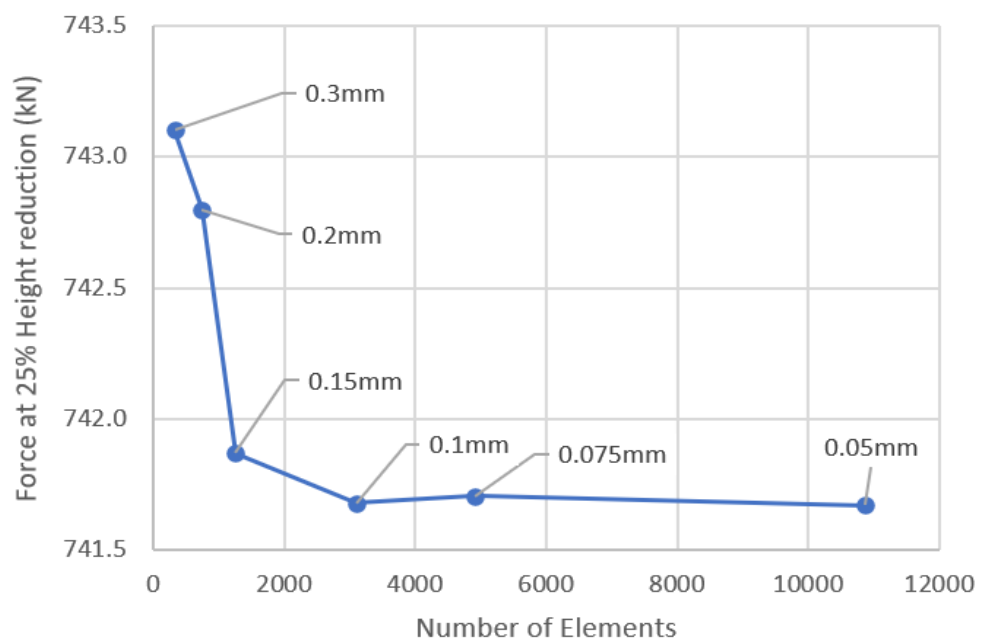
Figure 68: Mesh independence study of the ring compression test FE model. Labels refer to the element size that produced the number of elements for each mesh test.

5.2.5.5.   Friction Model

Friction is typically characterised by two models: either Coulomb's law or the Tresca friction model. For Coulomb's law, the tangential frictional stress is expressed as a function of the normal contract pressure (Equation 14). A constant value for the coefficient of friction is only valid provided the ratio between the normal contact pressure and the yield stress remains below approximately 1.3 - 1.5 (Fereshteh-Saniee *et al.*, 2013; Cora *et al.*, 2008). Beyond this point, it is understood that the surface asperities at the contact interface have deformed so that the real and apparent contact areas are equal. This leads to the frictional stress becoming constant and no longer proportional to the normal contact pressure, resulting in a decreasing coefficient of friction as the contact pressure increases.

Under these conditions, the tangential frictional stress is better modelled by the Tresca friction model (Equation 15). However, it has been shown that neither friction model (with static values for μ or m) can accurately reflect the dynamic friction conditions present in bulk-metal forming (Woodhead, 2015a; Cora *et al.*, 2008) and a dynamic coefficient of friction is required. Because Ansys (2021a) had already been chosen as the computational modelling software for this thesis, the subsequent dynamic friction relationship was derived from Coulombs law as this is how friction is fundamentally modelled by ANSYS.

5.2.5.5.   Friction Model

5.2.6.   Summary of Methodology

The methodology used for ring compression testing is summarised as follows:

- ASTM International E9-09 was followed for ring compression testing with an exception for the guidelines surrounding geometry, lubrication, and strain-rates.

- Material to be tested was AMS5643-H1150 with a molybdenum disulphide solid paste lubricant (contact region 1) and with no lubrication (contact region 2).

- A total of 40 specimens were tested with 20 specimens for each contact region.

- The first load step was set to 15 tonnes and then increased in increments of 5 tonnes up to 65 tonnes.

- Test specimens were made with an OD:ID:H ratio of 6:3:2 and measured ∅19.05mm x ∅9.53mm x ∅6.35mm.

- Coulomb's law to be used as the base friction law for all computational modelling.

Equipment used:

- 75-tonne four-column hydraulic press.

- Tungsten Carbide compression platens (Grade YG15).

5.3.   Ring Compression Test Analysis

The analysis for the ring compression test is split into two sections. The first section determines the friction-pressure relationship via the conventional interpolation method while the second section uses a new iterative interpolation method. These two methods are referred to as Direct FCC interpolation and Iterative FCC Interpolation.

5.3.1.   Direct FCC Interpolation

The Direct FCC interpolation method for determining the coefficient of friction from ring compression tests is as follows. The ring compression test is simulated in a computational model across a range of friction coefficients (for this study the required range required was 0.05 - 0.16). This model runs over a single load-step with the force on the upper platen applied at 10 Tonnes per second. The maximum force is controlled by increasing the time of the load-step until the model reaches the desired maximum load. Figure 69 shows the displacement contours from simulations for the friction coefficients 0.05 and 0.15 as the ring is compressed by approximately 1mm, 2mm and 3mm. It can be seen that as the friction coefficient increases, outward material flow is resisted which causes an inward flow of material. This is most clear at higher compressions as the inside diameter of the ring transitions from concave to convex.

From these simulations, the results history for the percentage reduction in inner diameter is plotted against the percentage reduction in height to create a series of FCCs. Finally, the experiment ring compression data is compared to the simulated results and the coefficient of friction is determined by interpolating between the constant friction curves. The experimental data for region one is shown in Figure 70 along with the constant friction FCCs ranging from 0.05 to 0.1. By interpolating between the FCCs and calculating the average forming pressure at each load step, the pressure-friction relationship can be determined and is plotted in Figure 71.
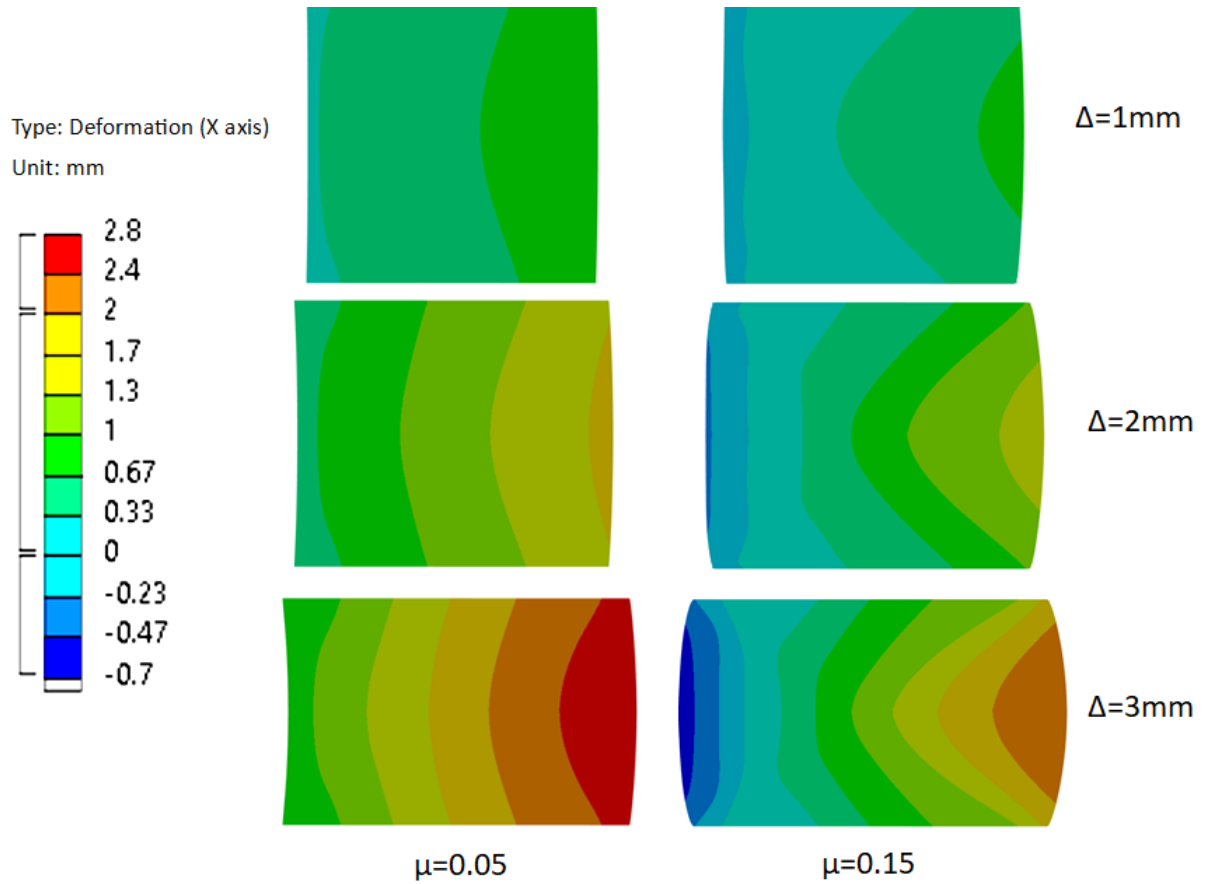
Figure 69: Radial displacement field for constant friction coefficient of 0.05 and 0.15 with a change in height of 1, 2, and 3mm. Positive displacement represents an outward flow of material and negative an inward flow of material.
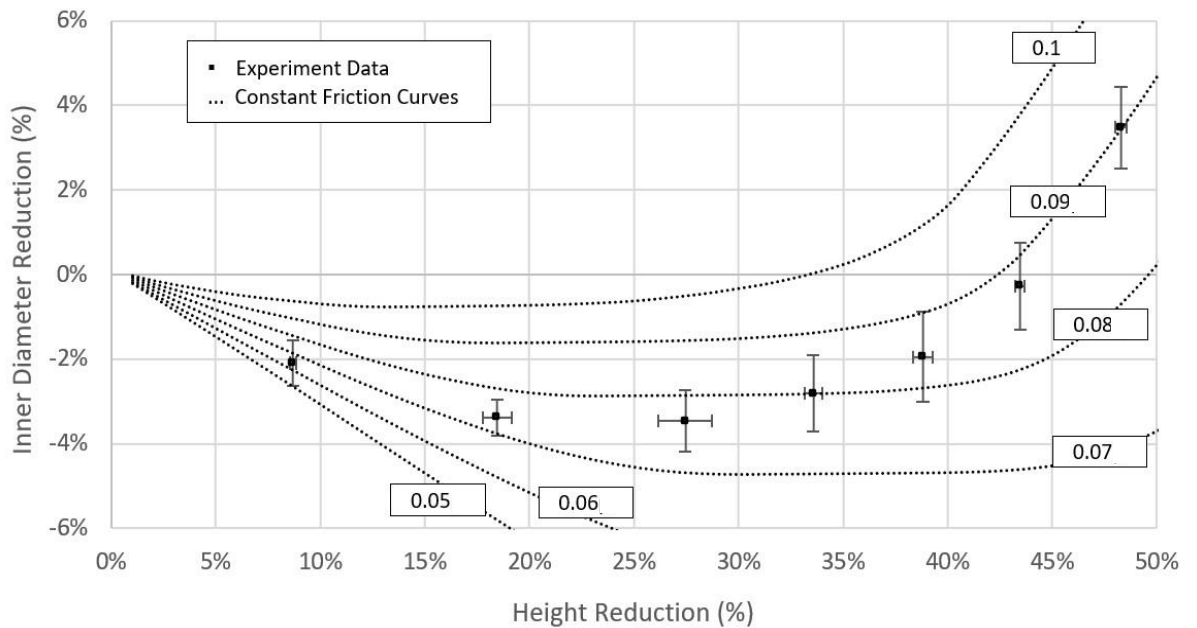
Figure 70: Ring compression test data for AMS5643-H1150 with a Molykote G-N Plus paste (contact region 1) and FCC's ranging from 0.05μ- 0.1μ. Experiment error bars represent a 95% confidence interval for experimental results.
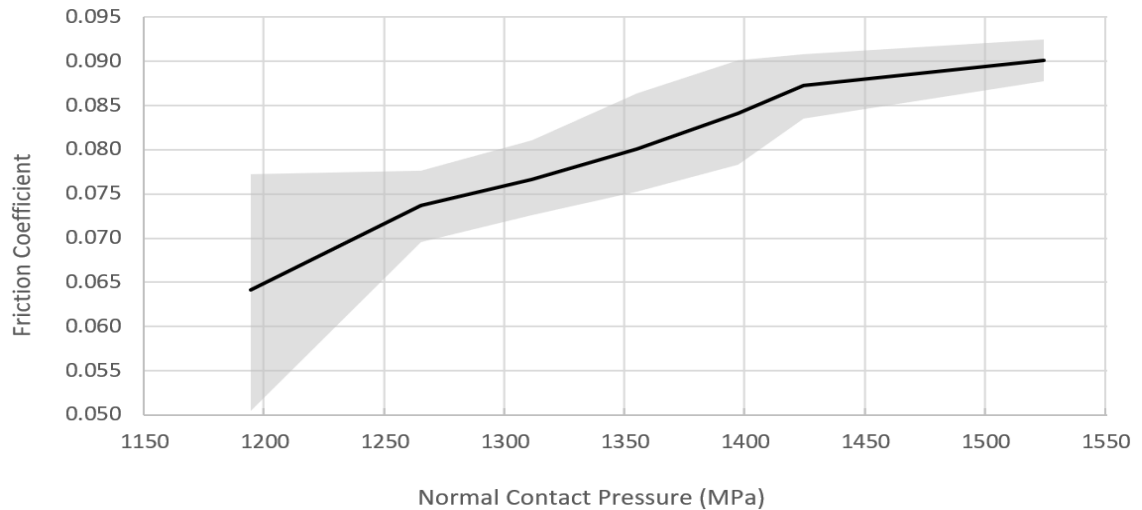
Figure 71: Variation in the coefficient of friction against contact pressure for AMS5643-H1150 with a Molykote G-N Plus paste (contact region 1). Shaded region represents 95% confidence interval for measured coefficient of friction.

By programming the friction-pressure relationship from Figure 71 into the ANSYS simulation environment, it is possible to check the accuracy of this analysis by comparing the computational model to the experimental data from Figure 70. To do this, a custom command was programmed using Ansys's Parametric Design Language (APDL) to replace a static coefficient of friction with a pressure dependent lookup table (Figure 72).

```
Commands
  1  MPDE,MU,CID
  2  TB,FRIC,CID,,,ISO
  3
  4  TBField,NPRES,0
  5  TBDATA,1,0.064
  6
  7  TBField,NPRES,1194
  8  TBDATA,1,0.064
  9
 10  TBField,NPRES,1265
 11  TBDATA,1,0.074
 12
 13  TBField,NPRES,1312
 14  TBDATA,1,0.077
 15
 16  TBField,NPRES,1355
 17  TBDATA,1,0.081
 18
 19  TBField,NPRES,1398
 20  TBDATA,1,0.085
 21
 22  TBField,NPRES,1425
 23  TBDATA,1,0.087
 24
 25  TBField,NPRES,1524
 26  TBDATA,1,0.09
```

Figure 72: Scripting for the implementation of a variable friction coefficient using Ansys Parametric Desing Language (APDL). Lines 1-2 are initialisers that instruct Ansys that the friction coefficient (FRIC) on the contact elements (CID) are to behave isotopically (ISO) and be defined by the variable TB. Normal contact pressure of each element (NPRES) is given in MPa.

This custom friction model is able to produce a good prediction for the ring compression experiment data up to approximately a 30% height reduction, after which the computational model begins to underpredict the reduction in inner diameter (Figure 73).
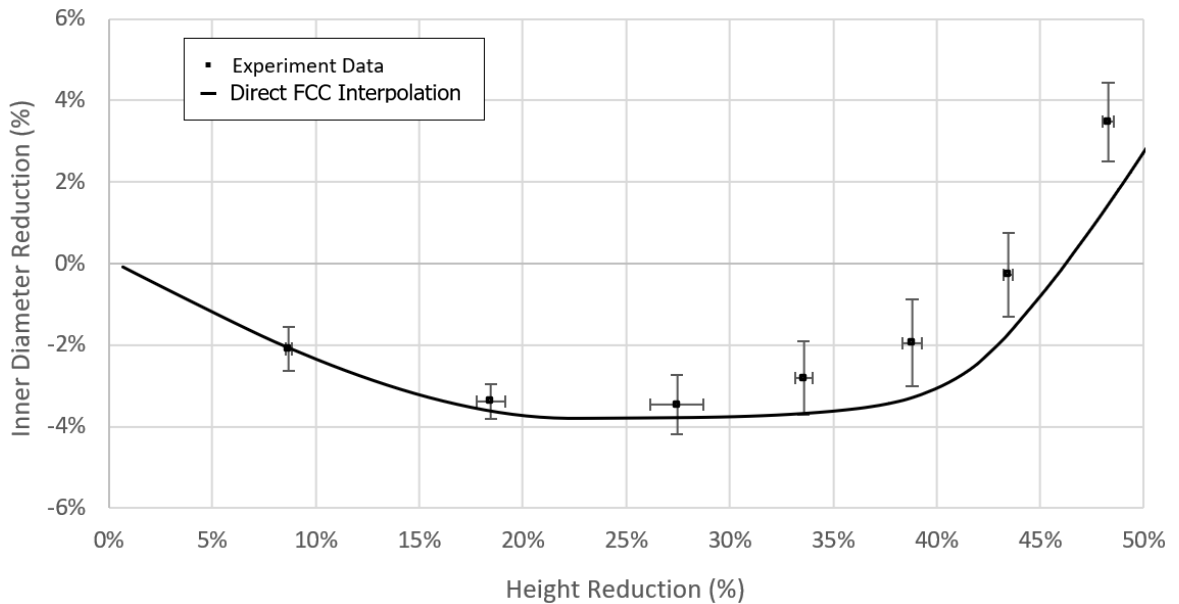
Figure 73: Comparison of the ring compression test data and the prediction using the Direct FCC interpolation method.

The cause for this error in the FCC interpolation method is inherent to how the friction coefficient is determined and is demonstrated in Figure 74. At a height reduction of 33.5%, the friction coefficient is evaluated to be 0.08 but the gradient of the experiment data is significantly steeper than the 0.08 constant friction curve. It is clear that the friction coefficient should be greater than 0.08 to maintain the gradient of the experiment data and reach the next data point at 38.8%. However, the other constant friction curves provide no information as to how much greater the friction coefficient should be because each of these curves were defined from the origin and not from the 33.5% data point.
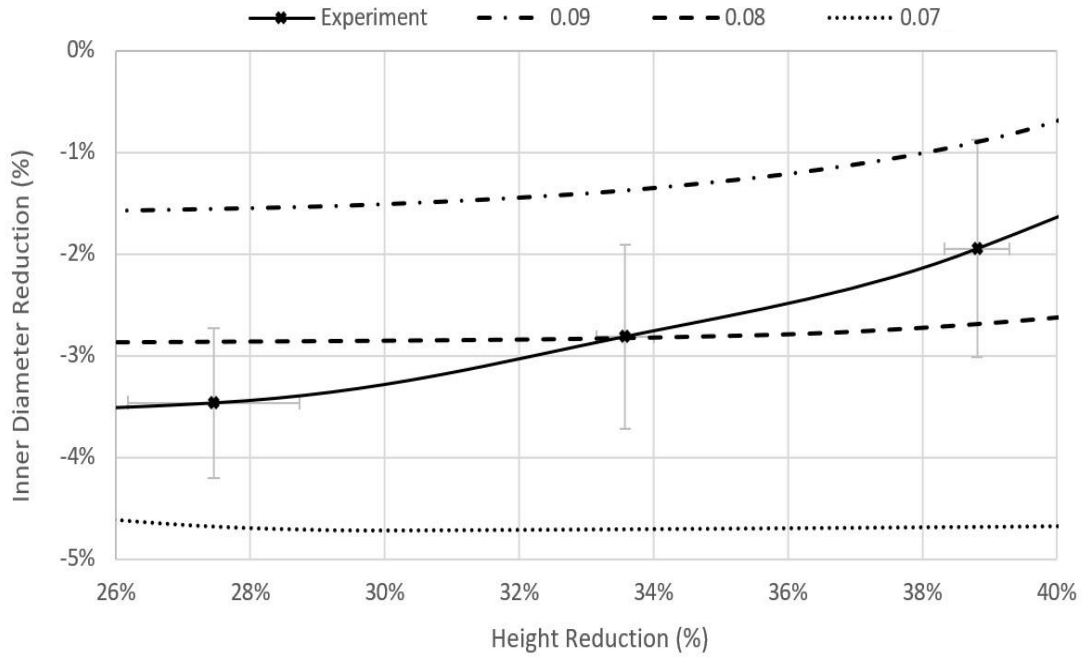
Figure 74: Detailed view from the FCCs from Figure 70.

By contrast, the experimental results from region two (dry – no lubrication) do not fluctuate significantly and remained constant at 0.15 within experimental error (Figure 75).

Figure 75: Ring compression test data for AMS5643-H1150 Dry (contact region 2) and FCC's ranging from 0.13- 0.16. Experiment error bars represent a 95% confidence interval for experimental results.

5.3.2. Iterative FCC Interpolation

To improve the modelling accuracy for region one, an iterative approach to interpolating the FCCs is proposed (Figure 75). Firstly, constant friction curves are created from the initial geometry up to the change in height recorded at the end of the first load step. The friction coefficient for that load step is then interpolated between the FCCs. New constant friction curves are then generated starting from the geometry at the end of the first load to the end of the second load step with the friction coefficient again interpolated for this second load step. This is repeated across all load steps and results in a friction-pressure relationship that ensures the computational model reproduces the original experimental data.

Figure 76: Schematic for the Iterative FCC interpolation methodology.

Figure 77 shows the results of this method when applied to the ring compression data for region one. Because the friction coefficient is modelled as a constant throughout each load step the friction-pressure relationship results in a square profile with large step changes in the friction-pressure relationship (Figure 77). When the friction coefficient was allowed to vary dynamically during a simulation this led to convergence failures caused by large swings in friction stresses at the contact elements. These presented themselves as large oscillations in the residual force calculations during simulation sub-steps which if severe enough caused the solver to time-out and fail to converge. These frequency of convergence failures could be reduced but not entirely eliminated by increasing the number of simulation sub-steps at the cost of significantly longer solve time.

To smooth the square friction profile, a liner approximation of the friction pressure relationship was made by taking the friction coefficient value at the average contact pressure between load steps. This method eliminated any convergence issues without the need to increase the model's number of simulation sub-steps whilst still providing a good approximate for the frictional behaviour of the ring compression test coupons.
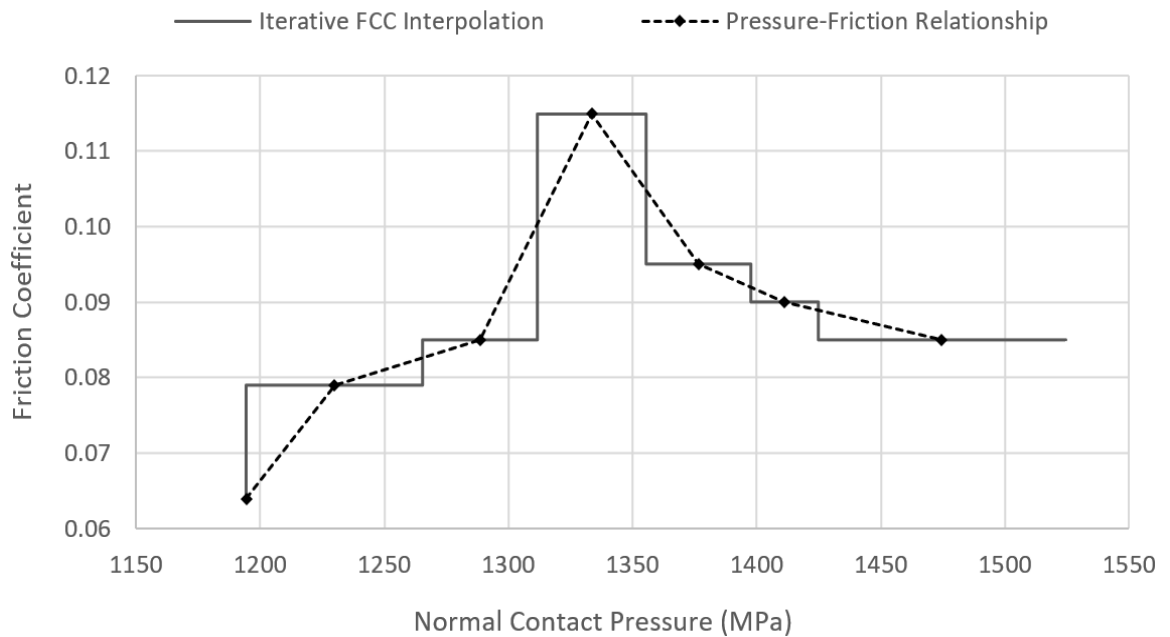
Figure 77: Pressure-friction relationship derived via iterative FCC interpolation.

When compared to direct FCC interpolation, the iterative FCC interpolation method produces a better prediction for the original ring compression data for contact region one and remains within the 95% confidence interval across its entire test range (Figure 78). A comparison of the two friction-pressure relationships and modelling error is shown in Figure 79 and Figure 80.
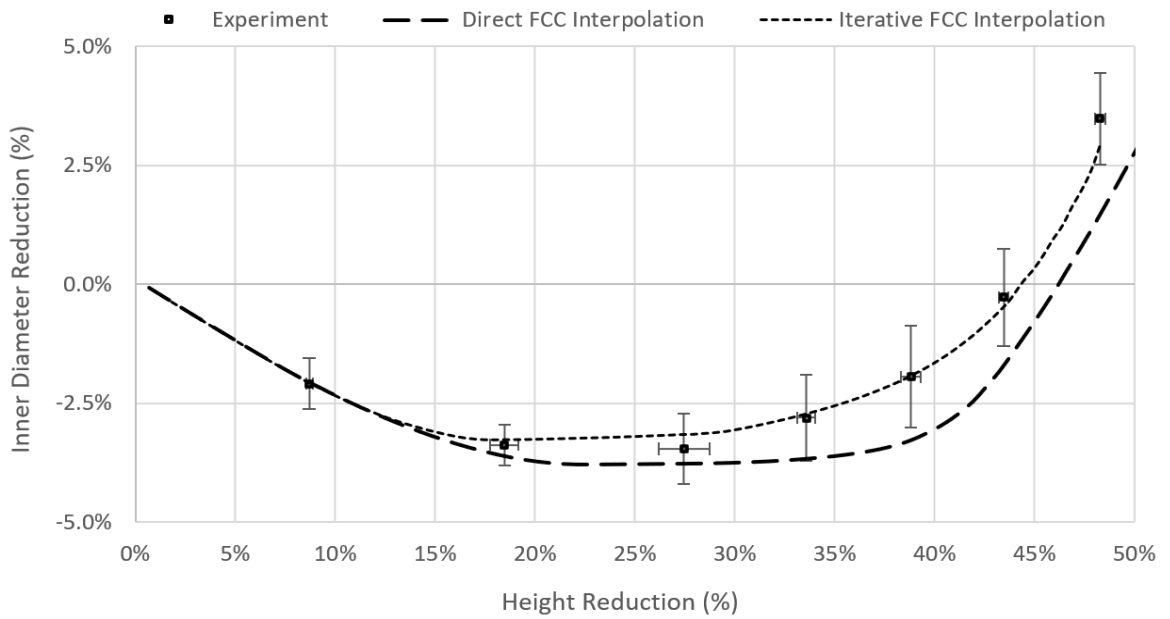
Figure 78: Comparison of the interpolation and Iterative friction models to the ring compressions experiment data.
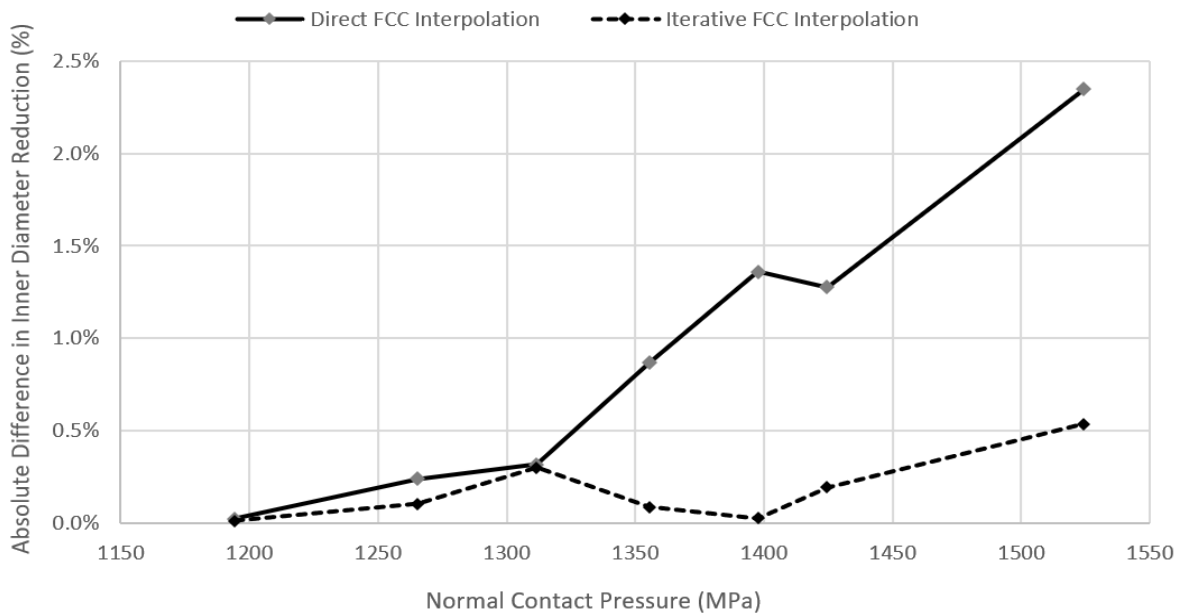
Figure 79: FCC interpolation error relative to experimental data.
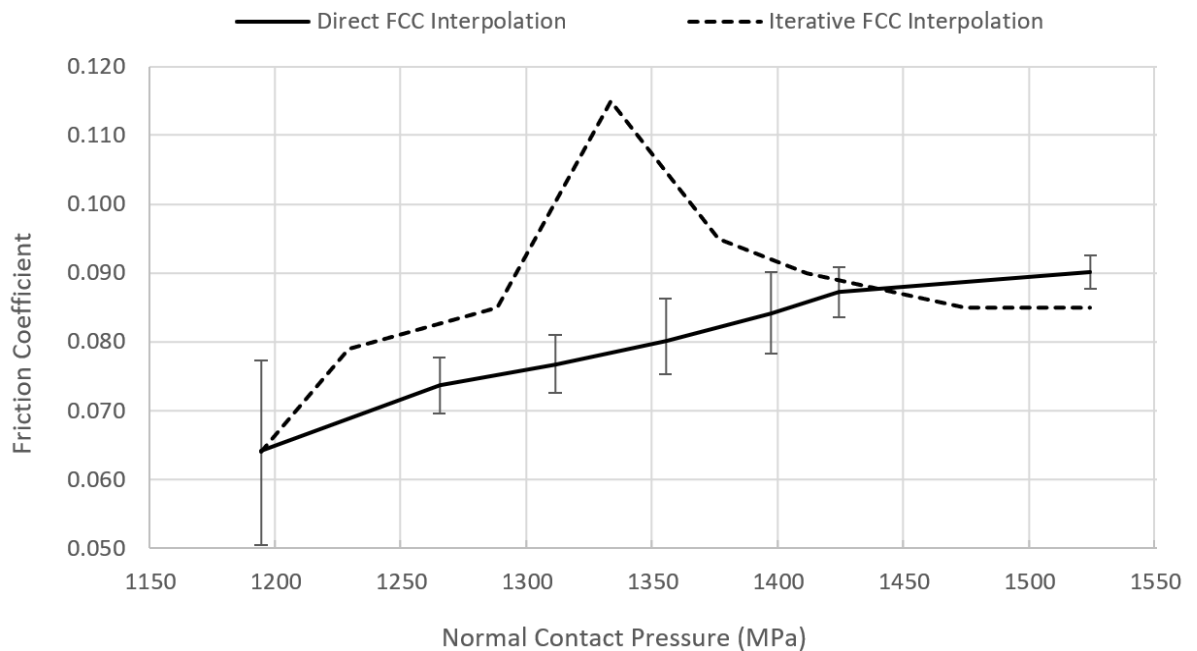
Figure 80: Friction-pressure relationship comparison for contact region 1 using both direct and iterative FCC interpolation methods.

When viewed in a broader context, the significant improvements of the Iterative-FCC method do not completely diminish the usefulness of the standard Interpolation method if the coefficient of friction remains constant across the entire contact pressure range. Under these specific conditions the interpolation method can still produce accurate results without the need for further computational modelling.

However, small changes in the evolution of the coefficient of friction can have a significant impact on the forming loads experienced during a forging process. To demonstrate this, a finite element simulation of the staking process for a spherical plain bearing is used to compare the pressure-friction relationships derived from both analysis methods (the details of this model are presented in Chapter 6) As shown in Figure 81, the Iterative-FCC model was able to better predict the forming load across all ranges of anvil compression. At a peak anvil compression of 0.46mm, the error in the forming load of the Interpolation method is ~30% compared to only ~5% for the Iterative-FCC method.
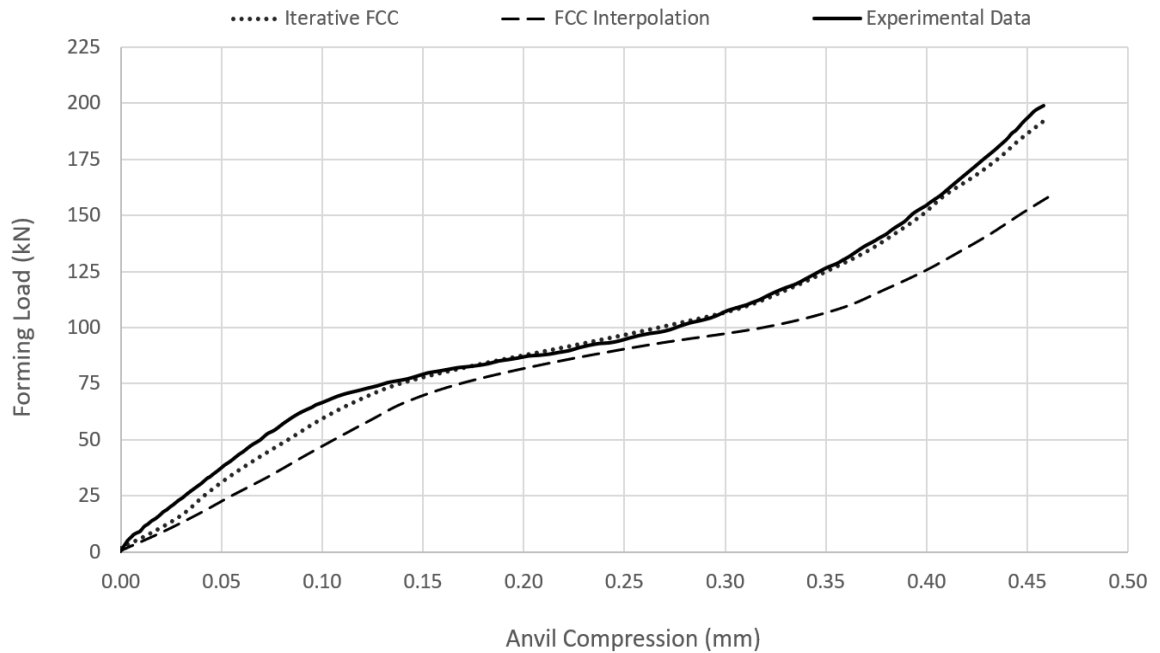
Figure 81: Performance of the two ring compression analysis methods compared to the forming loads experienced during the staking of a production spherical-plain bearing.

5.4. Summary

This chapter characterises the friction-pressure relationship for AMS5643-H1150 under the two contact conditions experienced during staking. The first condition is lubricated with a molybdenum disulphide solid paste and the second condition is dry with no additional lubrication.

For the first contact condition, ring compression tests are analysed with the conventional direct FCC interpolation method. This results in a friction-pressure relationship that cannot reproduce the experimental results beyond a compression greater than 30%. A new method for analysing ring compression tests is proposed that interpolates the coefficient of friction iteratively across each load step. This iterative method is able to produce a friction pressure relationship that when programmed into the computation model reproduces the ring compression test results with a significantly reduced error at contact pressures exceeding 1.35GPa.

For the second contact condition, the conventional direct FCC interpolation method finds the coefficient of friction to be largely invariant with pressure. Within the uncertainty of the experimental data, the friction coefficient remains constant at a value of 0.15.

Therefore, these results have shown that if the coefficient of friction varies significantly with contact pressure (as shown with contact region 1), then direct FCC interpolation is not a suitable method by which to evaluate the friction-pressure relationship. Under these conditions, the proposed iterative FCC interpolation method is better suited to capturing the evolution of the friction coefficient during plastic deformation.

The final friction-pressure relationships for contact regions one and two are shown in Figure 82 which can be used with confidence in the subsequent development of the staking computation models.
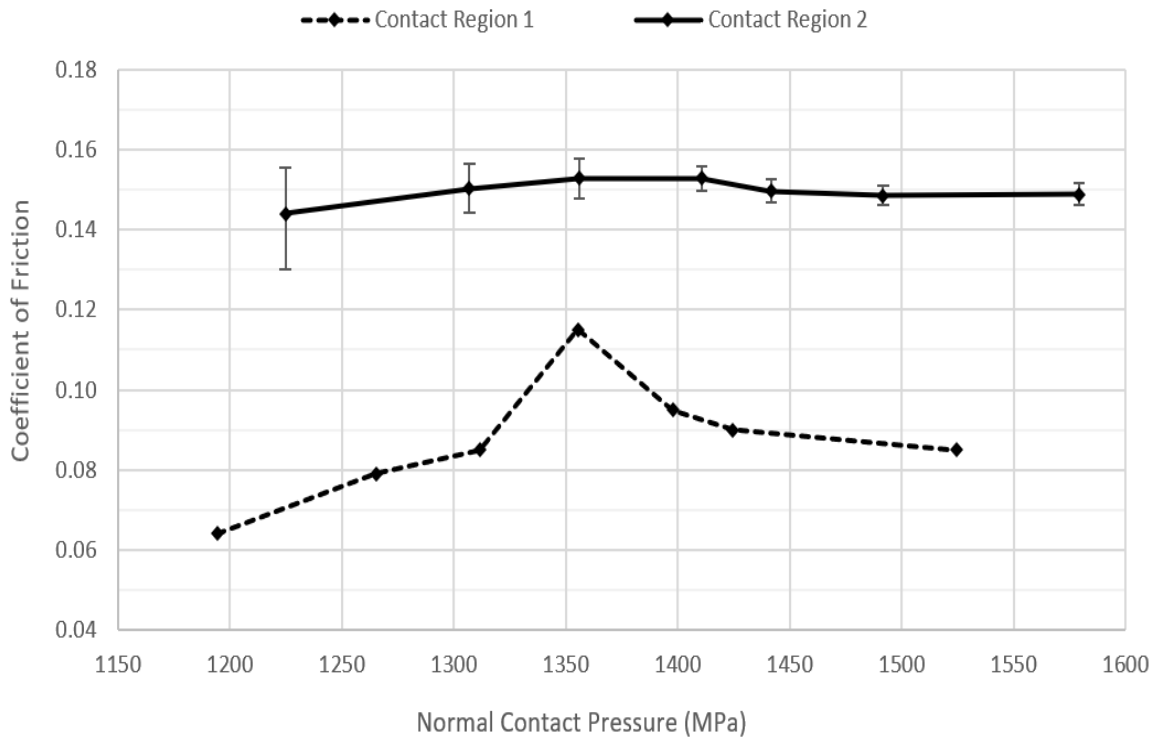
Figure 82: Friction pressure relationship for AMS5643-H1150 under dry and lubricated conditions.

Chapter

6

Virtual Design of Experiments

FEA has become a standard analysis tool for metal joining processes and when combined with Design of Experiments (DOE) methodologies, academic research has shown the potential for virtual DoE to allow for the rapid analysis of manufacturing parameters and their influence on final formed products. However, within the domain of bulk-metal joining, FEA tools are rarely used in industrial applications and relegate the use of DoE to physical trials which are severely constrained by financial costs and time. Presented in this chapter is the process and methodology for developing a Virtual-DoE for the modelling of staked spherical bearings.

6.1. Background

The first uses of statistical inference, randomisation, and regression modelling to influence the practice of experimental research date back to the late 19th and early 20th century (Peirce and Jastrow, 1885; Peirce, 1887; Smith, 1916). This was brought together by Fisher (1926) and codified into the DoE methodology as a response to the two most common statistic-based criticisms aimed at the conclusions drawn from experimental evidence. The first claim is that the interpretation of the experiment is incorrect and that the wrong conclusions have been drawn (correlation does not imply causation). The second claim is that the measured outputs of the test may have arisen even if the conclusions drawn had been false, such as when patterns in data are perceived as a result of natural variation and not by experimental design (Fisher, 1935). Both claims are derived from the same position, that conclusions drawn from experimental evidence are only valid if they are statistically significant.

A DoE is a series of tests where the input variables are purposefully changed between their respective upper and lower bounds in a systematic order. In the case of a full factorial DoE, each possible combination of variable upper and lower bound will be tested. The measured response is then analysed via a regression analysis to determine which of the input variables have a statistically significant relationship with the response (Taguchi, Chowdhury, and Wu, 2007). One of the major limiting factors that can negatively impact the implementation of a DoE is that as the number of input variables increases, the number of tests increases exponentially. To reduce this financial and costly burden of studying manufacturing processes, the physical testing requirements can be replaced by FEA models to create a Virtual-DoE (Kim, 2010; Al-Momani and Rawabdeh, 2008).

6.2. Virtual Design of Experiment Setup

The basic process for developing a virtual-DoE is the same as a DoE except for additional FEA-specific processes. Figure 83 summarises the basic DoE process. The first phase of the Virtual-DoE for this investigation is split into three sections; bearing geometry characterisation, input variable and output response identification, and the design of a computational model suitable to model the staking process.

Identify Factors	Screening Tests	Conduct Experiments	Analyse Data	Verification
•Determine the desired response outputs of the DoE	•Reduce the number of variables to the most influential	•Perform the designed experiments to collect data on the required response outputs	•Carry out a regression analysis of all experiments to evaluate the weighting of each variable and combination of variables	•Verify the accuracy of the regression analysis against the orginal dataset
•Identify the potential parameters that could influence the response output	•Determine any non-linear variables			

Figure 83: Overview of the design of experiments methodology

6.2.1. Geometry Characterisation

A fundamental requirement for a DoE is to understand the range of possible values that an input variable can have and to determine its respective upper and lower limits. Except for the anvil staking force and pre-stake torque, any potential input variable will be a geometric feature with an overview shown in Figure 84. A study of 176 live bearings (either in current or recent production) was undertaken and two key findings were made: (1) bearing groove geometry can be split into three distinct classes, and (2) the geometric features of a bearing scale with the overall size of that bearing.

The geometry of the groove machined into the outer race is controlled by two dimensions, Groove Pitch and Groove Depth. Groove Pitch is defined as the radial distance from the centre of the outer race groove to the outer race diameter. Individually, both Groove Pitch and Groove Depth cluster tightly around three values that do not vary significantly. When both dimensions are plotted against each other, a clear clustering appears that allows for all bearings to be grouped into one of three groove geometry classes: Type 1, 2 and 3 (Figure 85). These classes broadly represent small, medium, and large bearings.
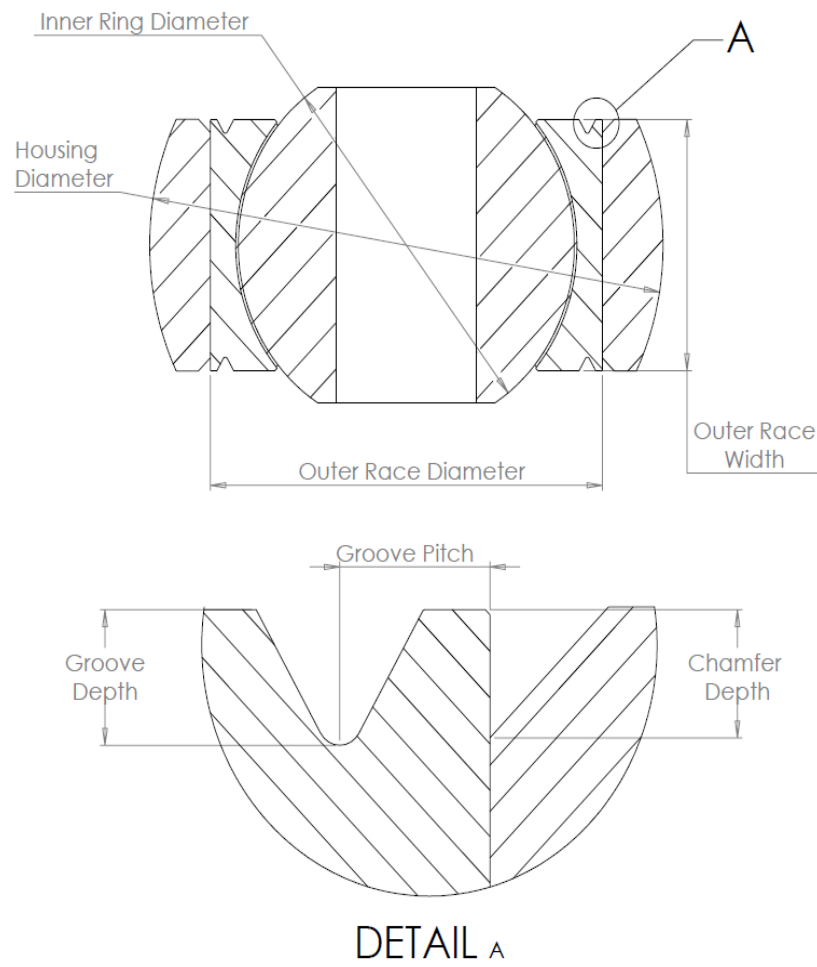
Figure 84: Schematic of key bearing and housing geometries.

Figure Redacted

Figure 85: Bearing type classification with respects to the variation of groove pitch and groove depth.

Within each of these classes, there is still a wide range of geometric values across all bearing dimensions, however, the size of these dimensions scale in sympathy with each other. For example, a key consideration in bearing design is the contact pressure between the liner and the inner ring. To reduce the contact pressure on the liner, the liner surface area is increased by enlarging the inner ring diameter. Then to avoid compromising on the outer race's ability to contain the inner ring, the outer race width is also increased (Figure 86).

Figure Redacted
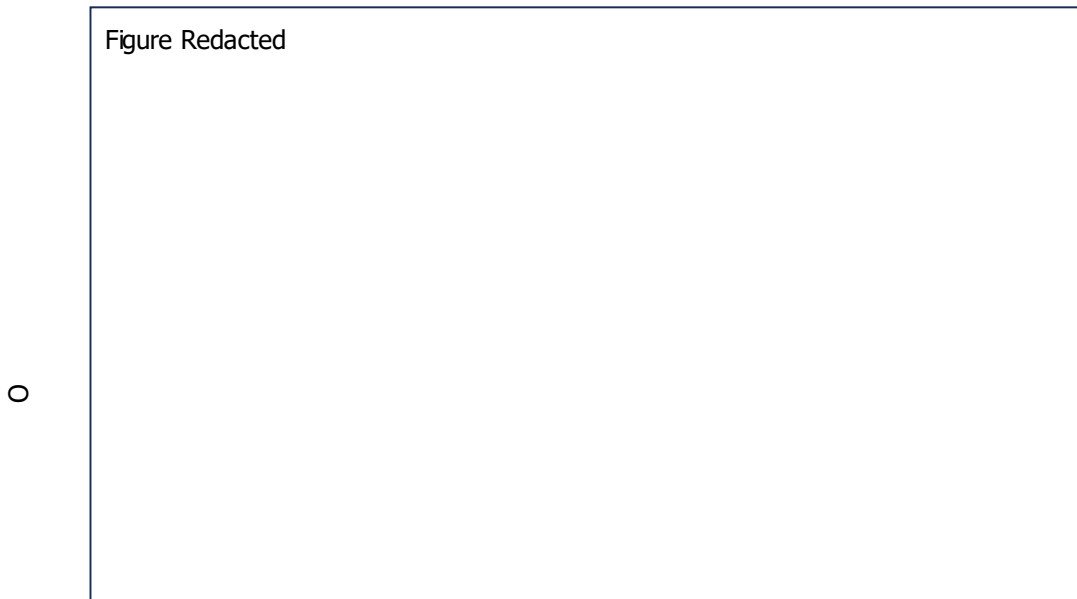
Figure 86: Relationship between Outer race width and Inner ring diameter.

It was found that nearly all the geometric features were proportional to the outer race diameter and followed simple linear relationships. Using these geometric relationships allows for the modelling of a standard bearing for any given outer race diameter. Table 12 lists the geometric relationships required to construct a Type 3 bearing with Type 1 and 2 geometric relations shown in Appendix C. These relationships were later used to define the bearing geometries within the computational model.

Whilst this investigation encompasses all three bearing geometry classes, presented in the main body of this thesis is only the development and analysis of the Type 3 bearing model. This is due to the similarity of construction of all three models. Performance summaries of Type 1 and Type 2 bearings are shown where relevant with any key differences to the Type 3 model discussed where applicable.

Table 12: Geometric characterisation of Type 3 bearings, their dimensional variation, and maximum and minimum absolute values.

[REDACTED]

6.2.2. Parameter Identification

Before the computational model could be constructed, the DoE output responses needed to be defined and the input variables that could influence them identified. This process forms the 'feature list' for the computation model to accommodate. The output responses were defined in the project objectives (Section 1.3) and are the key performance metrics for staking spherical bearings: pushout strength and post-stake torque. The main factor that governs pushout strength is the geometry of the formed staking lip and its interaction with the housing. The geometry of the staking lip is influenced by both geometric features of the bearing (such as the outer race diameter, groove depth, groove pitch, and housing chamfer) and machine operator controls (anvil staking force).

The potential geometric factors that could influence the post-stake torque by contrast are far more numerous. The primary mechanism that drives post-stake torque is the inward metal flow of the outer race into the inner ring. As the outer race staking lip begins to deform and contacts the housing's chamfer, it forces the housing to expand under the pressure of the staking anvils. Once the anvils are released, the housing undergoes elastic relaxation and radially compress the outer race and liner against the inner ring which generates torque. This results in all the potential input variables for the pushout strength also being included for post-stake torque as well as any variables that directly impact the liner contact area (such as the inner ring diameter and outer race width).

Whilst many additional geometric features could also impact the pushout strength and post-stake torque, the project objectives limit the scope of this investigation to just the design variables established in SKF design rules (SKF, 2003) and international spherical bearing standards (SAE International, 2018). Therefore, geometries such as the angle of the staking anvils were not included as an input variable. The complete list of all input variables is listed in Table 13.

Table 13: Full list of input variables.

Pushout Strength		Post-Stake Torque	
• Staking Force		• Staking Force	• Housing Diameter
• Outer Race Diameter	• Housing Diameter	• Outer Race Diameter	• Interference Fit
• Groove Depth	• Interference Fit	• Groove Depth	• Inner Ring Diameter
• Groove Pitch		• Groove Pitch	• Pre-Stake Torque
• Chamfer Depth		• Chamfer Depth	• Outer Race Width

6.2.3. Computational Model

The computational model created to simulate the staking of the bearings was made using the simulation software package ANSYS Workbench (ANSYS, 2021a). The Model is split into two phases. The first is the staking phase where the two staking anvils (upper and lower) form the staking lip into the housing. In the second pushout phase, the pushout plate presses down on the outer race to pushout the bearing. The housing is supported and held in place by the housing support (Figure 87). The preparation of this model is detailed across Eight steps: modelling assumptions, material definition, modelling environment, contact definition, displacement control, and torque definition, model setup and workflow, and mesh independence.
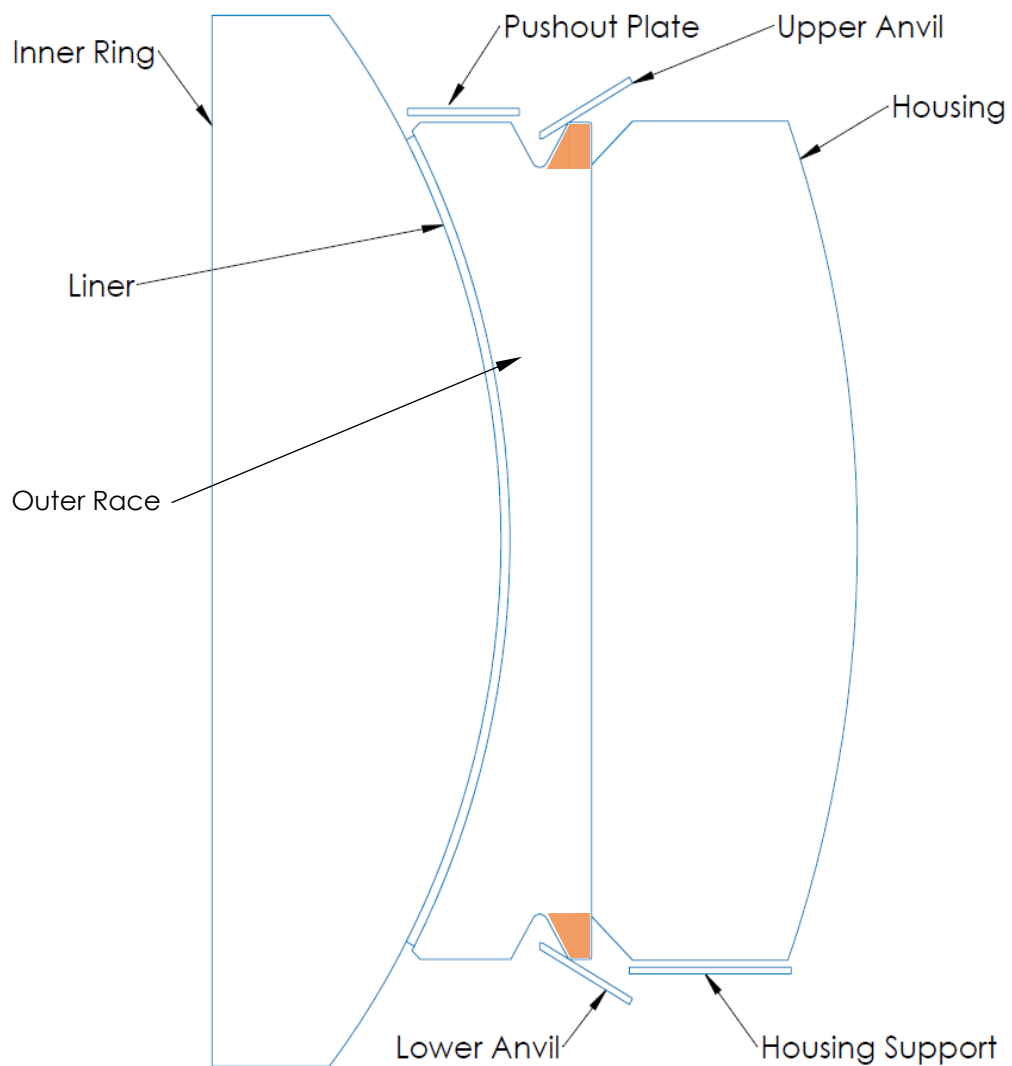
Figure 87: Computational model overview. Cross-sectional view of all modeled bodies. The staking lip regions are highlighted in orange.

6.2.3.1. Modelling Assumptions

With any computational model, it is often not possible nor reasonable to model every detail of a system and therefore, simplifications must be made to make it computationally feasible. The following is a list of assumptions and simplifications made for this computational model.

- Perfect conformity between the inner ring and liner

- The liner is to be modelled as isotropic

- The deformation of the staking lips results in a negligible amount of thermal energy and can be assumed to be adiabatic

- The integrated shanks seen on housings such as rod ends, and tie rods can be ignored; allowing for 2D-axisymmetric modelling to be used

- The staking anvils are modelled as a rigid body

- Any special coatings on the inner ring are ignored.

6.2.3.2. Material Definition

A critical part of any model is the accurate characterisation of the material's mechanical properties. The materials used for aerospace plain spherical bearings and for both the staking and pushout tooling are as follows:

- Inner ring, 440C

- Outer race, AMS5643 H1150

- Housing, AMS5643 H1025

- Staking Anvils and Pushout tooling – Tungsten Carbide

- Self-Lubricating Liner, X1-40 woven PTFE-glass fibre composite.

No plastic deformation was expected of the inner ring, so its mechanical properties were simplified and assumed to be perfectly elastic with a Young's modulus of 200GPa and Poisson's ratio of 0.3 (Atlas Steels, 2008). By contrast, the outer race and housing experiences plastic deformation during staking and pushout. The plastic behaviour for AMS5643 H1150 and H1025 are implemented using the same APDL script as detailed in Section 5.2.5.1 and Figure 67.

The staking anvils and pushout tooling are made from tungsten carbide with a Young's modulus of approximately 670 GPa. It is common practice however for dies used in cold metal working processes to be modelled as rigid bodies because of the significant difference in stiffness when compared to steel (Woodhead *et al.,* 2015b; Kalpajian and Schmid, 2008). This also has the additional benefit of increasing the computational efficiency of the model. Therefore, the staking anvils and pushout tooling are modelled as rigid bodies.

Lastly, the elastic moduli of the liner (X1-40) have already been studied by SKF (2008) and was found to be non-linear with respect to contact pressure. This was implemented into ANSYS using a similar APDL script as previously used to define a variable friction coefficient (Section 5.3.1) and detailed in Figure 88.

```
Commands
 1  MPDE,MU,CID
 2  TB,EX,CID,,,ISO
 3
 4  TBField,NPRES,0
 5  TBDATA,1,1328
 6
 7  TBField,NPRES,1
 8  TBDATA,1,1328
 9
10  TBField,NPRES,10
11  TBDATA,1,1425
12
13  TBField,NPRES,100
14  TBDATA,1,2259
15
16  TBField,NPRES,500
17  TBDATA,1,5064
18
19  TBField,NPRES,1000
20  TBDATA,1,6501
```

Figure 88: Scripting for the implementation of a variable Elastic Modulus. Lines 1-2 are initialisers that instruct Ansys that the Elastic Modulus (EX) on the contact elements (CID) are to behave isotopically (ISO) and be defined by the variable TB. The lookup table that defines TB for each element is based on the normal contact pressure of each element (NPRES) with units in MPa.

6.2.3.3. Modelling Environment

Bearing Staking the ring compression tests (Chapter 5) share many of the same modelling characteristics as both are low strain-rate, open-die cold metal forming processes and therefore it is suitable to follow the same modelling approach: a Transient Structural modelling environment with an implicit solver. An Explicit Dynamic solver was considered but for the same challenges would prove to be impractical for this application. After the mesh independence studies were concluded, the smallest elements of the model were found to have a characteristic length of approximately 0.02mm (Section 6.2.3.8). Following the Courant–Friedrichs–Lewy condition (Equation 31) the maximum allowed time-step was calculated to be 4×10^{-9} seconds. Whilst control mechanisms such as mass scaling (Dyna Support, 2023) can help increase the maximum time-step and reduce the total computation time, early tests indicated a computational time of at least an order of magnitude greater than an equivalent model in a transient structural environment.

6.2.3.4. Contact Definition

The seven contact regions within the computational model of the staking process are split into four groups: liner, steel dry, steel lubricated, and bonded, with a summary of all contact conditions listed in Table 14. The friction-pressure relationship for the liner was provided by SKF (Karras, 2018) and two steel conditions were evaluated from Chapter 5.

Table 14: Summary of contact definitions for the Virtual Design of Experiments.

Contact	Target	Condition	Coefficient of Friction Value	
			Contact Pressure (MPa)	Friction Coefficient
Inner ring	Self-lubricating liner	Dry, Variable friction coefficient	1	0.142
			5	0.104
			10	0.085
			60	0.043
			120	0.048
Outer Race	Upper and Lower Staking Anvils	Lubricated (Molykote G-N Plus Paste), Variable friction coefficient	Contact Pressure (MPa)	Friction Coefficient
			1194	0.064
			1265	0.079
			1315	0.085
			1355	0.115
			1398	0.095
			1425	0.090
			1524	0.085
Outer Race	Pushout Plate, Housing, and Housing Support	Dry, Non-variable friction coefficient	0.15	
Self-lubricating liner	Outer Race	Bonded	N/a	

Building off of the friction modelling for the ring compression test in Chapter 5, it was deemed appropriate to model all contact definitions using the same methodology, justification, and implementation as detailed in Section 5.2.5. and 5.3.1. In summary, friction contacts were defined following Coulombs law with APDL command scripts added to allow for a variable friction coefficient (Figure 72). All sliding contacts were defined with a Normal Lagrange formulation with contact detection set as Nodal-Projected Normal from Contact.

6.2.3.5. Displacement Control

Due to the nature of a transient structural solver, each time step must be solved following a static equilibrium condition. This requirement poses several challenges concerning model stability and the control of the staking anvils. The staking model was split into four stages.

1. Initialisation - No external forces are applied to the bearing. Both the bearing torque and the outer race/housing geometric interference are allowed to stabilise so that a pre-stake torque measurement can be taken.

2. Staking - The two staking anvils contact the outer race and compress the staking lip regions into the chamfer housing. At the end of the load step, the maximum staking force is recorded.

3. Relaxation - The staking anvils are removed from the outer race to measure the post-stake torque.

4. Pushout - The pushout plate and housing support (whose boundary conditions were previously set to inactive) are brought into the model to pushout the outer race from the housing.

The original intention was for the staking anvils to be controlled by following a force profile across all stages. However, using this method resulted in severe model instability during the third stage when the force applied to the staking anvils approaches zero. The solution to this problem was to control the staking anvils via displacement commands in the computational model. Within the staking calculator tool, the anvil displacement could then be converted back into an equivalent staking force. Table 15 reflects this change in the staking anvil control mechanism as a new input variable and the addition of staking force as an additional DoE response.

Table 15: Revised list of DoE input variables.

Staking Force	Pushout Strength	Post-Stake Torque
- Anvil Staking Depth - Outer Race Diameter - Groove Depth - Groove Pitch - Chamfer Depth - Housing Outer Diameter	- Anvil Staking Depth - Outer Race Diameter - Groove Depth - Groove Pitch - Chamfer Depth - Housing Outer Diameter - Interference Fit	- Anvil Staking Depth - Outer Race Diameter - Groove Depth - Groove Pitch - Chamfer Depth - Housing Outer Diameter - Interference Fit - Inner Ring Diameter - Pre-Stake Torque - Outer Race Width

6.2.3.6. Torque Definition

Torque is not a quantity that can be directly defined in a FE model. For this investigation, torque will be measured as a function of the normal contact pressure between the liner and the inner ring and is defined as

$$Torque = \mu r A \sigma_N, \qquad\qquad [\,53\,]$$

where μ is the coefficient of friction of the liner, r is the radius of the liner, A is the surface area of the liner and σ_N is the average liner normal contact pressure. For each simulation, μ will be evaluated from SFKs pressure-friction relationship as per Table 14. From the study of the 176 live bearings (as described in Section 6.2.1), the upper and lower bound of the pre-stake torque was determined to be 0.3 Nm – 5 Nm for Type 3 bearings.

To set the pre-stake torque of a bearing, the contact surface of the liner was offset from the liner creating interference between the liner and the inner ring. During the first sub-step of the simulation, this interference would be solved resulting in a normal contact pressure against the liner. However, a unique liner offset is required for each individual bearing to achieve the same pre-stake torque due to the influence of bearing geometry. This liner offset initially could only be determined via trail and error and would prove to be impractical for large sets of simulations. To predict the required liner offset, a level 3 full-factorial DOE was run (from model initialisation to the end of the sub-step of the staking FE model) to determine the relationship between the bearings geometry and liner offset on the pre-stake torque (See Table 18 for the list of the input parameters and corresponding values). The only parameters not tested were the housing diameter and interference fit because the housing was supressed during these simulations to remove the influence of the housing on pre-stake torque. From this DOE, a Pre stake torque relationship was derived with an error of ±0.02Nm.

$$[\text{REDACTED}] \qquad\qquad [\,54\,]$$

By rearranging Equation 54, the required liner offset could be evaluated and automated within Ansys to ensure the correct pre-stake torque was applied before the staking phase of the simulation.

6.2.3.7. Model Setup and Workflow

To increase computational efficiency, an axisymmetric analysis was used to reduce the FE model to a 2D analysis, significantly reducing the computation cost of the resulting model compared to a 3D analysis (Figure 90). As previously discussed in 6.2.3.5, the staking model can be split broadly into the four phases of initialisation, staking, relaxation, and pushout. These phases were split into eight load steps with the dynamics of the model visualised in Figure 91 and the workflow detailed as follows.

Initial Contact Initialisation

Before a measurement of the pre-stake torque can be made any interference fits in the model need to be resolved. liner/inner ring interference is generated by virtually offsetting the contact surface of the inner ring to penetrate the inner ring. Outer race/housing interference in produced by modelling their geometries such that they overlap each other. In the first load step any penetration of the contact surfaces is resolved by pushing the two bodies apart until they are tangential. To eliminate any interaction from the staking anvils, both anvils are moved 0.01mm away from the housing. With no externally controlled boundary conditions on the bearing, there is a large risk of model instability and rigid body motion to develop. The model is stabilised by turning on "weak spring" to prevent any rigid body motion.

Pre-Stake Torque Measurement

All motion of the staking anvils is stopped and with all contact interfaces stabilised, the average contact pressure of the liner/inner ring interface is measured to calculate the pre-stake torque of the bearing (Equation 53).

Anvil Contact

Both staking anvils are brought back into contact with the bearing with 0.01mm of compression.

Staking

With the geometry of the bearing constrained between the controlled motion of the two staking anvils, weak springs are now turned off and the anvils fully stake the bearing. The motion of the Anvils is controlled by an APDL script (Figure 89) that looks up the required anvil compression distance for each simulation (Table 17). The staking load is recorded as the maximum force in the Y direction during this load step measured at the contact between the staking anvil and outer race.

```
Commands
  1  UAnvilDisp = ARG1          ! Upper Anvil Displacement
  2  *dim,tabf,table,9,,,LStep
  3  tabf(1) = 0,0.01,0.01,-0.01,UAnvilDisp,0,4,4,4  ! Displacement value
  4  tabf(1,0) = 0,1,2,3,4,5,6,7,8   ! Load Step
  5  d,UAnvil,UX,0               ! Fixed in X Direction
  6  d,UAnvil,UY,%tabf%          ! Y motion controlled by tabf
  7
  8  LAnvilDisp = ARG2
  9  *dim,tabg,table,9,,,LStep
 10  tabg(1) = 0,-0.01,-0.01,0.01,LAnvilDisp,0,-4,-4,-4 ! Displacement value
 11  tabg(1,0) = 0,1,2,3,4,5,6,7,8 ! Load Step
 12  d,LAnvil,UX,0              ! Fixed in X Direction
 13  d,LAnvil,UY,%tabg%         ! Y motion controlled by tabf
 14
 15  PushoutPlateDisp = ARG3
 16  *dim,tabh,table,9,,,LStep
 17  tabh(1) = 0,0,0,0,0,0,0,-0.2,PushoutPlateDisp ! Displacement value
 18  tabh(1,0) = 0,1,2,3,4,5,6,7,8 ! Load Step
 19  d,PushoutPlate,UX,0         ! Fixed in X Direction
 20  d,PushoutPlate,UY,%tabh%    ! Y motion controlled by tabf
```

Figure 89: Scripting to control both staking anvils and the pushout plate during the analysis.

Anvil Separation

The staking anvils are moved back to their starting position so that they no longer contact the bearing. At the point of anvil separation there can be convergence issues due to the anvil contacts jittering between contacted and separated (5.2.5.3) exacerbated by the bearing being no longer geometrically constrained. For this load step only, the inside corner of the inner ring has its displacement in Y fixed to stabilise the bearing during anvil separation (Figure 90).

Post-Stake Torque Measurement

The fixed displacement on the corner of the inner ring is removed and with no external forces acting on the bearing, the average contact pressure of the inner ring/liner contact is measured to determine the post-stake torque. The staking anvils are moved 4mm away from the bearing to avoid interfering with load steps 7 and 8.

Pushout Plate and Support Contact

At the start of the simulation, the pushout plate started 0.1mm away outer race and the housing support 0.1mm away from the housing to avoid interfering with load steps 1-6. To bring these bodies into contact with the bearing assembly, the pushout plate is lowered 0.2mm. First contact with the bearing happens at 0.1mm, with the plate and bearing assembly all moving downward and contacting the housing support at 0.2mm. The housing support remains stationary throughout all loads step with its displacement fixed in both X and Y directions.

Pushout

Now that all bodies have made contact, the pushout plate continues to move downward driving the outer race out of the housing that being constrained by the housing support . The motion of the pushout plate is controlled by an APDL script (Figure 89) that looks up the required pushout distance for each simulation (Table 17). The pushout strength is recorded as the maximum force in the Y direction during this load step measured at the contact between the pushout plate and the outer race.
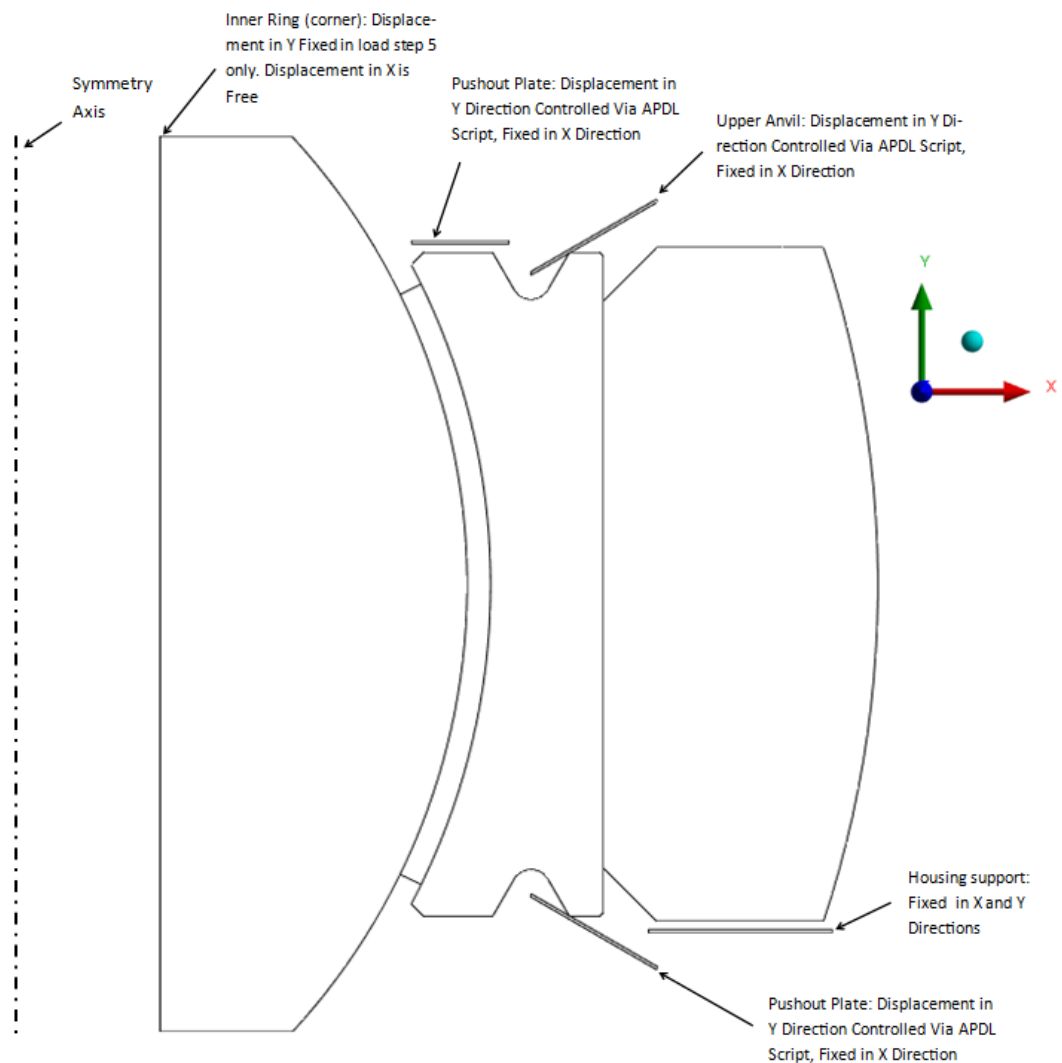
Figure 90: Schematic of boundary conditions applied to the staking model.
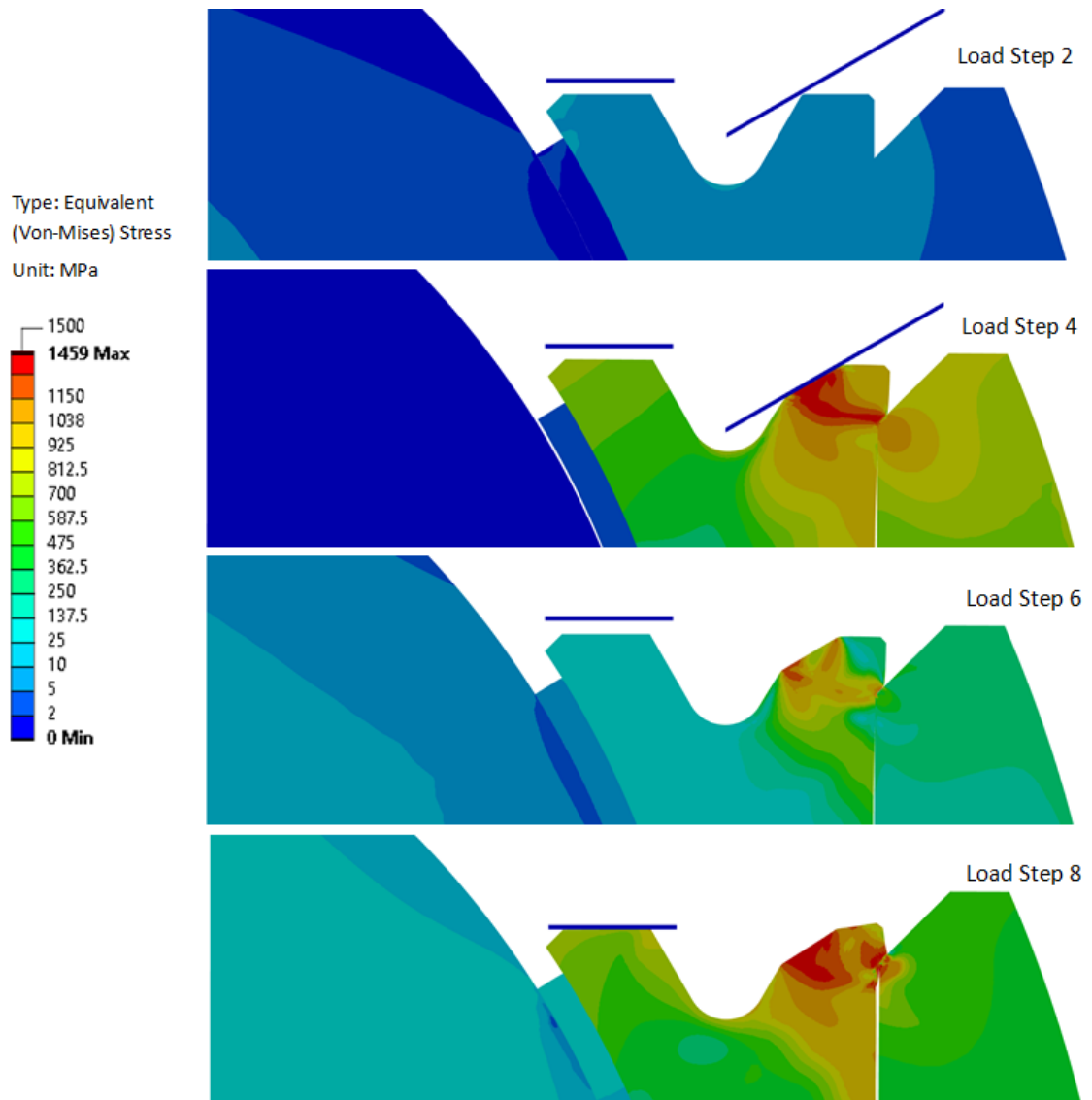
Figure 91: Equivalent Von-Mises Stress field of the staking model demonstrating the overall flow of the model at four key points. (Top to bottom) Measurment of the liner pre-stake torque, maximum staking load, measurement of the post-stake torque, and lastly the maximum pushout strength.

6.2.3.8. Mesh Independence

The conventional method for simple geometries is to gradually reduce the global element size until the maximum displacement, stress or contact forces (depending on the particular analysis method) have converged to within an acceptable tolerance of typically 0.5% (As seen in Section 5.2.5). However, due to the presence of small geometric features (relative to the overall size of the model) and large stress gradients expected to be concentrated in these regions, a global element size approach would result in a very inefficient computational model. The high degree of plastic deformation near these regions requires a high mesh density to accurately model and in addition, if the mesh is too coarse it will result in the simulation failing to due to excessive element distortion. The majority of the model does will not require such high mesh densities which will result in an excessive number of elements in large regions of the model where it is not required.

With a global element size of 1mm and without any of local mesh refinement, the initial FE model of the staking process would fail to solve during the first phase of staking. Because of the need for localised mesh refinement, a baseline mesh was established with the following controls and sizing features applied to the geometry of the model in anticipation of areas that required local mesh refinement.

- Global element size of 1mm. (this global parameter gets overwritten by any localised mesh refinement)

- Outer Race element size of 0.5mm

- Two Inflation layers added to the liner-inner race contact to aid with liner contact pressure convergence

- To avoid shear locking (Colorado, 2017) of the high aspect ratio of the liner, the thickness of the liner was divided to into 4 elements

- Spheres of influence were added to the root of the housing chamfer and staking anvil contact points with a 0.5mm radius and 0.1mm element size

- Element divisions along the following edges: the long edge of the liner (30 divisions), radius of the v-groove of the outer race (5 divisions), outer diameter of the outer race that contacts the housing inner diameter (50 divisions), and along the housing's chamfer (15 divisions)

- To smooth the transition between regions of high and low mesh density, the global element size growth rate was lowered from its default value of 1.2 to 1.05.

These localise mesh refinements were arrived at with the visual assistance of the Structural Error results plot. Each time the simulation failed to solve, the Structural Error result from the last time-step that successfully converged indicates areas of the mesh that required further refinement. Structural Error is the measure of maximum difference between stress values at a node that is shared between multiple elements. Large values of Structural Error indicate regions where stress is changing rapidly across elements and that a finer mesh would be required to accurately capture this stress gradient. It also is a strong marker for elements that were driving convergence issues causing the failed solutions.

With the coarsest mesh that could still produce a stable and successful solution established, a series of mesh independence studies were carried out to determine the parameter values for each region of mesh refinement. Following the same process as the ring compression FE model as previously detailed in Section 5.2.5.4, a Type 3 mid-point bearing (Section 6.3.2, Table 17) was simulated with one of the local mesh refinement features incrementally changed to increase to local mesh density until the model's response had converged to within 0.5% for each of the: maximum staking force, maximum pushout strength, and average liner contact pressure. With the first mesh refinement parameter set, this process was repeated for each parameter to achieve an independent mesh. The final converged parameter values are detailed in Table 16.

Table 16: Comparison between initial mesh and final independent mesh parameter values for a Type 3 bearing. ID locations visualised in Figure 92.

Location	ID	Mesh refinement Method	Initial Value	Final Value
Liner to Inner race contact face	1	Number of Inflation Layers	2	4
Housing Chamfer root	2	Sphere of Influence	0.5mm Radius 0.1mm Element Size	0.5mm Radius 0.04mm Element Size
Staking Lip Root	3	Sphere of Influence	0.5mm Radius 0.1mm Element Size	1mm Radius 0.04mm Element Size
Staking Anvil Contact	4	Sphere of Influence	0.5mm Radius 0.1mm Element Size	0.25mm Radius 0.02mm Element Size
Housing Chamfer Edge	5	Edge Divisions	30	75
Outer Race V-groove Root	6	Edge Divisions	5	12
Liner Width	7	Edge Divisions	4	6
Inner Race Outer Diameter	8	Edge Divisions	30	100
Outer Race Outer Diameter	9	Edge Divisions	50	250
Outer Race	N/a	Element Size	0.5mm	0.3mm
Whole Model	N/a	Element Size	1mm	0.7mm
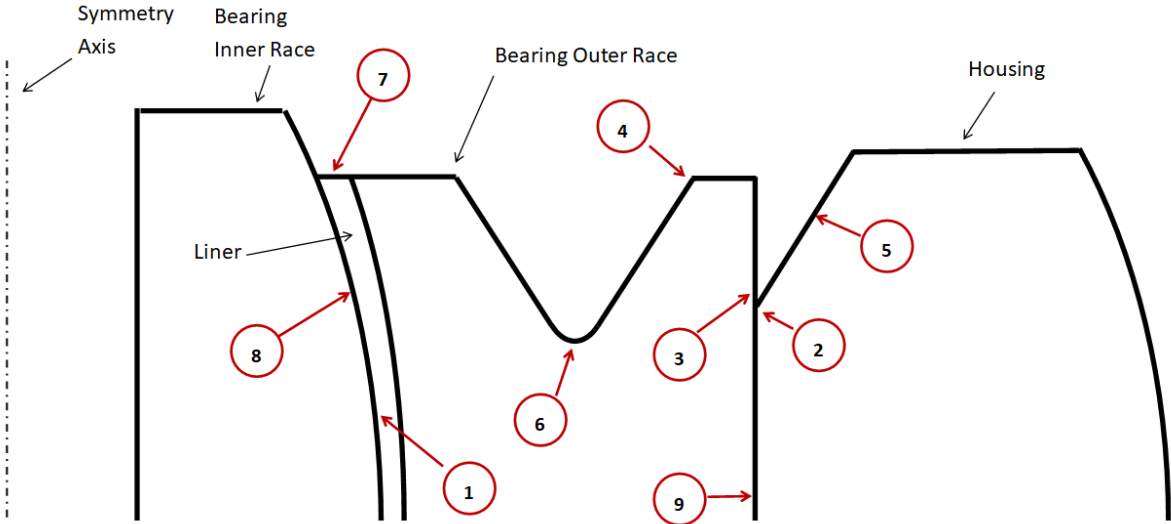
Figure 92: Schematic detailing the location of mesh refinement controls. Only top half of the model is shown as all controls are mirrored onto the lower half. IDs described in Table 16.

6.3. Definitive Screening Design

From Section 6.2.2, ten unique parameters were identified that could impact the pushout strength and post-stake torque, however, it is unlikely that all ten parameters would have a similarly equal impact on staking. Adding unnecessary parameters to a DoE that have little to no impact only serves to add noise to the measured response, making the identification and characterisation of important factors more difficult. Therefore, a screening test was carried out to reduce the number of potential input variables.

6.3.1. Design Resolution

Screening tests are commonly referred to as fractional factorial designs and allow for the quick identification of the most important input effects. This is achieved by running a reduced number of tests at the cost of design resolution. Design resolution is a description of how much the impacts of each effect are aliased (confounding) with other effects. The most common fractional factorial design resolutions are:

- Resolution III – No main effects are aliased with any other main effect, but main effects are aliased with 2-factor interactions,

- Resolution IV – No main effects are aliased with any other main effect or 2-factor interactions, but some 2-factor interactions are aliased with other 2-factor interactions and main effects are aliased with 3-factor interactions,

- Resolution V – No main effects or 2-factor interactions are aliased with any other main effect or 2-factor interactions, but 2-factor interactions are aliased with 3-factor interactions and main effects are aliased with 4-factor interactions (Minitab, 2020a).

Typically, the number of runs scale with design resolution. Plackett-Burman and Taguchi designs are popular resolution III screening designs due to their ability to identify influential 1st order and main effects with as few runs as possible. Their use though relies on the assumption that all 2-way and higher interactions are not impactful as all main effects are heavily aliased. This problem is severely exaggerated with increasing numbers of variables. Definitive Screening Designs (DSD) are resolution IV designs that include a midpoint value for each variable. The addition of a midpoint value allows the increased design resolution and estimation of square terms not possible with resolution III designs. The total number of runs for a DSD is N=2K+1 where K is the number of variables being screened. A DSD was chosen for this screening test as it offered the best balance between time and design resolution.

6.3.2. Parameter Input Range

A DSD requires an upper, lower and midpoint value for each input parameter (Table 15) to define the model's design space. To the author's best knowledge, how to determine these limits is not explicitly stated in any literature or methodology and appears to be at the researcher's discretion. It is a trade-off between maximising the design space of the model at the cost of that model's accuracy. Setting narrow limits increases the likelihood that the change in response will be relatively small and consistent. Conversely, wider limits increase the probability of large changes in the measured response occurring at the extreme values of the input variables. This could make it challenging to accurately model the response in both the centre and extremes of the design space.

Typical values for manufacturing-focused DoE set the upper and lower bounds to approximately 80% and 20% of the machines operating limits. As agreed with SKF, this range was deemed as an acceptable compromise to cover enough of their product range to ensure the final model would be of sufficient value. However, as previously shown in Figure 86, many of the geometric features of a bearing scale with respect to the overall bearing size. This makes the absolute dimensions unsuitable for a DSD (of any DoE) as it would generate nonsensical bearing geometries such as a 96mm wide bearing with a thickness of only 11mm. Instead, the inputs to the DSD are ± 1 standard deviation as derived from the bearing geometric characterisation in Table 12. These standard deviations were then converted back into absolute dimensions to construct the bearing geometry for each test.

The only two non-geometric inputs are the pre-stake bearing torque and anvil staking depth. Whilst the pre-stake bearing torque limits could be attained from the engineering drawings, the anvil staking depth limits were determined from computational modelling trials. A mid-point Type 3 bearing (all input parameters set to the middle of their respective ranges) was modelled with the anvil staking depth increased from 0.26mm to 0.55mm. The relationship between the resulting staking force and both the pushout force and post-stake torque is shown in Figure 93. These curves allow for the identification of the upper and lower limits for the anvil staking force.
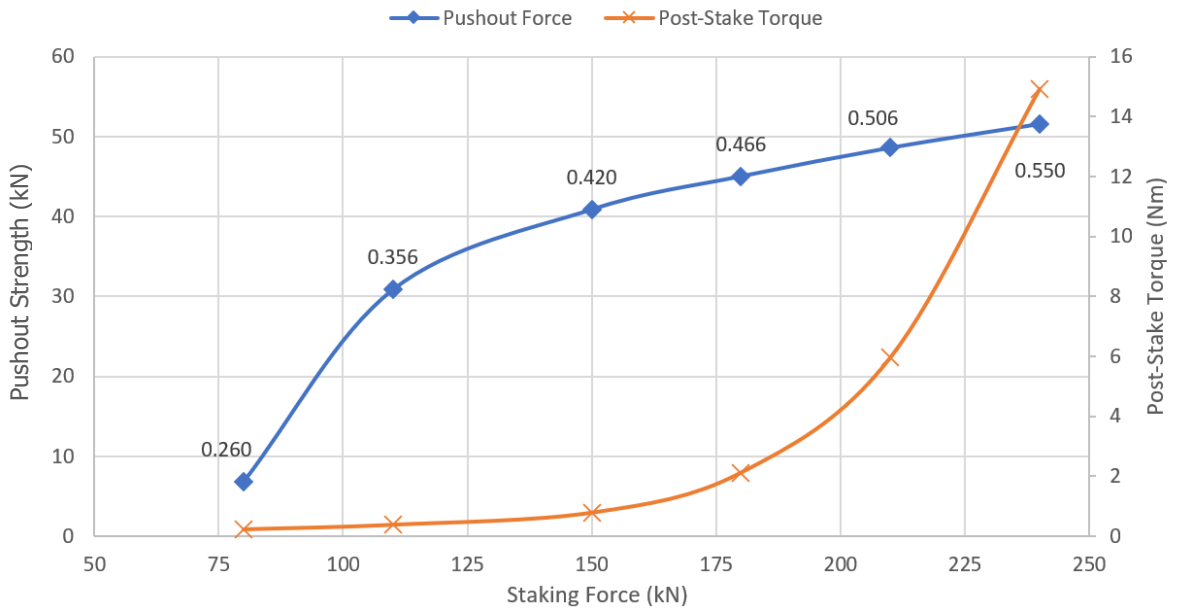
Figure 93: Relationship between the staking force and both the pushout strength and post-stake torque. Data labels represent the equivalent anvil staking depth in mm.

From Figure 93, there are two inflection points from the response of pushout force and post-stake torque. The first inflection point occurs at an anvil staking depth of 0.35mm (110kN staking force) and represents the lower limit for the ideal stake. As the anvil staking depth is increased, the staking lip is deformed into the housing chamfer and the contact region between the two bodies increases (Figure 94 and Figure 95). This contact region is referred to as the lip contact area.
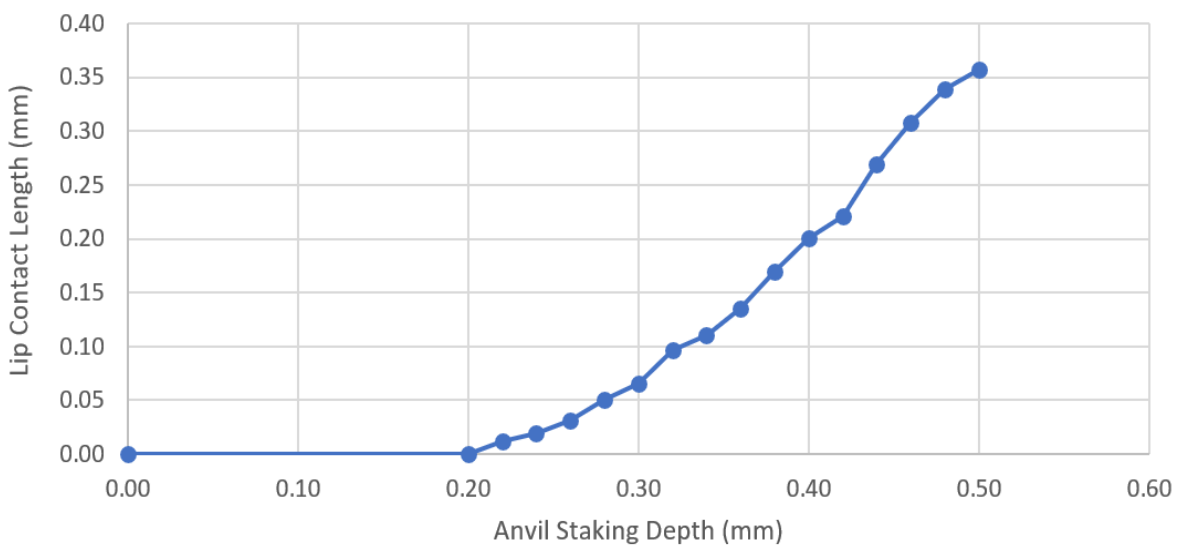
Figure 94: Lip contact length during staking. The staking lip does not contact the housing chamfer until 0.2mm of anvil displacement.

Before approximately 0.35mm of anvil staking depth, the staking lip is not sufficiently formed and does not engage with the housing chamfer (Under-staked). During the pushout phase, the small lip contact area results in the inside corner at the root of the housing chamfer rounding off. The shallow angle of the poorly formed staking lip is then able to expand the housing as it is pushed out. The housing is therefore unable to support the bearing and results in the distinct inflection point in Figure 93 where the pushout force is severely reduced. After approximately 0.4mm of anvil staking depth, the lip contact length increases linearly with the anvil staking depth and is sufficiently formed to engage with the housing chamfer during pushout. The housing does not experience any significant plastic deformation due to the larger contact area and instead, the failure mode during pushout is the deformation of the staking lip.
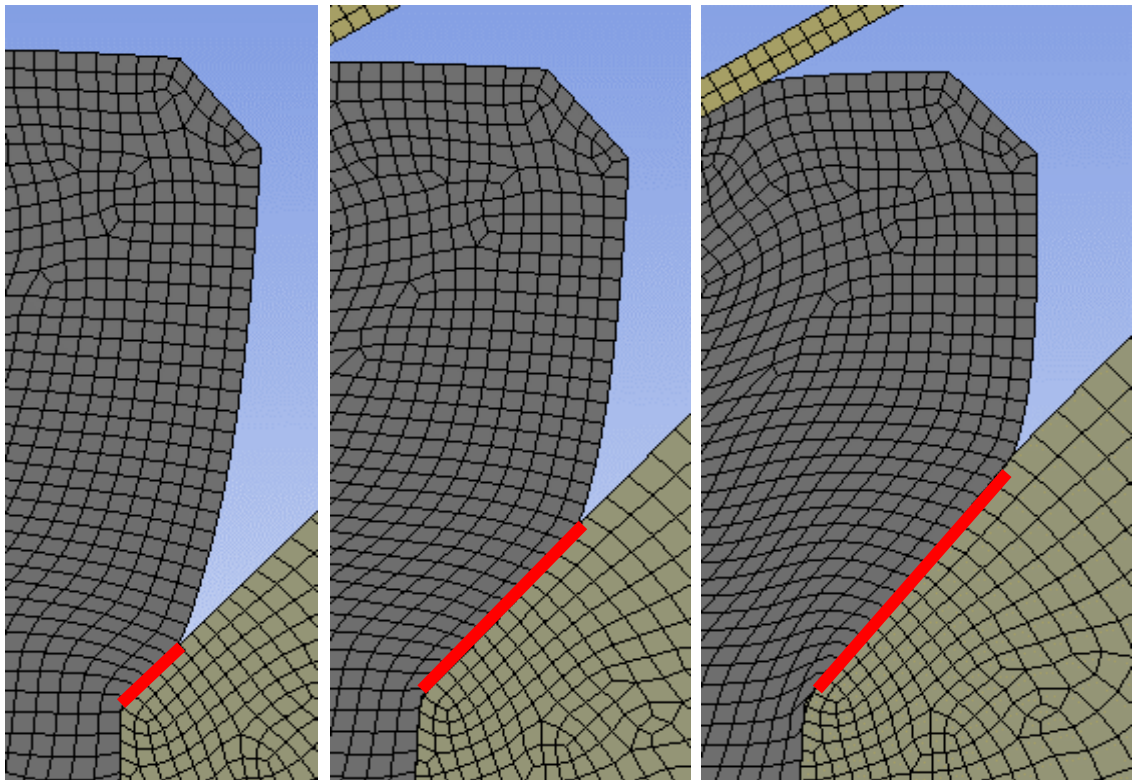
Figure 95: Detailed view of the staking lip with the lip contact area highlighted in red at anvil staking depths of (Left) 0.3mm, (Middle) 0.4mm, and (Right) 0.5mm.

The second inflection point from Figure 93 is not as precisely defined as the first but occurs at approximately an anvil staking depth of 0.45mm - 0.50mm (180kN - 210kN staking force) and represents the upper limit for the ideal stake. Before this point, the post-stake torque increases gradually with the staking force before a rapid increase. When the staking lip first begins to yield, it can freely expand radially with the resulting staking force determined entirely by the force to overcome the flow stress in the staking lip. As the staking lip contacts the housing's chamfer, the housing can support the staking lip and begins to resist the deformation of the lip increasingly as the lip contact area also increases (Figure 95). Beyond an anvil staking depth of 0.45mm-0.50mm, the resistance of the staking lip begins to drive the material flow of the outer race inwards and toward the inner ring (Over-staked). This compresses the liner against the inner ring and causes a rapid rise in post-stake torque. From these two inflection points, the ideal stake for a Type 3 bearing can be estimated to exist between an anvil staking depth of 0.35mm and 0.51mm.

However, this range of inputs was deemed too wide after preliminary trails and resulted in problems with the model's overall accuracy. The location of the two inflection points that defined an over or under staked bearing change with respect to the bearing geometry, in particular the housing's chamfer depth. This pushed the computation model in some tests into highly non-linear regions beyond the inflection points, reducing the overall accuracy of the final staking model for the majority of input parameter combinations (assuming a normal distribution for each input parameter). Prediction accuracy at the centre of the design space, where the model's behaviour is relatively insensitive to parameter change, is sacrificed in an attempt to capture the highly sensitive behaviour at extreme parameter input combinations. These undesirable interactions can be hard to identify or to estimate their impact of the final model's accuracy prior to carrying out a DOE (Discussed in further detail in Section 8.3.4).

With the efficiency of the definitive screening design process requiring only 21 tests to derive a relatively good staking model, five definitive screening designs were conducted with the anvil staking depth range varying from a maximum range of 0.35mm-0.51mm down to as small as 0.41mm-0.47mm in 0.02mm increments. The performance of each screening test was compared against a large set of 430 randomised test bearing simulations (See Section 6.4.1). These trails confirmed concerns that an anvil staking depth of 0.35mm-0.51mm was too wide and severely comprised the accuracy of the model. 0.49mm-0.39mm was as wide as the model could accommodate without severely impacting overall accuracy.

The final DSD table of inputs and run order for Type 3 bearings were produced using the statistical software package Minitab (2020b) and is detailed in Table 17. For the remainder of this investigation, the upper and lower parameter inputs will be referred to as 100% and -100% deviation from the mid-point value. A full summary of the computational model settings for each bearing type can be found in Appendix C.

Table 17: List of input parameters and run order for the definitive screening design for Type 3 bearings. +, - and 0 represent the upper (100%), lower (-100%) and midpoint (0%) parameter values respectively.

Factor		Inner Ring Diameter	Groove Depth	Groove Pitch	Outer Race Diameter	Outer Race Width	Chamfer Depth	Housing Diameter	Interfere-ence	Pre-stake Torque	Anvil Staking Depth
Units		mm	mm	mm	mm	mm	mm	mm	mm	Nm	mm
Model Limits (mm)	Upper										
	Mid-point					[REDACTED]					
	Lower										
Run Order											
1		0	+	+	+	+	+	+	+	+	+
2		0	-	-	-	-	-	-	-	-	-
3		+	0	-	-	+	-	+	+	+	-
4		-	0	+	+	-	+	-	-	-	+
5		+	-	0	-	+	+	-	+	-	+
6		-	+	0	+	-	-	+	-	+	-
7		+	-	-	0	-	+	+	-	+	+
8		-	+	+	0	+	-	-	+	-	-
9		+	+	+	-	0	-	-	-	+	+
10		-	-	-	+	0	+	+	+	-	-
11		+	-	+	+	-	0	-	+	+	-
12		-	+	-	-	+	0	+	-	-	+
13		+	+	-	+	-	-	0	+	-	+
14		-	-	+	-	+	+	0	-	+	-
15		+	+	+	-	-	+	+	0	-	-
16		-	-	-	+	+	-	-	0	+	+
17		+	+	-	+	+	+	-	-	0	-
18		-	-	+	-	-	-	+	+	0	+
19		+	-	+	+	+	-	+	-	-	0
20		-	+	-	-	-	+	-	+	+	0
21		0	0	0	0	0	0	0	0	0	0

6.3.3. Screening Results

The primary output from the DSD was three regression models that predicted the response to staking force, pushout strength and post-stake torque. To produce the regression models, a stepwise regression was carried out to eliminate terms that were not statistically significant in predicting their respective responses. By default, Minitab's stepwise regression adds and removes terms from the model until all variables in the model have p-values less than 15%. Terms with a p-value greater than 15% are rejected as there is a greater than 15% chance that the improvement to the overall model could have occurred from random chance. The p-value criteria for the stepwise was tightened to 5% to ensure the greater statistical significance of any term in the final model.

Initially, each regression model for the Type 3 bearings contained all ten parameters containing linear, square, and 2-way interactions. Each model's variance was calculated with their R-squared adjusted values found to be 0.999, 0.994, and 0.984 for staking force, pushout strength, and post-stake torque respectively. These results provided strong evidence for the rejection of the null hypothesis and proved the potential of this methodology to predict the results of the computational model.

To increase the efficiency of the final DoE it was necessary to eliminate input variables which contributed the least to the model's R-squared adjusted value. Using Minitab's analysis tools and Pareto charts, the parameter which contributed the least was eliminated and the stepwise regression re-run. This process was repeated until only one input variable remained. By monitoring the change in each model's R-squared adjusted value, all ten variables could be ranked by the order of their impact (Figure 96). A decision was made to eliminate the parameters groove depth, inner ring diameter, outer race width, and Housing Diameter from the final DoE model.
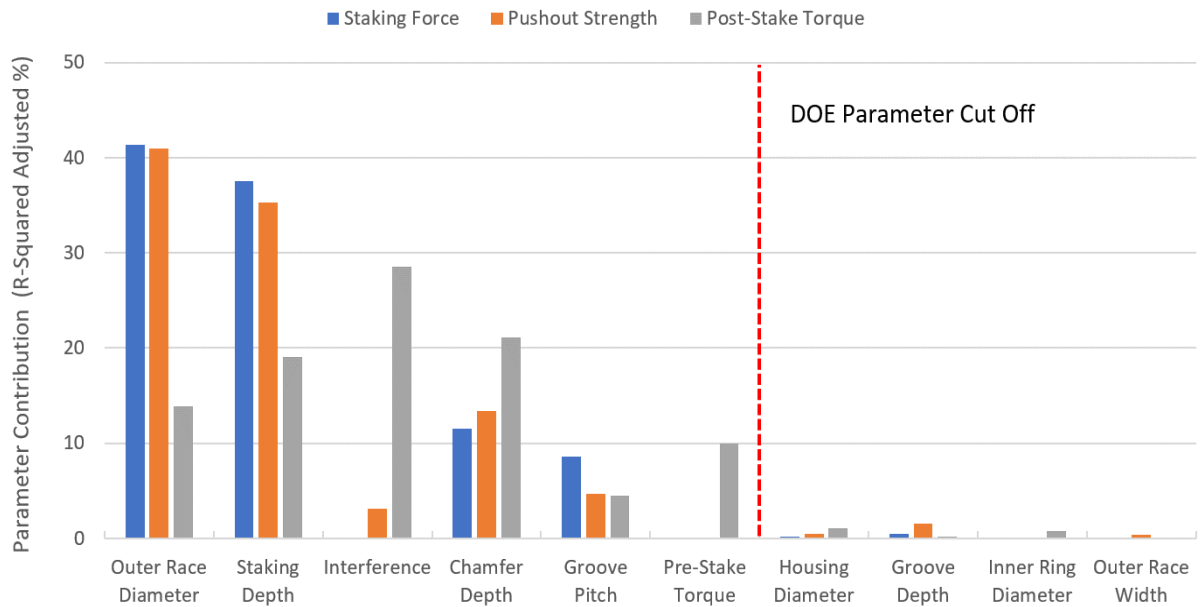
Figure 96: Relative contribution for each variable as a measure of its impact on the R^2 adjusted value (Type 3 Bearings).

These results (including the four removed variables) were consistent across all three bearings categories with very a similar distribution of relative parameter contribution. With only six parameters left in the model, the 5% stepwise regression analysis was re-run and the new R-squared adjusted values were found to have decreased minimally to 0.990, 0.986, and 0.955 (Table 18).

Table 18: Regression model Comparison after four variables were removed for the Type 3 bearings.

Regression Model	R-Squared Adjusted		
	Staking Force	Pushout Strength	Post-stake Torque
All 10 Parameters	0.999	0.994	0.984
6 Parameters (Groove depth, Inner ring diameter, Outer race width, and Housing Diameter removed).	0.990	0.986	0.955

The secondary purpose of the DSD was to identify any non-linear terms and their impact on the regression models. This was achieved using factorial plots where the fitted mean value is plotted against each variable (Figure 97). The fitted mean value for the variables Groove Pitch, Outer Race Diameter, and Pre-Stake Torque produced a linear relationship across all three regression models. Therefore, only two levels would be required in the final DoE to sufficiently model these variables.

By contrast, the variables chamfer depth, interference, and anvil staking depth all showed a non-linear response to post-stake torque. The only other non-linear response was seen by the anvil staking depth for the pushout strength. To capture this non-linear behaviour, these variables will require three levels for the final DoE. Therefore, the final full factorial DoE model was a mixed-level design requiring $2^3 \times 3^3 = 216$ simulations and the inputs values for all the DoE are shown in Table 19.

Table 19: Final Virtual-DoE parameter inputs for bearing Type 3.

Variable	Level	Value
Staking Depth (mm)	3	
Outer Race Diameter (mm)	2	
Interference (mm)	3	[REDACTED]
Chamfer Depth (mm)	3	
Groove Pitch (mm)	2	
Pre-stake Torque (Nm)	2	
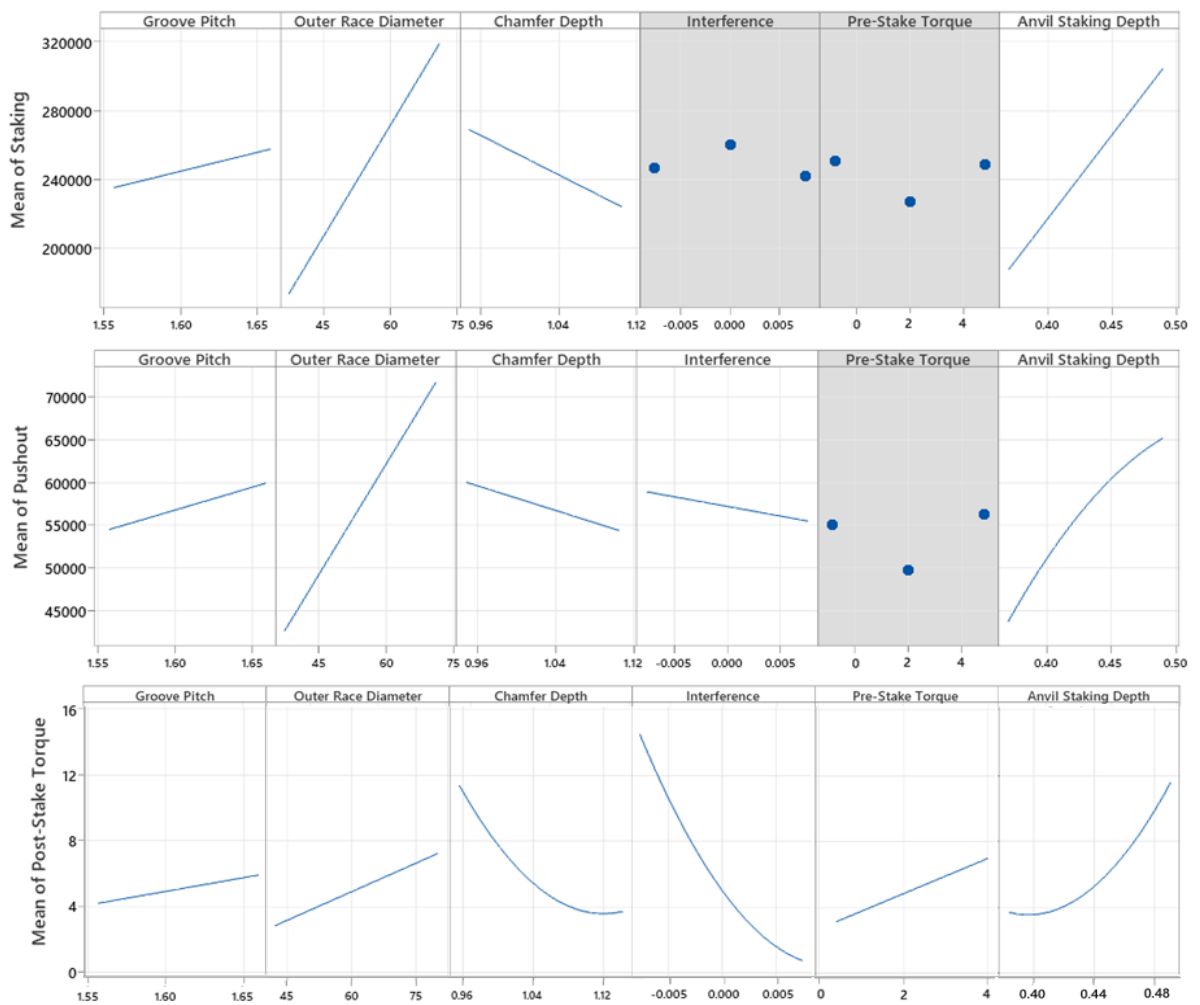
Figure 97: Main effects plot for staking force, pushout strength, and post-stake torque for Type 3 bearings. Grey background represents a term not in the regression model.

6.4. Virtual Design of Experiments Results.

As previously discussed, presenting in this section is the Virtual-DoE results for the Type 3 bearings and the development of the staking calculator tool. The same analysis was carried out for Type 1 and 2 bearings with their results presented in Appendix C.

6.4.1. Regression Model

With the completion of 216 simulations, 3 regression models were produced with a stepwise regression of 5% to predict the staking force, pushout load, and post-stake torque (Table 20). Their R-squared adjusted values were calculated to be 0.99, 0.98, and 0.94 respectively. These values are greater than those produced in the DSD indicating the regression model's near-perfect ability to account for the variance across all 216 simulations. This was to be expected as the Virtual-DoE was a full-resolution design (compared to the resolution IV DSD) and therefore no term in the model was confounded with any other term.

Table 20: Virtual-DoE regression equations for a Type 3 Bearing. Models Terms: (A) Anvil Staking Depth, (B) Chamfer Depth, (C) Groove Pitch, (D) Interference, (E) Outer Race Diameter, and (F) Pre-stake Torque. All inputs are in mm and Nm.

Response	Regression Model
Staking Force (N)	[REDACTED]
Pushout strength (N)	[REDACTED]
Post-Stake Torque (Nm)	[REDACTED]

However, this is only an indication of the regression model's ability to predict the Virtual-DoE simulations and does not represent the true performance of the models. In manufacturing, each parameter varies continuously between their respective upper and lower bounds. To derive a meaningful uncertainty to describe the model's performance, a new batch of simulations was run with randomised values for each of the input parameters.

The upper and lower limits used for the Virtual-DoE model were set to ±1 standard deviation to cover the majority of SKFs bearing designs without severely compromising the model's accuracy. For the randomised dataset these limits were increased to match the entire range of possible bearing geometries (+100% and -100% represent the original Virtual-DoE model upper and lower input limits with some parameters now extending up to ±300%). In total, 430 randomised tests were simulated and when combined with the Virtual-DoE simulations, the total runtime was approximately 280 hours (AMD CPU Ryzen 9 3950X @4.2GHz).

From this dataset, the model's error was calculated as a function of each parameter's deviation from its mid-point (Figure 98). Whilst this is beneficial for understanding the behaviour of each parameter, it does not provide any overall understanding of the model's uncertainty. To achieve this, each of the 430 simulations were ranked by its maximum absolute parameter deviation, grouped, and their errors averaged together (Figure 99). This uncertainty as a function of parameter deviation provided a 'fingerprint' that establishes the model's overall performance necessary to develop a staking calculator tool.
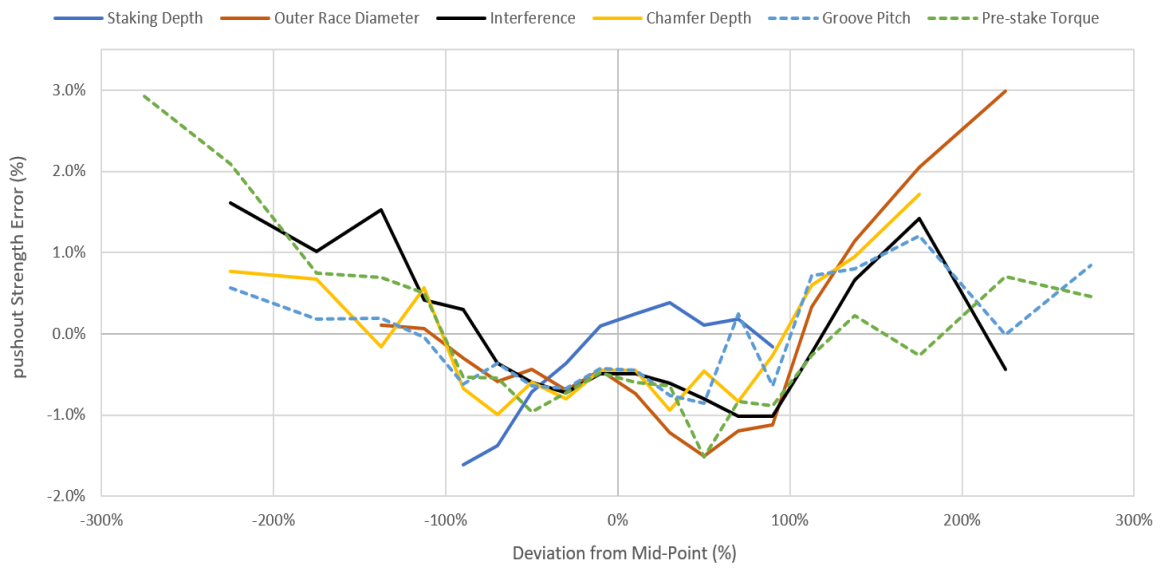
Figure 98: Pushout strength error as a function of each input parameter (Type 3 bearing model). -100% and 100% represent the lower and upper limits for each of the Virtual-DOE parameters.
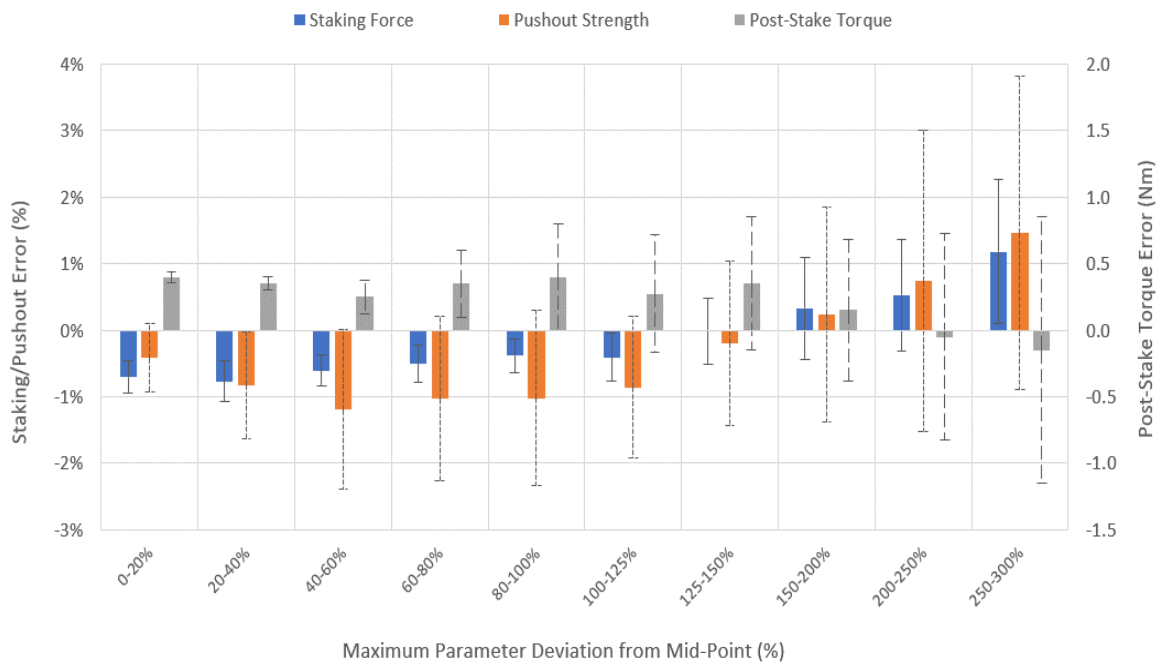
Figure 99: Virtual-DOE model error with 95% confidence intervals for a Type 3 bearing. The 20-40% band represents the model's error when the parameter with the greatest absolute deviation from its respective mid-point value is between 20-40%.

6.4.2. Staking Tool

A list of requirements for the staking tool are summarised as follows.

- A simple user interface so somebody not connected to the project could use the tool

- Use non-proprietary software

- Accept both imperial and metric inputs

- Visuals to indicate where the bearing being analysed exists between the limits of the model

- Accommodate the input of manufacturing tolerances

- Present a relationship between the staking force and both pushout strength and post-stake torque

- Demonstrate the impact of each variable such that the end user can understand how to modify the bearing's geometry to achieve the desired staking results.

MATLAB (MathWorks, 2022) and Python (Python, 2024) are both well-established and popular software packages used for complex numerical calculations and contain General User Interface (GUI) tools suitable for this type of application (Karras, 2018; Woodhead, 2015a). However, their advanced features and custom GUI tools were not of major importance as these were not necessary to create the staking tool. Excel was instead chosen to build the staking tool within due as it is universal across all of SKFs user base (including non-engineering teams) therefore encouraging wider adoption and engagement with the tool. In addition, it could be assumed that all users would already be familiar with navigating Excels user interface compared to either MATLAB or Python. The overall design of the staking tool is split into three steps. Firstly, the groove classification lookup chart (Figure 100) allows the end user to identify which groove geometry type the bearing belongs to.

Figure Redacted

Figure 100: Lookup chart to determine what groove geometry classification the bearing being analysed falls within.

Secondly, the end user is presented with a geometry input window (Figure 101) where all the necessary bearing geometry and manufacturing tolerances for the staking calculator are entered. At this stage, the user will also select the relevant groove classification, unit system, and manufacturing tolerance distribution (Section 6.4.3).

Bearing Geometry - User Inputs					

Groove Classification: Type III Manufacturing Tolerance Distribution: Uniform

Unit System: Metric

Input Dimensions	Nominal Value		Relative Manufacturing Tolerance		
			Min	/ Max	
Bearing Outer Race Diameter	38.127	mm	-0.0126	0	mm
Bearing Outer Race Width	20.900	mm	0	0.1	mm
Bearing Groove Pitch Diameter	34.8	mm	-0.05	0.05	mm
Bearing Groove Depth	1.3	mm	0	0.05	mm
Rod End Width	21.014	mm	-0.05	0.05	mm
Rod End Staking Chamfer	1.0880	mm	-0.052	0.052	mm
Rod End Spherical Diameter	55.1	mm	-0.025	0.025	mm
Bearing/Rod End Interference Fit	0	μm	-2.7	2.7	μm

Figure 101: Input window for all of the bearing and housing geometries required for the staking tool.

Lastly, a summary report is presented to the user (Figure 102) to validate that their inputs are within the limits of the staking model. The green regions (within +-100%) represent the upper and lower bounds of the Virtual-DoE that the regression equations were defined within. Orange regions are outside of the model's original parameter limits but produce acceptable results. Red regions represent conditions where the model produces results that cannot be used as the errors are no longer acceptable.
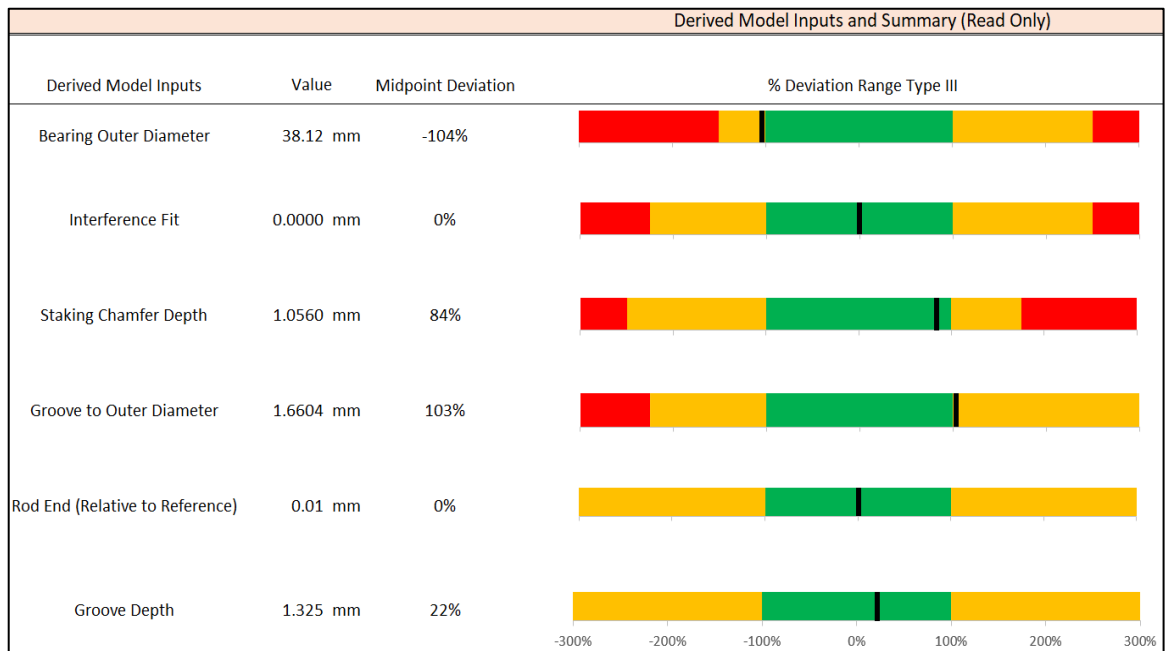
Figure 102: Report window for the user to identify where their bearing sits in relation to the model limits for each parameter. Red regions represent the geometric limits of the staking calculator for each parameter.

Once the inputs have been checked to ensure that no parameter is outside of the calculator's limits, the pushout strength and post-stake torque are plotted as a function of the staking force (Figure 103). This is achieved by fixing the model's inputs and iterating across all possible values for the anvil staking depth. For each anvil staking depth increment, there is a corresponding staking force, pushout strength and post-stake torque value.

As part of the design requirements for the staking tool, it was necessary to show the impact of the manufacturing tolerances on both pushout strength and post-stake torque. To model this uncertainty, a Monte Carlo simulation is carried out within the staking tool where the inputs for the model are randomised between its tolerance limits (as defined in Figure 101) across 10,000 runs. The distribution and mean error of these 10,000 data points is calculated by grouping them together in anvil staking depth increments of 5%, with 0% and 100%

representing the minimum and maximum anvil staking depth for each staking model. This data is represented in the output of the staking model as two contour bands as shown in Figure 103. The first uncertainty band is the inherent uncertainty of the model in its ability to match the DoE simulations from which they were derived (Figure 99). The second uncertainty band is the combination of the model's inherent uncertainty in addition to the uncertainty caused by the manufacturing tolerance of each input to the model.
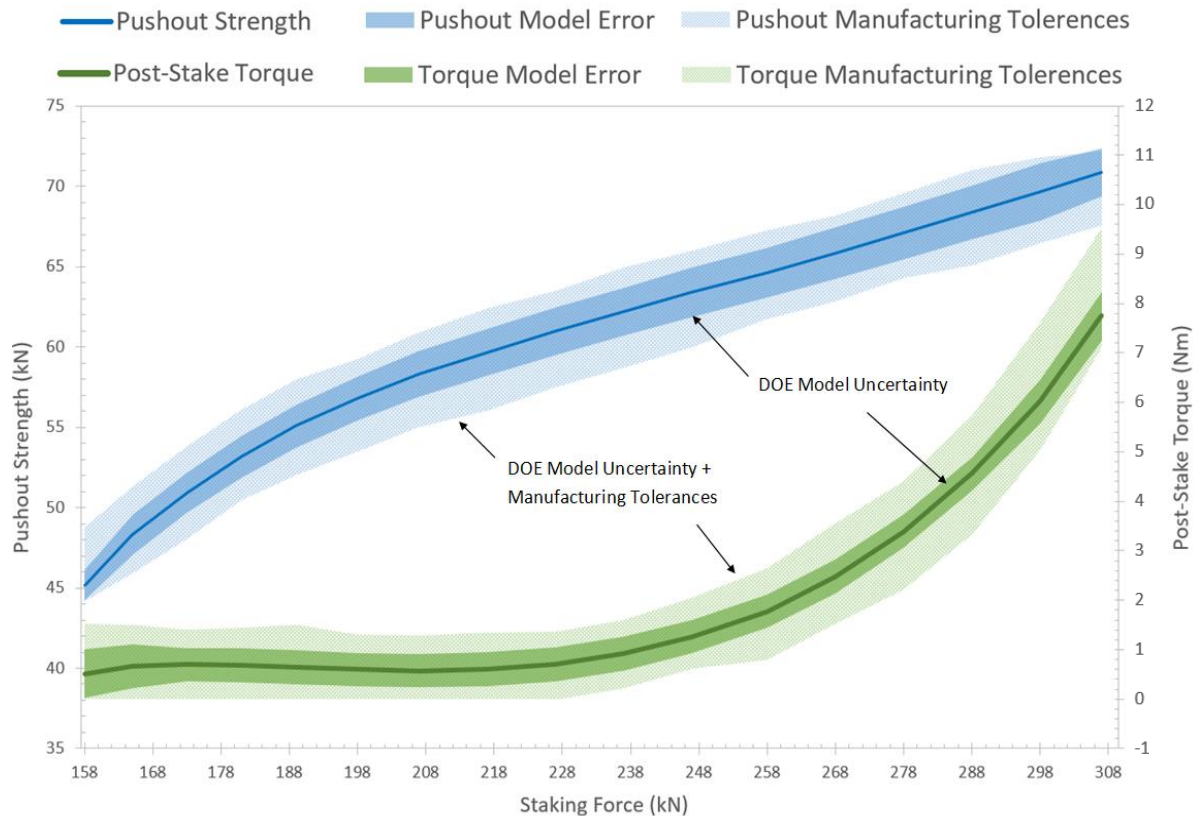
Figure 103: Staking design tool. The Inner and outer shaded bands represent a 95% confidence interval for the model's inherent uncertainty and the combination of the model's uncertainty and manufacturing tolerances respectively.

6.4.3. Manufacturing Tolerance Distribution

Under typical manufacturing conditions, it would be reasonable to assume that across a large enough sample size the value of any measured dimension would roughly follow a normal distribution. The actual distribution however is rarely perfectly normal and can be impacted by many different factors. The Probability Density Function (PDF) that defines the profile of a distribution curve is measured using four metrics: the mean of the distribution, standard deviation, skewness, and kurtosis (Figure 104).

First Moment:
mean - measure of location

$\bar{x}$ →

Second Moment:
Standard deviation - measure of spread

$-s$ $+s$

Third Moment:
skewness - measure of symmetry

Fourth Moment:
kurtosis - measure of peakedness
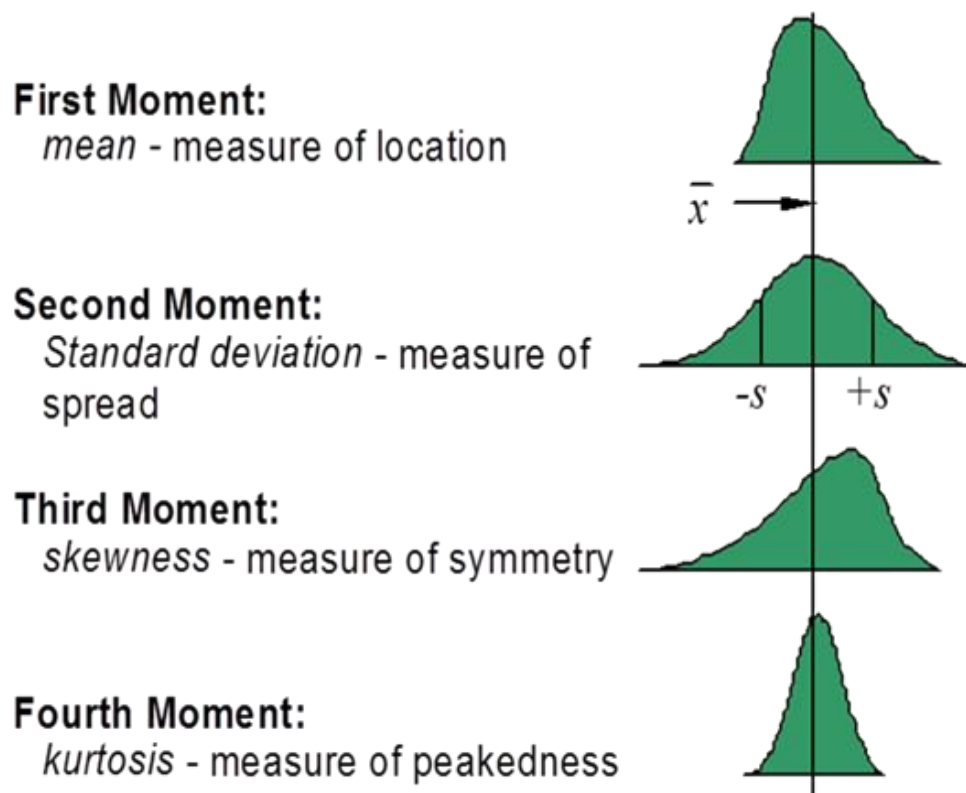
Figure 104: Variation and definition of a probability distribution function (Sigmetrix, 2022).

Within SKFs manufacturing processes it is often the case that the stated tolerances on the engineering drawings are fairly wide relative to the process capability of both the machines and their operators. This results in a peakier distribution as dimensions are held significantly tighter to the nominal drawing value than that allowed by the tolerance window. By contrast, bearings often come out of the nosing process with pre-stake torque value outside of the tolerance window and require re-working to bring them back into specification. This re-working is a relatively imprecise process and would be expected to result in a more uniform distribution.

For the error analysis of this model in subsequent chapters, a uniform distribution for the manufacturing tolerances will be used for all model inputs as this represents a worst-case scenario by producing the greatest model uncertainty.

6.5. Summary

In this chapter, a Virtual-DoE capable of modelling the staking process and producing closed-form solutions relating the staking force to both the pushout strength and post-stake torque was developed. The initial work consisted of characterising the geometry of SKFs bearings where it was found that the geometry defining the staking groove fitted into three distinct categories. As a result, it was necessary for each category to have its own separate Virtual-DOE. This was to avoid the issue where test runs would have required either impossible or unrealistic geometry combinations. Screening tests were carried out to eliminate variables that would have a negligible impact on the final model with the six retained variables (in order of impact) being the outer race diameter, staking depth, interference, chamfer depth, groove pitch, and pre-stake torque.

Using a stepwise regression of 5% to ensure the statistical significance of each model term, the uncertainties of each of the three staking models were evaluated. The resulting Virtual-DoE model was found to show a strong correlation with the computational model from which it was derived. Across all three models within their nominal parameter limits, the 95% confidence interval for both the staking force and pushout strength did not exceed ±1.7% and post-stake torque ± 0.5 Nm. These uncertainties increase by approximately a factor of 2 as parameters reach ±300% to accommodate all possible bearing geometries. Whilst not unexpected and still within acceptable limits, this increase was a result of the desire by SKF to keep the total number of models to a minimum. This compromise is discussed in further detail in Section 8.3.

As part of the development of the staking models, it was necessary to establish the upper and lower limits for the anvil staking depth. The results of this investigation identified the mechanism that drives the increase in both the pushout strength and post-stake torque with anvil staking depth. As the anvils are brought into contact and begin to compress the outer race staking lip, there exist three distinct phases to the staking process. Initially, the staking lip has not deformed sufficiently to engage with the housing chamfer and there is a significant drop-off pushout strength. The second phase is characterised by a linear increase in pushout strength and a minimal change in post-stake torque as the contact between the staking lip and chamfer increases. Lastly, once the staking lip makes sufficient contact with the chamfer the outer race begins to deform inward, compressing the inner ring, and leading to a rapid increase in post-stake torque. This results in two inflection points that define the upper and lower bound for the ideal stake.

7

Chapter

Validation and Implementation

In the previous chapter, a Virtual-DoE was undertaken to produce a series of closed-form solutions that relate the staking force to both the pushout strength and post-stake torque. An accurate correlation was found between the computational runs and regression models which validated the Virtual-DoE process and allowed for highly efficient regression models to be used in place of computational modelling. However, before the potential of the regression models can be exploited, they must first be validated against physical test data.

Presented in this chapter is the physical testing of production bearings to determine the accuracy of the regression models across their design space. The final regression models are analysed to determine the impact of the input parameters to the model. Just as in Chapter 6, only the validation of the Type 3 model is detailed in this thesis with the additional detail for models Type 1 and 2 detailed in Appendix D.

7.1. Staking Trials

For each of the three bearing types, three regression models were produced each containing six unique input parameters and up to four-way interactions. When combined with the extended range of possible values for each parameter, it resulted in a very large design space. It is impossible within the scope of this research project to comprehensively validate the entire design space against physical testing. Instead, a randomised test programme is proposed to characterise the regression model's error.

7.1.1. Test Methodology

To validate the hydraulic presses' operating settings, the first bearing of each batch is staked and then checked by pushing out the bearing from its housing. At a production rate of approximately two batches of staked bearings per week, this provided a source of randomised test data by which to validate the regression models against. As per current manufacturing practices, no additional information is recorded about the first bearing of each batch other than the staking force required to meet the drawings stated pushout strength. Therefore, new process controls were introduced for the machine operators to follow to collect the necessary information which is summarised in Table 21. The overall process follows four stages: physical measurements of the bearing and housing, staking the bearing, post-stake torque check, and pushing out the bearing from its housing.

Table 21: Summary of measured parameters for the staking trials.

Bearing Geometry	Housing Geometry	Staking Outputs
• Outer Race Diameter • Outer Race Width • Groove Pitch • Groove Depth • Pre-Stake Torque	• Inner Diameter • Outer Spherical Diameter • Housing Width • Chamfer Depth	• Staking Force • Post-Stake Torque • Pushout Strength

Machine operators were instructed to select a random bearing and housing to avoid any potential risk of systematic error or human bias interfering with the staking trials. Once the first-off pair had been marked, all required dimensions were taken with pre-stake torque measured using a mechanical dial torque clock (Figure 105). The calibration certificates for all torque gauges are presented in Appendix E.

Figure 105: Dial Torque Clock (RS Components, 2023)

This process measuring torque is very sensitive to operator inputs and is affected by several factors such as rotation speed (sliding velocity) and the misalignment of the bearing during rotation. It is common for bearings to achieve a very high torque before rotation of the bearing is achieved (breakout torque) before settling down to a much lower torque whilst rotating (running torque). Operators have observed the breakout torque to vary considerably between bearings and to be sensitive to changes in ambient temperature, humidity, and the duration of time that the bearing has been stationary between rotations. This is thought to be a result of the phenolic resin in the liner adhering to the inner ring. By contrast, the running torque is more consistent and is the standard method for torque measurements. To maintain consistency across operators, the standard SKF process is to break out the bearing by rotating it three times before measuring the torque whilst rotating at a constant speed of approximately 0.25 revolutions per second. For this investigation both the pre and post-stake torque was measured following SKFs standard process.

7.1.2. Staking Force Calibration

A hydraulic hand press is used to pushout the bearing with a standalone load cell to measure the pushout strength (Figure 106). The display for the load cell is set to hold at the maximum force achieved during pushout and is calibrated and maintained by SKFs standards and compliance department (Appendix E).
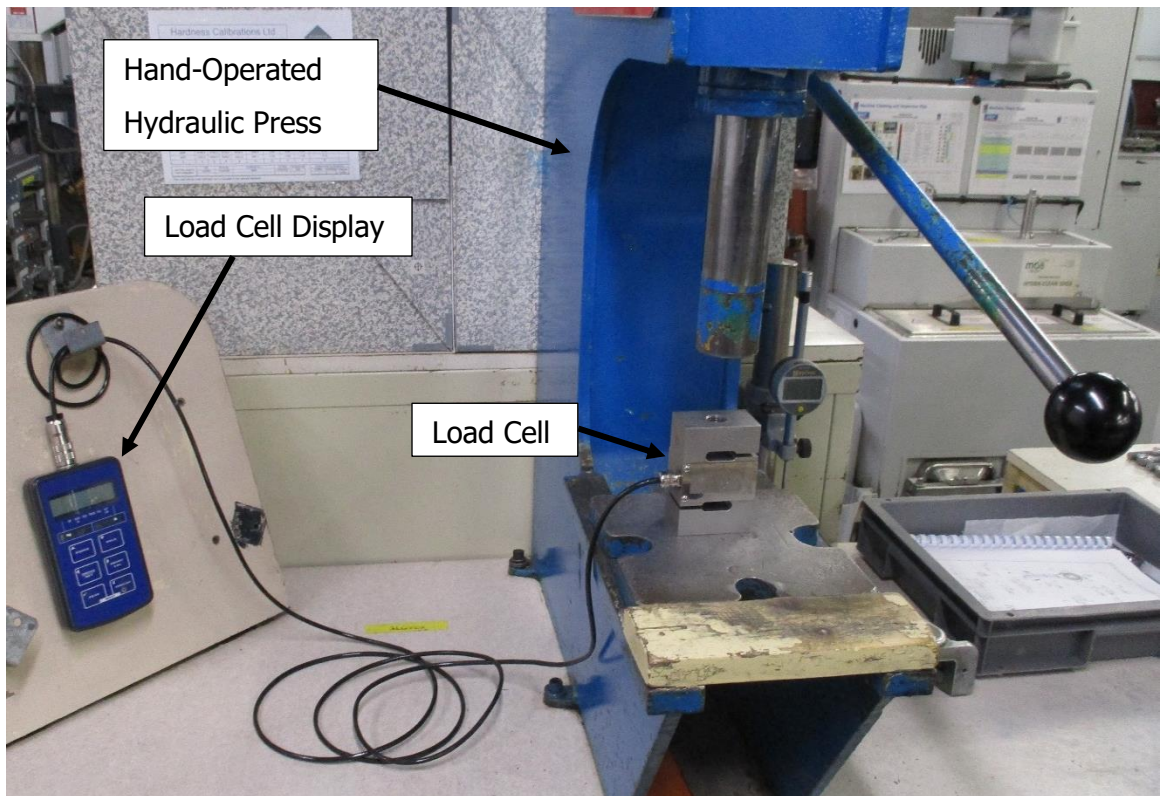
Figure 106: Pushout Strength test setup.

The hydraulic press used for staking relies on a simple diaphragm pressure gauge that is not calibrated (Figure 107). Pressure is set by winding in a screw on the side of the machine until the desired indicated force is shown on the dial. Once the correct force is set the guard cage is brought down, which lowers the hydraulic ram and stakes the bearing. Calibration of the gauge is not a concern for SKF because if the resulting pushout strength is not sufficient, then the staking force is increased by 0.5 tonnes and re-staked. The absolute value of the staking force is functionally irrelevant with the indicated staking force from the dial acting as little more than a rough estimate. However, to validate the regression models it is necessary to know the absolute staking force and required calibrating the press.

Figure 107: (A) Staking Press, (B) Staking tonnage dial, (C) Staking Region and guides.

To calibrate the staking press, a pancake load cell was inserted below the lower staking anvil and was connected to a strain data logger via a full-Wheatstone bridge to record the force from the load cell in mV (Appendix E). A sweep was carried out from the minimum to the maximum capacity of the press (4-38 tons indicated), and it was found that the press over-predicted the absolute staking force by an average of approximately 20% (Figure 108). A lookup table was produced from this data to convert the indicated staking force to the absolute staking force (Appendix D).
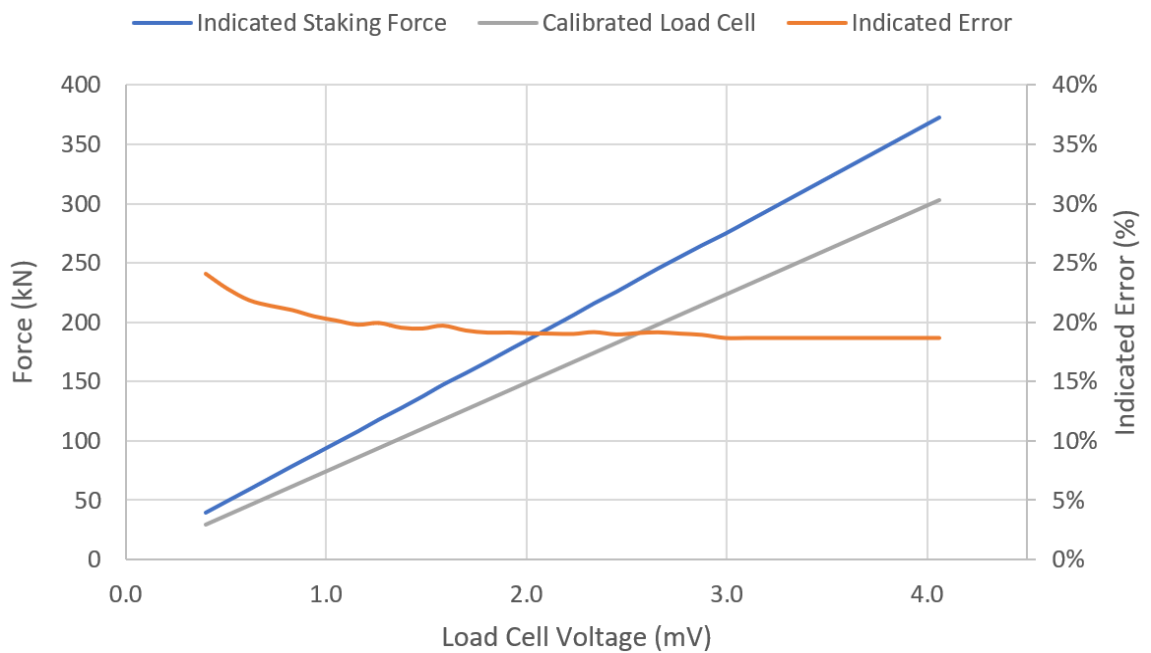
Figure 108: Calibration results for the staking press.

7.2. Type 3 Results

Over a period of 18 months, 153 batches of bearings were staked into a rod end of which 45 were categorised as Type 3 bearings. For each of these bearings, the variance of each of the six input variables was plotted against the input range (Design Space) of the Type 3 regression model (Figure 109). By visual inspection, all parameters except for Outer Diameter and Pre-Stake Torque, and Groove Pitch have good coverage across the entire design space. The coverage of the design space was quantified by comparing the input range of each parameter against the maximum and minimum experimental data points. This resulted in a coverage of 76% with the individual coverage for each parameter shown in Figure 110.
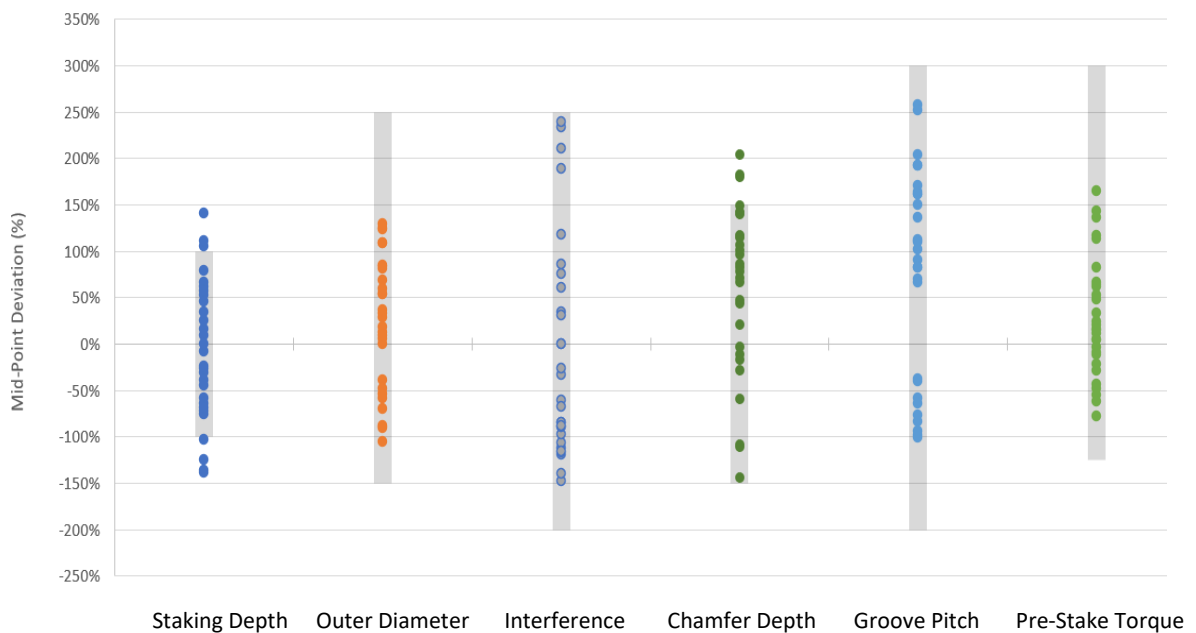
Figure 109: Staking trials parameter variance for Type 3 bearings. Grey bars represent the maximum and minimum limits for each of the six inputs parameters.

The experimental data collected from the staking trials are representative of the natural variation of production bearings. From Figure 110, the Pre-Stake Torque for these bearings only covered 48% of the regression model's design space, with similar coverage seen for the Outer Diameter and Groove Pitch. As will be discussed in greater detail in Section 8.3.3, this disparity is due to both the attempt to cover all possible bearings from SKFs design catalogue and the infrequency of manufactured bearings with those extreme geometries.
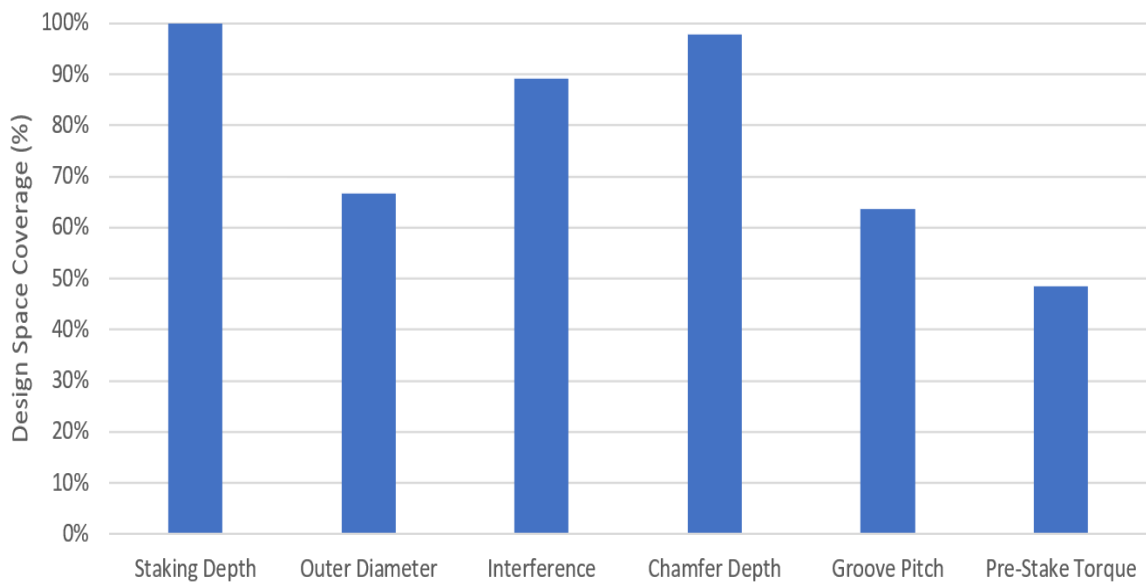
Figure 110: Coverage of the design space for each input parameter.

To improve the test data coverage against the model design space, historic staking records from SKF were requested. However, the data SKF have collected prior to the start of this thesis only included the machine settings for the first successful stake of each batch. These production logs contained; batch number, staking tonnage (±0.5 tonnes), pushout strength (±100 lbs), and if the post-stake torque was over, under, or within tolerance. This make using the historic SKF data unusable for the purpose of assessing either pushout or post-stake torque models with the main limitations summarised as follows.

- Staking tonnage cannot be used as an input for either model its uncertainty (±5kN) would result in an output uncertainty for either the pushout strength or post stake too large to meaningfully compare against.

- Pushout strength uncertainty (±450N) is too large to compare the pushout strength model against

- There is no quantifiable post-stake torque data.

- No measurements of the bearing and housing geometric features exist so only the nominal drawing value could be used as inputs: further increasing the uncertainty of each models' predictions.

7.2.1. Pushout Strength Correction

Each staked bearing from the staking trials was compared against the prediction from the Pushout Strength regression model to evaluate its accuracy. Across 45 Type 3 bearings, the average error was found to be +5% with a standard deviation of ±7% with no correlation with run order as shown in Figure 111.
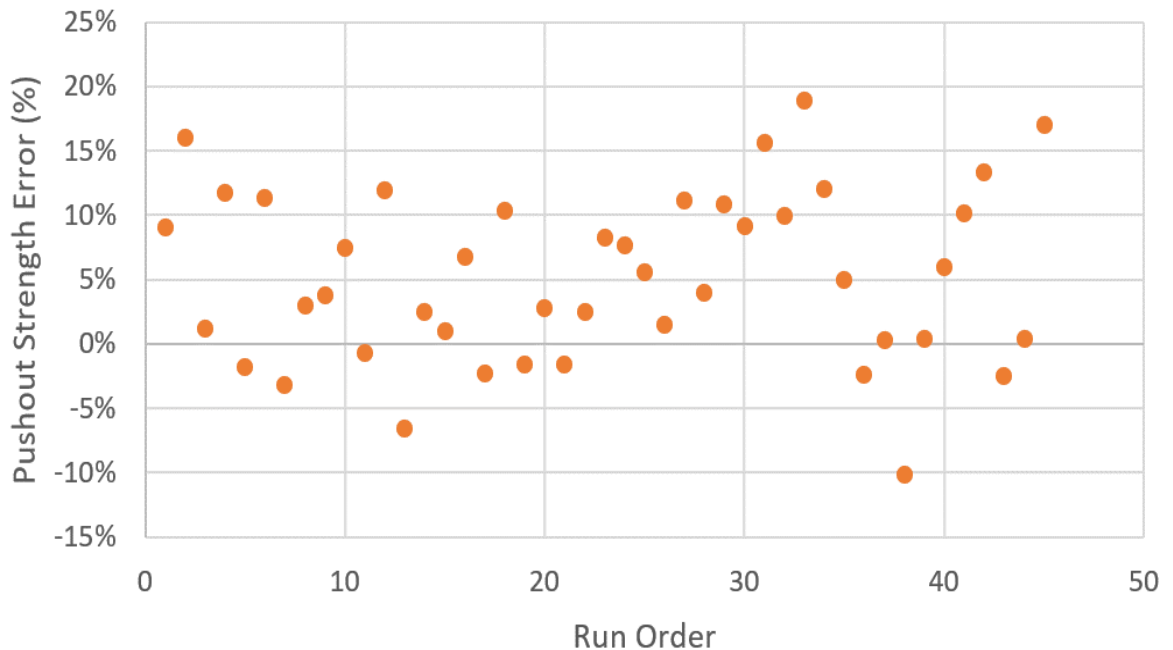
Figure 111: Staking trials raw error for the pushout strength of Type 3 bearings. Positive error represents an over-prediction of the model relative to experiemtal results.

There are many potential sources of error that could have originated from either the development of the regression model or experimental measurements. Whilst some of this uncertainty can be attributed to random error, any systematic error that can be identified can be corrected to reduce the model's error. For example, by reordering the experimental results from Figure 111 by Anvil Staking Depth, a positive trend can be observed whereby the pushout error increases with increasing Anvil Staking Depth (Figure 112). This correlation is likely due to the inability for the FEA model to accurately capture tearing at the staking lip root (this limitation is discussed in more detailed in 8.3.1). During pushout load proof testing, this failure mode is often seen on bearings with a large staking lip formed under high staking forces (Figure 95). Under these conditions, the larger size of the staking lip will cause for it to get caught on the housing chamfer instead of deforming, tear at the staking lip's root, and resulting in a premature failure of the joint at a lower than predicted pushout strength. In the staking FE model, staking force is controlled by the anvil staking depth which explains the increased pushout strength error correlation with anvil staking depth.
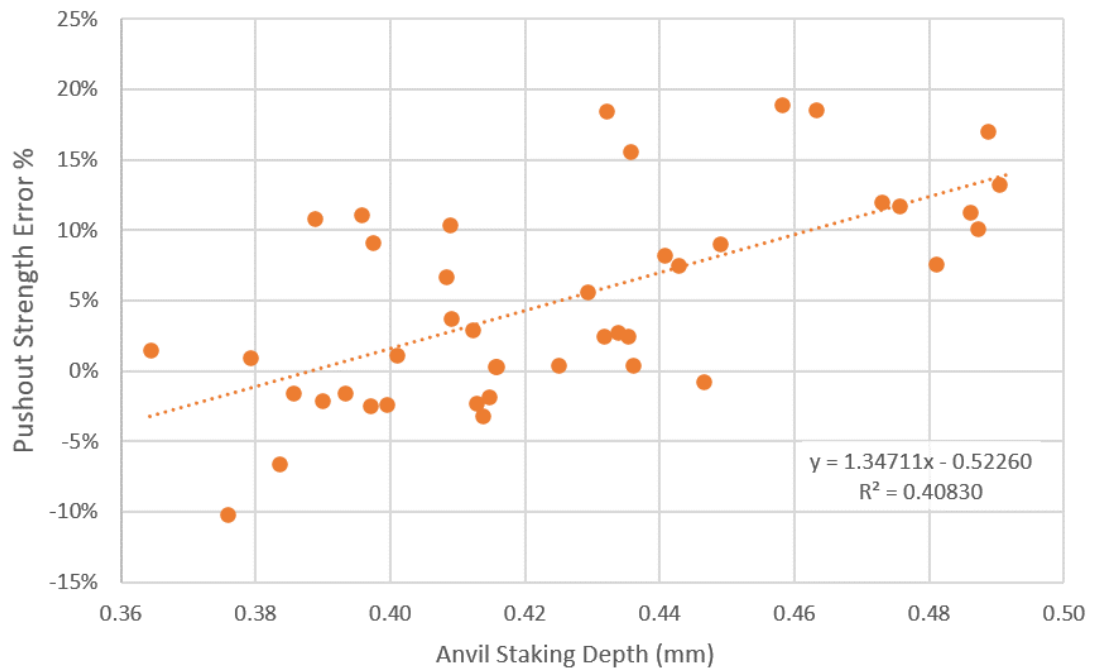
Figure 112: Pushout Strength error as function of Anvil Staking Depth. Positive error represents an over-prediction of the model relative to experiemtal results

Because of the limited sample size and the random error inherent within the staking trial results, there is a large risk of over-correction when applying correction factors to the raw data. This can occur when correction factors are chosen that are not statistically significant and result in poorer performance of the final model in regions of the design space that have not yet been tested. To reduce this risk, several statistical tests were introduced to validate the appropriate correction factors.

R-Squared Adjusted

R-Squared is a prediction of how well the model fits the data with 1 being perfect correlation and 0 no correlation. R-Squared Adjusted compensates the raw R-Squared value based on the number of terms in the model, as R-Squared increases with an increasing number of terms. R-Squared Adjusted is used to compare correlations between models.

R-Squared Predicted

R-Squared Predicted determines how well a model predicts the response to new observations. It is equivalent to systematically removing observations from the raw dataset and comparing the change in the resulting regression model correlation. If a large difference is found between R-Squared Adjusted and R-Squared Predicted, then it indicates a model that is over-fit and contains terms that are not important.

T-Value

T-value is a measure of the ratio between the coefficient within a model and its standard error. Magnitudes greater than 2 are considered sufficient to reject the null hypothesis.

Variance Inflation factor

The Variance Influence Factor (VIF) describes how much multicollinearity (correlation between predictors) exists in the regression analysis (Table 22). Multicollinearity can cause an increase in the variance of regression coefficients and make it difficult to evaluate the individual impact of each predictor. A VIF value greater than 5 suggests that the regression coefficient is poorly estimated due to severe multicollinearity.

Table 22: Guidelines for interpreting Variance Inflation Factor (VIF)

VIF	Status of Predictor
VIF = 1	Not Correlated
1 < VIF > 5	Moderately Correlated
VIF > 5	Highly Correlated

Minitab (2020b) was used to analyse the Pushout Strength error and was programmed to limit the regression analysis to 2-way and 2nd order interactions to reduce the impact of multicollinearity and possible model over-fit. When left at the programme defaults of 4-way and 4th order terms with a P-value stepwise regression limit of 0.15, Minitab produced a regression model with 22 terms that reduced the error for the pushout strength from 9±7% to 0±3%. The regression model achieved an R-squared adjusted value of 96% but a significantly lower R-squared predicted value of 58%. With the majority of 2nd, 3rd, and 4th order terms having VIF values greater than 5, the Minitab default settings resulted in a regression model with significant multicollinearity and a high risk of over-fitting.

When limited to 2-way and 2nd order interactions with a P-value stepwise regression limit of 0.05, the following regression model correction was produced along with its respective coefficient analysis (Table 23) and model summary statistics (Table 24).

$$Pushout\ Error\ (\%) = 0.883 - 0.819 * Groove\ Pitch\ + 1.090\ Anvil\ Staking\ Depth \qquad [\ 55\ ]$$

Table 23: Pushout strength error coefficient analysis.

Term	Coefficient	Coefficient Standard Error	T-Value	P-value	VIF
Constant	0.883	0.214	4.12	3.6×10^{-4}	-
Groove Pitch (mm)	-0.819	0.126	-6.49	8.4×10^{-7}	1.01
Anvil Staking Depth (mm)	1.090	0.137	7.98	2.4×10^{-8}	1.01

Table 24: Model summary statistics.

Mean	Standard Error	95% Confidence Interval	R-Squared Adjusted	R-Squared Predicted
0.00%	3.41%	6.70%	79.6%	75.7%

As can be seen from Table 23 and Table 24, the analysis of the residual errors from the raw pushout error staking trails was found to be significantly correlated to both the Groove Pitch and Anvil Staking Depth as per the five introduced statistical tests.

1) All terms achieved an absolute T-Value greater than 2 indicating that the coefficient of each term is significantly relevant to the uncertainty of the coefficient

2) All terms had a P-Value of ≈ 0 indicating with almost absolute certainty that each term can reject the null hypothesis

3) VIF values of 1.01 for both Groove Pitch and Anvil Staking Depth demonstrate almost no collinearity between the two terms

4) The correction model achieved an R-Squared Adjusted result of ≈ 80% indicating that the majority of the variance in the pushout staking results can be explained by this model

5) An R-Squared Predicted value of ≈ 76% represents a 4% drop relative to the R-Squared Adjusted result, indicating a minimal risk of model over-fit.

By applying the correction model to the output of the staking calculator tool, the error in the prediction for the pushout strength of Type 3 bearings was reduced from [REDACTED] to 0% ± 3.4%. Both the raw and corrected results compare favourably to SKFs internal pushout tool [REDACTED] which for the same data set had an error of [REDACTED] (Figure 113). The significant improvement of the mean error to near 0% was expected however because the same data that was used to determine the correction factors was also used to assess the model's corrected performance. Whilst a 4% decrease in the R-Squared Predicted value indicates a low risk of over correlation with regards to the model's random error, there still remains a degree of uncertainty as to the true mean error of the corrected model if it was assessed with an additional set of test data from future staked bearings. A corrected model error of 0% ± 3.4% represents a potentially unrealistic best-case scenario.

To address this concern and to assess the models true mean error, the model correction process was repeated five times with only half of the test data was used for training. In each instance, 22 test results were randomly selected from the total data set and a correction equation was derived. The remaining 23 test results were used to assess the fit of the corrected model. Results from this randomised testing are shown in Table 25.

Table 25: Randomised model correction performance.

Model	Description	Model Fit
Raw Pushout Model	No correction. All 45 test results used for assessment	5% ± 7%
Corrected (Full)	All 45 test results used for both model correction and assessment	0% ± 3.4%
Corrected (Half) 1	22 Randomly selected test results for model correction. Assessed on remaining 23.	-0.5% ± 4.1%
Corrected (Half) 2		-0.9% ± 3.6%
Corrected (Half) 3		1.0% ± 4.7%
Corrected (Half) 4		0.6% ± 4.0%
Corrected (Half) 5		0.1% ± 4.1%

By running a Monte Carlo simulation of 10,000 runs for each corrected half model, the uncertainty of all five models were be combined to give an average error of 0.1% ± 4.2%. As expected, the performance of the corrected half models is worse than the corrected full model but the difference between them is comparatively small especially when compared to the raw model's uncertainty. Most importantly, the zero mean error of the corrected full model does

not show signs of significant over-fit as near zero mean errors seen with all half models, with an averaged half model mean error of 0.1% and a maximum 1.0% across all 5 tests. Therefore, the conservative and statistically rigorous approach taken with the corrected full model has been validated and indicates that the true mean error must be close to zero.

Figure Redacted
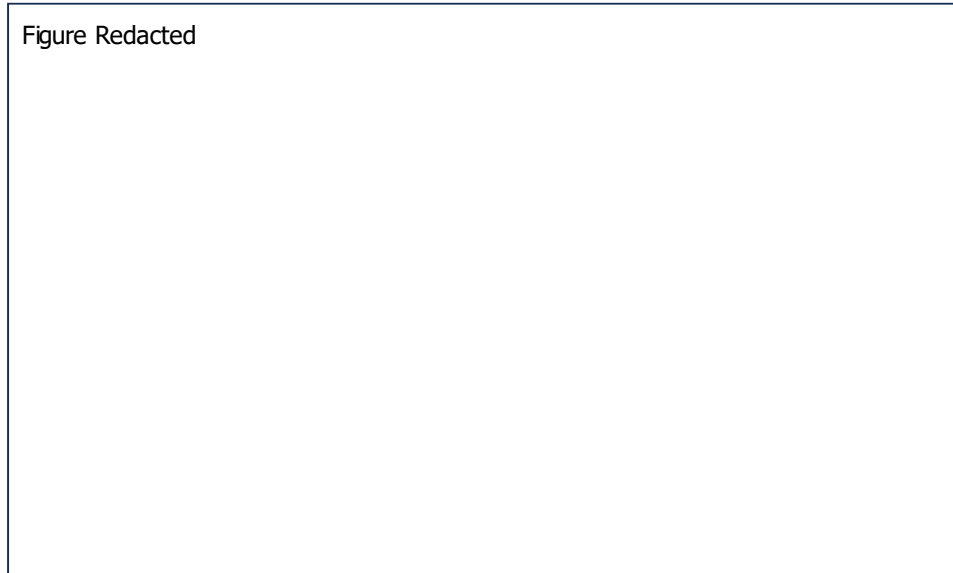
Figure 113: Pushout Strength error Comparison between the current SKF staking guidance (ETI D18), raw staking trials data and after model correction.

This process was repeated for the Type 1 and 2 models with similar behaviour seen between full and half corrected models. A summary of their performance shown Table 26.

Table 26: Model comparison for pushout strength (95% confidence intervals)

	Pushout Strength Error		
	Corrected Model (Full)	Corrected Model (Half)	SKF Internal Tool
Type 1	0.0% ± 5.1%	-0.1% ± 7.1%	[REDACTED]
Type 2	-0.02% ± 6.3%	-0.2% ± 7.9%	[REDACTED]
Type 3	0.0% ± 6.7%	0.1% ± 8.4%	[REDACTED]

7.2.2. Post-Stake Torque Correction

For the correction of the Post-Stake Torque model, the same methodology and process were used as that for the Pushout strength. Carrying out a 2-way and 2nd order regression analysis with a P-value stepwise regression limit of 0.05 resulted in the following regression equation along with its respective coefficient analysis (Table 27) and model summary statistics (Table 28).

$$Post\ Stake\ Torque\ Error\ (Nm) = -1.088 + 0.096 * Post\ Stake\ Torque + 70.0 * Interference \qquad [\ 56\ ]$$

Table 27: Post Stake Torque error coefficient analysis.

Term	Coefficient	Coefficient Standard Error	T-Value	P-value	VIF
Constant	-1.088	0.165	-6.61	9.6×10^{-7}	-
Post-Stake Torque (Nm)	0.096	0.017	5.78	≈ 0	1.11
Interference (mm)	70.0	12.2	5.76	7.2×10^{-6}	1.11

Table 28: Model summary statistics.

Mean (Nm)	Standard Error	95% Confidence Interval	R-Squared Adjusted	R-Squared Predicted
0.00	0.503	0.986	94.5%	93.1%

As with the Pushout Strength correction, each of the five statistical tests were satisfied with a particularly strong R-Squared Adjusted value of 94.5%. When paired with a small decrease of 1.4% to an R-Squared Predicted value of 93.1% it can be asserted that there is a high degree of confidence between the correction model and the Post-Stake Torque error.

The presence of the Post-Stake Torque term in Equation 56 implies a scaling issue within the original regression model that is not associated with any of the model's input parameters. This 9.6% scaling issue could be linked to multiple different sources, but the most likely cause is an error in the compressive stiffness of the composite liner. The contact pressure between the liner and inner ring (and therefore the torque of the staked bearing) scales linearly with liner stiffness.

By applying the correction model to the output of the staking calculator tool, the error in the prediction for the Post-Stake Torque of Type 3 bearings was reduced from 0.5 ± 0.9 Nm down to 0 ± 0.5 Nm as shown in Figure 114. SKFs internal staking tools do not provide any prediction for the Post-Stake Torque of their bearings and therefore unlike the pushout load, there is no baseline model to compare against. Similar to the pushout strength full corrected model (7.2.1) the post-stake torque model was corrected against all 45 test results and produced a zero mean error. To check for model overfit, the same half model correction was carried out across five tests as done with the pushout strength model (Table 30).

Table 29: Randomised model correction performance.

Model	Description	Model Fit (Nm)
Raw Post-stake Torque Model	No correction. All 45 test results used for assessment	0.51 ± 0.92
Corrected (Full)	All 45 test results used for both model correction and assessment	0.00 ± 0.49
Corrected (Half) 1		-0.10 ± 0.57
Corrected (Half) 2		0.21 ± 0.62
Corrected (Half) 3	22 Randomly selected test results for model correction. Assessed on remaining 23.	0.18 ± 0.65
Corrected (Half) 4		-0.05 ± 0.57
Corrected (Half) 5		0.27 ± 0.71

By running a Monte Carlo simulation of 10,000 runs for each corrected half model, the uncertainty of all five models were be combined to give an average error of 0.08 ± 0.64 Nm. Just as found in 7.2.1, the difference between the full and half corrected models is comparatively small when compared to the raw model. The zero mean error of the corrected full model does not show signs of significant over-fit as near zero mean errors seen with all half models, with the only slight exception being Test 5 with a 0.27 Nm mean error. This validates the full corrected model and demonstrates that there is very little evidence of model over-correction.
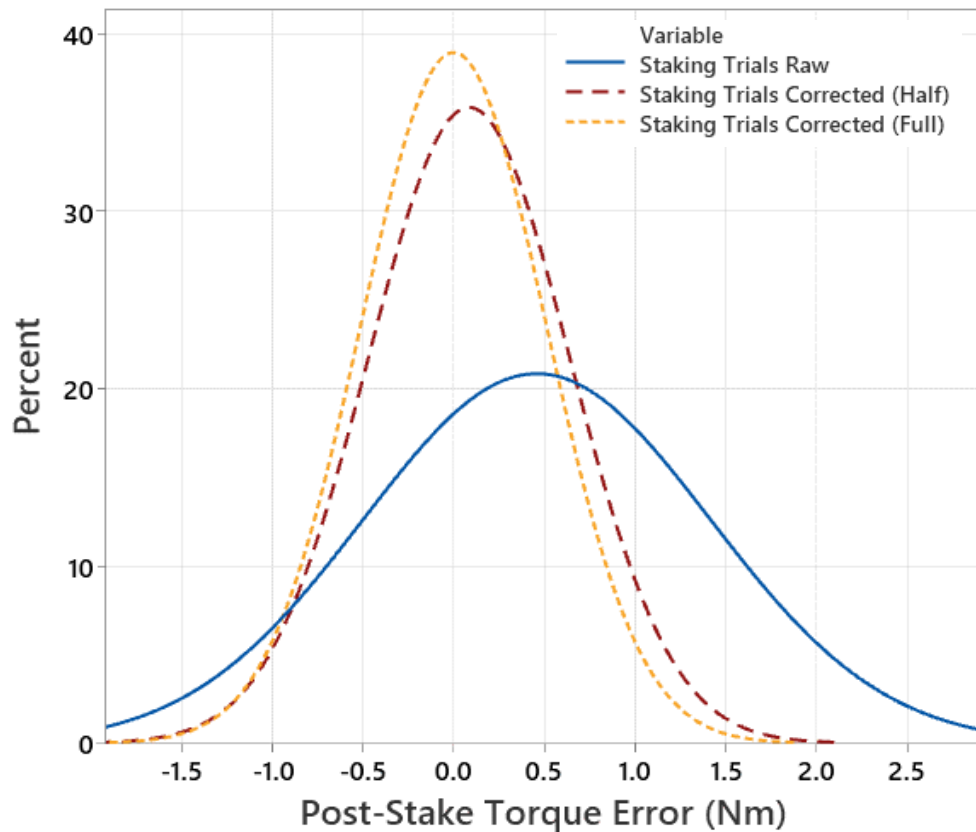
Figure 114: Post-Stake Torque error comparison between the raw staking trials data and after model correction.

An analysis of SKFs drawing tolerances found that the variance of the Post-Stake torque manufacturing tolerance was on average [REDACTED] with a maximum and minimum tolerance of [REDACTED] (Figure 115). Using the smallest tolerance of [REDACTED] results in an 11% probability that a Type 3 bearing will exceed the Post-Stake Torque drawing tolerance. A more reasonable estimation of the failure rate of the Type three model was found by simulating a normal distribution for the drawing tolerance of [REDACTED] and comparing it against the Type 3 model distribution. A Monte Carlo simulation of 100,000 test runs was carried out with the relative frequency of events where the Type 3 model exceeded the drawing tolerance and converged to a probability <0.2% (Figure 116). This equates to a failure rate of approximately 1 in 500. This process was repeated for the Type 1 and 2 models with a summary of their performance shown in Table 30.

Figure Redacted
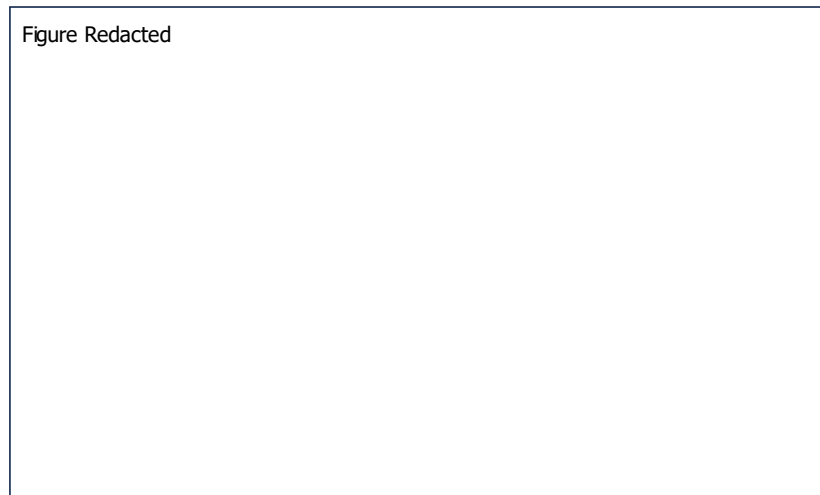
Figure 115: Normal distribution of the Type 3 regression model and SKFs Post-Stake torque drawing tolerances. Only positive torque values are shown as the two distributions are symmetric about the zero point.
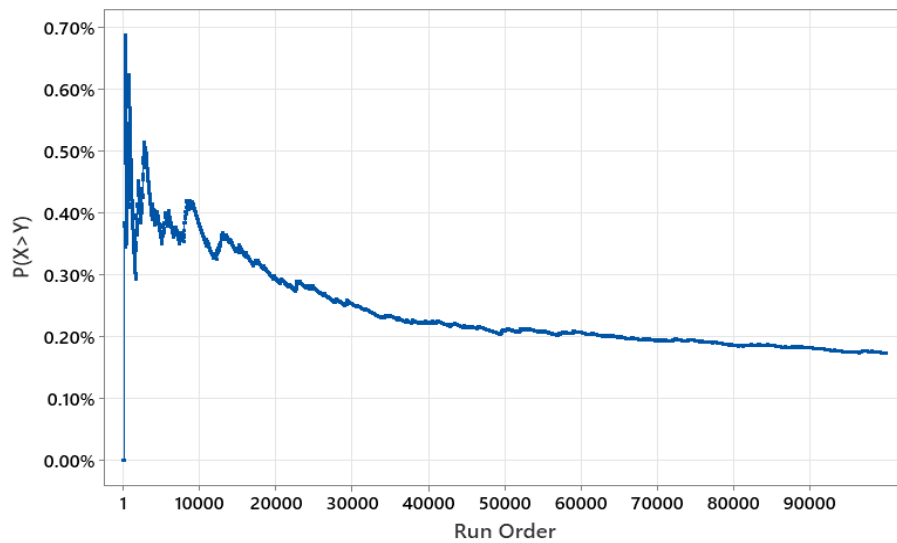
Figure 116: Monte Carlo simulation over 100,000 runs showing the relative frequency that a prediction from the Type 3 model P(X) will be greater than the SKF design tolerance P(Y).

Table 30: Model comparison for post-stake torque (95% confidence intervals)

	Post-Stake Torque Error	SKF Engineering Drawing Tolerance (Min-Max)	Failure Rate
Type 1	0.00 ± 0.60Nm	[REDACTED]	< 6.0%
Type 2	0.02 ± 0.59Nm	[REDACTED]	< 2.5%
Type 3	0.00 ± 0.98Nm	[REDACTED]	< 0.2%

7.3. Implementation and Parameter Analysis

The development and validation of both the Pushout Load and Post-Stake Torque regression models have resulted in a powerful staking tool that exceeds SKFs internal analysis tools. The accuracy of the staking tool provides confidence not only internally but also to customers as evidence of their deep understanding of the staking process. It also enables a "first-time-right" capability that can significantly reduce the likelihood of needing to re-work high torque bearings or the need for manufacturing trials for new bearing designs: both eliminating waste and reducing costs. However, the regression equations are not intuitive to read and an understanding of how each parameter affects the overall model is difficult to ascertain by visual inspection. The quality of a staked bearing can be characterised into one of four regimes as a function of the model's two outputs as shown in Figure 117. Regime 1: A staked bearing with both high torque and low pushout strength is the least desirable outcome as it fails to meet its minimum strength requirement and requires extensive reworking to bring the torque back within tolerance. This type of staked bearing is particularly challenging as the only fix for a bearing that is not able to meet the strength requirement is for the operators to stake the bearing to a higher load which further increases the post-stake torque. Regime 2 and 3: A staked bearing with either high post-stake torque or low pushout strength. In both conditions further reworking is required. Regime 4: A staked bearing with high pushout strength and low torque represents the ideal scenario.
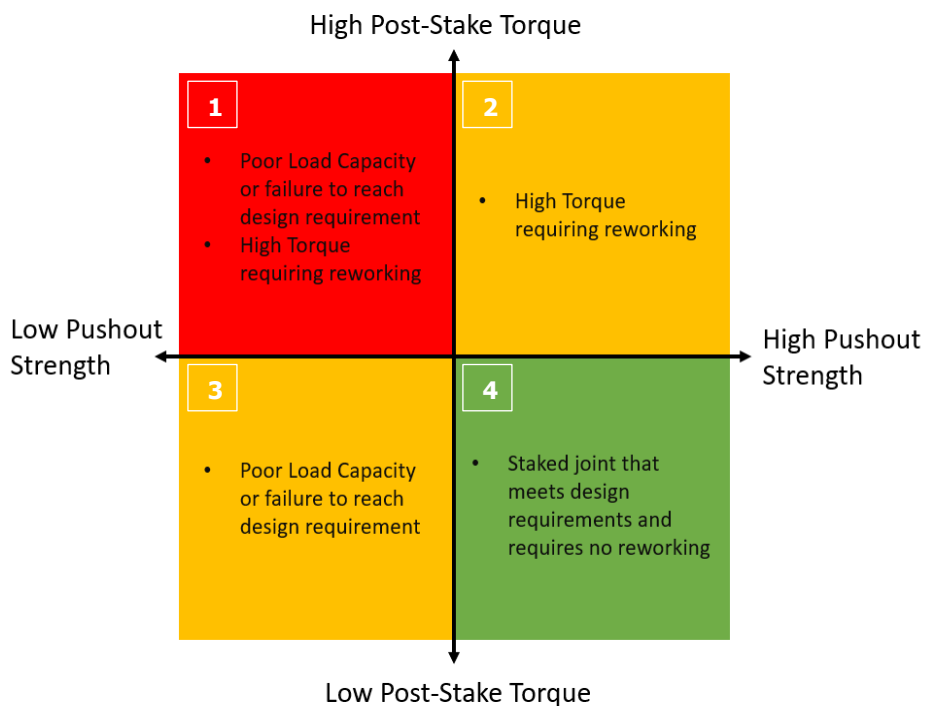
Figure 117: Quality characterisation of a staked bearing.

By using Figure 117 as a reference, each of the input parameters can be assessed for their impact on staking using the following process:

- A "nominal" bearing is input into the staking tool with each parameter is set to the centre of their respective input ranges.

- The staking force is then increased from its minimum to its maximum value (in 25% increments) to create a profile relating the Pushout Strength to the Post-Stake Torque as a function of the staking force.

- This is repeated for each input parameter in turn at both its respective minimum and maximum input values.

- A graph is then produced with contour lines of constant staking force and constant parameter input values.

The result of this analysis is shown in Figure 118 through Figure 122. As a visual aid, the contour lines where smoothed using Excel's cubic spline fit function to help the user identify trends in how each parameter impacted the staking process. However, because there is only computed data at each contour intersect, caution should be taken when interpolating along a contour line and it is unadvisable to interpolate between two contours simultaneously.

7.3.1. Chamfer Depth

As shown in Figure 118, increasing the chamfer depth both increases pushout strength and reduces the post-stake torque across nearly the entire range of staking force inputs, particularly at larger staking forces.
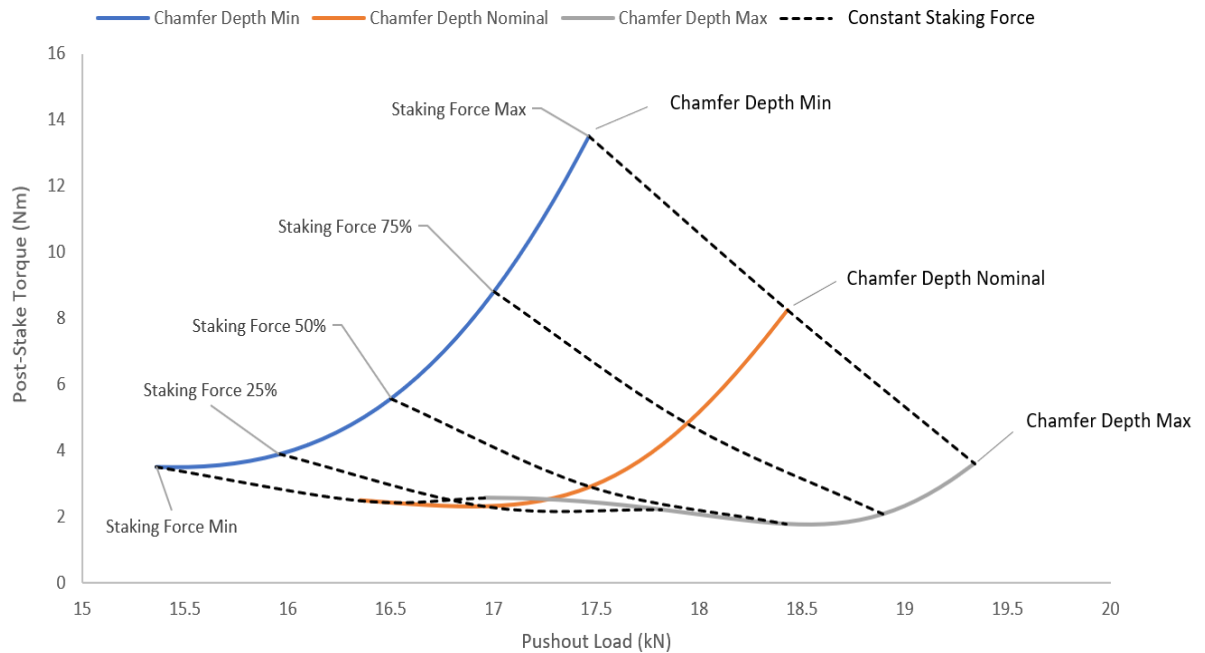
Figure 118: The impact of chamfer on bearing staking.

As the chamfer depth is decreased, the rate at which the post-stake torque increases with staking force also increases. When a bearing is staked, the unsupported region of the staking lip is deformed into the recess of the chamfer on the housing. By decreasing the chamfer depth and effectively raising the height of the chamfer root, the staking lip is better supported and a reduction in material flow into the housing chamfer is seen. Consequently, as the staking anvil is brought further down, and the staking force rises, more material will begin to flow inward towards the centre of the bearing and increase the contact pressure between the liner and inner ring. This reduced volume of the staking lip in the chamfered recess, and an increased inward flow of material towards the centre of the bearing, result in the undesirable condition of higher post-stake torque and lower pushout strength. By comparison to each of the other input parameters, chamfer depth is the only parameter capable of having a simultaneously positive impact on both the pushout strength and post-stake torque.

7.3.2. Interference Fit

As seen in Figure 119, increasing the interference fit between the bearing and housing results in a large increase in Post-Stake Torque in return for a relatively small increase in pushout strength.
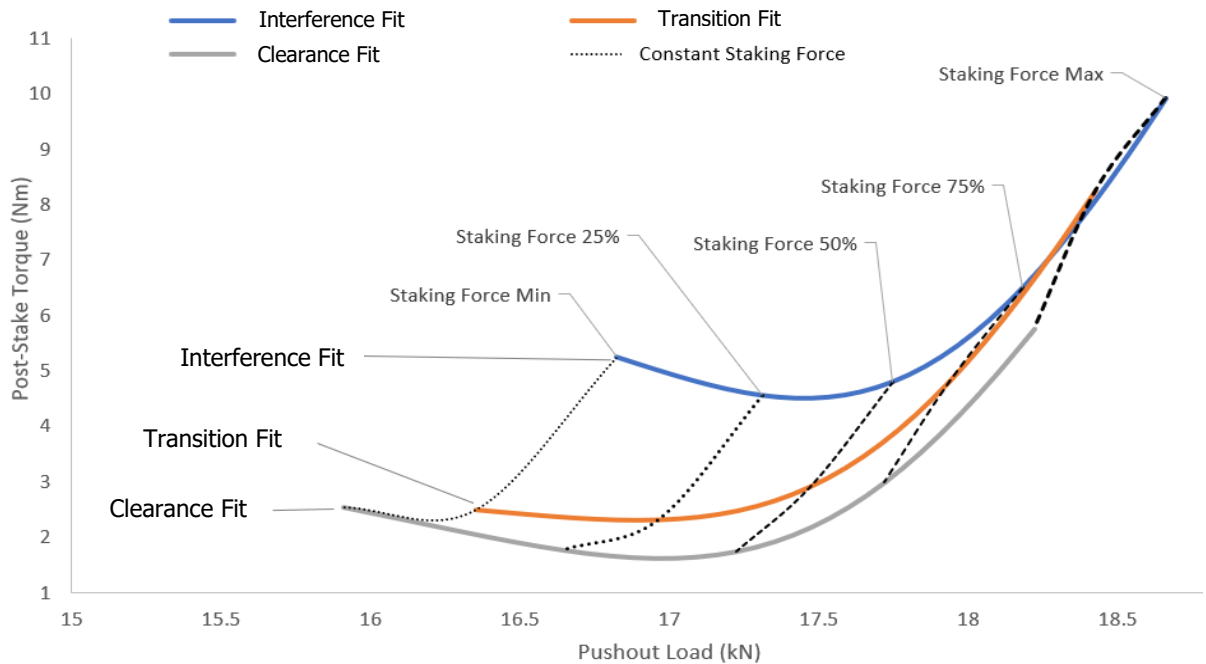
Figure 119: The impact of Interference fit on bearing staking.

The rise in pushout strength with interference fit is generated from the increased contact pressure between the parallel faces of the outer race and housing. When viewed in isolation, large interference fits are undesirable given the relatively small increase in pushout strength it provides. However, interference fits are required for all critical bearings (typically military applications or where the staked joint is a single point of failure) to reduce the risk of fretting damage and bearing backlash.

7.3.3. Bearing Outer Diameter

As seen in Figure 120, increasing the outer diameter of a bearing results in an increase in the pushout strength of the staked joint with minimum change in the post-stake torque below 50% staking force. Beyond 50%, post-stake torque increases with the outer diameter as a result of the increased contact area between the inner ring and the liner.
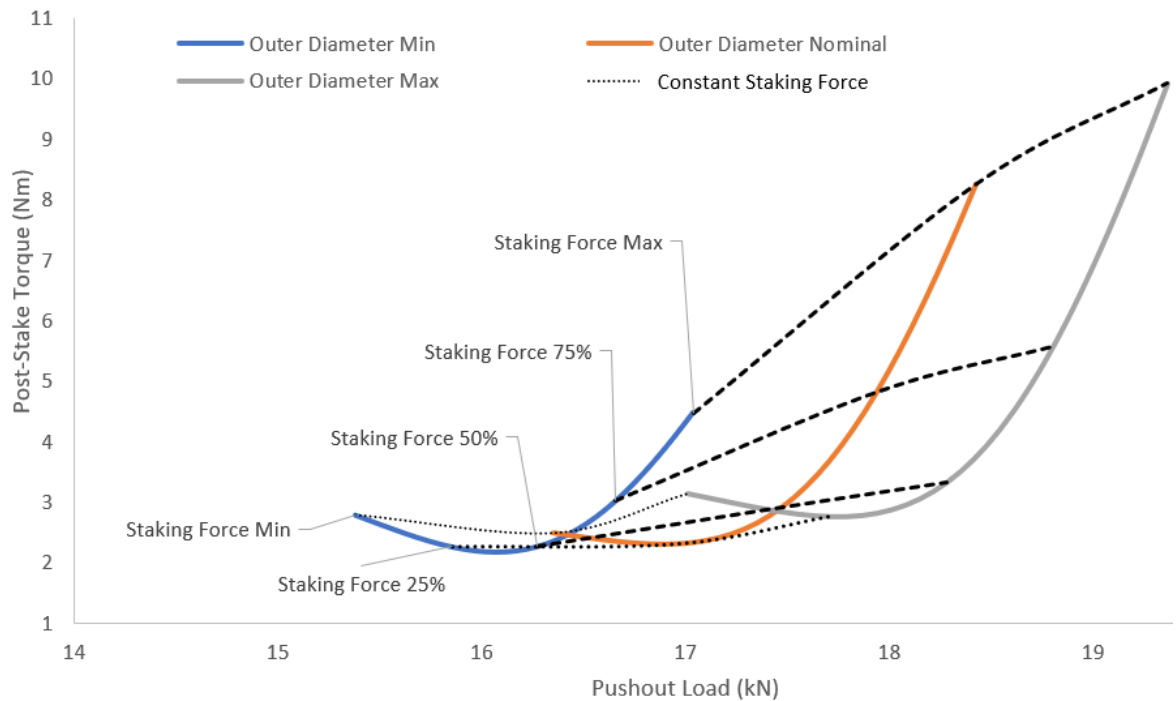
Figure 120: The impact of bearing outer diameter on staking.

If the design of the bearing and housing assembly permit, then for the same pushout strength requirement, a larger outer diameter staked at a lower staking force results in a lower post-stake torque.

7.3.4. Pre-Stake Torque

As seen in Figure 121, an increase in the Pre-Stake Torque increases the Post-Stake Torque of the staked joint across all staking force values, with little change in the pushout load. The Pre-Stake Torque can be controlled and adjusted prior to staking through rolling and end loading. However, this approach to torque adjustment works by manipulating the liner conformity which could have a negative impact on the performance of the regression model which was developed assuming perfect conformity of the liner.
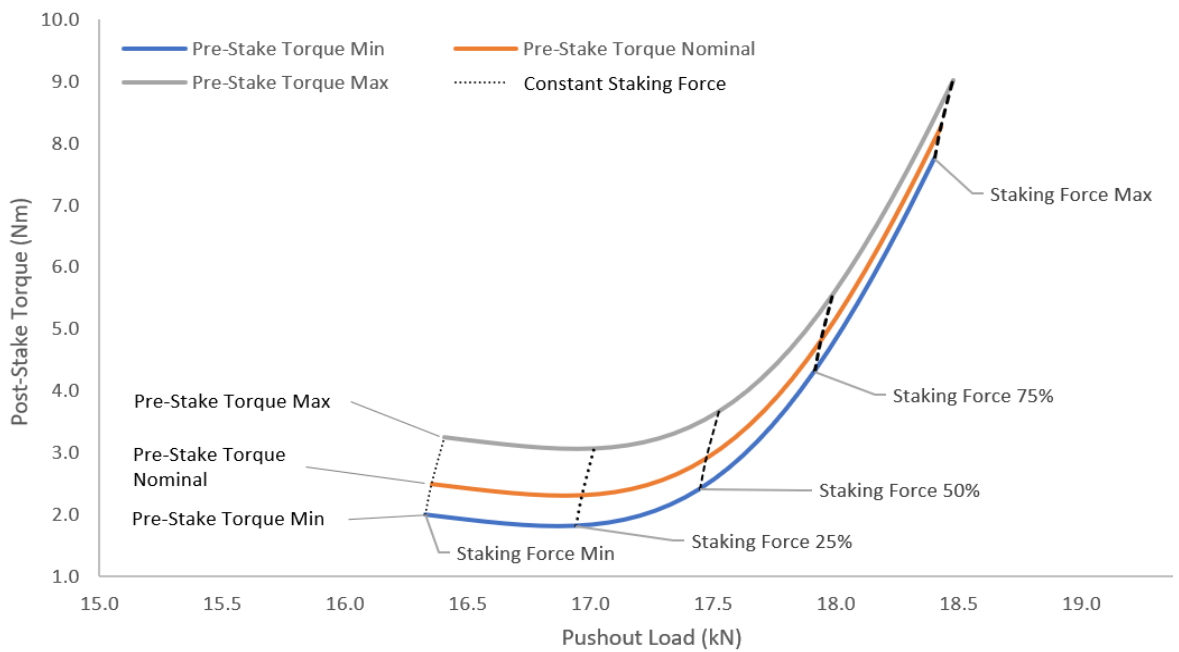
Figure 121: The impact of Pre-stake torque on bearing staking.

7.3.5. Groove Pitch

As seen in Figure 122, unlike all the previous input parameters there is no significant or consistent pattern when changing the value of the groove pitch. This result was to be expected as during the DoE screening process, groove pitch was estimated to be the least impactful parameter.
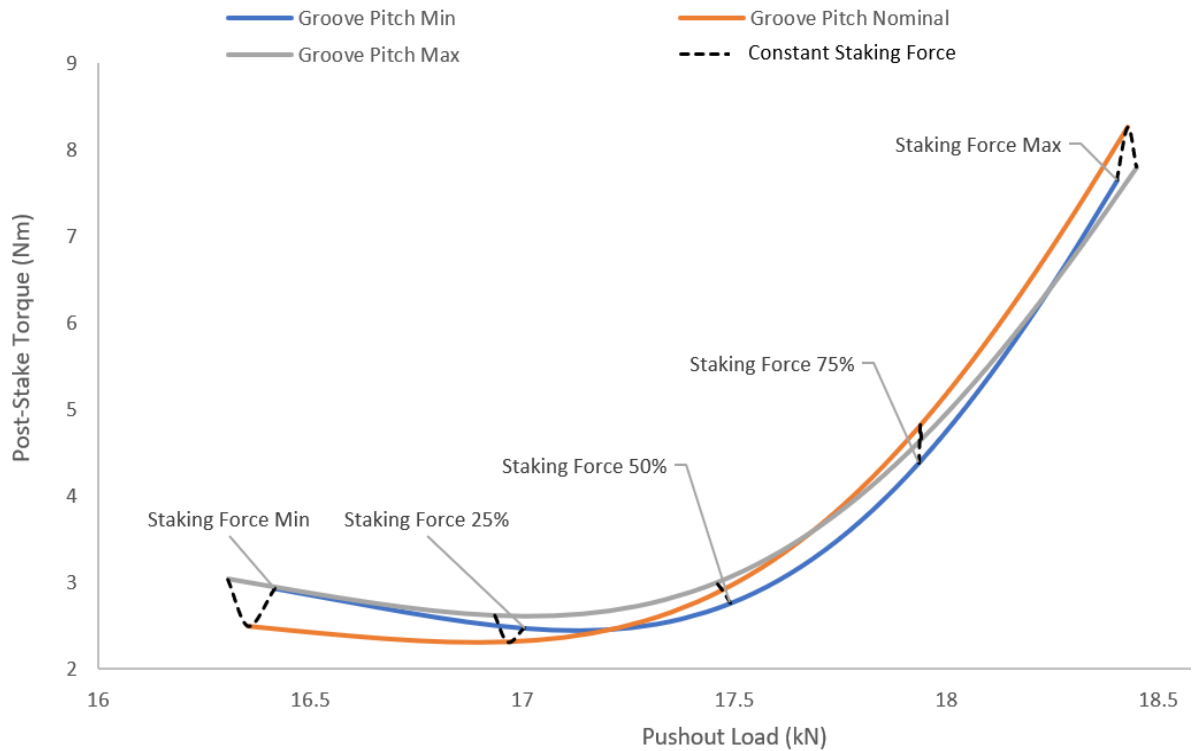
Figure 122: The impact of Groove Pitch on bearing staking.

7.3.6. Summary of Parameter Impact

Figure 123 details the relative impact of the six parameters when compared against each other. For the geometric parameters, comparative data was taken from the 50% staking force contour lines for Figure 118 through Figure 122. For the anvil staking depth parameter, the relative impact value was derived from the staking force maximum and minimum data points from the nominal contour lines of Figure 118. Included in Figure 123 are the relative impact predictions from the definitive screening test from Figure 96.
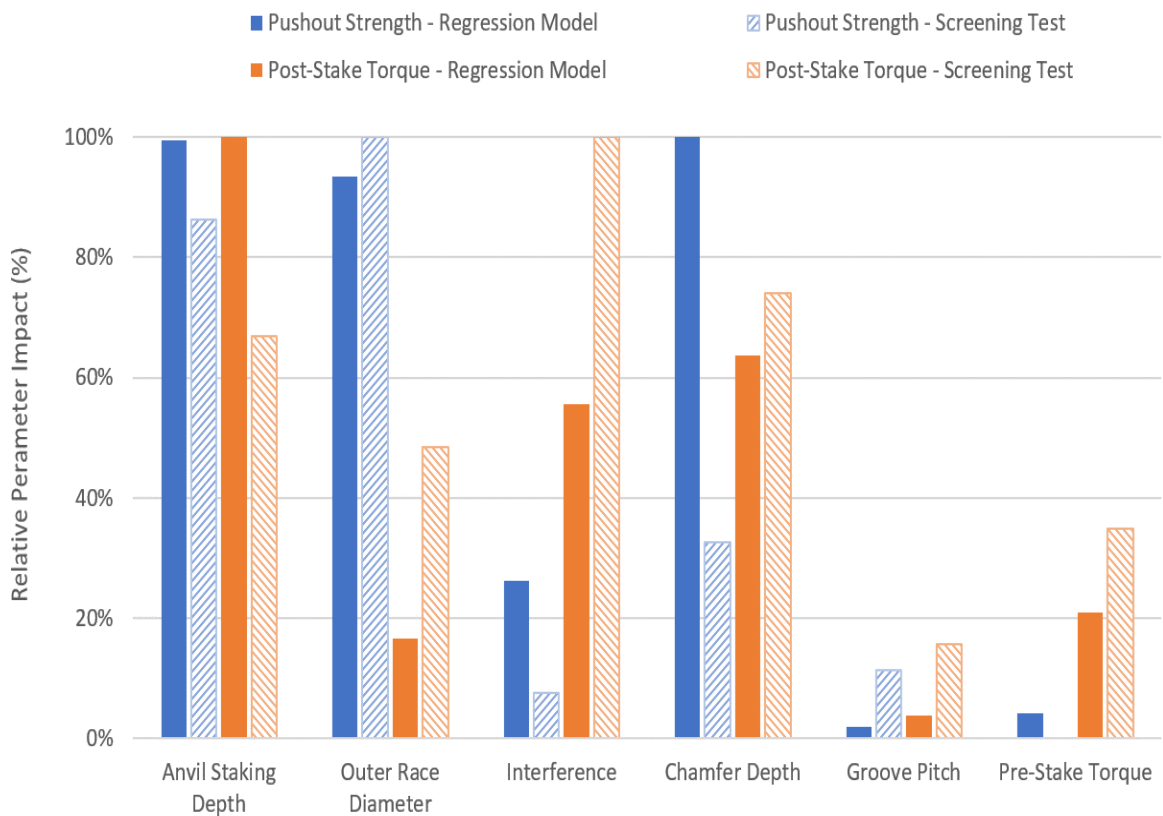
Figure 123: Relative impact of each of the parameters compared against the prediction from the screening tests.

The relative impact of the parameters for both regression models was in good agreement with the predictions from the definitive screening test. However, two significant outliers were found with the impact of the interference fit on post-stake torque and chamfer depth on pushout strength.

Whilst many potential sources could have caused this discrepancy, the most likely reason is due to the aliasing present between second-order terms with the resolution IV screening test. Except for these two parameters, the parameters that scored highly in the screening test remain impactful after validation of the full factorial DoE (Figure 124), which also applies to parameters that scored low in the screening test. This validates the process by which the parameters for the Virtual-DoE were selected and gives high confidence that no significant parameters may have been eliminated in the screening test.
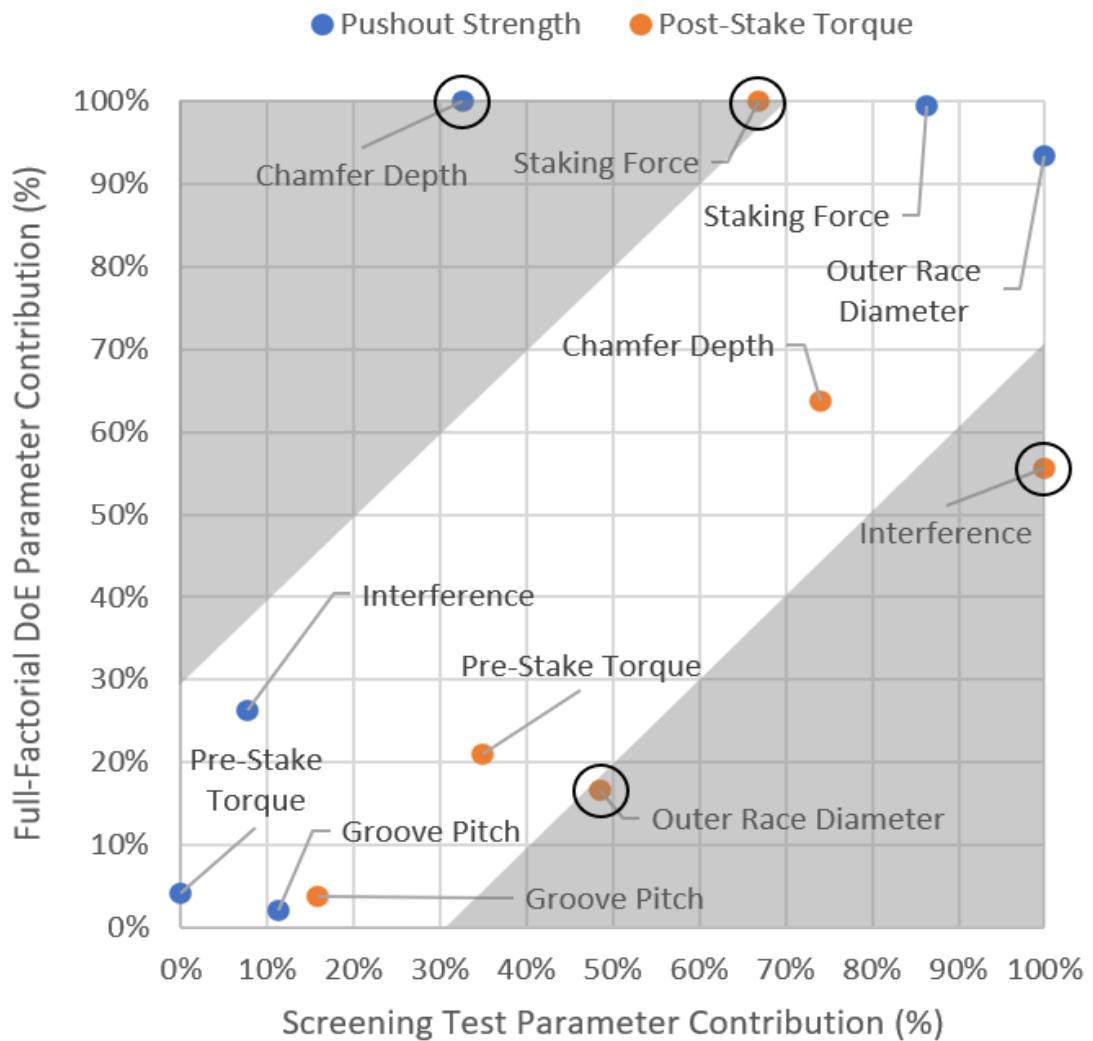
Figure 124: Comparison between screening test and full-factorial parameter contribution. Shaded regions represent a shift of more than 30% with outliers circled.

7.4. Sensitivity Analysis.

A sensitivity analysis was carried out on the corrected regression models to understand how manufacturing tolerances could influence the post-stake torque and pushout strength of a staked bearing. This was achieved by running a Monte Carlo simulation with the value of each parameter randomised in turn between its manufacturing tolerance limits. A list of the manufacturing tolerances for a Type 3 bearing is shown in Table 31.

Each of the geometric and pre-stake torque tolerances were derived from a survey of engineering technical drawings and represent the maximum acceptable variance of each parameter. The variance in staking force was determined by the resolution of the pressure gauge on the staking press (Figure 107). As previously discussed in Section 6.4.3, a uniform distribution was used for this analysis as it represents a worst-case condition. For each parameter, 10,000 randomised calculations were performed and the 95% confidence interval for the pushout and post-stake torque variance is shown in Figure 125.
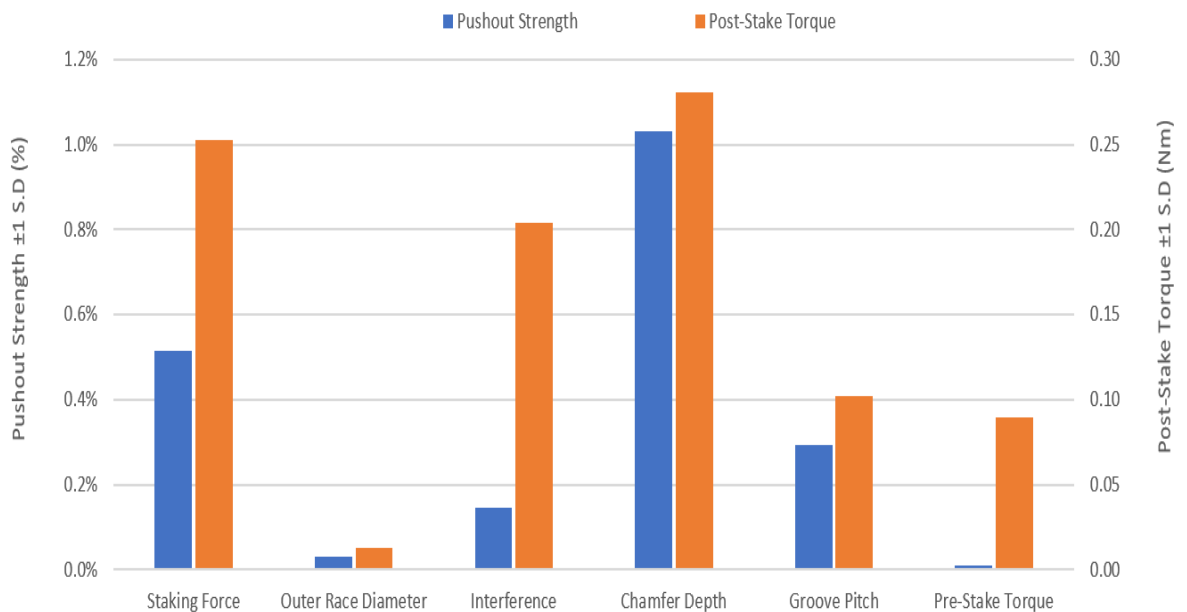
Figure 125: Impact of the manufacturing tolerances for each input parameter.

Table 31: Manufacturing tolerances for a Type 3 bearing.

	Relative Manufacturing Tolerance		
	Minimum	Maximum	Units
Staking Force			kN
Outer Race Diameter			mm
Interference	[REDACTED]		µm
Chamfer Depth			mm
Groove Pitch			mm
Pre-Stake Torque			Nm

The variance in Pushout Strength is largely dominated by the manufacturing tolerance of the chamfer depth. In contrast to the Pushout strength, the variance in Post-Stake Torque is more evenly distributed across all parameters (Figure 126) with the chamfer depth, staking force, and interference fit contributing to the majority of the variance. When all manufacturing tolerances are combined, the total Pushout Strength uncertainty is ±2.3% and Post-Stake Torque is ±0.49Nm and compares to the regression model accuracy of ±3.4% and ±0.50Nm respectively. Given that the overall uncertainty of the model is the combination of both the regression uncertainty and manufacturing tolerances, reducing the manufacturing tolerances improves the overall model. This is particularly true for the Post-Stake Torque as the manufacturing tolerances have an uncertainty almost equal to that of the regression model.
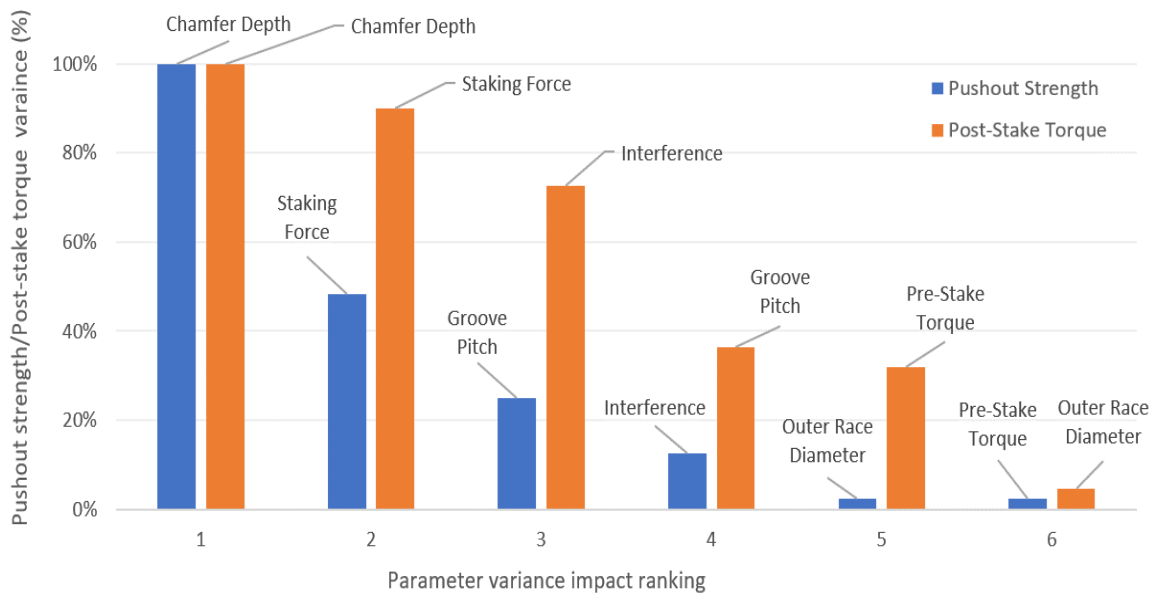
Figure 126: Relative impact of the manufacturing tolerances on both the Pushout strength and Post-Stake torque.

The main cause for the variance contributed by the chamfer depth is due to its manufacturing tolerance being a combination of the tolerance from the outer race width, the housing width, and the housing chamfer. This results in a relatively large stack tolerance of [REDACTED] which is approximately 50% of the type 3 regression models input range of [REDACTED]. When speaking with the machine operators at SKF, tightening the tolerances of the outer race width and housing width from their standard tolerance of [REDACTED] is easily accomplished with tolerances as low as [REDACTED] possible. However, controlling the depth of the housing chamfer is harder due to the challenges posed in measuring an internal chamfer.

The uncertainty for the staking force is limited to the resolution of the dial gauge on the staking press [REDACTED] and the ability to adjust the hydraulic pressure valve on the rear of the press. With a similar setup to the hand-operated pushout test rig (Figure 106), a stand-alone load cell could be permanently installed in the staking press and allow for the uncertainty of the staking force to be reduced to <0.5 kN. Achieving this precision however would be time-consuming and a tedious process due to the limited fine control over the hydraulic pressure valve. This would not be practical within a normal manufacturing environment and instead, a hydraulic press with an electronically controlled hydraulic actuator would be required.

The last major manufacturing tolerance that severely impacts the staking process is the interference fit between the outer race and the housing. SKF can control both dimensions to create an interference fit of [REDACTED] by match-machining and honing the housing to fit an individual bearing, however, this process is not scalable for general production.

As part of quality assurance, the diameter and bore for each bearing and housing are measured prior to staking to ensure that they are within tolerance however, the individual parts are not marked or catalogued and are simply assigned pass/fail. Because the individual parts are not tracked within a batch the current staking process is to select a bearing and housing at random for staking. If the parts were serialised and tracked, then an algorithm could optimise which bearing and housing should be paired together to reduce the variance in interference fits across a batch of staked bearings.

7.5. Summary

This chapter aimed to validate the staking tool produced from the Virtual-DoE and to explore the impact of the model's input parameters. The validation of the staking tool was achieved by collecting geometric, torque, and staking force data from the first-off of each batch of bearings manufactured over an 18-month period. New process controls were introduced to SKFs manufacturing channel to collect the required test data.

Across all three bearing classes, the prediction of the staking tool's Pushout Strength model far exceeds the performance of SKFs current internal tool (Table 32). As for the Post-Stake Torque, despite the larger uncertainty of the Type 3 model, the failure rate was considerably lower at <0.2% particularly when compared to the Type 1 model of <6% (Table 33). The cause for this sharp rise in failure rate is due to the much narrower range of Post-Stake Torque tolerance given for the Type 1 bearings.

Table 32: Model comparison for pushout strength (95% confidence intervals)

	Pushout Strength Error	
	Corrected Regression Model	SKF Internal Tool
Type 1	0.00% ± 5.1%	[REDACTED]
Type 2	-0.02% ± 6.3%	[REDACTED]
Type 3	0.00% ± 6.7%	[REDACTED]

Table 33: Model comparison for post-stake torque (95% confidence intervals)

	Post-Stake Torque Error	SKF Engineering Drawing Tolerance (Min-Max)	Failure Rate
Type 1	0.00 ± 0.60Nm	[REDACTED]	< 6.0%
Type 2	0.02 ± 0.59Nm	[REDACTED]	< 2.5%
Type 3	0.00 ± 0.98Nm	[REDACTED]	< 0.2%

The improved accuracy of the staking tool provides a deeper understanding of the staking process that SKFs internal tools could not. It enables a "first-time-right" capability that significantly reduce the likelihood of needing to re-work high torque bearings or the need for manufacturing trials for new bearing designs.

Overall, good correlation was seen between the screening tests and the final impact analysis (Figure 123). This gave a high degree of confidence that the screening process could correctly identify all the critical parameters. The analysis of each parameter resulted in the following recommendations:

- Chamfer Depth is the most sensitive parameter and has the greatest impact on both the Pushout Strength and Post-Stake Torque. It is also the only variable to fit into regime four across the entire design space (Figure 117) which can lower the post-stake torque whilst simultaneously increasing pushout strength.

- The value of the Chamfer Depth is determined by the stack-up of three dimensions (outer race width, housing width, and housing chamfer) which results in a relatively large manufacturing tolerance. Given the staking processes sensitivity to small changes in the Chamfer Depth, tightening the tolerance of these three dimensions should be a priority for manufacturing.

- Groove pitch should be eliminated as a design variable and remain as a fixed constant given its minimal impact on the staking process.

- [REDACTED]. Increasing the interference fit has a minimal impact on the Pushout Strength for a large increase in Post-Stake Torque.

Chapter

8

Discussion

This investigation was initiated to support the manufacturing of self-lubricating spherical plain bearings with the aim to characterise the key parameters that influence the staking process. Through the combination of computational modelling and a design of experiment methodology, the critical process parameters have been identified and successfully integrated into a staking tool consisting of a series of closed-form equations. An analysis of these equations (Figure 118 - Figure 122) provided an insight into the behaviour of each process parameter from which a series of recommendations can be constructed to guide the design of bearings and optimise the staking process. The most surprising finding being the sensitivity of the chamfer depth and that a small increase in this parameter significantly reduces the post-stake torque whilst increasing the pushout load. As a case study, the findings from this investigation demonstrate the suitability of a virtual design of experiments to solving and analysing complex cold-metal joining processes.

This chapter discusses the key findings and limitations of this investigation in relation to the primary research question and aim and interprets these findings within the context of the wider literature.

8.1. Summary of Findings

From a possible 19 geometric and process parameters, ten parameters (Inner ring diameter, groove depth and pitch, outer race diameter and width, chamfer depth, housing diameter, Interference fit, pre-stake torque, and anvil staking depth) have been identified to have the potential to impact the staking process and analysed through a definitive screening design. Four parameters (Housing diameter, groove depth, inner ring diameter, and outer race width) are not significantly contributing to either the pushout load or post-stake torque and are thus ignored. The six remaining parameters (Groove pitch, outer race diameter, chamfer depth, Interference fit, pre-stake torque, and anvil staking depth) are carried forward into a virtual design of experiments. The regression analysis of the 216 FE simulations has produced three regression models able to predict the staking force and pushout load to within ±1.7% and post-stake torque to within ±0.5 Nm (95% confidence intervals).

After validation against production bearings over an 18-month period, the error for the pushout strength regression model is estimated to be 0% ± 3.4% which compared extremely well against SKFs internal tool of [REDACTED]. The post-stake torque model performs equally well with an error of 0 ± 0.5 Nm. From a survey of SKFs engineering drawings, the post-stake torque tolerance varies from a maximum of [REDACTED] to a minimum of [REDACTED]. This results in an expected failure rate (whereby the predicted post-stake torque error is greater than the drawing tolerance) of less than 0.2%.

Once the performance of the regression models has been validated, each parameter is analysed separately to understand its impact on the staking process. The analysis identified that chamfer depth, anvil staking depth, and outer race diameter are the three key factors that predominantly control the output of the staking process. More importantly, the chamfer depth is the only parameter that can simultaneously decrease the post-stake torque while also increasing the pushout load. However, because the size of the chamfer depth is determined by the three geometric features (outer race width, housing width, and housing chamfer) its resulting manufacturing tolerance is the combination of all three tolerances and is the main driver of the variance within the model.

8.2. Interpretation of Findings

8.2.1. Virtual Design of Experiments

The research question posed at the start of this investigation splits naturally into two distinct areas of focus. Firstly, *what are the fundamental mechanisms that affect the staking process?* And secondly, *what is the magnitude of their impact on staking?* The development phase of the Virtual-DoE consisted in building a computational model of the staking process and provide critical insight into the underlying mechanisms at play (Section 6.2 and 6.2.3.8). The second phase of the Virtual-DoE follows the traditional DoE process and has been able to quantify the magnitude of all relevant parameters (Section 6.4).

Despite the rigorous and methodical approach taken throughout this investigation, a number of key decisions made during the Virtual-DoE process are subjective. The most significant decisions required are, the selection of parameters for the screening test, how many parameters should pass the screening test, and how wide a range of values those parameters can have. In each of these instances, the choices are a balancing act between time and accuracy. One of the potential mistakes when conducting screening tests is to include every possible parameter with the belief that the test will identify all of the important factors.

In practice, it was found that adding parameters that have little to no effect on the output and can make identifying the important factors more difficult. This is due to the aliasing present in screening tests which results in some of the dominant factors becoming confounded with non-dominant factors; effectively lowering the significance of dominant factors and raising the significance of non-dominant factors. This can be reduced by increasing the resolution of the screening test to reduce aliasing between higher order terms evidently at the cost of requiring significantly more tests to complete.

8.2.2. Defining the optimal Stake

As previously discussed in Chapter 1, the understanding of what defines the optimal stake has historically been surrounded by ambiguity and a lack of detailed analysis that the wider aerospace manufacturing sector has failed to resolve. Despite small changes in recent revisions of bearing design standards (Aerospace Industries Association, 2020), the only measure to define a successful stake is if a 0.005-inch wire gauge cannot be fit between the staking lip and the housing chamfer (Figure 127).
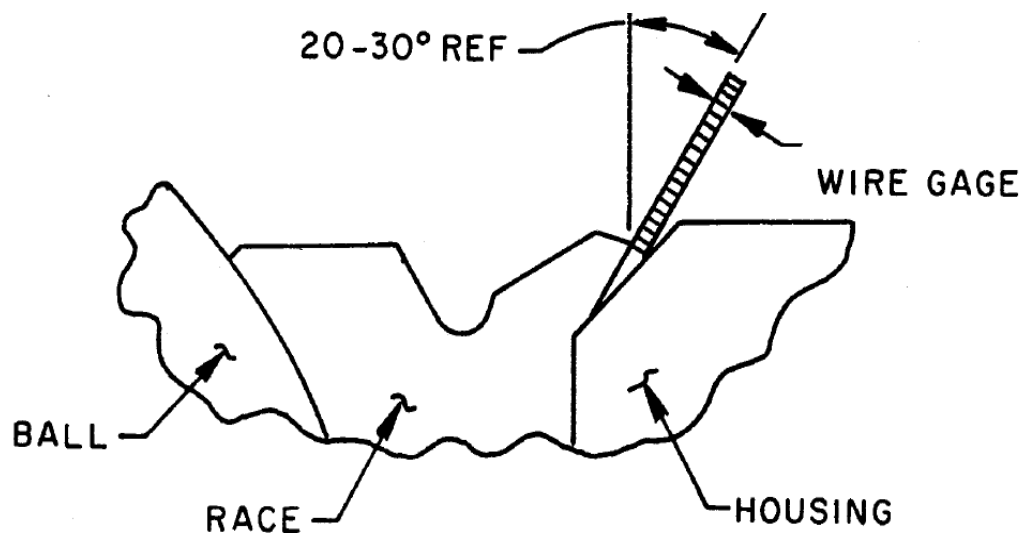
Figure 127: Test method for checking the quality of a bearing stake. (Airframe Control Bearing Group. 1989)

The wire gauge method does provide a crude method to control the area of contact between the staking lip and the housing chamfer, which the findings from this investigation provide further insight into.

In reference to Figure 93, as the staking force is increased and the length of the contact between the staking lip and the housing chamfer increases, there are two inflection points in the response to the pushout load and the post-stake torque. The first represents the minimum contact length required for the staking lip to sufficiently engage with the root of the chamfer. The second represents the point where the staking lip is sufficiently supported by the housing that the outer race begins to deform inwards towards the inner ring, compressing the liner and increasing the post-stake torque. It can therefore be argued that these two inflection points define the region of the optimal stake where the maximum pushout load is achieved for the minimum increase in post-stake torque.

For a Type 3 bearing, this region occurs when the length of the contact between the staking lip and the housing is between approximately 25% to 40% of the length of the housing chamfer. By contrast, the wire gauge method would require a contact lip length of approximately 60% and could be considered an over-staked bearing. However, attempting to define the optimal stake by the staking lip's contact length is not advised because the relative location of the two inflection points changes with variation of the bearing's geometric features. The answer to the question, what defines the optimal stake? should not be a singular statement but instead, be a series of guidelines and recommendations about how each parameter can be tuned to maximise the pushout-strength and minimise the rise in post-stake torque. A summary of these recommendations is given in Table 34.

Table 34: Recommendations for optimising the staking process.

Parameter	Effect on the staking process
Staking Force (Figure 103)	The staking calculator tool should be used to identify the region between the two inflection points in the pushout strength and post-stake torque response. The optimal staking force exists in this region.
Chamfer Depth (Figure 118)	Increasing the chamfer depth significantly increases the pushout strength and reduces the post-stake torque.
Interference Fit (Figure 119)	Increasing the interference fit provides a small increase in Pushout Strength for a large increase in post-stake torque. The relative benefit of increased pushout strength diminishes with an increase in staking force.
Outer Race Diameter (Figure 120)	To increase the pushout strength and decrease the post-stake torque, a larger outer race diameter can be used with a smaller staking force percentage.
Pre-Stake Torque (Figure 121)	Pre-stake torque has a minimal effect on Pushout Strength. Increasing the pre-stake torque increases the post-stake torque and therefore should be kept as small as possible.
Groove Pitch (Figure 122)	Minimal effect on either Pushout Strength of Post-Stake Torque

8.2.3. Wider Applicability of Approach

One of the primary objectives of this investigation was to develop a staking tool to aid in the manufacturing of spherical bearings by identifying the optimal staking force for a bearing. Considering the performance of the staking tool in both isolation and relative to the SKFs internal tools, this objective can be deemed successfully met. However, the developed staking tool has far greater potential than simply a manufacturing aid. By continuing to analyse the regression equations, an understanding of the mechanisms involved in staking has been developed and the current version of the staking tool is capable of supporting the design of bearings. By integrating the staking tool into the design phase, process parameters and bearing geometry can be experimented with and investigated virtually well in advance of physical manufacturing and before commitments are made on engineering drawings with customers.

Whilst the regression equations produced for this investigation are specific to just this case study of SKFs spherical bearings, the understanding of the mechanisms involved in staking can be generalised to a variety of bearing retention methods (Section 2.2.5) such as those described below.

Roller Swaging

Roller swaging is a common method for installing bearings with grooved, ductile outer races similar to anvil staking. Instead of staking the entire staking lip at once, two to three rollers incrementally form the staking lip by rolling in the outer race groove and gradually increasing the pressure on the rollers (Figure 28). This method can permit bearing replacement without damaging the housing.

Ball Impression/Point Stake

This method is used where ease of installation is required with non-grooved spherical bearings. An anvil containing 3-8 ball bearings (or done manually with a die punch) deforms the housing into the outer chamfer of a bearing (Figure 29). As there is minimal contact between the die and housing, this method can only sustain minimal axial loads but can be easily performed in the field due to the low staking forces required.

Segmented Stake

This is a common method for installing bearings (both spherical and rolling element) with hardened races into ductile housings. The housing is designed slightly thicker than the width of the bearing outer race and is staked in one step but only partially around its circumference in 4-8 segments (Figure 29).

Swaged Sleeve

This method is most often used for retaining bearings in magnesium housings when both outer race and housing are made of hardened materials. A ductile intermediate sleeve is staked into chamfers in both the bearing and housing providing limited axial load capacity but can be replaced without damaging the housing (Figure 30).

These bearing retention methods are the most similar to anvil staking and therefore facilitate the greatest degree of knowledge transfer from this investigation. By contrast, cold metal joining processes such as composite cold forging, draw forging and electromagnetic forming are too distinct from anvil staking to directly transfer the same findings into their respective fields. However, given the low cost, quick development, powerful understanding, and scalability of the Virtual-DoE process, it is possible to apply this methodology to many metal joining process such as but not limited to; clinching, hemming, riveting, rolling, hydroforming and electromagnetic forming.

8.3. Limitations

The notable limitations of this investigation can be broadly split into three categories: computational modelling, the Virtual-DoE process, and the staking calculator tool.

8.3.1. Computational Modelling

Computational models sit at the heart of any Virtual-DoE and their accuracy and level of refinement ultimately determine the quality of the Virtual-DoE. With any computational model, assumptions and simplifications are an inevitable part of the process which will negatively affect their output. The performance of the staking calculator tool has validated the underlying computational model used in this investigation, but several limitations could be improved upon.

In Section 7.2, systematic errors have been found with both the pushout load and the post-stake torque models. For the pushout load model, an overestimate of the pushout strength is observed at +5%. The likely source of error is an inability for the staking lip to tear in tension during the pushout of the bearing. ANSYS does natively support the option to model this tensile failure mode but not when using custom material models (used to model the plastic compressive behaviour) or within a transient structural environment. A potential workaround is to use ANSYS's Parametric Design Language (APDL) to write a programme that at the start of each sub-step, a check is done to locate any elements exceeding the tensile elongation limit. These elements could then have their elastic stiffness reduced to zero which would emulate a tensile failure. Coding within APDL is a specialised skillset and attempting to write custom code to interact with the solver engine is far outside the scope of this investigation.

For the Post-Stake Torque, a scaling issue is observed whereby the error in Post-Stake Torque increases with the predicted value of the Post-Stake Torque. This points directly to an issue with the modelling of the composite liner, specifically, either the compressive stiffness or the assumed liner conformity. The material data for the liner was taken from SKFs internal investigation into liner stiffness (SKF, 2008). To reduce the effect of noise at low contact pressures, their investigation started at a contact pressure of 20MPa which for an average Type 3 bearing gives an approximate torque of 6Nm. This represents a high torque bearing and therefore most simulations were reliant on liner stiffness values extrapolated from contact pressures below the minimum SKF had tested for.

One of the assumptions made during the development of the computational model was that the liner was in perfect conformity with the inner ring and not in either open-mouth or church-window condition (Figure 128). This is a potentially serious concern with regard to the post-stake torque because during staking, any torque rise is generated when the outer edges of the outer race pinch in on the inner ring at high staking loads. If the bearing is in the open-mouth condition, then any torque rise would be delayed as a greater degree of inward flow of the outer race is needed before contact is made with the inner ring. Conversely, a bearing in the church-window condition experiences a rise in torque much sooner as it is already in contact with the inner ring and is very sensitive to the staking force. Liner conformity is checked once per batch by splitting a bearing in half (by casting it in resin and cutting it with a diamond saw) and taking five measurements of the liner thickness at different sections of the liner. From the viewpoint of including the liner conformity as a potential parameter in the Virtual-DoE, this current measurement process is flawed for the following reasons:

- Significant hoop stresses remain in the outer ring after it is formed around the inner ring during the nosing process (Woodhead, 2015). By splitting the bearing these residual stresses will cause the outer ring to relax and change the conformity measurement,

- Liner conformity is only measured on a single bearing per batch as part of quality assurance. However, each finished bearing will have its torque adjusted by either rolling or end loading to bring the breakout torque to within specification. This process alters the conformity of the liner to control the breakout torque and therefore each bearing will be different within a batch,

- The tolerance for liner conformity is ±0.001 inches and is measured to a resolution of ±0.0005 inches (5 tenths). From earlier trials with the computational model, a uniform compression of the liner by ±0.0005 inches would be equivalent to a torque of approximately 0.7 Nm for an average Type 3 bearing.

Alternate means of measuring bearing conformity would be to use NDT techniques such as X-ray computed tomography which is capable of spatial resolutions as small as 0.1 microns (Maire and Withers, 2014).
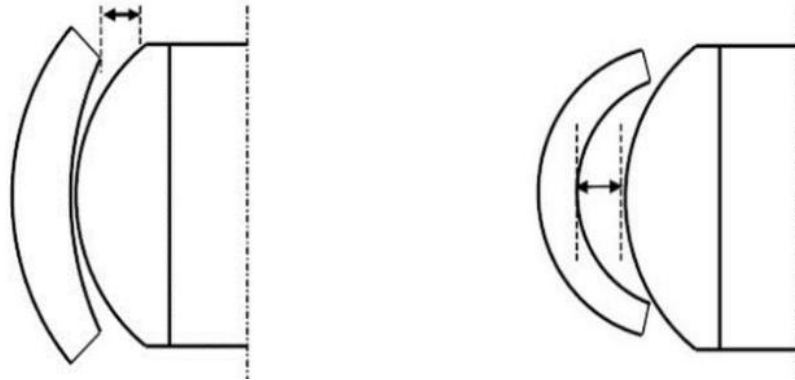
Figure 128: Conformity of the outer race in either an open-mouth condition (Left) or church-window condition (Right).

Despite the limitations of the computational model with the lack of a tensile failure mode, liner material properties, and liner conformity, the resulting inaccuracy of the Virtual-DoE models are relatively small and were further reduced during the validation phase. This suggests a robustness to the Virtual-DoE process that if the underlying behaviour is correct, then small modelling or scaling errors can be effectively corrected.

8.3.2. Design of Experiments: Screening and Validation

As previously discussed with the limitations of the computational model, any fundamental issues with the model cannot be identified until the end of the project. This means that all of the screening tests could have been carried out with a potentially flawed and uncorrected model. This could result in an important parameter being excluded at the screening stage due to either: a false-negative where a significant parameter is incorrectly deemed to be irrelevant, or a false-positive from a less significant parameter overshadowing an important parameter.

To check for this possibility, the correction factors derived in Section 7.2 were applied to the results from all of the screening tests. It was found that applying these correction factors resulted in only minor changes to the relative importance of each parameter. The only notable change seen was a reduction in the importance of the interference fit to the post-stake torque for Type 3 and Type 2 bearings. Nevertheless, this did not impact the overall results of any of the screening tests with the same six parameters still selected before and after post-correction was applied. This highlights the importance of constructing an accurate computational model before conducting any experiments to avoid the risk of invalidating the screening results post-correction and consequentially the entire set of experiments.

One of the key motivations that would push any investigation towards a Virtual-DoE and away from a practical-based DoE, would be if there was a restriction on the number of physical test specimens that could be manufactured and tested. Therefore, there will always be a number of challenges in validating the entire design-space from a Virtual-DoE. As seen with this investigation, only 45 batches of Type 3 bearings were produced over an 18-month period resulting in a coverage of 76% of the design-space despite efforts made to bias the DoE towards bearing geometries most likely to be manufactured. For any Virtual-DoE this difference would be expected, however, the particular circumstances of this investigation resulted in this difference being exaggerated.

[REDACTED], a small number were either prototype or one-off bearings that contained geometries significantly different to those of typical customer bearings (Figure 129). This was not realised until very late in this investigation and resulted in the design-space being extended beyond normal manufacturing variance.

An additional consequence of this over-extended design-space was an increase in the range of values for the parameters in the screening test. For the Groove Pitch parameter in particular, the extended range caused by these outlier geometries would have increased the relative importance of this parameter. Given the low score this parameter originally achieved, a reduction of the design-space may have reduced its impact sufficiently to have justified excluding it from the Virtual-DoE.

Figure Redacted
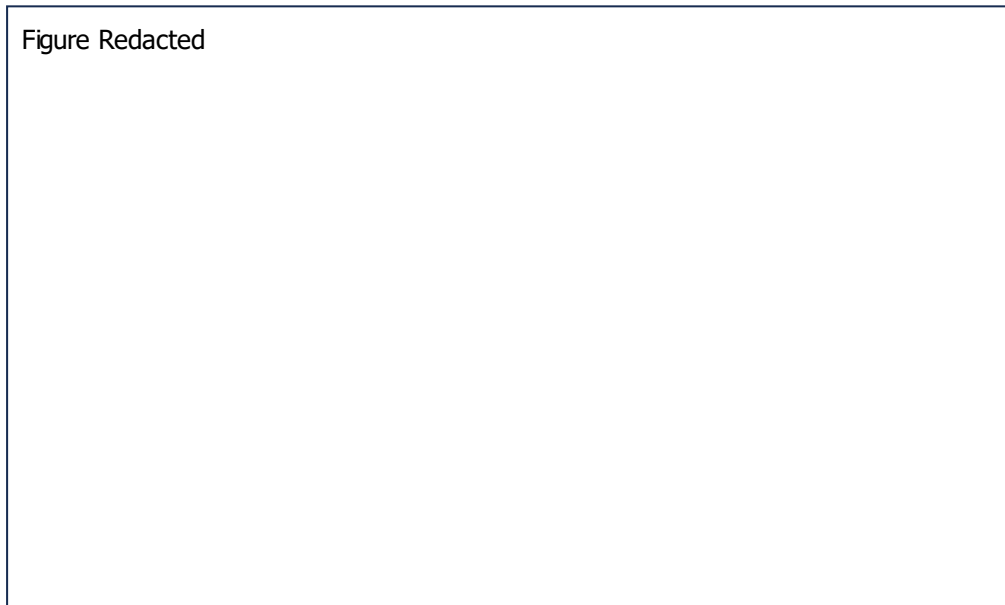
Figure 129: Groove pitch distribution of Type 3 bearings. Highlighted in red are the seven outlier geometries from prototype or one-off bearings that passed though manufacturing.

8.3.3. Staking Tool

The contour plots of Figure 118 through Figure 122 provide a critical understanding of how each parameter impacts the staking process and form part of the primary contribution of this thesis. These contour plots were integrated into a staking tool with user feedback, including those outside of the core engineering team, being very positive as it provided an intuitive understanding of the dynamics at play during staking (SKF, 2023). During the prototype phase of the staking tool, early builds were given to the SKFs product engineering team to see how they interacted with the tool. Whilst the overall feedback was positive, there was a consistent misunderstanding of the limitations of the tool.

As with any DoE, the predictions and outputs from the model are only valid within the limits of the model as defined by the design-space of the DoE. The engineers quickly noticed that the depth of the outer race groove was not included in the model (as it was eliminated in the screening tests) which came as a surprise to them as their design rules previously stressed the importance of the groove depth being greater than the chamfer depth. This resulted in a series of proposed bearing geometries whereby the groove depth was significantly less than the chamfer depth; now that there was no implied control over this parameter. These bearings, if manufactured, would have behaved drastically different to the predictions of the staking tool. The results from the screening tests indicated that the groove depth parameter was insignificant to staking, but this is only true under the conditions of the screening test which were based on a survey of SKFs recent production bearings. If the variation in groove pitch was larger, or if another parameter such as chamfer depth was smaller, then the results from the screening test could have indicated that the groove pitch might be significant.

From this feedback, additional limits and tool-tips and were added to the input fields of the staking tool to prevent this situation from arising and provide greater clarity to the user. These challenges and oversights arose in part because the staking tool was being used as part of the preliminary design process for new bearings and not just for analysis as originally intended. This use case has seen design aids such as the contour plots added to the staking tool and it is anticipated that as users gain more confidence with the staking tool, more bearing-design focused updates will be required to meet user expectations. However, as more design focused features are added over time, it may soon be required to move away from the Excel based tool and to a more powerful software package better suited to developing custom user interfaces and visuals such as Matlab or Python.

One of the limitations placed on this investigation was to limit the scope of the Virtual-DoE to the parameters that could be manipulated as per international spherical bearing standards (SAE International, 2018). The only notable potential parameters excluded from this investigation were the angles of the outer race groove (60 degrees), housing chamfer (45 Degrees), and the staking anvil (90 degrees). Despite the highly likely impact on staking that these three parameters could have, the reason for not including them is two-fold.

Firstly, it was essential to validate the findings of this methodology through physical testing, and therefore, this investigation was constrained to designs of current existing bearings. In this regard, there was very little manufacturing support to produce custom bearings or tooling not within SKFs current capacity.

The second reason why these parameters were not investigated was to maintain compatibility with tooling in the wider industry and aerospace standards. The vast majority of spherical plain bearings found within the aerospace industry are considered "standard bearings" and manufactured following specific aerospace standards that control all aspects of the bearing's geometry and design. These standard parts allow for multiple vendors to supply the same product, allowing for a diverse and robust supply chain that includes standard tooling for installation. Of all the bearings produced by SKF with machined v-grooves, approximately 65% are sold directly to customers for in-field installation with the remaining 35% staked internally at SKF. To maintain compatibility with standard tooling, custom-designed bearings are (with limited exceptions) merely derivatives of the standard bearings with only small changes made to non-contact surfaces. Regardless of whether the angles of the groove, chamfer or staking anvil are currently optimal, the introduction of bearings that would require proprietary tooling and re-qualification would face significant resistance from both customers and standards groups. Between the limitations of manufacturing capacity and resistance to fundamental changes to bearing design, studying parameters such as groove pitch angle, chamfer angle, and anvil geometry would currently be limited to a purely theoretical design study. Therefore, the study of these parameters was considered outside the scope of this investigation.

Early work by Zhang (2018 and 2017) indicated that there is scope for optimisation of these traditionally "fixed" parameters. Their research found that the contact angle of the anvil has a large impact on both forming forces and pushout strength with the optimal angle existing between 45 and 60 degrees but is heavily influenced by the bearing groove geometry. The complexity of this interaction highlights the limitation of conventional parametric design studies with no explicit relationship able to be drawn between the input variables and desired output. From the performance demonstrated in this thesis, the Virtual-DOE process would be

best placed to efficiently characterise this interaction and firmly state what the optimal value of these parameters should be. If improved geometries for the staking anvils and groove were found and supported by the depth of analysis provided by the Virtual-DOE, then this would provide good leverage for the industry to consider adoption.

8.3.4. Scalability

As a general rule for a DOE, the larger the design-space then the worse the prediction within that design-space. If the design-space can be minimised, it is reasonable to expect the measured response to remain relatively stable and easy for the DoE regression equations to fit. However, as the design-space increases, the measured response can transition from a linear to non-linear behaviour, especially at the extremes of parameter input values. For example, the anvil staking depth parameter was originally set from 0.35mm - 0.51mm to capture the entire response from under-staked to over-staked bearings. For the majority of this range, the response of the post-stake torque is small, but beyond 0.47mm the post-stake torque increases dramatically, creating two distinct regimes. This behaviour is challenging for a regression equation to handle and would result in a poor prediction across the design-space trying to accommodate the two regimes. For this investigation, a decision was made to reduce the anvil staking depth range to 0.39mm - 0.49mm to improve the prediction in the centre of the model which is where the ideal stake would likely be found. A similar approach was taken for each of the other parameters to narrow their input ranges to prioritise the accuracy of the regression equations across a narrower range of bearings instead of trying to accommodate extreme edge cases. This choice was driven by the desire to produce a tool that would be biased towards the majority of bearing designs.

Although not studied as part of this investigation, Virtual-DoE are scalable even after the initial analysis. For example, if more levels are required to accurately capture the effect of the anvil staking depth, additional levels can be added to create midpoints between the current parameter limits. Instead of re-running the DoE resulting in another 360 experiments, only the extra 144 unique experiments created by these new midpoints need to be solved and can be appended to the original DoE dataset. This same approach can also be used to extend the range for a parameter by treating its current maximum and minimum values as "mid-points" and adding additional levels beyond current limits. How this scalability could be approached is demonstrated in Table 35.

Table 35: Proposed increase of parameter level to improve model accuracy [REDACTED]

Anvil staking Depth Range	Level	Value (mm)							
Current	3		■			■		■	
Additional Midpoints	5		■	■		■	■	■	
Expanded Range	5	■	■			■		■	■

9

Conclusions and Future Work

The work presented in this thesis details the development of a virtual design of experiments methodology to model the staking of self-lubricating spherical plain bearings. This investigation is a case study for the combination of computational modelling with the applied statistical methods of a design of experiments to analyse and predict the behaviour of complex metal joining processes by plastic deformation.

The natural variation within the staking process (i.e., component geometry, material properties, frictional behaviour, and process controls) have been incorporated into the modelling process to represent manufacturing conditions as accurately as possible. The virtual design of experiment method has identified the relevant parameters that impact the staking process and has characterised their behaviour as a series of closed-form solutions.

The outputs from this investigation have resulted in three contributions to knowledge to both the scientific and engineering community.

Major Contribution:

1) Evidence that the combination of the two disciplines, computational modelling, and the applied statistical methods of a design of experiments, is suitable for analysing and predicting the behaviour of complex metal joining processes

Minor Contributions:

2) Characterisation of the relevant geometric features and process control settings that impact the pushout strength and post-stake torque of a staked self-lubricating spherical plain bearing

3) New methodology for analysing the results from a ring compression test to better capture the non-linear behaviour of the friction coefficient during forging conditions

In addition, contributions 1) and 3) have been composed into their own respective works and published in peer reviewed articles.

Published Works:

Hatherell, J., Marmier, A., Dennis, G., Curry, W. and Matthews, J. (2023) Exploring the potential for a FEA-based Design of Experiments to develop design tools for bulk-metal joining processes. *International Conference on Engineering Design* (ICED), Bordeaux, France, 24-28 July 2023. (Appendix F)

Hatherell, J., Marmier, A., Dennis, G., Curry, W. and Matthews, J. (2023) An Iterative Numerical Approach to Evaluate the Variable Friction Coefficient of Steel AMS5643 Using Ring Compression Tests. *Tribology Transactions.* 67(1), pp. 15-21. (Appendix G)

9.1. Summary of Work

The objectives of this investigation all contribute to the thesis's aim to characterise the amplitude and mechanisms that influence the pushout load and post-stake torque. The following summary details how each of these objectives have been addressed with a summary of the key findings and conclusions.

1) *Characterise the mechanical and friction properties necessary for the modelling of the staking process.*

The bearing's outer race and housing experiences plastic deformation during staking. This plastic behaviour is reached through uniaxial compression tests following the ASTM International E9-09 standard (Chapter 4. A total of sixty cylindrical test specimens (30 for each material) have been produced and evaluated at strain-rates varying from 0.01 to $1s^{-1}$. It was identified in the literature review (Chapter 2) that the friction coefficient (as defined by Coulomb's friction law) can vary with contact pressure under cold-forming conditions. The two friction regimes during staking (outer race/housing, and the outer race/staking anvils) have been replicated with ring compression testing to evaluate the friction-pressure relationship (Chapter 5). The main findings and conclusions for this objective are as follows.

- For both the outer race and housing materials (AM5643 H1025 and H1150) the yield strength, strength coefficient, and strain hardening exponent are sensitive to strain-rate.

- The yield stress follows a power-law relationship, $\sigma_y = K_y \dot{\varepsilon}^{\,m}$, with the coefficients given in Table 8.

- The flow stress is best modelled using a modified Hollomon strain-hardening relationship, $\sigma = K\dot{\varepsilon}^A \bar{\varepsilon}^{(n\dot{\varepsilon}^B)}$, with the coefficients given in Table 10.

- The friction behaviour between the outer race and housing (Region 2, dry contact) remains stable across a range of contact pressures and can be approximated using Coulomb's friction law with a constant friction coefficient of 0.15.

- The friction behaviour between the outer race and staking anvil (Region 1, lubricated with a molybdenum disulphide solid paste) does not remain constant with contact pressure with a peak friction coefficient of 0.115 at 1325MPa (Figure 82).

- If the coefficient of friction varies significantly with contact pressure (as shown with contact region 1), direct FCC interpolation is not a suitable method by which to evaluate the friction-pressure relationship. Under these conditions, the newly proposed iterative FCC interpolation method is better suited to capturing the evolution of the friction coefficient during plastic deformation.

2) Identify the key process parameters and characterise their impact on the staking process.

In Chapter 6, the key process parameters have been identified by using a variant of the DoE method called a definitive screening design (DSD). Ten potential parameters were screened to evaluate the relative impact of each parameter with respect to the Pushout Strength and Post-Stake Torque. From these tests, the top six parameters were identified and the remaining four were excluded from any further analysis. The speed and efficiency of a DSD is achieved at the cost of aliasing between higher-order parameter terms. Therefore, a full factorial Virtual-DoE was carried out using the six critical parameters identified from the DSD. The output of the Virtual-DoE was a series of closed-form solutions that relate the six input parameters to the Staking Force, Pushout Strength, and Post-Stake Torque. The findings and conclusions for this objective are as follows.

- The six most significant parameters that influence the staking process are in descending order: Anvil Staking Depth, Chamfer Depth, Outer Race Diameter, Interference fit, Pre-Stake Torque, and Groove Pitch. Their relative contribution to the Staking Force, Pushout Strength, and Post-Stake Torque shown in Figure 96.

- The regression equations from the full factorial DoE are able to show a strong correlation against the computational model for all three bearing categories (Figure 99). Against randomised computational simulations, within the DoE parameter limits the Staking Force and Pushout Strength error in the regression equations does not exceed ±1.7% and for the Post-Stake Torque ±0.5Nm (95% confidence interval).

- The parameter limits were set to 20% and 80% of their respective maximum parameter distributions to bias the model's accuracy towards the majority of the bearings being manufactured. However, the regression equations remained reasonably accurate relative to the computational model as the parameters extend beyond the parameter limits of DoE. This indicates that the choice of parameter limits was initially set too conservatively and could be set wider to encompass a wider range of inputs.

- Given the speed and computational efficiency of closed-form solutions compared with computational modelling, The computational costs of developing a Virtual-DoE model would quickly see a return on investment and could replace direct computational modelling for repetitive analysis tasks of any system that follows a parametric design.

3) Validate the closed-form solutions against experimental results.

The Virtual-DoE has intentionally been designed to be biased towards the standard bearing sizes that SKF most commonly manufacture. Therefore, to validate the output from the Virtual-DoE, data has been collected from the first-off of each batch of staked bearings over 18 months and compared against the Virtual-DoE model (Chapter 7). The findings and conclusions for this objective are as follows.

- Analytical methods are not suitable to predict the Staking force or Pushout Strength of staked bearings. This is likely the result of the assumptions and simplifications that these methods must make regarding rigid boundary conditions and strain hardening.

- The performance of the corrected regression equations far surpasses the prediction capability of SKFs internal staking tools (Table 32 and Table 33).

- The deviation between the Virtual-DoE and manufactured bearings is likely driven predominantly by issues with the underlying computational model, specifically the modelling of the composite liner and lack of tensile failure mode for the staking lip. However, a regression analysis on the model's errors has corrected for and eliminated nearly all of the systematic errors within the model and has significantly reduced the random error.

- Validation of the Virtual-DoE regression equations can only happen once the final model is built. Therefore, any fundamental or scaling issues inherent to the computational model cannot be identified prior to screening tests and may impact the parameter selection process. However, in this investigation, the only two significant changes between the screening test and the validated Virtual-DoE are a drop in the significance of the interference fit (for the Post-Stake Torque) and a rise in the significance of the chamfer depth (for the Pushout Strength). With the exception of these two parameters, the parameter impact scores remain relatively consistent and give a high degree of confidence that no significant parameters may have been eliminated in the screening test.

- Analysis of the manufacturing tolerances has identified that the staking force, interference fit, and chamfer depth are the leading causes of variance in the staking process.

4) *Produce a non-proprietary, and easy-to-use virtual tool to support manufacturing and the implementation of new designs.*

The closed-form solutions from the output of the Virtual-DoE have been programmed into Microsoft Excel, a widely used application that does not require specialist training (Chapter 6). Visualisations have been created to understand the impact of each parameter against the Pushout Strength and Post-Stake Torque (Chapter 7). The tool's capabilities and conclusions for this objective, are as follows.

- The staking tool was developed in collaboration with SKFs engineers who have assessed the staking tool in day-to-day operations. From their feedback, the staking tool is split across five sheets to fit their design workflow: groove definition (Figure 100), geometry inputs (Figure 101), input summary (Figure 102), the relationship between staking force and the pushout strength and Post-Stake Torque (Figure 103), and individual parameter response charts (Figure 118- Figure 122).

- The manufacturing tolerance of the Groove Pitch is nearly 50% of the range of the Groove Pitch. Given its negligible impact on staking and the narrow range of values that it can take in the model, this parameter should be considered constant for all future bearing designs. This would eliminate the Groove Pitch as a potential variable and half the number of experiments required for the full-factorial DoE.

- The visualisations developed in Chapter 7 has identified the effect of each parameter on the overall staking process and how they can be controlled to achieve the ideal stake.

  o Staking Force – The optimal staking force can be identified using the staking calculator tool and exists between the two inflection points in the pushout strength and post-stake torque responses.

  o Chamfer Depth – Increasing the chamfer depth significantly increases the pushout strength and reduces the post-stake torque for all staking forces.

  o Interference Fit – Increasing the interference fit provides a slight increase in Pushout Strength for a large increase in post-stake torque. The relative benefit of increased pushout strength diminishes with an increase in staking force.

- o Outer Race Diameter – A larger outer race diameter can increase the pushout strength and decrease the post-stake torque when paired with a decrease in staking force percentage.

- o Pre-Stake Torque – Pre-stake torque has a minimal effect on Pushout Strength. Increasing the pre-stake torque increases the post-stake torque and therefore should be kept as small as possible.

- o Groove Pitch – Minimal effect on either Pushout Strength or Post-Stake Torque.

9.2. Future Work

Many areas could be further investigated with respect to both the staking process and the application of the Virtual-DoE method to cold-metal forming. The author envisions several key areas of research that can build-upon the work from this investigation.

Virtual-DoE Process

Due to the time constraints of this investigation, a relatively conservative approach was required with parameter limits to ensure the accuracy of the model. This choice was taken due to the inability to predict the uncertainty of a Virtual-DoE process until it is completed. Chapter 8 includes a workaround whereby a Virtual-DoE can be scaled to either increase the scope or accuracy of the model with additional experiments appended to the original dataset. Despite the benefits of this scalable approach, this can be an inefficient practice if no measurable accuracy is gained from additional experiments. To gain widespread adoption in industrial applications, a higher certainty of a "first-time-right" methodology is required. Whilst the Resolution IV Definitive Screening Test used in this investigation was effective for identifying the right parameters to include in the Virtual-DoE, it cannot provide any information to assist in selecting suitable parameter limits or if higher parameter levels (beyond level 3) would be beneficial. This work currently involves a considerable amount of computational modelling and a "trial and error" workflow.

Therefore, future research should focus on the screening phase of the Virtual-DoE process with a particular focus on alternative screening methods to 1) better predict the performance of the full-factorial DoE at the screening test phase and 2) increase the efficiency of the overall process by reducing the reliance on additional experiments.

Anvil and Groove Geometry

Previous research has shown that during roller swaging, the geometry of the anvils and the outer race groove play an important role in both the Pushout Strength and Post-Stake Torque. In addition, it has been shown that the standard bearing and anvil geometries could be further optimised. Given the geometric similarities of the anvils and bearings, similar scope for geometry optimisation is expected for anvil staking. However, the complexity of these interactions highlights the limitation of conventional parametric design studies to draw explicit relationships between the input variables and desired outputs. From the performance demonstrated in this thesis, the Virtual-DOE process would be best placed to efficiently characterise this interaction and firmly state what the optimal value of these parameters should be. If improved geometries for the staking anvils and groove were found and supported by the depth of analysis provided by a Virtual-DOE, then this would provide good leverage for the industry to consider adoption.

Liner Conformity

One of the simplifications made with the computational model is that at the start of each simulation, each bearing had perfect conformity between the inner ring and the liner. The source of conformity issues originates from the nosing process where the outer race is formed around the inner ring during the manufacture of a bearing. During the early development phase of the computational model, liner conformity was a programmable parameter comprising two variables, radial offset, and radius of curvature. Adjusting these two variables to set the liner in either the church-window or open-mouth condition had a noticeable impact on the pressure distribution of the liner after staking. However, the current method for measuring liner conformity involves cutting the bearing in half which destroys the bearing and prevents liner conformity from being parameter within the Virtual-DoE. Non-destructive techniques such as X-ray computed tomography with spatial resolutions as small as 0.1 microns are a promising option for quantifying liner conformity without destroying the bearings.

Serialisation and Data Acquisition

The quality assurance process at SKF relies on a simplistic pass/fail criterion at each manufacturing stage with no records kept of the actual measured parameter. Within any given batch, each bearing is treated as identical to every other bearing. This lack of ongoing data acquisition results in a relatively poor understanding of the true manufacturing tolerance distribution and has severely limited the amount of historical data that this investigation could have used. The author strongly recommends that SKF introduce digital serialisation to track each bearing through manufacture and begin to build a database to bridge the gap between what is stated on engineering drawings and what is produced.

Another challenge posed by the lack of serialisation is the large uncertainty in the interference fit; currently, bearings and housings are randomly paired together for staking. If bearings and housings were serialised, optimal pairs could be selected to maintain a smaller interference fit tolerance without the need to control the bearing and housing bores to smaller tolerances at a considerable cost.

Machine Learning

The regression analysis carried out in Chapter 6 generates an explicit expression that describes the relationship between the inputs and outputs by assigning weights to each input variable. To achieve the desired performance of the regression analysis the input ranges needed to be tightly controlled resulting in limited input ranges and the need for multiple regression models to be created to fully cover all possible bearing geometries.

The methodology of the Virtual-DOE and its regression analysis share many similarities with machine learning models, in particular the algorithms of Supervised Learning (regression) and Neural Networks (reinforcement learning). Where they differentiate from the analysis of a Virtual-DOE is the use of hidden layers as intermediary stages between the input and output that change the model's behaviour depending on the activation function used. This contrasts with the Virtual-DOE method where the response to an input variable within a bearing type remains consistent no matter its magnitude which limits the scope of each bearing type to a narrow range of input values.

These hidden layers and activation functions could allow for significantly wider ranges for the input variables to be considered without impacting the model's overall performance and eliminate the need to create multiple discrete models for each bearing type.

References

Aerospace Industries Association (2020) NAS0331 Bearing Installation And Retention By Swaging Or Staking. Virginia: Aerospace Industries Association.

Airframe Control Bearing Group (1989) Bearing installation and retention by swaging or staking. London: SAE. Unpublished.

Al-Momani, E. and Rawabdeh, I. (2008) An Application of Finite Element Method and Design of Experiments in the Optimization of Sheet Metal Blanking Process. Jordan Journal of Mechanical and Industrial Engineering. 2(1), pp. 53-63.

Altan, T., Ngaile, G. Shen, G. (2005) Cold and Hot Forging: Fundamentals and Applications. Ohio: ASM International.

Alves, M.L., Martins, P.A.F. and Rodrigues, J.M.C. (2003) Simulation of Three-dimensional Bulk Forming Processes by Finite Element Flow Formulation. *Journal of modelling and simulation in materials science and engineering.* 11(1), pp. 803–821.

Ampep (1993) AMPEP Self-Lubricating & Metal/Metal Plain Bearings. Clevedon: Ampep Ltd. Unpublished internal company document.

ANSYS (2021a) ANSYS Workbench 2021R1. Available from: www.ansys.com. [Accessed 11 April 2022].

ANSYS (2021b) Discussion of Implicit and Explicit Methods and Timestep Size. Available from: https://courses.ansys.com/wp-content/uploads/2021/02/Lesson3_DiscussionOfTimeStepSize.pdf. [Accessed 15 June 2022].

Ashcroft, I.A., Mubashar, A. (2011). Numerical Approach: Finite Element Analysis. In: da Silva, L.F.M., Öchsner, A., Adams, R.D. (eds) Handbook of Adhesion Technology. Springer, Berlin, Heidelberg. https://doi.org/10.1007/978-3-642-01169-6_25

ASTM International (2018) *E9-09 Standard Test Methods of Compression Testing of Metallic Materials at Room Temperature*. Pennsylvania: ASTM International.

Atlas Steels (2008) Stainless Steel – Martensitic - 1.4125 (440C) Bar Datasheet. Available from: www.atlassteels.com.au/documents/Atlas%20Grade%20datasheet%20440C%20rev%20May%20200 8.pdf. [Accessed 15 November 2020].

Avitzur, B. (1967) Strain-hardening and strain-rate effects in plastic flow through conical converging dies. Journal of Engineering for Industry. 89(3), pp. 556-562.

Badrossamay, M. (2016) An introduction to forging process. Department of mechanical engineering, Isfahan university of technology.

Baghani M., Eskandari A.H., Zakerzadeh M.R. (2016) Transient growth of a micro-void in an infinite medium under thermal load with modified Zerilli–Armstrong model. Acta Mech. 227, pp. 943–953. DOI: 10.1007/s00707-015-1490-4.

Bahmani, M.A., Niayesh, K. and Karimi, A. (2009) 3D Simulation of magnetic field distribution in electromagnetic forming systems with field-shaper. *Journal of materials processing technology*. 209(5), pp. 2295-2301.

Bajaj, S., Wakode, D. and Musale, G. (2014) Optimization of Sheet Metal Forming Process Parameters using Optimization Tool. SAE Technical Paper 2014-28-0030, DOI.org/10.4271/2014-28-0030.

Bay, N. (1979). Cold pressure welding - the mechanisms governing bonding. *Journal of Engineering for Industry*. 101(2), pp. 121–127.

Bay, N. (1983) Mechanisms Producing Metallic Bonds in Cold Welding. Welding Journal. 62(5), pp. 137–142.

Bayraktar, E., Levaillant, C. and Altintas, S. (1993) Strain Rate and Temperature Effect on the Deformation Behaviour of the Original Hadfield Steel. Journal of Physics. 3(7), pp. 61-66.

Baheti, A. (2021) Activation Functions in Neural Networks. Available from: https://www.v7labs.com/blog/neural-networks-activation-functions. [Accessed 25 April 2024].

Bhadeshia, H. and Honeycombe, R. (2017) *Steels: microstructures and properties*. 4th ed. London: Elsevier.

Billade, B. R. and Dahake, P. S. K. (2018). Optimization of Forming Process Parameters in Sheet Metal Forming Of Reinf-Rr End Upr-Lh/Rh for Safe Thinning. *Journal of Engineering Research and Application*. 8(8), pp. 1-7.

Black, J.T. and Kohser, R.A. (2008). *Materials and Processes in Manufacturing*. 9th ed. Hoboken: Wiley.

Borsellino, C., Bella, G.D. and Ruisi, V.F. (2007) Study of new joining technique: flat clinching. *Key Engineering Materials*. 344, pp. 685-692.

Bossi, R.H. and Georgeson, G.E. (1992) *Computed tomography analysis of castings*. Boeing Defence and Space Group. Seattle: Aerospace and Electronics Division.

Bridgman, P.W. (1952) *Studies in Large Plastic Flow and Fracture*. McGraw-Hill: New York.

Buschhausen, A., Weinmann, K., Altan, T. and Lee, J. (1992) Evaluation of Lubrication and Friction in Cold Forging using a Double Backward-Extrusion Process. *Journal of material processing technology*. 33(2), pp. 95–108.

Cao, H.D., 1987. Plastic Forming and Rolling Mechanics Principles. Machinery Industry Press, pp. 134 - 137.

Carter (2020) *Aerospace installation tools*. Available from: https://www.carterbearings.co.uk/aerospace-bearing-tools. [Accessed: 16 November 2020].

Chandramouli, R. (2014) Analysis of forming - Slab Method [online]. California: IDC Technologies. Available from: www.idc-online.com/technical_references/pdfs/Analysis_of_forming_Slab_Method.pdf. [Accessed 29 January 2023].

Chavdar, B., Goldstein, R., Yang, X., Butkovich, J. and Ferguson, L. (2015). Hot hydroforging for lightweighting. In: *Proceedings of the 5th International Conference on Distortion Engineering*. Bremen, September 2015.

Chavdar, B., Goldstein, R. and Ferguson, L. (2016). Hot hydroforging of lightweight bimaterial gears and hollow products. In: *Proceedings of the 23rd IFHTSE Congress*. Savannah, April 2016. pp 175-183.

Chitkara, N.R. and Butt, M.A. (1992). A general numerical method of construction of axisymmetric slip-line fields, *International Journal of Mechanical Science* . 34(11), pp. 833-848.

Cho, J.R., Song, J.I., Noh, K.T. and Jeon, D.H. (2005) Nonlinear Finite Element Analysis of Swaging Process for Automobile Power Steering Hose. *Journal of Materials Processing Technology*. 170(1), pp. 50–57.

Chu, Y.Y. and Lee, R.S. (2013) Effect of Field Shaper Geometry on the Lorentz Force for Electromagnetic Sheet Impact Forming Process. *Proceedings of the Institution of Mechanical Engineers, Part B: Journal of Engineering Manufacture*. 227(2), pp. 324-332.

Chunfeng, L., Zhiheng, Z., Jianhui, L., Yongzhi, W. and Yuying, Y. (2002) *Journal of Materials Processing Technology*. 123, pp. 225-228.

Coleman, P. (2012) CRESCENDO – Collaborative and Robust Engineering using Simulation Capability Enabling Next Design Optimisation. TRIMIS – Transport Research and Innovation Monitoring and Information System. Available from: https://cordis.europa.eu/project/id/234344. [Accessed 10 November 2022].

Collins, I.F. and Williams, B.K. (1985) Slip-line fields for axisymmetric tube drawing. *International Journal of Mechanical Science*. 27(4), pp. 225-233.

Colorado (2017) Shear locking for solid elements in bending. Available from: https://www.colorado.edu/engineering/CAS/courses.d/AFEM.d/AFEM.pdf. [Accessed 10 October 2022]

Cora, Ö.N., Akkök, M. and Darendelier, H. (2008) Modelling of Variable Friction in Cold Forging. *Engineering Tribology*. 222(1), pp. 899-908.

Cui, X., Yu, H. and Wang, Q. (2018) Electromagnetic impulse calibration in V-shaped parts. *International Journal of Advanced Manufacturing Technology*. 97(5), pp 2959-2968.

Cui, X., Zhang, Z., Du, Z., Yu, H., Qiu, D., Cheng, Y. and Xiao, X. (2020). Inverse bending and springback-control using magnetic pulse forming. Journal of Materials Processing Technology. 275(1).

Deng X.G., Hui S.X., Ye W.J., Song X.Y. (2014) Construction of Johnson-Cook model for Gr2 Titanium through Adiabatic heating calculation. Applied Mechanics and Materials. 487, pp. 7–14.

Dieter, G.E. (1961) Metallurgy and metallurgical engineering series. London: McGraw-Hill.

Dixit, U.S. (2020) Modelling of metal forming: a review. *Mechanics of Materials in Modern Manufacturing Methods and Processing Techniques.* 1, pp. 1-30. https://doi.org/10.1016/B978-0-12-818232-1.00001-1.

Drgon (2020) *Quad roller swage tool*. Available from: https://ajdrgon.net/tools/quad-roller-swage-tool. [Accessed: 16 November 2020].

Du, Z., Yan, Z., Cui, X., Chen, B., Yu, H., Qiu, D., Xia, W. and Deng, Z. (2021) Springback control and large skin manufacturing by high-speed vibration using electromagnetic forming. Journal of Materials Processing Technology. 299(1).

Dupont (2022) *Molykote G-N plus Data Sheet*. Available from: https://www.dupont.com/resource-center. [Accessed 22 February 2022].

Dwivedi, R., Choundhary, M., Sahgal, K. and Purohit, R. (2021) Analysis of Friction Factor in Cold Forging by using Ring with Triangular Boss Compression Test. *Advances in Materials and Processing Technologies*. 8(3), pp. 1422-1440.

Dyna Support (2023) Available from: www.dynasupport.com/howtos/general/mass-scaling. [Accessed 12 February 2023].

Dynamic Metals (2022) *17/4PH Stainless Steel*. Available from: https://dynamicmetalsltd.com/products/stainless-steel/17-4ph. [Accessed 16 February 2022].

Eckert, C., Isaksson, O. and Earl, C. (2019) "Design margins: a hidden issue in industry", *Design Science,* Vol. 5(9), pp. 1–24. https://doi.org/10.1017/dsj.2019.7

El-Azab, A., Garnich, M. and Kapoor, A. (2003) Modeling of the electromagnetic forming of sheet metals: state-of-the-art and future needs. *Journal of Materials Processing Technology.* 142(1), pp. 744-754.

Ettouney, O. and Hardt, D.E. (1983) A method for in-process failure prediction in cold upset forging, *ASME Journal of manufacturing science and engineering*. 105(1), pp. 161–167.

Farmer, L.E. and Oxley, P.L.B. (1971) A slip-line field for plane-strain extrusion of a strain-hardening material, *Journal of physical solids*. 19(6), pp. 369-372.

Fereshteh-Saniee, F., Fallah-Nejad, K., Beheshtiha, A. S. and Badnava, H. (2013) Investigation of Tension and Compression Behavior of AZ80 Magnesium Alloy. *Materials and Design*. 50(1), pp. 702–712.

Fisher, R.A. (1926) The arrangement of field experiments. Journal of the Ministry of Agriculture. 33, pp. 503–513.

Fisher, R.A. (1935) The Design of Experiments. Macmillan: London.

Fischer, F.D., Rammerstorfer, F.G. and Daxner, T. (2006) Flaring – An Analytical Approach. *International Journal of Mechanical Sciences*. 48(11), pp. 1249-1255.

Foster, A.D., Copeland, T.J., Cox, C.J., Hall, P.W., Watkins, M.A., Wright, R. and Lin, J. (2009) Error Analysis and Correction in the Slab Method for Determining Forming Forces. *International Journal of Mechanical Education*. 37(4), pp. 304-317.

Gay, R. (2013) Friction and wear behaviour of self-lubricating bearing liners. PhD, Cardiff University.

Ghaei, A., Taheri, A.K. and Movahhedy, M.R. (2006) A new upper bound solution for analysis of the radial forging process. International Journal of Mechanical Sciences. 48 (11), pp. 1264-1272.

Gisbert, C., Bernal, C. and Camacho, A.M. (2015) Improved analytical model for the calculation of forging forces during compression of bimetallic axial assemblies. *Procedia Engineering*. Volume 132, pp. 298-305.

Gitschel, R., Kolpak, F., Hering, O. and Tekkaya, A.E. (2021) Increasing the Lightweight Potential of Composite Cold Forging by Utilizing Magnesium and Granular Cores. *Metals*. 11(1), pp 1-16.

Godet, M. Play, D.F and Berthe, D. (1980) An attempt to provide a unified treatment of tribology through load carrying capacity, transport, and continuum mechanics. *Journal of Lubrication Technology.* 102, pp. 153-164.

Gong, L., Yang, X., Kong, K and Zhong, S. (2018) Optimal design for outer rings of self-lubricating spherical plain bearings based on virtual orthogonal experiments. *Advances in mechanical engineering*. 10(6). pp 1-11.

Groche, P. and Tibari, K. (2006) Fundamentals of Angular Joining by Means of Hydroforming. *CIRP Annals - Manufacturing Technology.* 55(1), pp. 259–262.

Groche, P. and Türk, M. (2011). Smart structures assembly through incremental forming. *CIRP Annals - Manufacturing Technology.* 60(1), pp. 21–24.

Groche, P., Wohletz, S., Brenneis, M., Pabst, C. and Resch, F. (2014) Joining by forming. A review on joint mechanisms, applications, and future trends. *Journal of Materials Processing Technology*, Vol. 214(10), pp. 1972-1994. https://doi.org/10.1016/j.jmatprotec.2013.12.022.

Grote, K.H. and Antonsson, E.K. (2009) *Springer Handbook of Mechanical Engineering*. New York: Springer.

Gumm, P. (1964). Kombination Von Umformung und Kaltpresschweissen Beim Fliespressen und Rohrziehen. Dissertation, Braunschweig Technical University.

Hammers, T., Marre, M., Rautenberg, J., Barreiro, P., Schulze, V., Biermann, D., Brosius, A. and Tekkaya, A.E. (2009) Influence of Mandrel's Surface and Material on the Mechanical Properties of Joints Produced by Electromagnetic Compression. *Steel Research International*. 80(5), pp. 366-375.

Han, H. (2002) *Determination of Flow Stress and Coefficient of Friction for Extruded Anisotropic Materials under Cold Forming Conditions*. Stockholm: Royal Institute of Technology.

Haratmeh, H.E., Arezoodar, A.F. and Farzin, M. (2017) Numerical and experimental investigation of inward tube electromagnetic forming. *International Journal of Advanced Manufacturing Technology*. 88(1), pp. 1175-1185.

Hartley, C.S. (1973) Upper bound analysis of extrusion of axisymmetric, piecewise homogeneous tubes. International Journal of Mechanical Sciences. 15 (8), pp. 651-663.

Hazawi, K.A.R., Abdel-Magied, R.K. & Elsheikh, M.N. (2017) An experimental analysis of a flaring process for tube ends using a novel spinning tool. International Journal of Advanced Manufacturing Technology. 92(1), pp. 157–165. https://doi.org/10.1007/s00170-017-0106-7.

He, A., Xie, G., Zhang, H. and Wang, X. (2014) A modified Zerilli–Armstrong constitutive model to predict hot deformation behavior of 20CrMo alloy steel. Materials and Design. 56(1), pp. 122-127.

Hollomon, J.H. (1945) Tensile deformation, Transactions of the Metallurgical Society of AIME. Vol. 162, pp. 268-290.

Hoo, J. J. C. and Green, W.B. (1998) *Bearing Steels: Into the 21st Century*. Pennsylvania: ASTM International. https://doi.org/10.1520/stp1327-eb

Horwatitsch, D., Merstallinger, A. and Steinhoff, K. (2012). Evaluation of the Ring Compression Test for the Parameter Determination of Extended Friction Models. In: Weiland, H., Rollett, A.D., Cassada, W.A. (eds) ICAA13 Pittsburgh: Springer. https://doi.org/10.1007/978-3-319-48761-8_98.

Hosford, W.F. and Caddell, R.M. (2007) *Metal Forming: Mechanics and Metallurgy*. 3rd ed. Cambridge: Cambridge University Press.

Hu, C., Chen, H., Zhang, W. and Ohshita, H. (2023) Enhancing the sensitivity of a tribological testing method to enable development of lubricants for cold forging. Tribology International. 179, pp. 1-10.

Isik, K., Soyarslan, C., Richter, H. and Tekkaya, A.E. (2011). Analysis of formability of advanced high strength steel sheets with phenomenologically based failure criteria with separate treatment of instability, shear and normal fracture. LS-DYNA 8th European Users Conference, Strasbourg, France.

Jäger, A., Hänisch, S., Bröckerhoff, S., Tekkaya, A.E., 2012. Method for producing composite parts by means of combination of deep drawing and impact extrusion. Patent Number EP2707158B1.

Jin, R., Chen, W. and Sudjianto, A. (2003) "An efficient algorithm for constructing optimal design of computer experiments". In Volume 2: 29th Design Automation Conference, Parts A and B, Vol. 2, pp. 545–554. https://doi.org/10.1115/detc2003-dac-48760

Joseph, V. R., Gu, L., Ba, S. and Myers, W. R. (2019) "Space-filling designs for robustness experiments", *Technometrics*, Vol. 61, pp. 24–37. https://doi.org/10.1080/00401706.2018.1451390

Kahhal, P., Yeganehfar, M. and Kashfi, M. (2021) An Experimental and Numerical Evaluation of Steel A105 Friction Coefficient Using Different Lubricants at High Temperature. *Tribology Transactions*. 65(1), pp. 25-31.

Kalpajian, S. (1997) *Manufacturing Processes for Engineering Materials*, 3rd ed. California: Pearson Education.

Kalpajian, S. and Schmid, S.R. (2008) *Manufacturing Processes for Engineering Materials*, 5th ed. California: Pearson Education.

Kamble, D.N. and Nandedkar, V.M. (2011) Slab Method Modification and Its Experimental Investigation for Hot Forming Process. Materials and Manufacturing Processes. 26(5), pp. 677-683. https://doi.org/10.1080/10426910903179948.

Kapelevich, A.L. (2009) Direct design of asymmetric gears: approach and application. In JSME International Conference on Motion and Power Transmissions. Japan 2009.

Kapelevich, A.L. (2011) Asymmetric Gears: Parameter Selection Approach. *Applied Mechanics and Materials*. 86(1), pp. 70-73.

Karras, (2018). Tribology And Condition Monitoring Of Composite Bearing Liners. PhD, Cardiff University.

Kaviti, A.K. and Thakur, A.K. (2021) Prediction of coefficient of friction by using ring with triangular boss compression test. *Advances In Materials And Processing Technologies.* 8(3), pp. 2999-3012.

Kazeminezhad, M., Karimi Taheri, A., 2006. Calculation of the rolling pressure distribution and force in wire flat rolling process. J. Mater. Process. Technol. 171, 253–258.

Khan, O,U., Jamal, A., Arshed, G.M., Arif, A.F.M. and Zubair S.M. (2004) Thermal analysis of a cold rolling process—a numerical approach, Numerical Heat Transfer, Part A: Applications. 46 (6), pp. 613-632.

Khraisat, W. (2023) Strain hardening exponent and strain rate sensitivity exponent of dual-phase steels at quasi-static strain rates during tensile testing. *Cogent Engineering*. 10(2). DOI: 10.1080/23311916.2023.2274548

Kim, B.C., Park, D.C. and Kim, H.S. (2006) Development of composite spherical bearing, *Composite Structures*, Vol. 75, pp. 231–240. https://doi.org/10.1016/j.compstruct.2006.04.027.

Kim, H.S. (2010) A combined FEA and design of experiments approach for the design and analysis of warm forming of aluminium sheet alloys. *International Journal of Advanced Manufacturing Technology*, Vol. 51, pp. 1-14. https://doi.org/10.1007/s00170-010-2620-8

Kiuchi, M., Shintani, K. and Hwang, Y.M. (1992) Mathematical Simulation of Clad Sheet Rolling and Sandwich Sheet Rolling. *Annals of the CIRP*. 41(1), pp. 289–292.

Kobayashi, S. (1982) A review on the finite-element method and metal forming process modeling. *Journal of Applied Metalworking*. 2(1), pp. 163-169.

Kobayashi, S., Altan, T. and Oh, S.I. (1989) *Metal Forming and the Finite Element Method*. 4th ed. Oxford: Oxford University Press.

Kosaraju, S. (2020) Time integration Methods. Fidelis Engineering Associates [Online]. Available from: www.fidelisfea.com/post/time-integration-methods. [Accessed 23 February 2024].

Krishna, R.H. and Jena, D.P. (2019) Analytical and numerical modelling of open-die forging process for elliptical cross-section of billet. Measurement. 134, pp. 855-865.

Kudo, H. (1990) Towards net-shape forming. *Journal of Materials Processing Technology*. 22(3). pp 307-342.

Kunogi, M. (1956) A New Method of Cold Extrusion. *Journal of Scientific Research Institute*. 50(1437), pp. 215–246.

Kwan, C.T., Fang, C.H., Chiu, C.J., Chen, S.W. and Wen, H.W. (2004) An Analysis of the Nosing using elasto-plastic and rigid-plastic methods. Journal of material process technology. 23(3), pp. 190-196

Kweon, H.D., Kim, J.W., Song, O. and Oh, D. (2021) Determination of true stress-strain curve of type 304 and 316 stainless steels using a typical tensile test and finite element analysis. *Nuclear Engineering and Technology*. 53(2). pp. 647-656.

LaBerge, K.E., Handschuh, R.F., Roberts, G. and Thorp, S. (2016). Performance investigation of a full-scale hybrid composite bull gear. In: *Proceedings of the 72nd American Helicopter Society International Annual Forum*. West Palm Beach, May 2016. 3(1), pp 2591-2597.

Lancaster, J.K. (1982) Accelerated wear testing as an aid to failure diagnosis and materials selection. *Tribology International*. 15, pp. 323-329.

Lange, K., Kammerer, M., Pöhlandt, K. and Schöck, J. (2008) Fließpressen – Wirtschaftliche Fertigung metallischer Präzisionswerkstücke. Springer Verlag, Berlin.

Larson, M.G and Bengzon, F. (2013) The Finite Element Method: Theory, Implementation, and Applications. Cambridge University Press.

Lee, W.S. and Liu, C.Y. (2006) The effects of temperature and strain rate on the dynamic flow behaviour of different steels. Material Science and Engineering A. 426(1), pp. 101–113

Lehman, J. S., Santner, T. J. and Notz, W. I. (2004) Designing computer experiments to determine robust control variables. Statistica Sinica 14 (2), pp. 571–590.

Li, T., Zhao, B., Lu, X., Xu, H. and Zou, D.A. (2019) Comparative Study on Johnson Cook, Modified Zerilli-Armstrong, and Arrhenius-Type Constitutive Models to Predict Compression Flow Behavior of SnSbCu Alloy. Materials (Basel). 12(10). DOI: 10.3390/ma12101726.

Liu, Y.M., Ma, G.S., Zhang, D.H. and Zhao, D.W. (2015) Upper bound analysis of rolling force and dog-bone shape via sine function model in vertical rolling. Journal of Materials Processing Technology. 223, pp. 91-97.

Lu, J., Qiu, M. and Li, Y. (2016) Wear models and mechanical analysis of PTFE/Kevlar fabric woven liners used in radial spherical plain bearings. *Wear*. 364(1). pp 57-72.

Luan, X., Hu, Y. and Chen, Y. (2015) Finite Element Simulation Analysis of Double Nosing Process in the Assembly of Spherical Plain Bearings. *International Journal of Research in Engineering and Science*. 3(51). pp 1-7.

Ma, Z.E., 1980. The research on the deformation and spinning force calculation for the cylindrical power spinning. Proceedings of the First Chinese Conference on Spinning, 33–51

Maire, E., and Withers, P.J. (2014) Quantitative X-ray computed tomography. *International Materials Reviews*. 59(1). pp 1–43.

Male, A. and Cockcroft, M.G. (1966). A Method for the Determination of the Coefficient of Friction of Metals Under Conditions of Bulk Plastic Deformation. *Journal of the Institute of Metals*. 93(3), p.241.

Male, A. and DePierre, V. (1970). The Validity of Mathematical Solutions for Determining Friction From the Ring Compression Test. *Journal of Lubrication Technology*. 92(3), pp. 389–395.

Marinov, V. (2010) Manufacturing Processes for Metal Products. Iowa: Kendall/Hunt.

Martin, F., Martin, M.J., Sevilla, L. and Sebastian, M.A. (2015) The ring compression test: Analysis of dimensions and canonical geometry. *Procedia Engineering*. 132(2015), pp. 326-333.

MathWorks (2022) Matlab Software Package. Available from: https://uk.mathworks.com/products/matlab.html. [Accessed 10 November 2022].

MathWorks (2024) Machine learning overview. Available from: https://uk.mathworks.com/discovery/machine-learning.html [Accessed 27 April 2024].

Matsubara, T., Yasui, K., Yoshida, Y., Wang, Z.G., Ishikawa, T. and Suganuma, T. (2011) Influence of processing conditions on joint strength in backward extrusion forged bonding. *Materials Research Innovations*. 15(1), pp. 443-445.

Merklein, M., Allwood, J.M., Behrens, B.A., Brosius, A., Hagenah, H., Kuzman, K., Mori, K., Tekkaya, A.E. and Weckenmann, A. (2012). Bulk forming of sheet metal. *CIRP Annals*. 61(2), pp. 725–74.

Merklein, M., Tekkaya, A.E., Brosius, A., Opel, S. and Koch, J. (2011) Overview on Sheet-Bulk Metal Forming Processes. In: Proceedings of the 10th International Conference on Technology of Plasticity. pp. 1109–1114.

Merklein, M., Grobel, B. Loffler, M., Schneider, T. and Hildenbrand, P. (2015) Sheet-bulk metal forming – forming of functional components from sheet metals. In: *4th International conference on new forming technology*. Erlangen, August 2015.

Mielnik, E.M. (1991) Metalworking Science and Engineering. New York: McGraw-Hill.

Minitab (2020a) What is the design resolution in a factorial design? Available from: https://support.minitab.com/en-us/minitab/20/help-and-how-to/statistical-modeling/doe/supporting-topics/factorial-and-screening-designs/what-is-design-resolution. [Accessed 14 February 2022].

Minitab (2020b) Minitab Statistical Software. Available from: https://www.minitab.com/en-us/products/minitab. [Accessed 10 February 2022].

Molykote (2023) Molykote G-N Plus Paste. Available from https://www.dupont.com/products/molykote-g-n-plus-paste.html. [Accessed 30 January 2023].

Moon, H.K., Lee, M.C. and Joun, M.S. (2007) An approximate efficient finite element approach to simulating a rotary forming process and its application to a wheel-bearing assembly. *Finite Elements in Analysis and Design*. 44(2007). pp 17-23.

Mori, K.I., Bay, N., Fratini, L., Micari, F. and Tekkaya, A.E. (2013) Joining by Plastic Deformation. *CIRP Annals, Manufacturing Technology*. Vol. 62(2), pp. 673-694. https://doi.org/10.1016/j.cirp.2013.05.004.

Mori, K. and Nakano, T. (2016) State of the art of plate forging in Japan. Production engineering. 10(1), pp. 81–91.

Mucha, J. (2011) The analysis of lock forming mechanism in the clinching joint. *Materials & Design*. 32, pp. 4943–4954.

Napierala, O., Dahnke, C. and Tekkaya, A.E. (2019) Simultaneous deep drawing and cold forging of multi-material components: Draw-forging. *CIRP Annals*. 68(1) pp. 269-272.

Narayanan, R.G., Mitchell, M.R., Link, R.E., Gopal, M. and Rajadurai, A. (2008) Influence of Friction in Simple Upsetting and Prediction of Hardness Distribution in a Cold Forged Product. *Journal of Testing and Evaluation*. 36(4) , pp. 1–13.

Nerenst, T.B, Ebro, M., Nielsen, M. Eifler, T. and Nielsen, K.L. (2021) Exploring barriers for the use of FEA-based variation simulation in industrial development practice. *Design Science*, Vol. 7(21), pp. 1-22. https://doi.org/10.1017/dsj.2021.21

Neugebauer, R., Kraus, C. and Dietrich, S. (2008) Advances in Mechanical Joining of Magnesium. *CIRP Annals - Manufacturing Technology* . 57(1), pp. 283–286.

Noh, H.G., An, W.J., Song, W.J., Kang, B.S. and Kim, J. (2005) Experimental and Numerical Study on Patterned Emboss Forming Using Electromagnetic Forces. *International journal of precision engineering and manufacturing*. 16(7), pp. 1477-1454.

Onodera, Y. and Chiba, A. (2009) Evaluation of Friction Coefficient by Simulation in Bulk Metal Forming Process. *Metallurgical and Materials Transactions*.

Opela, P., Schindler, I., Kawulok, P., Vancura, F., Kawulok, R. and Rusz, S. (2015) Hot flow stress models of the steel C45. *Metalurgija*. 54(3), pp. 453-596.

Orsolini, A. (2010) *Major Project Task 1, Compressive Testing*. MSc Advanced Mechanical Engineering. Bristol University. 41, pp. 224-232.

Orsolini, A. and Booker, J.D. (2012) Modelling capabilities required for the double nosing process in the assembly of spherical plain bearings. *Journal of Engineering Manufacture*. 226(5), pp. 930-940.

Ossenkemper, S., Dahnke, C., Ben Khalifa, N. and Tekkaya, A.E. (2017). Producing steel-aluminium-composite shafts with conventional cold forging tools. In: Proceedings of the 50th ICFG Plenary Meeting. Shanghai, China

Ossenkemper, S. (2018a) Verbundfließpressen in konventionellen Fließpresswerkzeugen. TU Dortmund.

Ossenkemper, S., Dahnke, C. and Tekkaya, A.E. (2018b) Analytical and experimental bond strength investigation of cold forged composite shafts. *Journal of Material Processing Technology*. 264(1), pp 190-199.

Oudjene, M. and Ben-Ayed, L. (2008) On the parametrical study of clinch joining of metallic sheets using the Taguchi method. *Engineering Structures*, Vol. 30(6), pp. 1782–1788. https://doi.org/10.1016/j.engstruct.2007.10.017.

Öztürk, E., Yıldızlıa, k., Memmedov, R. and Ülgen, A. (2018) Design of an experimental setup to determine the coefficient of static friction of the inner rings in contact with the outer rings of radial spherical plain bearings. *Tribology International*. 128(2018). pp 161-173.

Parghazeh, A. and Haghighat, H. (2016) Prediction of central bursting defects in rod extrusion process with upper bound analysis method, Transactions of Nonferrous Metals Society of China. 26(11), pp. 2892-2899.

Peirce, C.S. and Jastrow, J. (1885) On Small Differences in Sensation. *Memoirs of the National Academy of Sciences*. (3), pp. 73-83.

Peirce, C.S. (1887) *Illustrations of the Logic of Science*. Open Court: Chicago.

Play, D.F. and Pruvost, B. (1984) Comparative dry Wear of PTFE Liner Bearing in Cylindrical and Spherical Geometry. ASME Journal of Tribology, 106(2), pp. 185-191.

Play, D.F. (1985) Mutual Overlap Coefficient and Wear debris motion in dry oscillating friction and wear tests. *ASLE Transactions*. 28, pp. 527-535.

Python (2024) Python programming language. Available from : https://www.python.org/ [Accessed 10 February 2024].

Qi, X., Ma, J., Jia, Z., Yang, Y. and Gao, H. (2014) Effects of weft density on the friction and wear properties of self-lubricating fabric liners for journal bearings under heavy load conditions. *Wear*. 318(1). pp 124-129.

Rajak, A.K. and Kore, S.D. (2017) Experimental investigation of aluminium–copper wire crimping with electromagnetic process: Its advantages over conventional process. *Journal of Manufacturing Processes.* 26(1), pp 57-66.

Rajak, K.M., Kumar, R., Basumatary, H. and Kore, S.D. (2018). Numerical and Experimental Study on Effect of Different Types of Field-Shaper on Electromagnetic Terminal-Wire Crimping Process. *International Journal of Precision Engineering and Manufacturing*. 19(3), pp 453-459.

Razani, N.A., Dariani, B.M. and Soltanpour, M. (2018) Analytical approach of asymmetrical thermomechanical rolling by slab method, *International Journal of Advances Manufacturing Technology*. 94 (4), pp. 175-189.

RS Components (2023) Dial Torque Clock. Available from: https://uk.rs-online.com/web/p/torque-testers/0663904. [Accessed 09 January 2023].

Rubio, E.M., Camacho, A.M., Sevilla, L., Sevilla, L. and Sebastián, M.A. (2005) Calculation of the forward tension in drawing processes. Journal of Material Process Technology. 162, pp. 551–557.

Rubio, E.M. (2006) Analytical methods application to the study of tube drawing processes with fixed conical inner plug: Slab and Upper Bound Methods. Journal of Achievements in Materials and Manufacturing Engineering. 14(2), pp. 119–130.

SAE International (2014) AS81820 Bearings, Plain, Self-Aligning, Self-Lubricating, Low Speed Oscillation, General Specification. Warrendale: SAE International.

SAE International (2018) AS14104 Bearing, Plain, Self-Lubricating, Self-Aligning, Low Speed, Narrow, Chamfered Outer Ring, -65°F to 325°F. Warrendale: SAE International.

Salimi, M. and Sassani, F. (2002) Modified slab analysis of asymmetrical plate rolling. *International Journal of Mechanical Science*. 44(9), pp. 1999-2023.

Salimi, M. and Kadkhodaei, M. (2004) Slab analysis of asymmetrical sheet rolling. *Journal of Material Process Technology*. 150(3), pp. 215-222.

Samołyk, G. (2013) Investigation of the cold orbital forging process of an AlMgSi alloy bevel gear. *Journal of Materials Processing Technology*. 213(10), pp. 1692-1702.

Samuel, K.G. (2006) Limitations of Hollomon and Ludwigson stress-strain relations in assessing the strain hardening parameters. Journal of Physics D: Applied Physics. 39(1) 203-210.

Santner, E. and Czichos, H. (1989) Tribology of Polymers. *Tribology International*. 22, pp. 103-109.

Sarema, B., Matope, S. and Sterzing, A. (2022) "Design of experiments procedure for evaluating the formability of sheet metals components in forming processes" *Southern African Institute of Industrial Engineers 33rd Annual Conference, KwaZulu-Natal, 3-5 October 2022.*

Sarker, I.H. (2021) Machine Learning: Algorithms, Real-World Applications and Research Directions. SN Computer Science. 2(160). https://doi.org/10.1007/s42979-021-00592-x

Schäfer, R., Pasquale, P. and Stephan, K.D. (2010). Industrial Application of the Electromagnetic Pulse Technology. In: Proceedings of the 4th International Conference on High-Speed Forming-ICHSF. March, 2010, Ohio.

Sener, B. and Yurci, M.E. (2017) Comparison of Quasi-Static Constitutive Equations and Modeling of Flow Curves for Austenitic 304 and Ferritic 430 Stainless Steels. Acta Physica Polonica A. 131(3), pp 605-607.

Shaun, T. (2007) Asperities. Available from: https://commons.wikimedia.org/wiki/File:Asperities.svg. [Accessed 24 April 2021].

Shen, X., Gao, P., Liu, Z. and Chen, X. (2014) Elastic Properties of the Fabric Liner and Their Influence on the Wear Depth of the Spherical Plain Bearing. *Journal of Nanomaterials*. 2014(1). pp 1-7.

Shrot A., Bäker M. (2012) Determination of Johnson–Cook parameters from machining simulations. Computational Material Science. 52(1), pp. 298–304.

Sieczkarek, P., Wernicke, S., Gies, S., Tekkaya, A.E., Krebs, E., Wiederkehr, P., Biermann, D., Tillmann, W. and Stangier, D. (2016). Wear behaviour of tribologically optimized tool surfaces for incremental forming processes. *Tribology International.* 104(1), pp. 64–72.

Sieczkarek, P., Wernicke, S., Gies, S., Tekkaya, A. E., Krebs, E., Wiederkehr, P., Biermann, D., Tillmann, W. and Stangier, D. (2017) Improvement Strategies for the Form filling in Incremental Gear Forming Processes, *Production Engineering*. 11(6), pp. 623-631.

Sigmetrix (2022) Understanding Statistical Tolerance Analysis. Available from: https://www.sigmetrix.com/case-studies-2/tolerance-analysis-case-studies-white-papers/statistical-tolerance-analysis-2/. [Accessed 16 September 2022].

Simon, M. and Sauerwein, C. (2000) Quality control of light metal castings by 3D computed tomography. In: *15th world conference on non-destructive testing*. Rome, 15-21 October 2000.

SimScale (2022) How To Keep the Courant Number Below 1?. Available from: https://www.simscale.com/knowledge-base/what-is-a-courant-number. [Accessed 12 February 2023].

SimScale (2024) Elastic-plastic material models. Available from: https://www.simscale.com/docs/simulation-setup/materials/plastic-materials. [Accessed 28 February 2024].

Sinha, M.K., Deb, S. and Dixit, U.S. (2009) Design of a multi-hole extrusion process. Materials and Design. 30(2), pp. 330-334.

SKF (2002) Internal Engineering and Technical Instruction directive. Clevedon: SKF Ltd. Unpublished internal company document.

SKF (2003) Self-lubricating plain spherical bearing design manual. Clevedon: SKF Ltd. Unpublished internal company document.

SKF (2008) Technical Report Liner Compressive Stiffness Analysis. Clevedon: SKF Ltd. Unpublished internal company document.

SKF (2017). Aerospace Plain Spherical Competitor Analysis. Clevedon: SKF Ltd. Unpublished internal company document.

SKF (2019). Internal Sales Report. Clevedon: SKF Ltd. Unpublished internal company document.

SKF (2021) Channel 22 (Rod End Staking) Process Report. Clevedon: SKF Ltd. Unpublished internal company document.

SKF (2022a) SKF portfolio. Available from: www.skf.com/uk. [Accessed 04 December 2022]

SKF (2022b) SKF production logs for November 2022. Clevedon: SKF Ltd. Unpublished internal company document.

SKF (2023) User feedback survey on the staking tool. Clevedon: SKF Ltd. Unpublished internal company document.

Smith, K. (1916) On the 'best' values of the constants in frequency distributions. Biometrika, 11(3), pp. 262–276.

Sofuoglu, H. and Rasty, J. (1999) On the measurement of friction coefficient utilizing the ring compression test. *Journal of Engineering Materials and Technology*. 123(3), pp. 338-348.

Sofuoglu, H., Gedilkli, H. and Rasty, J. (2001) Determination of friction coefficient by employing the ring compression test. *Journal of Engineering Materials and Technology*, *Transactions of the ASME*. 123(3), pp. 338-348

Sofuoglu, H. Gedikli, H. (2002) "Determination of Friction Coefficient Encountered in Large Deformation Processes," *Tribology International*. 35(1), pp. 27–34.

Sun, J., Liu, Y.M., Hu, Y.K., Wang, Q.L., Zhang, D.H. and Zhao, D.W. (2016) Application of hyperbolic sine velocity field for the analysis of tandem cold rolling, Internal Journal of Mechanical Sciences. 108-109, pp. 166-173.

Swift, K.G. and Booker, J.D (2003) *Process selection: from design to manufacture*. 2nd ed. London: Elsevier.

Swift, K.G. and Booker, J.D (2013) Manufacturing process selection handbook: from design to manufacture. London: Elsevier.

Taguchi, G., Chowdhury, S. & Wu, Y. (2007) *Taguchi's Quality Engineering Handbook*. Michigan: John Wiley & Sons, Inc. https://doi.org/10.1002/9780470258354.ch4.

Tang, M. and Kobayashi, S. (1982) An investigation of the shell nosing process by the finite element method. *Journal of Engineering Industry.* 104(82), pp. 305-311.

Tekkaya, A. E., Ben Khalifa, N., Grzancic, G. and Hölker, R. (2014) Forming of lightweight metal components: Need for new technologies. *Procedia Engineering*. 81(1), pp. 28-37.

Thomsen, E.G., Bierbower, J.B. and Yang, C.T. (1954) An Experimental Investigation of the Mechanics of Plastic Deformation of Metals. Berkeley: University of California Press.

Thomson, P.F. and Brown, J.H. (1982) A study of deformation during cold rolling using visioplasticity, *International Journal of Mechanical Science*. 24(9), pp. 559-576.

University of Cambridge (2021) Analysis of deformation processes. Available from: https://www.doitpoms.ac.uk/tlplib/metal-forming-3 [Accessed 13 January 2021].

Valberg, H.S. (2012) *Applied Metal Forming: Including FEM Analysis*. Cambridge: Cambridge University Press.

Vanhulsel, P., Wonterghem, M.V., Waele W.D., and Faes, K. (2011) Groove Design for Form Fit Joints Made by Electromechanical Pulse Crimping. In: Proceedings of the conference Sustainable Construction and Design 2011. February 2011. pp. 432-441.

Wagener, H.W. and Haats, J. (1994). Pressure welding of corrosion resistant metals by cold extrusion. *Journal of Materials Processing Technology*. 45(1–4), pp. 275–280.

Wang, Q., Khan, M.K. and Bathias, C. (2012) Current understanding of ultra-high cycle fatigue. *Theoretical and Applied Mechanics Letters.* 2(3).

Wang, W., Ma, Y., Yang, M., Jiang, P., Yuan, F. and Wu, X. (2018) Strain Rate Effect on Tensile Behaviour for a High Specific Strength Steel: From Quasi-Static to Intermediate Strain Rates. *Metals.* 8(1), pp 1-11.

Wang, Q., Chen, J., Zhou, H., Wang, X. and Hu, Z. (2021) Research on Multi-Stage Composite Loading Process Control Method for Roller Staking of Self-Lubricating Spherical Plain Bearings. *Applied Sciences*. 11(23), pp. 1-14.

Wang, Q., Chen, J., Liu, C., Zhou, H., Wang, X. and Hu, Z. (2022) Research on loading parameters of roller swaging process of self-lubricating spherical plain bearings. *International Journal of Advanced Manufacturing Technology.* 118, pp. 3737-3747.

Weber, F., Gebhard, J., Gitshel, R., Goyal, S., Kamaliev, M., Wernicke, S. and Tekkaya, A.E. (2021) Joining by forming –A selective review. *Journal of Advanced Joining Processes.* 3(1).

Weddeling, C., Woodward, S.T., Marre, M., Nellesen, J., Psyk, V., Tekkaya, A.E. and Tillmann, W. (2011) Influence of Groove Characteristics on Strength of Form-Fit Joints. *Journal of Materials Processing Technology.* 211(5), pp. 925–935.

Weddeling, C., Demir, O.K., Haupt, P. and Tekkaya, A.E. (2015a) Analytical methodology for the process design of electromagnetic crimping. *Journal of Material Process Technology*. 222(1), pp. 163–180.

Weddeling, C., Walter, V., Haupt, P., Tekkaya, A.E., Schulze, V. and Weidenmann, K.A., (2015b). Joining zone design for electromagnetically crimped connections. *Journal of Material Process Technology*. 225(1), pp. 240–261.

Wells, J.M. (2007) Quantitative XCT evaluation of porosity in an aluminium alloy casting. In: Crepeau, P.N., *Shape casting: 2nd international symposium*. 3-6 June 2018.

Wernicke, S., Gies, S. and Tekkaya, A.E. (2019). Manufacturing of hybrid gears by incremental sheet-bulk metal forming. *Procedia Manufacturing*. 27(1), pp. 151–157.

Wernicke, S., Hahn, M., Gerstein, G., Nürnberger, F. and Tekkaya, A.E. (2020). Strain path dependency in incremental sheet-bulk metal forming. *International Journal of Material Forming*. 14(4), pp 547-561.

Wernicke, S., Hahn, M. and Tekkaya, A.E. (2021). Fundamental research and process development for the manufacturing of load-optimized parts by incremental sheet-bulk metal forming. In: Merklein, M., Tekkaya, A.E. and Behrens, B.A., ed (2021) *Sheet Bulk Metal Forming*. New York: Springer International Publishing, pp. 53-77.

Will, J. (2015) Robust design optimization in virtual prototyping – promises and challenges. In NAFEMS - International Association Engineering Modelling.

Wohletz, S., Özel, M. and Groche, P. (2013) Combined cold extrusion of aluminium and steel - A production technique combining high strength and lightweight material in a cold state. *New Developments in Forging Technology.* pp. 319-323.

Woodhead, J., Truman, C.E., Booker, J.D. and Davydov, V. (2014) Measurement of forming stresses in plain spherical bearings using neutron diffraction. *Materials Science*. 777(1). pp 58-64.

Woodhead, J. (2015a) *Stochastic modelling of the cold-forming nosing process*. PhD. Bristol University.

Woodhead, J., Truman, C.E. and Booker, J.D. (2015b) Modelling of dynamic friction in the cold forming of plain spherical bearings. *Contact and Surface* 2015. Valencia, 21-23 April 2015. Southampton: WIT Press, pp.141-152. https://doi.org/10.2495/secm150131

Wu, J., Ma, Z., Zhou, Y. and Lu, C. (2013) Prediction of Failure Modes during Deep Drawing of Metal Sheets with Nickel Coating. *Journal of material science and technology*. 29(11), pp. 1059-1066.

Wu, Y., Dong, X. and Yu, Q. (2015) Upper bound analysis of axial metal flow inhomogeneity in radial forging process, International Journal of Mechanical Sciences. 93, pp. 102-110.

Zhang, T., 2009. Spinning Process. Chemical Industry Press of Beijing, pp. 99–100.

Zhang, Q., Jin, K. and Mu, D. (2014) Tube/tube joining technology by using rotary swaging forming method. *Journal of Materials Processing Technology.* 214(10), pp. 2085-2094

Zhang, Q., Hu, Z., Ma, J., Qi, X. and Yang, Y. (2017) Investigation of the roller swaging process for self-lubricating spherical plain bearings assembly. *Journal of Materials Processing Technology*. 241(1), pp. 36-45.

Zhang, Q., Hu, Z., Su, W., Zhou, H., Qi, X. and Yang, Y. (2018a) Investigation on housing chamfer parameters in roller swaging for self-lubricating spherical plain bearings assembly, *International Journal of Advanced Manufacturing Technology*, Vol. 95, pp. 1089-1099. https://doi.org/10.1007/s00170-017-1280-3.

Zhang, S.H., Song, B.N., Gao, S.W., Guan, M., Zhou, J. and Chen, X.D. (2018b) Upper bound analysis of a shape-dependent criterion for closing central rectangular defects during hot rolling. Applied Mathematical Modelling. 55, pp. 674-684.

Zhu, Y. (2017) Best practices for contact modelling using ANSYS [Webinar]. ANSYS, July 2017.

Appendix A: Pushout Investigation

This report was conducted to investigate the difference in pushout load when pushing out on the ball face compared to the outer race.

The bearing geometry being modelled can be seen in Figure A130 and represents a mid-range sized bearing with a Type III groove. The FEA model used to create the "staking-tool" was used for this investigation with the material designation of AMS5643 H1150 for the outer race and AMS5643 H1025 for the rod end.
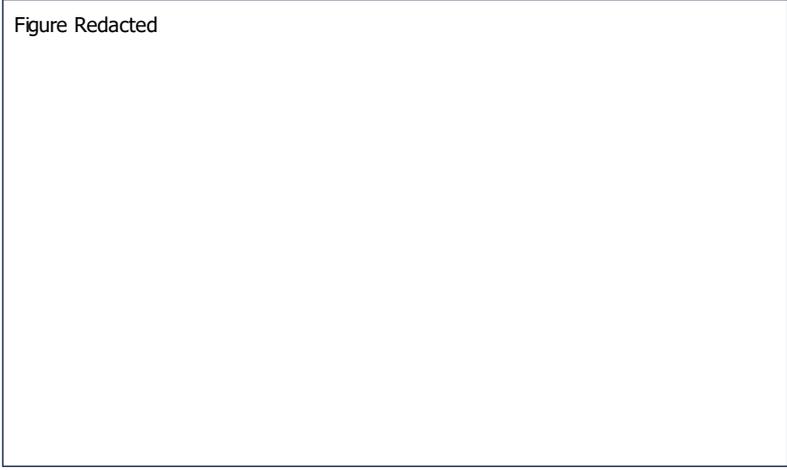
Figure Redacted

Figure A130: Bearing and rod end geometry. All dimensions in mm.

For each of the two pushout methods the bearing was staked to 3 different levels: minimum viable stake, maximum stake, and over-staked. The minimum and maximum conditions are defined by the "staking-tool" and are equivalent to a staking force of 180kN and 245kN respectively. The overstake condition was set to the maximum range of the staking-tool at an equivalent staking force of 305kN.

The load profile for each staking and pushout condition can be seen in Figure A131 with the peak pushout load summarised in Figure A132. In summary, the peak pushout load is approximately equal between the ball and outer race if the bearing is staked to its minimal condition. As the stake is further formed, then pushing out via the ball produces a larger peak pushout load. However, under all staked conditions, pushing out via the ball results in a more compliant joint compared to the outer race.

Figure Redacted

Figure A131: Pushout load comparison between pushing out via the ball face and the outer race for 3 staking conditions; minimum viable staking force, maximum staking force, and an over-staked bearing.

Figure Redacted

Figure A132: Peak pushout load for each staking condition.

When pushing out via the outer race, the pushout anvil is close enough to the upper staking lip such that pushout force is predominantly supported by the contact between the upper staking lip and the rod end chamfer. (upper staking lip is defined as the lip on the side of the pushout tool). This concentrates stresses around the upper staking lip (Figure A133 Upper) and causes it to shear during pushout with minimal inward radial movement of the outer race.

However, when pushing out via the ball face, the load path passes through the opposite end of the outer race and into the lower section of the rod end. The outer race then begins to pivot about the upper staking lip leading to a more complex stress state (Figure A133 Lower) and a greater inward radial displacement of the upper section of the outer race. This mechanism explains the greater compliance of the staking joint when pushing out via the ball face as was seen in Figure A131.
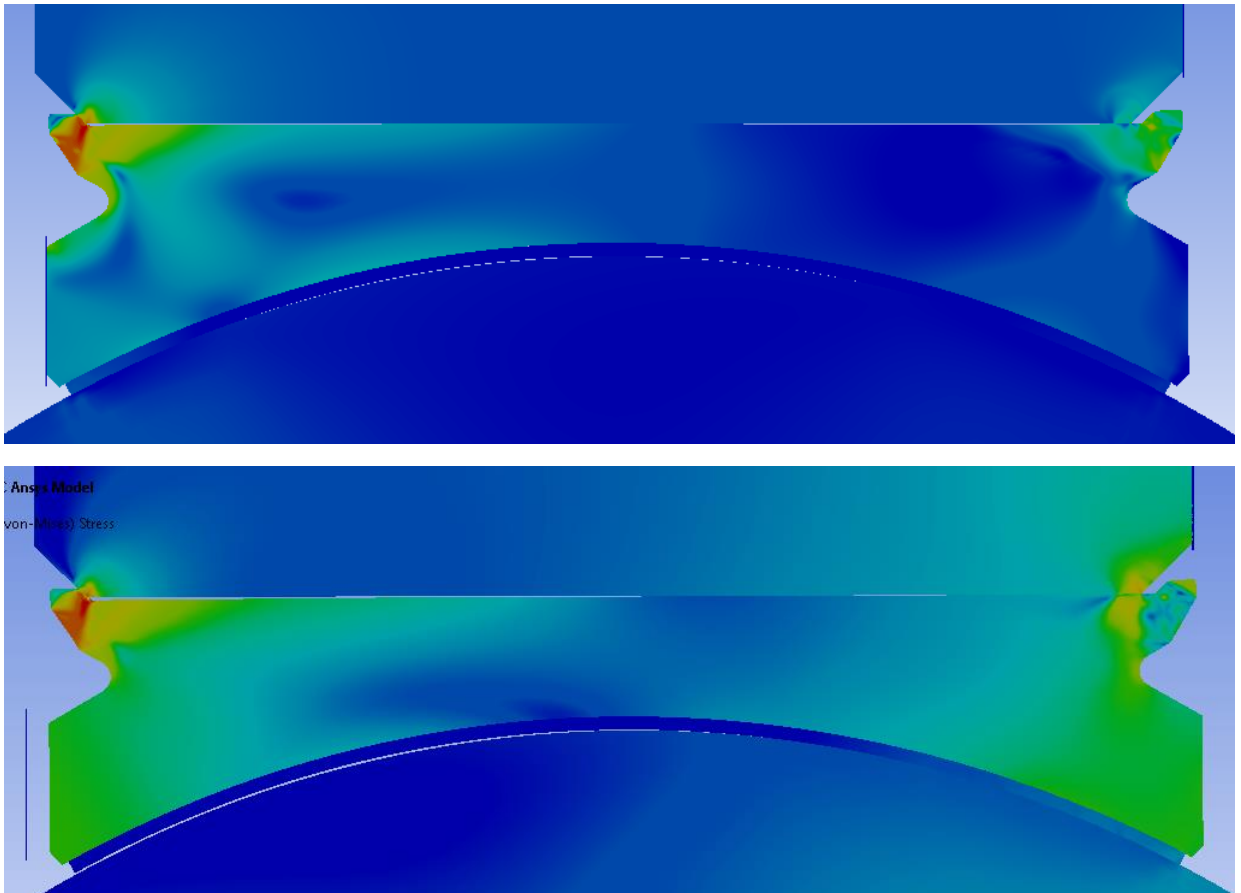
Figure A133: Stress contour plot at peak pushout load via the outer race (Upper) and ball face (Lower). In both instances the pushout anvil is moving left to right and the stress contours are equally scaled.

When the outer race is pushed out by the ball face, a large contact pressure is generated between the lower end of the outer race and rod end. This contact area during pushout is shown in Figure A134 and a comparison between the ball face and outer race contract pressure is shown in Figure A135.
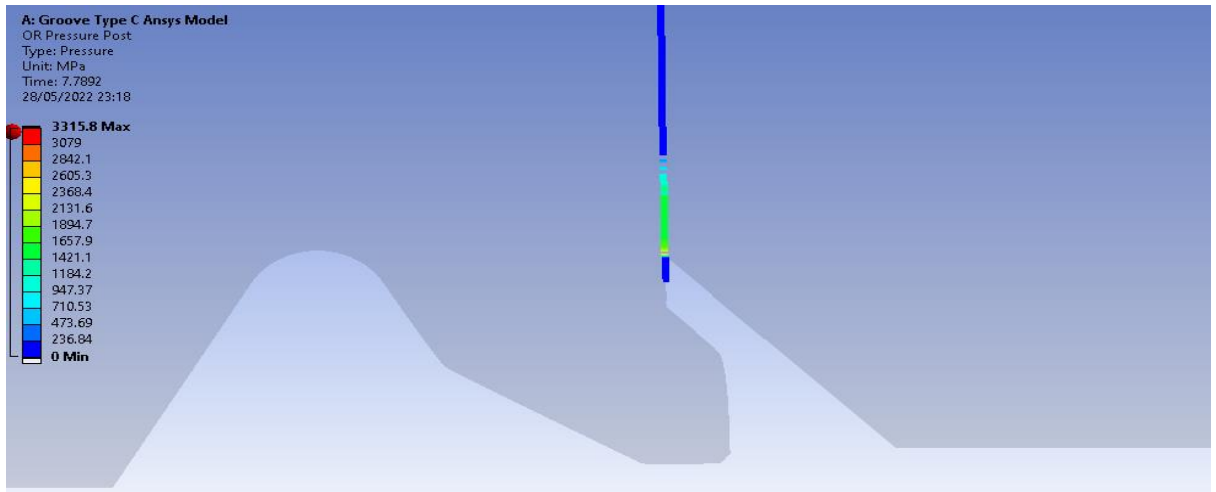
Figure A134: Contact pressure plot between the outer race and rod end during pushout.
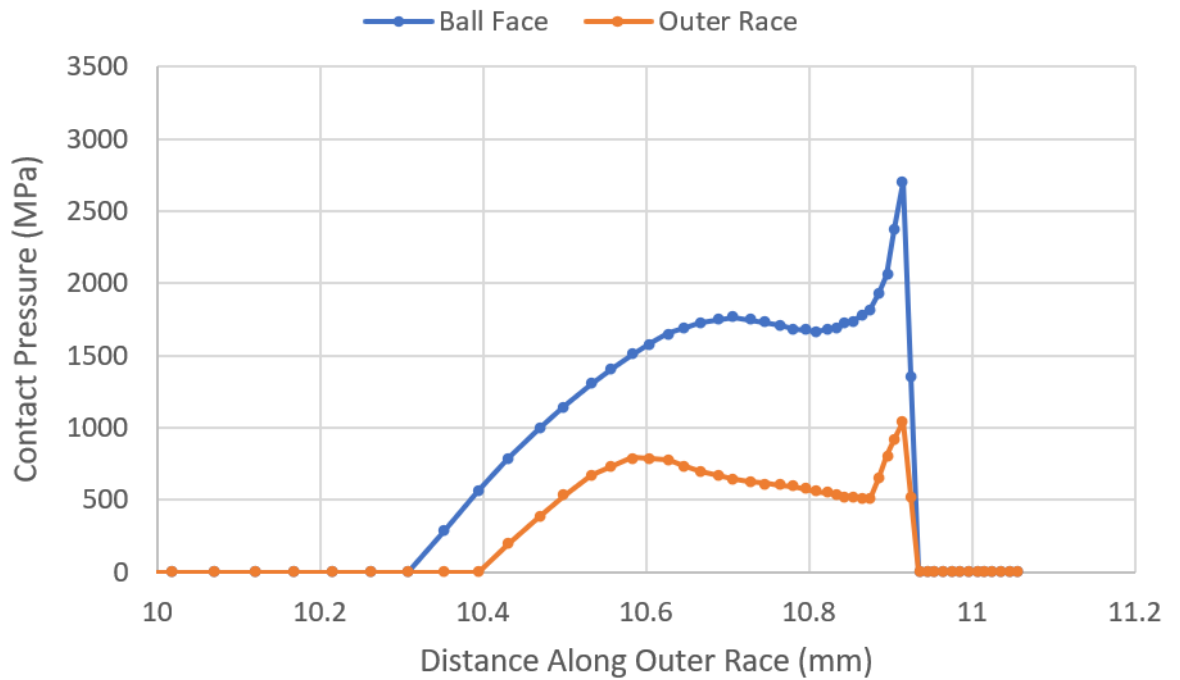
Figure A135: Contact pressure profile between the outer race and rod end under the max stake condition.

Assuming a friction coefficient of 0.15, the increase in contact pressure from pushing out via the ball face results in a frictional force of approximately 6-9 kN. This frictional force mostly accounts for the difference in pushout load for the max stake condition (10.1 kN) and can be attributed as the main mechanism that generates the increase in pushout load.

Appendix B: Anvil Staking Analytical Model

As previously discussed, to convert Zhang et al. (2017) roller swaging model to an anvil staking model it was proposed that only the horizontal projected area (S_1 and S_2) was required to be changed. The axisymmetric nature of a bearing during anvil staking results in a projected area that forms the shape of an annulus. The outer and inner radius of this annulus is defined by x_c and x_a respectively (Figure B136) and therefore the horizontal projected area is given as:

$$S_{1,2} \begin{cases} S_1 = \pi(x_c{}^2 - x_b{}^2) \\ S_2 = \pi(x_b{}^2 - x_a{}^2) \end{cases}$$

[57]

Figure B136: Schematic of the deformation zone.

However, the proposed analytical model did not provide a good match when compared against FE models. The three models in this comparison (Figure B137) are; the FEM from section xx(Baseline), the baseline FEM with the housing set as a rigid boundary condition (Rigid Housing), and lastly the rigid housing FEM but with the material property simplified to Perfectly-Plastic behaviour.

Figure B137: Comparison of the proposed Anvil Staking analytical model and various FEA models.

The poor agreement between the baseline FEM and analytical model was initially attributed to the FEM containing features that the analytical model cannot account for such as deformable housings and strain hardening.

To bring the two into feature parity, the baseline FEM was first simplified by setting the housing to a rigid boundary condition. As expected, this increased the forming load significantly after 0.4mm of roller reduction as now the stress in the outer race was not being transferred into the elastic deformation of the housing. The third model removed the strain hardening exponent to generate a Perfectly-Plastic material profile which brought the forming load closer to the analytical model.

The anvil staking model shares the same limitations as Zhang *et al*. Roller Swaging model which results in the key parameters of the model only being defined between 0.3mm and 0.6mm. Within this range, the Anvil Staking model closely matches the results from the Perfectly-Plastic FEM when a correction factor of x1.7 is applied (Figure B138)
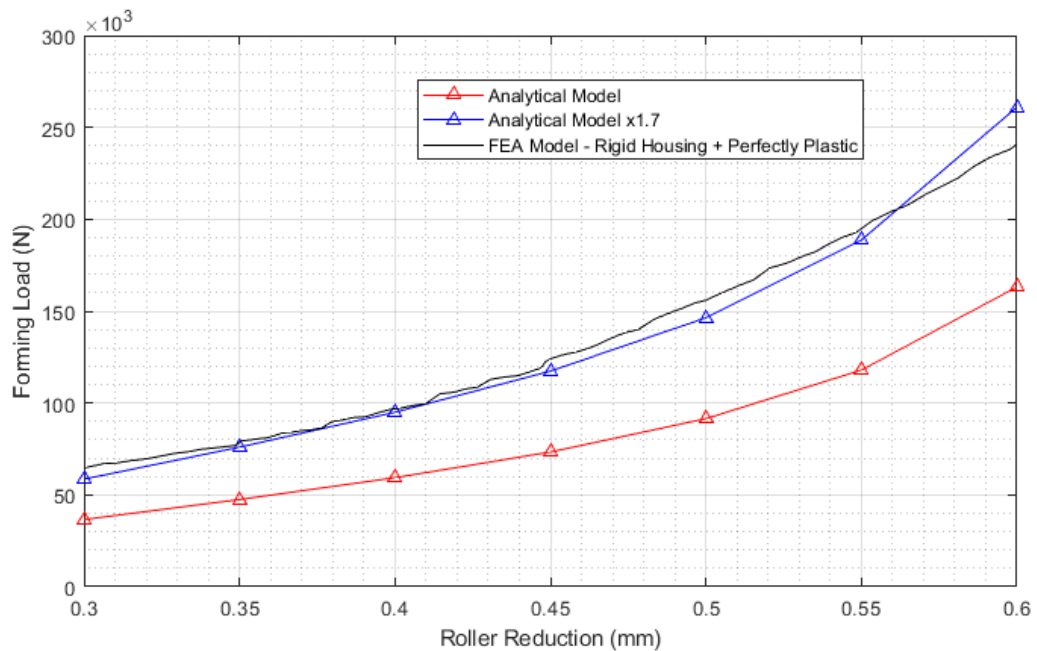
Figure B138: Analytical Model with an applied correction factor of x1.7.

This is a crude approach to correcting the Anvil Staking model and would possibly require a different correction value for each bearing size. A preferred approach would be to go back and further modify Zhang *et al*. equations. The contact pressure per unit area (p_1 and p_2) did not originally account for the hoop stress but it seems clear that this cannot be ignored for Anvil Staking.

Nevertheless, even if better agreement can be found, the fundamental limitations of a closed-form analytical model (rigid boundary conditions, no strain hardening, displacement range limits) mean that it will always fail to predict the true forming load. Multiple researchers have come to the same conclusion in the creation of closed-form solutions for their forging models (Fischer *et al*., 2006; Foster *et al*., 2009; Gisbert *et al*., 2015) with Foster and Gisbert going on to use a correction factor to achieve a satisfactory analytical model.

Appendix C: Regression Models

Bearing Geometry Characterisation

Table C36: Geometric characterisation of Type 1 bearings and their dimensional variation.

[REDACTED]

Table C37: Geometric characterisation of Type 2 bearings and their dimensional variation.

[REDACTED]

Table C38: Geometric characterisation of Type 3 bearings and their dimensional variation.

[REDACTED]

Virtual Design of Experiment Boundaries

Table C39: Final Virtual-DOE parameter inputs for bearing Type 1.

[REDACTED]

Table C40: Final Virtual-DOE parameter inputs for bearing Type 2.

[REDACTED]

Table C41: Final Virtual-DOE parameter inputs for bearing Type 3.

[REDACTED]

Virtual Design of Experiment Boundaries

Virtual Design of Experiment Validation Results
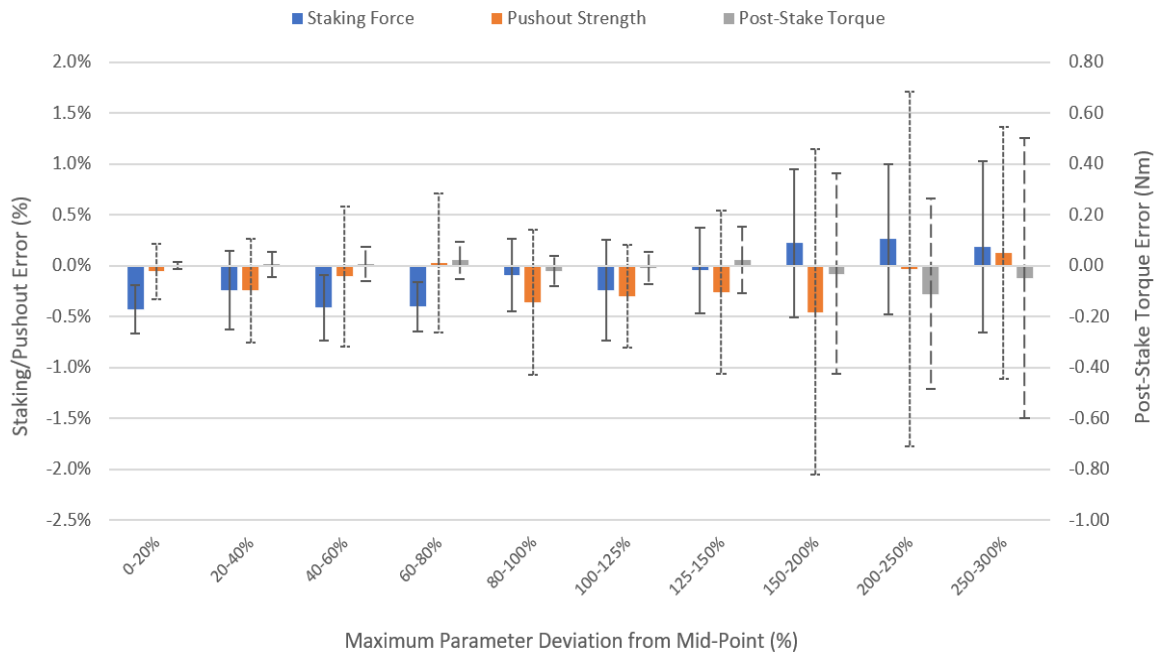
Figure C139: Virtual-DOE model average error with 95% confidence intervals for a Type 1 bearings. The 20-40% band represents the model's error when the parameter with the greatest absolute deviation from its respective mid-point value
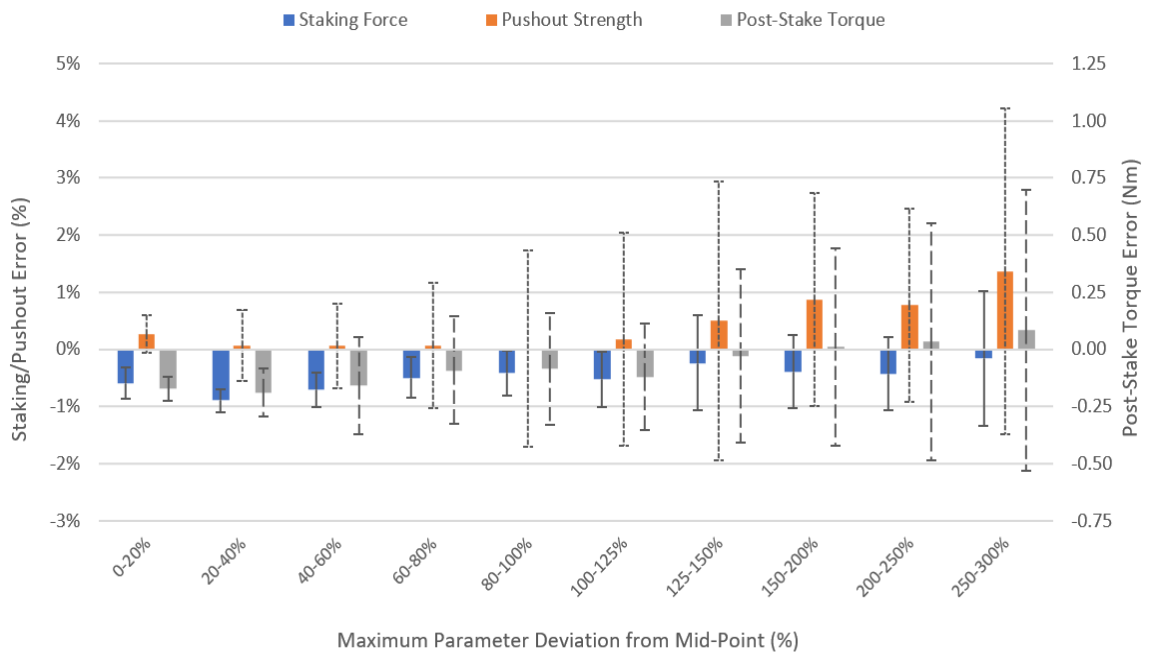
Figure C140: Virtual-DOE model error with 95% confidence intervals for a Type 2 bearings. The 20-40% band represents the model's error when the parameter with the greatest absolute deviation from its respective mid-point value is between
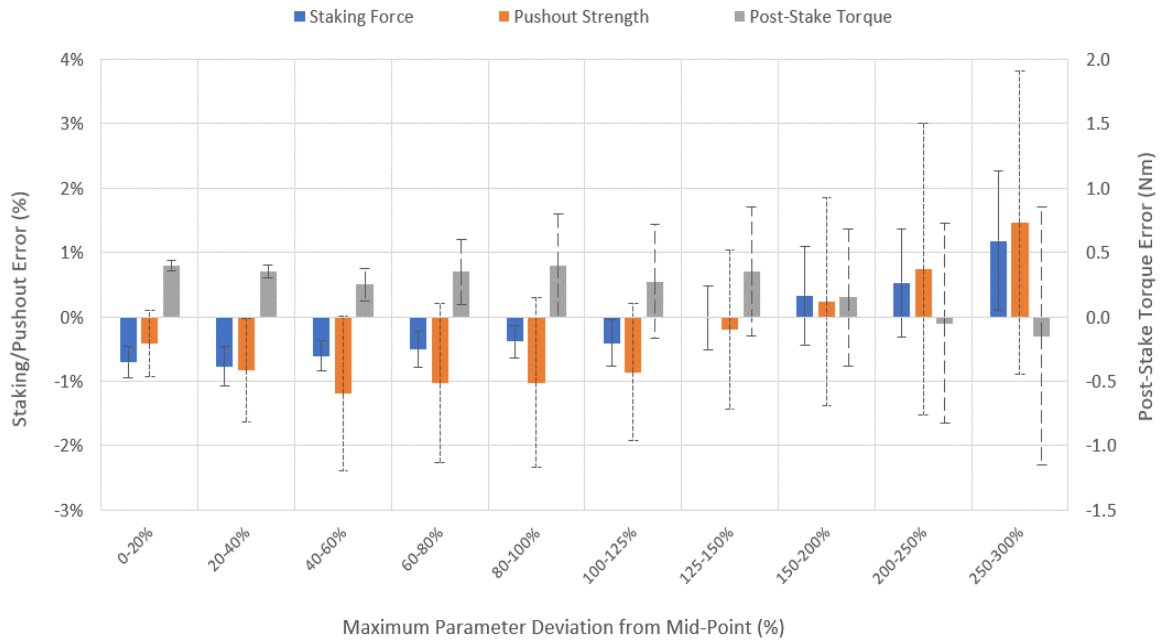
Figure C141: Virtual-DOE model error with 95% confidence intervals for a Type 3 bearing. The 20-40% band represents the model's error when the parameter with the greatest absolute deviation from its respective mid-point value is between 20-40%.

Virtual Design of Experiment Regression Models

Table C42: Virtual-DOE regression equations for a Type 1 Bearing. (A) Anvil Staking Depth, (B) Chamfer Depth, (C) Groove Pitch, (D) Interference, (E) Outer Race Diameter, and (F) Pre-stake Torque.

Response	Regression Model
Staking Force (N)	[REDACTED]
Pushout strength (N)	[REDACTED]
Post-Stake Torque (Nm)	[REDACTED]

Table C43: Virtual-DOE regression equations for a Type 2 Bearing. (A) Anvil Staking Depth, (B) Chamfer Depth, (C) Groove Pitch, (D) Interference, (E) Outer Race Diameter, and (F) Pre-stake Torque.

Response	Regression Model
Staking Force (N)	[REDACTED]
Pushout strength (N)	[REDACTED]
Post-Stake Torque (Nm)	[REDACTED]

Table C44: Virtual-DOE regression equations for a Type 3 Bearing. (A) Anvil Staking Depth, (B) Chamfer Depth, (C) Groove Pitch, (D) Interference, (E) Outer Race Diameter, and (F) Pre-stake Torque.

Response	Regression Model
Staking Force (N)	[REDACTED]
Pushout strength (N)	[REDACTED]
Post-Stake Torque (Nm)	[REDACTED]

Appendix D: Model Validation

Staking Press Correction Lookup Table

Table D45: Staking Press Calibration Lookup Table

Indicated Force (Tons)	Corrected Staking Force (kN)		Indicated Force (Tons)	Corrected Staking Force (kN)
4	29.8		22	174.3
5	37.8		23	182.7
6	46.0		24	190.4
7	54.0		25	198.2
8	61.9		26	206.4
9	70.2		27	214.6
10	78.3		28	223.2
11	86.5		29	231.2
12	94.2		30	239.2
13	102.5		31	247.2
14	110.5		32	255.1
15	118.1		33	263.1
16	126.6		34	271.1
17	134.8		35	279.0
18	142.7		36	287.0
19	150.8		37	295.0
20	158.7		38	303.0
21	166.7			

Type 1 Correction Results

Pushout Strength Correction

$$Pushout\ Error\ (kN) = -5.25 + 15.6 * Chamfer\ Depth \qquad [\ 58\ ]$$

Table D46: Pushout strength error coefficient analysis.

Term	Coefficient	Coefficient Standard Error	T-Value	P-value	VIF
Constant	-5.25	1.36	-3.87	7.3×10^{-4}	-
Chamfer Depth (mm)	15.6	4.25	3.66	1.2×10^{-3}	1.0

Table D47: Model comparison for pushout strength (95% confidence intervals)

	Pushout Strength Error	
	Corrected Regression Model	SKF Internal Tool
Type 2	0.0% ± 5.1%	[REDACTED]

Post-Stake Torque Correction

$$Post\ Stake\ Torque\ Error\ (Nm) = 0.225 + 0.11 * Predicted\ Torque \qquad [\ 59\ ]$$

Table D48: Pushout strength error coefficient analysis.

Term	Coefficient	Coefficient Standard Error	T-Value	P-value	VIF
Constant	0.225	0.081	2.8	4.1×10^{-2}	-
Predicted Torque (Nm)	0.110	0.0018	6.01	3.2×10^{-6}	1.00

Table D49: Model comparison for post-stake torque (95% confidence intervals)

	Post-Stake Torque Error	SKF Engineering Drawing Tolerance (Min-Max)	Failure Rate
Type 2	0.0 ± 0.6Nm	[REDACTED]	< 6%

Type 2 Corrections

Pushout Strength Correction

$$Pushout\ Error\ (kN) = -10.4 - 141 * Interference\ + 0.0637 * Predicted\ Pushout \quad [\ 60\ ]$$

Table D50: Pushout strength error coefficient analysis.

Term	Coefficient	Coefficient Standard Error	T-Value	P-value	VIF
Constant	-10.4	1.34	-7.75	5.5×10^{-5}	-
Interference (mm)	-141	20.5	-6.91	1.2×10^{-4}	1.09
Predicted Pushout Strength (kN)	0.0637	0.00847	7.41	6.8×10^{-5}	1.79

Table D51: Model comparison for pushout strength (95% confidence intervals)

	Pushout Strength Error	
	Corrected Regression Model	SKF Internal Tool
Type 2	-0.02% ± 6.3%	[REDACTED]

Post-Stake Torque Correction

$$Post\ Stake\ Torque\ Error\ (Nm) = -4.93 + 19.13 * Anvil\ Staking\ Depth \quad [\ 61\ ]$$

Table D52: Pushout strength error coefficient analysis.

Term	Coefficient	Coefficient Standard Error	T-Value	P-value	VIF
Constant	-4.93	1.42	-3.48	8.3×10^{-3}	-
Anvil Staking Depth (mm)	19.133	5.8	3.30	1.1×10^{-2}	1.00

Table D53: Model comparison for post-stake torque (95% confidence intervals)

	Post-Stake Torque Error	SKF Engineering Drawing Tolerance (Min-Max)	Failure Rate
Type 2	0.02 ± 0.59Nm	[REDACTED]	< 2.5%

Type 3 Corrections

Pushout Strength Correction

$$Pushout\ Error\ (\%) = 0.883 - 0.819 * Groove\ Pitch\ + 1.090\ Anvil\ Staking\ Depth \qquad [\ 62\ ]$$

Table D54: Pushout strength error coefficient analysis.

Term	Coefficient	Coefficient Standard Error	T-Value	P-value	VIF
Constant	0.883	0.214	4.12	3.6×10^{-4}	-
Groove Pitch (mm)	-0.819	0.126	-6.49	8.4×10^{-7}	1.01
Anvil Staking Depth (mm)	1.090	0.137	7.98	2.4×10^{-8}	1.01

Table D55: Model comparison for pushout strength (95% confidence intervals)

	Pushout Strength Error	
	Corrected Regression Model	SKF Internal Tool
Type 3	0.00% ± 6.7%	[REDACTED]

Post-Stake Torque Correction

$$Post\ Stake\ Torque\ Error\ (Nm) = -1.088 + 0.096 * Post\ Stake\ Torque + 70.0 * Interference \qquad [\ 63\ ]$$

Table D56: Pushout strength error coefficient analysis.

Term	Coefficient	Coefficient Standard Error	T-Value	P-value	VIF
Constant	-1.088	0.165	-6.61	9.6×10^{-7}	-
Post-Stake Torque (Nm)	0.096	0.017	5.78	≈ 0	1.11
Interference (mm)	70.0	12.2	5.76	7.2×10^{-6}	1.11

Table D57: Model comparison for post-stake torque (95% confidence intervals)

	Post-Stake Torque Error	SKF Engineering Drawing Tolerance (Min-Max)	Failure Rate
Type 3	0.00 ± 0.98Nm	[REDACTED]	< 0.2%

Appendix E: Calibration Certificates

[THIS APPENDIX HAS BEEN REMOVED AS IT CONTAINS PERSONAL INFORMATION]

Appendix F: ICED 23 Bordeaux 24th – 28th July 2023

Exploring the potential for a FEA-based Design of Experiments to develop design tools for bulk-metal joining processes.

Jacob Hatherell, Arnaud Marmier, Grant Dennis, Will Curry, Jason Matthews.

Over the last 20 years, finite element analysis (FEA) has become a standard analysis tool for metal joining processes. When FEA tools are combined with design of experiments (DOE) methodologies, academic research has shown the potential for virtual DOE to allow for the rapid analysis of manufacturing parameters and their influence on final formed products. However, within the domain of bulk-metal joining, FEA tools are rarely used in industrial applications and limit DOE trails to physical testing which are therefore constrained by financial costs and time.

This research explores the suitability of an FEA-based DOE to predict the complex behaviour during bulk-metal joining processes through a case study on the staking of spherical bearings. For the two DOE outputs of pushout strength and post-stake torque, the FEA-based DOE error did not exceed ±1.2% and ± 1.5 Nm respectively which far surpasses what was previously capable from analytically derived closed-form solutions. The outcomes of this case study demonstration the potential for FEA-based DOE to provide an inexpensive, methodical, and scalable solution.

Introduction

Bulk-metal forming is a key technology for a broad range of industrial products that combine high material utilisation with low cost and energy requirements at a mass production scale. Groche et al. (2014) and Mori et al. (2013) present a comprehensive review of metal forming operations and the current state of the art. In the development of new products, the trend towards lightweight designs and assemblies is perpetual and requires an ever-increasing need for design optimisation and a deeper understanding of the relationships between the properties and characteristics of the artefact and that of the manufacturing process (Hicks and Matthews, 2010). Robust design (RD), also referred to as Design of Experiments method (DOE), is a systematic and efficient method that aims to study the relationship between multiple input and output variables (Taguchi, Chowdhury and Wu, 2007) instead of relying on the costly use of design margins and overengineering or excessive quality control (Eckert, Isaksson and Earl, 2019). The aim is to choose the optimal value for each input parameter to achieve the desired response despite the potential variation in manufacturing conditions, loads or part tolerances. In general, DOE is a well-researched field, and its fundamental ideas are widely accepted among researchers (Sarema, et al., 2022; Joseph et al., 2019; Oudjene and Ben-Ayed, 2008; Lehman, Santner, and Notz, 2004; Jin, Chen, and Sudjianto, 2003). When paired with commercially available Finite Element Analysis (FEA) software, a virtual DOE can be undertaken that can achieve a higher level of verification and eliminate experimental effort and cost (Kim, 2010; Al-Momani and Rawabdeh, 2008). Despite these opportunities, there remains a gap in most engineering industries when it comes to the application of virtual DOE to evaluate the effect of geometrical, material and load variations (Nerenst et al., 2021; Will, 2015; Coleman, 2012). For the case of designing bulk-metal joining processes, the implementation of FEA has been largely limited to a case-by-case basis and is often left late in the development process. This can lead to large safety factors or overly optimistic designs that are susceptible to failure due to variations in load conditions or manufacturing tolerances. The investigation presented in this paper explores the suitability of an FEA-based DOE to predict the complex behaviour during bulk-metal joining processes with the aim of producing simple and effective design tools. This takes the form of a case study whereby a FEA-based DOE is carried out on the staking of spherical bearings, specifically, the modelling of the joint strength and the change in post-stake torque.

Spherical Bearing Staking

Staking, commonly referred to as upsetting or open die forging, is a cold forming process used in the assembly of plain spherical bearings into a housing. Self-lubricating plain spherical bearings consist of three main components; an inner race that enables the bearing to freely oscillate about three degrees-of-freedom; an outer race that conforms to the inner race and acts as a mating surface for external assemblies; and a composite fabric (liner) bonded to the inside of the outer race that provides lubrication and a low friction interface against the inner race (Figure 1). They are widely used in the aerospace industry due to their high impact resistance, load bearing capacity, and self-lubrication properties (Kim et.al., 2006; Zhang et.al., 2018) and are primarily seen in applications such as fixed and rotary wing pitch control links, dampers, control surfaces, cargo bay doors and undercarriages (Hoo and Green, 1998). In the staking process, the outer race is first prepared by machining circumferential v-grooves into both parallel faces (Figure 1A). These grooves form a thin lip on the outer race that when staked, conforms to the chamfer in a matching housing (Figure 1B). This process produces a lightweight and reliable mechanical joint requiring no additional components in the assembly. The primary concern during staking is the resultant joint strength between the bearing and its corresponding housing. For the first staked bearing of each batch, the machine settings are validated by testing the staked bearing's joint strength by pushing the bearing out of its housing, in doing so scrapping the part. If the joint strength is not greater than that stated in the part drawing, the staking force is increased in 5kN increments until the minimum joint strength is achieved. This setting is then carried forward for the rest of that batch of bearings. The secondary concern is the change in torque of the bearing during staking. The current understanding is that a bearing's torque would normally decrease (torque-dropout) if the staking load was sufficiently low enough. As the staking load increases, the bearing would return to its original torque and eventually lock-out if the staking load became too large. However, because bearing geometries are unique for each batch it results in large uncertainties in predicting the final torque of the staked bearing. This uncertainty results in a number of finished parts requiring expensive and time-consuming reworking to bring the post-stake torque back within tolerance.
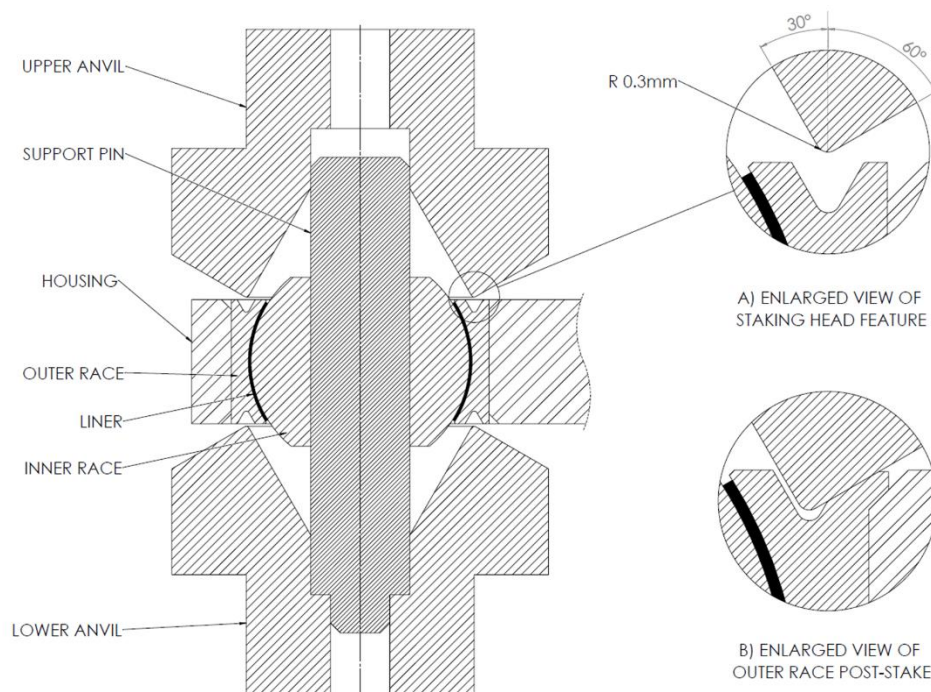
Figure 1. Cross-sectional schematic of the Staking process

Design of Experiments

Preliminary research identified nine potential design parameters that can influence the pushout strength and post-stake torque: staking force, outer race diameter, interference fit between bearing and housing, staking groove pitch, staking groove depth, housing diameter, Inner race diameter, outer race width, and the housing chamfer depth. A full-factorial Design of Experiments (DOE) would allow for the complete characterisation of the response function but with nine variables to model, this approach would take a prohibitively long time to solve. To reduce the computational workload a screening process was undertaken using a Definitive Screening Design (DSD) to identify the dominant factors and eliminate unnecessary design parameters from the study. DSDs have multiple advantages over traditional screening methods such as fractional factorial designs with their main benefits being the ability to identify non-linear terms and the reduction in confounding between 2nd order terms. A DSD requires an upper, lower and midpoint value for each of parameter to be tested, representing 80%, 20% and 50% respectively. However, many of the geometric features of a bearing scale with respect to the overall bearing size and therefore the absolute dimension for each of these parameters cannot be used for the DSD. For example, the bearing's width typically increases with the bearing's outer diameter. A study of 108 production bearings was carried out to determine the relationship between all of the bearing's dimensions with respect to the outer race diameter which is shown in Table 1. These relationships were used to define the geometries within the computational model with their uncertainties used as the inputs for the DSD model.

Table 1. Geometric characterisation of catalogue bearings and their dimensional variation

Dimension	Geometric Characterisation (mm) ±1 Standard Deviation						
Outer Race Diameter	54.9					±	16.2
Outer Race Width	Outer Race Diameter	x	0.442	+	0.104	±	2.51
Groove Depth	1.32					±	0.04
Groove Pitch	1.61					±	0.05
Groove Root Radius	0.36					±	0.02
Staking Chamfer	1.09					±	0.02
Inner Race Diameter	Outer Race Diameter	x	0.93	-	1.71	±	1.28
Inner Race Width	Outer Race Width	x	1.26	+	0.62	±	2.14
Inner Race Bore	Outer Race Diameter	x	0.66	-	4.91	±	2.88
Housing Width	Outer Race Width			+	0.11	±	0.01
Housing Diameter	Outer Race Diameter	x	1.137	+	11.77	±	4.41
Chamfer Depth	1.03					±	0.04
Interference Fit	0.000					±	0.008

Computational model

The computational model created to simulate the staking and pushout of the bearings was made using the simulation software ANSYS Workbench (ANSYS, 2021). Due to the symmetric nature of the staking process, a 2D-axisymmetric analysis was used to increase computational efficiency with mesh independency achieved with approximately 38,000 nodes and 13,000 elements. The exact node and element count per simulation varied with respect to the overall bearing size. To accurately capture the plastic deformation experienced during staking, the flow stress for the bearing steel (AMS5643 H1150) and housing (AMS5643 H1025) were modelled using a modified-Hollomon profile and were defined using the following equations,

$$\sigma_{(H1025)} = 1526\dot{\varepsilon}^{-0.0198} \ \bar{\varepsilon}^{\left(0.0528\dot{\varepsilon}^{-0.1398}\right)} \tag{1}$$

$$\sigma_{(H1150)} = 1369\dot{\varepsilon}^{-0.00627} \ \bar{\varepsilon}^{\left(0.0712\dot{\varepsilon}^{-0.0482}\right)} \tag{2}$$

where $\dot{\varepsilon}$ is the true strain-rate and $\bar{\varepsilon}$ is the true strain. The upper and lower staking anvils were modelled as rigid bodies as is typical for bulk-metal forming models (Woodhead et al., 2015; Kalpajian and Schmid, 2008). A coefficient of friction of 0.15 was used for all steel-steel contacts and 0.05 for the self-lubricating liner to inner-race contact. The original intention for the DSD model was for the staking force and bearing geometry to act as inputs and for the pushout strength and post-stake torque to be the outputs. This required the computational model to be split into three sub-steps: staking, post-stake torque measurement, and pushout strength measurement. During the post-stake torque measurement, the staking anvils must not contact the surface of the bearing so that the contact pressure between the inner-race and the self-lubricating liner can be calculated. This posed many challenges with regard to model stability if the staking anvils were to be controlled via a force input. It was decided to control staking anvils via a displacement command (staking depth), converting the staking force from an input parameter into one of the three outputs. The last alteration to the DSD was to reduce the magnitude of the uncertainties for the geometric relationships from Table 1. The DSD, and subsequent DOE, will combine a random combination of each parameter's uncertainty which is not reflective of the actual bearing designs. For example, ball diameter and outer race width scale directly with each other (max-max or min-min) and are never found with one parameter at its smallest value with the other at its largest. This can lead to self-intersecting geometries and ultimately model errors if the parameter variances are too large. For this reason, the variance of the inner race diameter, outer race width and housing diameter were reduced by half. The final DSD table of inputs and run order is detailed in Table 2. Going forward, the maximum and minimum parameter inputs from Table 2 will represent 100% and -100% deviation from the mid-point value.

Table 2. DSD design table. A list of input parameters and respective run order. +, - and 0 represent the upper (100%), lower (-100%) and midpoint (0%) parameter values, respectively.

Factor	Inner Race Diameter	Groove Depth	Groove Pitch	Outer Race Diameter	Outer Race Width	Chamfer Depth	Housing Diameter	Inter-ference	Staking Depth
Model Limits (mm)	0.6408	1.360	1.659	71.12	1.254	1.062	2.208	0.008	0.51
	0	1.315	1.608	54.93	0	1.027	0	0	0.43
	-0.6408	1.271	1.557	38.73	-1.254	0.992	-2.208	-0.008	0.35
Run Order									
1	0	+	+	+	+	+	+	+	+
2	0	-	-	-	-	-	-	-	-
3	+	0	-	-	+	-	+	+	-
4	-	0	+	+	-	+	-	-	+
5	+	-	0	-	+	+	-	+	+
6	-	+	0	+	-	-	+	-	-
7	+	-	-	0	-	+	+	-	+
8	-	+	+	0	+	-	-	+	-
9	+	+	+	-	0	-	-	-	+
10	-	-	-	+	0	+	+	+	-
11	+	-	+	+	-	0	-	+	-
12	-	+	-	-	+	0	+	-	+
13	+	+	-	+	-	-	0	+	+
14	-	-	+	-	+	+	0	-	-
15	+	+	+	-	-	+	+	0	-
16	-	-	-	+	+	-	-	0	+
17	+	-	+	+	+	-	+	-	0
18	-	+	-	-	-	+	-	+	0
19	+	-	+	+	+	-	+	-	-
20	-	+	-	-	-	+	-	+	+
21	0	0	0	0	0	0	0	0	0

Parameter Screening

The primary output from the DSD was three regression models that predict the staking force, pushout strength and post-stake torque. Each regression model contained all nine parameters with their linear, square, and two-way interactions with an R-squared value of 0.9997, 0.9944, and 0.9838, respectively. Using a Pareto chart, it was possible to identify which parameter was contributing the least towards each regression model's accuracy. By removing this parameter and recalculating the regression model, it was possible to calculate the effective contribution of that parameter. This was repeated for all parameters with the results against each of the three outputs shown in Figure 2. A decision was made to eliminate the parameters groove depth, inner race diameter and outer race width from the final DOE model. This was done because their contribution to the three outputs was minimal and to reduce the total number of runs in the final DOE (Figure 2).
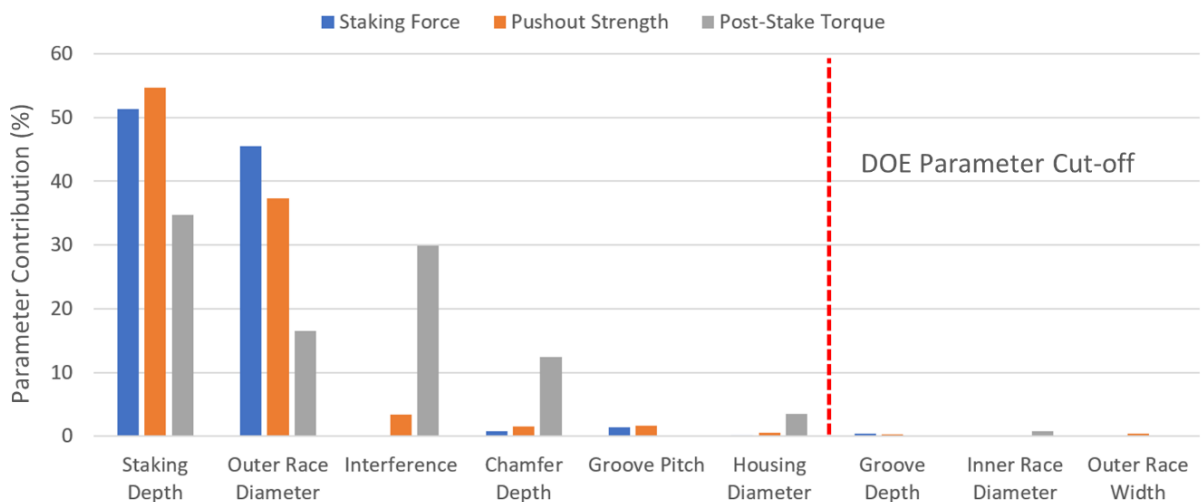
Figure 2. Relative Contribution for each DSD Parameter

The secondary output from the DSD was an indication of the linearity of each input parameter through main effect plots as demonstrated in Figure 3. When displayed in this format it is possible to determine if a parameter has a linear or non-linear effect on the model's output. Only two levels are required for a parameter in the DOE if the mean effects plot returns a linear response. If the response is quadratic, then a minimum of three levels is required. This is due to the DSD being a reduced three-level model and therefore has no information about higher-order interactions. When comparing the mean effects plots across all three DSD outputs, it was found that the outer race diameter and housing diameter always produced a linear response whilst all other parameters produced a quadratic response in at least one of the outputs. Therefore, the initial DOE model was a mixed-level design requiring 2^2 x 3^4 = 324 simulations.
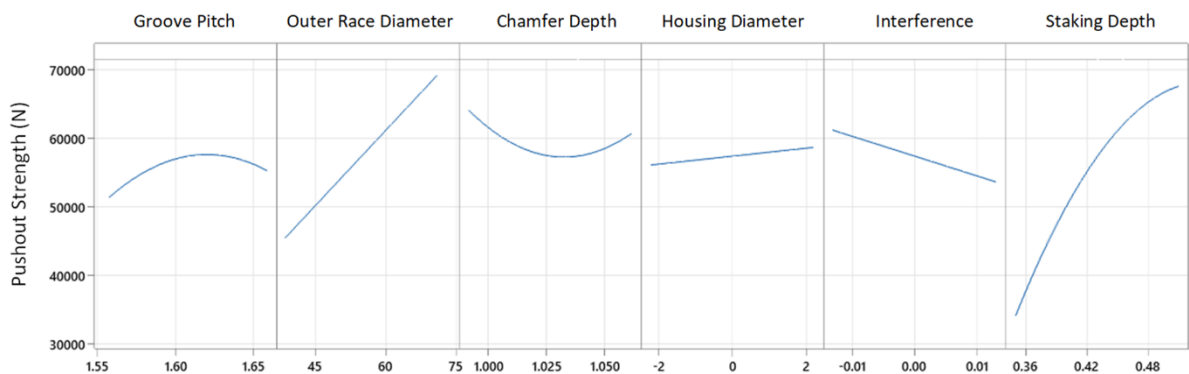
Figure 3. The main effects plot for pushout strength; showing a non-linear response for groove pitch, chamfer depth and staking depth. All dimensions in mm

After the 324 simulations were complete, it was necessary to validate if the mixed-level design's quadratic parameters were of sufficient resolution. To achieve this, three regression models were tested against a new batch of simulations produced by randomising the values for the input parameters. By comparing the residual error of each regression model against each parameter, it was possible to identify patterns in the residuals indicating a lack of resolution in any given parameter. The staking depth parameter was increased to five levels (Table 3) resulting in an additional 216 simulations to be completed with a final mixed-level DOE of 2^2 x 3^3 x 5^1 = 540 simulations.

Table 3. Final DOE parameter inputs

Parameter	Level	Value (mm)				
Staking Depth	5	0.35	0.39	0.43	0.47	0.51
Outer Race Diameter	2	38.730				71.127
Interference	3	-0.00762		0		0.00762
Chamfer Depth	3	0.992		1.027		1.062
Groove Pitch	3	1.557		1.608		1.659
Housing Diameter	2	-2.207				2.207

Results

With the competition of 540 simulations, three regression models were produced to predict the staking force, pushout load, and post-stake torque with R-squared values of 0.9999, 0.9989, and 0.9948, respectively. However, this is only an indication of the regression model's ability to predict the DOE simulations and does not represent the real-world performance of the models where each parameter would vary continuously between their respective limits. To derive a meaningful uncertainty to describe the model's performance, a new batch of simulations were run with randomised values for each of the input parameters. Whereas the upper and lower limits used for the DOE model were reduced to avoid geometric errors from extreme combinations of parameters, for the randomised dataset these limits were increased to match the entire range of possible bearing geometries (100% and -100% represent the original DOE model upper and lower input limits with some parameters now extending to ±300%). Any failed simulations due to impossible bearing geometries were removed from the randomised dataset. In total, 430 randomised tests were simulated and when combined with the DOE simulations the total runtime was 280 hours (AMD CPU Ryzen 9 3950x @4.2GHz). From this dataset, it was possible to calculate the model's error as a function of each parameter's deviation from its mid-point. Whilst beneficial for understanding the behaviour of each parameter, it does not help with developing an overall understanding of the model's error. To achieve this, each simulation was ranked by its maximum absolute parameter deviation, grouped, and their errors averaged together (Figure 4). With the model's statistical analysis complete, a staking design tool was created that calculates the pushout strength and post-stake torque as a function of the staking force as shown in Figure 5.
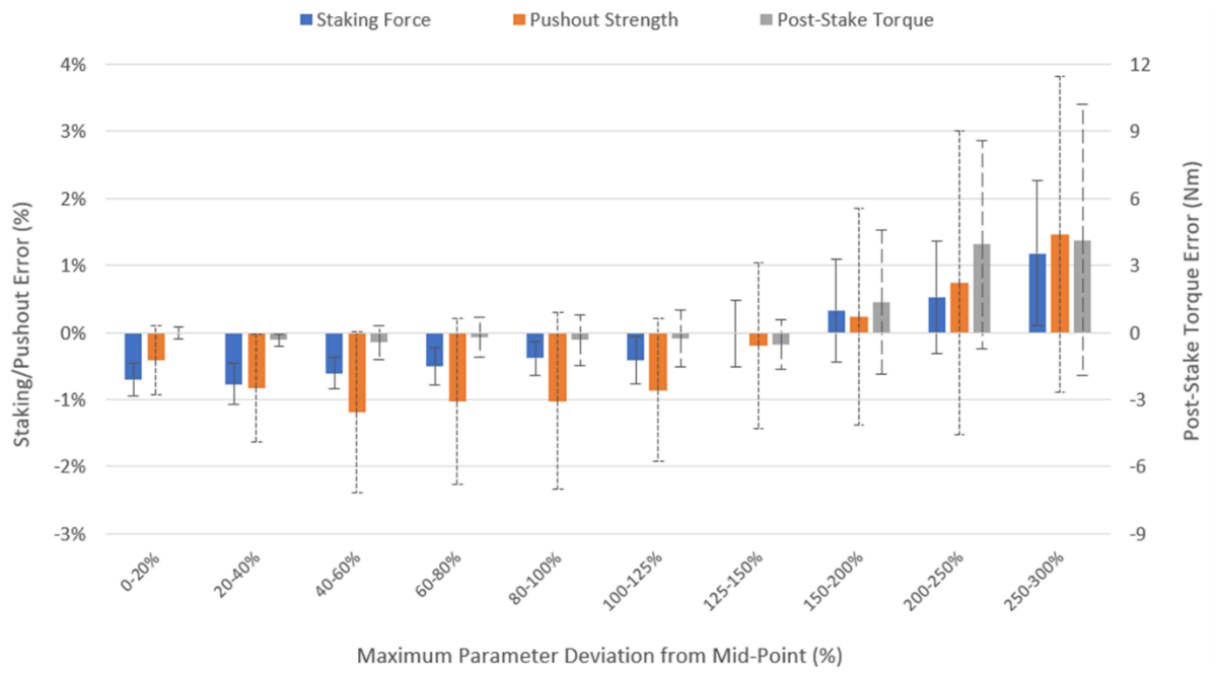
Figure 4. DOE model error with 95% confidence intervals.
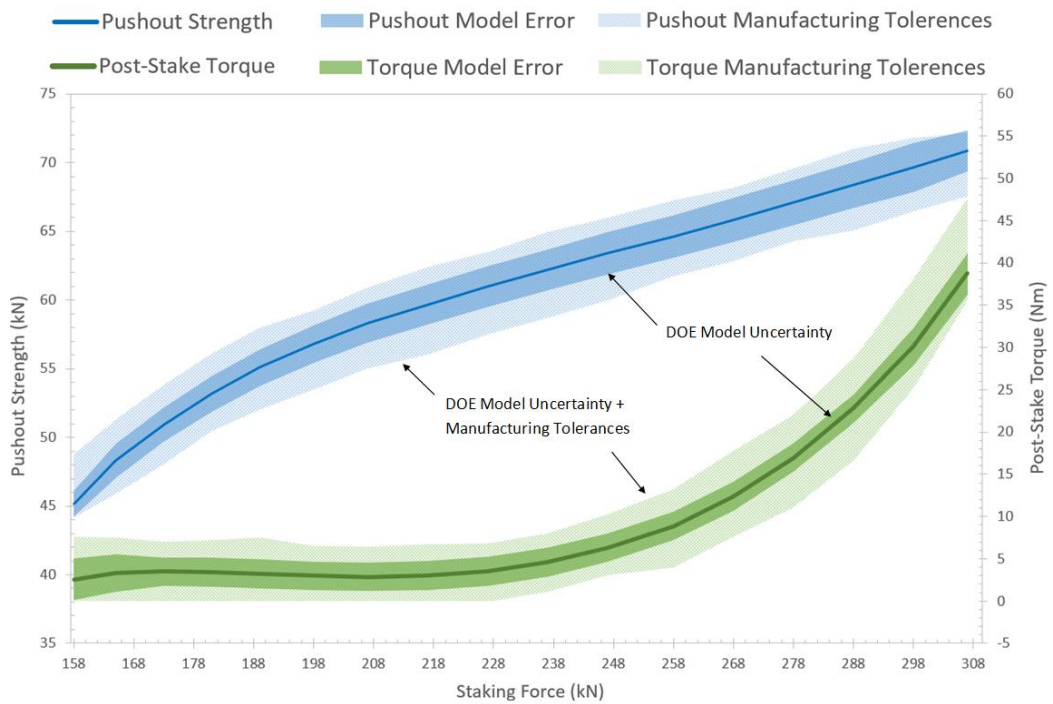
Figure 5. Example of the staking design tool output. The Inner and outer shaded bands represent a 95% confidence interval for the model's inherent uncertainty and the combination of the model's uncertainty and manufacturing tolerances, respectively.

The closed-form solutions that make up the staking design tool were further scrutinised to understand how manufacturing tolerances could influence the model. Through the use of Monte Carlo simulations, the manufacturing tolerances for the bearing's interference fit and chamfer depth were found to produce the greatest response (Figure 6). This probabilistic analysis provides greater insight into the staking tool's behaviour than just relying on the overall output from Figure 5.
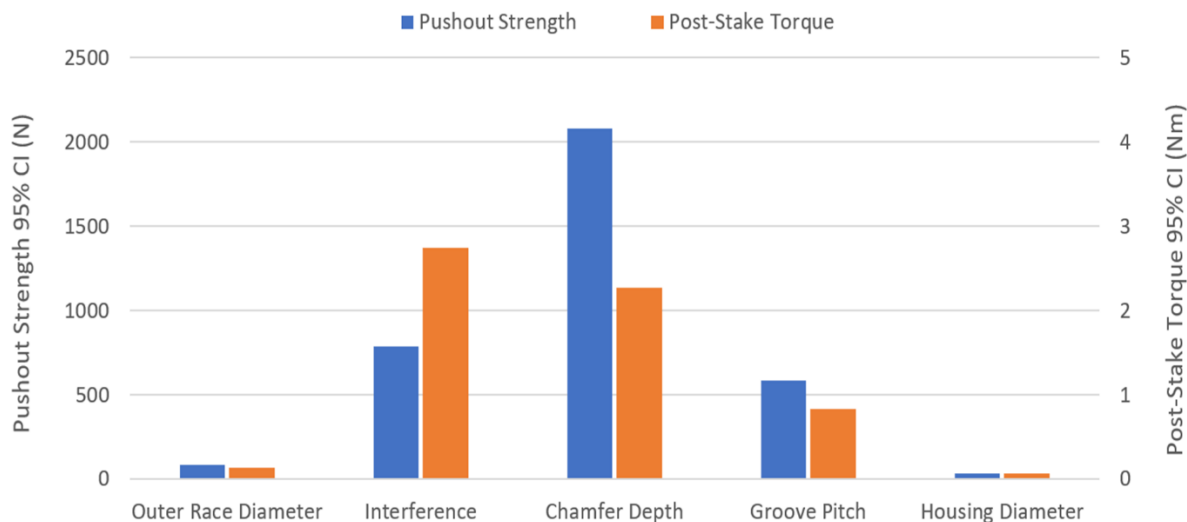
Figure 6. Impact of manufacturing tolerances

Discussion

The FEA-based DOE approach presented in this paper has proved to be successful for the product development of the staking of bearings. With process uncertainties for the staking force and pushout strength not exceeding ±1.2% and post-stake torque ± 1.5 Nm (within the DOE parameter limits), far exceeding what was previously capable from analytically derived closed-form solutions. These uncertainties increase by approximately a factor of three as parameters reach ±300% to accommodate all possible parameter inputs. Whilst not unexpected and still within acceptable limits, this increase was a result of the desire to create a single DOE to model the entire bearing design space. It is strongly suggested that for similar instances multiple DOE models should be created that focus on narrower regions of the design space. This has two primary benefits. The first is a reduction in each DOE model's uncertainty due to the reduced range of each of the parameter inputs. Secondly, if no geometric errors are encountered during the DOE screening stage, then depending on the required depth of post-analysis the randomised validation simulations may not be required saving considerable simulation time. Ultimately, this decision will depend on the individual requirements of each industry project and the sensitivity of the process's input parameters. Although this case study demonstrates the suitability of FEA-based DOE for metal joining processes, a key difference between industry projects and this case study was a lack of time constraints. The presented work was relatively unbounded in time, allowing for more parameters at higher levels to be studied for greater model accuracy at the cost of longer simulation times and post-analysis. However, DOE are by their nature scalable and as such can still provide meaningful results in shorter timeframes at the cost of the model's error. Additional input parameters could be requested at a later stage with the required extra runs simply being appended to the already solved dataset.

Conclusion

The purpose of this investigation was to prove the suitability of a FEA-based DOE approach to create closed-form solutions to complex bulk-metal joining processes. For the staking of bearings, the approach presented in this paper allowed the designer to produce representative results and it would be expected that this performance can be replicated in a variety of bulk-metal joining operations. When contrasted against either physical trials or an ad hoc style of FE design exploration, it was shown that a FEA-based DOE can provide an inexpensive, methodical, and scalable approach for developing a comprehensive understanding of the desired bulk-metal joining processes.

Future Work

The knowledge created from a FEA-based DOE is extensive but from the viewpoint of a designer, this knowledge can be hard to utilise to its full potential as a once previously complex metal joining process is now replaced with an equally complex series of regression equations. Further work is required to develop a standardised process for extracting the most relevant behaviour of the model and presenting it in a form that can be understood by an end user.

Acknowledgements

References

Al-Momani, E. and Rawabdeh, I. (2008) "An Application of Finite Element Method and Design of Experiments in the Optimization of Sheet Metal Blanking Process", *Jordan Journal of Mechanical and Industrial Engineering*, Vol. 2, pp. 53-63.

ANSYS (2021) ANSYS Workbench 2021R1. Available from: www.ansys.com. [Accessed 11 April 2022].

Coleman, P. (2012) CRESCENDO – Collaborative and Robust Engineering using Simulation Capability Enabling Next Design Optimisation. TRIMIS – Transport Research and Innovation Monitoring and Information System. Available from: https://cordis.europa.eu/project/id/234344. [Accessed 10 November 2022].

Eckert, C., Isaksson, O. and Earl, C. (2019) "Design margins: a hidden issue in industry", *Design Science,* Vol. 5(9), pp. 1–24. https://doi.org/10.1017/dsj.2019.7

Groche, P., Wohletz, S., Brenneis, M., Pabst, C. and Resch, F. (2014) "Joining by forming. A review on joint mechanisms, applications, and future trends", *Journal of Materials Processing Technology*, Vol. 214(10), pp. 1972-1994. https://doi.org/10.1016/j.jmatprotec.2013.12.022

Hicks, B. J. and Matthews, J. (2010)The barriers to realising sustainable process improvement: a root cause analysis of paradigms for manufacturing systems improvement. International Journal of Computer . Integrated. Manufacture., 23(7), 585-602. https://doi.org/10.1080/0951192X.2010.485754.

Hoo, J. J. C., and Green, W.B. (1998) *Bearing Steels: Into the 21st Century*. Pennsylvania: ASTM International. https://doi.org/10.1520/stp1327-eb

Jin, R., Chen, W. and Sudjianto, A. (2003) "An efficient algorithm for constructing optimal design of computer experiments". In Volume 2: 29th Design Automation Conference, Parts A and B, Vol. 2, pp. 545–554. https://doi.org/10.1115/detc2003/dac-48760

Joseph, V. R., Gu, L., Ba, S. and Myers, W. R. (2019) "Space-filling designs for robustness experiments", *Technometrics*, Vol. 61, pp. 24–37. https://doi.org/10.1080/00401706.2018.1451390

Kalpajian, S. and Schmid, S.R. (2008) *Manufacturing Processes for Engineering Materials*, 5th ed. California: Pearson Education.

Kim, H.S. (2010) "A combined FEA and design of experiments approach for the design and analysis of warm forming of aluminium sheet alloys". *International Journal of Advanced Manufacturing Technology*, Vol. 51, pp. 1-14. https://doi.org/10.1007/s00170-010-2620-8

Kim, B.C., Park, D.C., and Kim, H.S. (2006) "Development of composite spherical bearing", *Composite Structures*, Vol. 75, pp. 231–240. https://doi.org/10.1016/j.compstruct.2006.04.027

Lehman, J. S., Santner, T. J. and Notz, W. I. (2004) "Designing computer experiments to determine robust control variables". *Statistica Sinica, Vol.* 14(2), pp. 571–590.

Mori, K.I., Bay, N., Fratini, L., Micari, F. and Tekkaya, A.E. (2013) "Joining by Plastic Deformation". *CIRP Annals, Manufacturing Technology*. Vol. 62(2), pp. 673-694. https://doi.org/10.1016/j.cirp.2013.05.004

Nerenst, T.B, Ebro, M., Nielsen, M. Eifler, T. and Nielsen, K.L. (2021) "Exploring barriers for the use of FEA-based variation simulation in industrial development practice", *Design Science*, Vol. 7(21), pp. 1-22. https://doi.org/10.1017/dsj.2021.21

Oudjene, M. and Ben-Ayed, L. (2008) . "On the parametrical study of clinch joining of metallic sheets using the Taguchi method", *Engineering Structures*, Vol. 30(6), pp. 1782–1788. https://doi.org/10.1016/j.engstruct.2007.10.017

Sarema, B., Matope, S. and Sterzing, A. (2022) "Design of experiments procedure for evaluating the formability of sheet metals components in forming processes" *Southern African Institute of Industrial Engineers 33rd Annual Conference, KwaZulu-Natal, 3-5 October 2022.*

Taguchi, G., Chowdhury, S. & Wu, Y. (2007) *Taguchi's Quality Engineering Handbook*. Michigan: John Wiley & Sons, Inc. https://doi.org/10.1002/9780470258354.ch4

Will, J. (2015) "Robust design optimization in virtual prototyping – promises and challenges", In NAFEMS - International Association Engineering Modelling. https://www.dynardo.de/en/library/methodology/robust-design-optimization.html

Woodhead, J., Truman, C.E. and Booker, J.D. (2015) "Modelling of dynamic friction in the cold forming of plain spherical bearings", *Contact and Surface* 2015. Valencia, 21-23 April 2015. Southampton: WIT Press, pp.141-152. https://doi.org/10.2495/secm150131

Zhang, Q., Hu, Z., Su, W., Zhou, H., Qi, X. and Yang, Y. (2018) "Investigation on housing chamfer parameters in roller swaging for self-lubricating spherical plain bearings assembly", *International Journal of Advanced Manufacturing Technology*, Vol. 95, pp. 1089-1099. https://doi.org/10.1007/s00170-017-1280-3

Appendix G: Tribology Transactions

An Iterative Numerical Approach to Evaluate the Variable Friction Coefficient of Steel AMS5643 Using Ring Compression Tests

Jacob Hatherell, Grant Dennis, Will Curry, Arnaud Marmier, Jason Matthews.

The coefficient of friction is an important variable which must be defined to allow the accurate prediction of the forming geometry and stresses involved in metal forming processes. Literature has shown that the coefficient of friction does not remain constant with respect to variables including but not limited to contact pressure, sliding speed, surface roughness and surface morphology.

Ring compression tests provide a simple and efficient process by which to measure the variable coefficient of friction present in the bulk-metal process, however, the conventional interpolating method can result in a poor evaluation of the evolution of friction especially if the coefficient of friction changes significantly during a test.

In this paper, a novel approach to evaluate the relationship between the coefficient of friction and contact pressure is outlined using friction calibration charts generated via iterative computation models and ring compression tests. This relationship can be programmed into a computational model to allow for the coefficient of friction to behave as a dynamic variable. This approach improves on the prediction of the computational model when compared to conventional interpolation methods.

Introduction

The coefficient of friction between the workpiece and tooling must be correctly defined to be able to accurately predict the stresses, forming load, energy consumption and final part geometry in a metal forming process. However, it is inherently difficult to precisely quantify even within a simple static problem due to the number of factors that can influence the coefficient of friction (1,2). Some of these influencing factors include, but are not limited to, surface roughness and morphology (3-7), contact pressure (8-10), lubricants (11), workpiece and die material combinations, and temperature (12,14).

Whilst many of these parameters can be considered constant during a given metal forming process, parameters such as surface roughness dynamically change throughout the process due to both the high contact pressures and plastic deformation present which can result in a variable coefficient of friction. The current state of the art for computational modelling is not able to capture or model the behaviour of many of these dynamic parameters. Therefore, it is not possible to define a variable coefficient of friction within a computation modelling environment as a function of a parameter such as surface roughness or morphology. One of the few parameters that can be used to define a variable coefficient of friction within a computational model is the contact pressure between two mating surfaces which can be obtained from a ring compression test.

Building off the work of Kunogi (15), Male and Cockcroft (16) published a standard methodology for determining the coefficient of friction through the use of a ring compression test (Figure 1). The test consists of a ring compressed axially between two flat and parallel compression platens, such that the material undergoes plastic deformation. If the interface between the specimen and dies is of sufficiently low friction (assuming isotropic material properties, perfect-plastic behaviour, and homogenous deformation), then the inner diameter of the ring will expand together with the outer diameter. As the friction increases, sticking

will occur at the interface which resists the outward flow of material causing the specimen to bulge at the midplane (barrelling). Once the friction coefficient reaches a critical value it becomes favourable for material to flow inwards and results in the reduction of the inner diameter. The coefficient of friction is evaluated by interpolating between the relationship of the inner diameter and height of the specimen against analytically derived Friction Calibration Curves (FCCs) at constant coefficients of friction. This results in all the potential influencing factors on the coefficient of friction being reduced to a single parameter that is the contact pressure between the workpiece and dies.

The use of computational modelling to numerically derive the FCCs (10-11, 14, 17,19) has allowed for the incorporation material behaviours not possible via analytical methods such as strain-rate, strain-hardening and non-uniform contact pressures. Whilst the interpolation method for determining the coefficient of friction from a ring compression test is an efficient process, as will be later investigated, interpolating the coefficient of friction between FCCs can result in a poor evaluation of the evolution of friction with respect to contact pressure especially if the coefficient of friction is rapidly changing.

Despite evidence indicating that the coefficient of friction (under the correct conditions) can vary with respect to contact pressure (10,21-23), it is still common practice for the coefficient of friction to be quoted and modelled as a static value (17,24-27). The complex nature of friction and the comparably high cost required to investigate these phenomena gives little incentive to conduct research or change industrial practices. However, with respect to bulk-metal forming, one of the largest factors leading to a loss in production is excessive die wear or failure whereby friction is the leading contributing factor (28): highlighting the importance of understanding this phenomenon. Recent research has begun to see the integration of a variable friction coefficient into computational models with the aim to improve the accuracy of both sheet (26) and bulk-metal forming (10,19,30). This is an active

area of research and a continuing area of debate as to how to best implement variable friction coefficients into numerical and analytical models.

In this paper, a new method for determining the pressure-friction relationship is presented where ring compression tests are analysed with an iterative computational model. This will be compared to the conventional approach of interpolating experimental data against FCCs. For this study, the two methods will be referred to as the 'Iterative FCC" and "FCC interpolation." This research was in support of a wider study of work into the bulk-metal cold-forming process of staking which is widely used in the aerospace sector for the manufacture and assembly of spherical-plain bearings and rod-end links (31). This manufacturing process is characterised as a single-strike operation, similar to wire crimping and sheet metal pressing. Therefore, the material investigated in this research was steel AMS5643 with all testing conducted at room temperature to best replicate the conditions experienced in the manufacturing of spherical-plain bearings.

Methodology

Test Specimens

AMS5643 (H1150 condition) is a high strength, corrosion resistant steel used extensively within the aerospace industry. The chemical composition is given in Table 1. There is no consensus on the most suitable specimen dimensions for a ring compression test, however, it has been shown that increasing the inner diameter can lead to an increase in measurement accuracy (32). If the inner diameter is increased too much, then the ring risks buckling during deformation due to the thinner wall thickness. This can be compensated for by increasing the outer diameter in kind, but this will have the undesired effect of increasing the required forming load. The most commonly used ratio of outer diameter to inner diameter to height (OD:ID:H) used is 6:3:2 (10,18-19) with an inner diameter of 9.53 mm; therefore, these dimensions were chosen for this study (Figure 2). To maintain consistency between test specimens, the surface roughness (Ra) was machined to a finish of 1.6 μm and verified using a contact-type roughness meter.

Experiment Setup

A total of 20 specimens were produced to ensure that an adequate number of data points could be acquired to ensure statistically valid results. Molybdenum disulphide lubricant (G-n Plus) applied to each face of both the specimens and to the compression platens. Tests were conducted using a 640 kN, four-column press with tungsten carbide plates (Grade YG15) inserted into the compression platens to function as the upper and lower die surfaces.

The load profile of the press was set to 15 kN and increased in increments of 5 kN to reduce the height of the specimens in even increments from approximately 10 to 50% (Figure 1). Each load step was achieved at a constant velocity equivalent to a strain-rate of 0.1 s^{-1}. Whilst

the actual strain-rate will have deviated slightly during each load step (due to the changing height of the specimen), this approach was able to effectively eliminate strain-rate as a variable across all of the test runs.

Variation in Specimen Diameter

The inner diameter of a specimen may take on a non-circular shape after deformation, especially if there is any degree of anisotropic frictional or material behaviour, and therefore an averaged value for the inner diameter can be taken to account for this behaviour (10). To measure for any anisotropic behaviour, a sweep of the inner diameter was taken for each sample at every test load to obtain the maximum and minimum diameter. It was found across all load conditions, that the variance of the average inner diameter was greater than the average variance between the maximum and minimum diameter typically by a factor no less than three. An example of the ovality of the test specimens at a load of 50 kN is shown in Figure 3. It was therefore deemed appropriate to take an average of the maximum and minimum inner diameter when calculating the change in inner diameter because of the small measure of anisotropic behaviour relative to the variance between test specimens.

Barrelling Compensation

Friction at the interface between the die and test specimen will result in barrelling and an inhomogeneous strain field as the specimen is compressed (19). This creates a condition where the uniaxial stress state principle no longer holds true. Similar to Bridgman's correction factor (33), a bulge correction factor (C_f) was used to calculate the true stress (σ) of the ring specimens (34) at each load increment.

$$\sigma = C_f \frac{4P}{\pi(D^2 - d^2)} \qquad [\ 1\ ]$$

where P is the compressive load, D is the outer diameter and d is the inner diameter.

The bulge correction factor is derived analytically from the analysis of the stress distribution at the mid-plane (35) and is given as:

$$C_f = \left[\left(1 - \frac{2R}{a}\right)\ln\left(1 - \frac{a}{2R}\right)\right]^{-1} \qquad [\ 2\ ]$$

where R is the outer bulge radius of the sample in the vertical plane and a is the outer radius at the horizontal mid-plane of the specimen. From geometric relations, the bulge radius was calculated as

$$R = \frac{h^2 + (D - d)}{4(D - d)}, \qquad [\ 3\ ]$$

were h is the actual height of the test specimen.

Finite Element Simulation

Finite Element Model

The computational model created to simulate the ring compression tests were made using the simulation software ANSYS. Due to the symmetric nature of the tests, an axisymmetric analysis was used to increase computational efficiency with convergence achieved at 1734 nodes and 1579 elements. The flow stress model for AMS5643 followed a modified-Hollomon profile and is given as:

$$\sigma_{(MPa)} = 1526\dot{\varepsilon}^{-0.0198} \, \bar{\varepsilon}^{\left(0.0528 \, \dot{\varepsilon}^{-0.1398}\right)} \qquad [\; 4 \;]$$

where $\dot{\varepsilon}$ is the true strain-rate and $\bar{\varepsilon}$ is the true-strain. The upper and lower platens were modelled as rigid bodies as is typical for bulk-metal models (10,20).

Friction Model.

Friction is typically characterised by two models: either Coulomb's law or the Tresca friction model. For Coulomb's law, the tangential frictional stress is expressed as a function of the normal contract pressure and is given as:

$$\tau_f = \mu\sigma_N \qquad [\; 5 \;]$$

where τ_f is the tangential frictional stress, σ_N is the normal contact pressure and μ is the coefficient of friction. A constant value for the coefficient of friction is only valid provided the ratio between the normal contact pressure and the yield stress remains below approximately 1.3 - 1.5 (22, 35). Beyond this point, it is understood that the surface asperities at the contact interface will have deformed such that the real and apparent contact areas are equal. This leads to the frictional stress becoming constant and no longer proportional to the normal contact pressure, resulting in a decreasing coefficient of friction as the contact

pressure increases. Under these conditions, the tangential frictional stress is better modelled by the Tresca friction model and is given as

$$\tau_f = mk \qquad\qquad [\ 6\ ]$$

where m is the friction factor and k the materials shear strength. However, it has been shown that neither friction model can accurately reflect the dynamic friction conditions present in bulk-metal forming and that a hybrid between the two models is required (22).

The reference friction model used within ANSYS follows Coulomb's law and was used to create the FCCs.

Analysis and Discussion

FCC Interpolation

The conventional approach to determine the coefficient of friction from ring compression tests is as follows. The ring compression test is simulated in a computational model across a range of friction coefficients (for this study the required range required was 0.05-0.1). From these simulations, the results history for the percentage reduction in inner diameter is plotted against the percentage reduction in height to create the FCCs. Finally, the experiment ring compression data is compared to the simulated results and the coefficient of friction is determined by interpolating between the constant friction curves. The results of the FCC interpolation approach are shown in Figure 4. By interpolating between the FCCs and calculating the average forming pressure at each load step, the pressure-friction relationship was determined and plotted in Figure 5.

By running a custom command within the ANSYS simulation environment, the friction coefficient determined in Figure 5 could be programmed into the computational model. As

shown in Figure 6, this custom friction model was able to produce a good prediction for the ring compression experiment data up to approximately a 30% height reduction, after which the computational model begins to underpredict the reduction in inner diameter. At a height reduction of 33.5%, the friction coefficient is evaluated to be 0.08 but the gradient of the experiment data is significantly steeper than the 0.08 constant friction curve (figure 7). It is clear to see that the friction coefficient should be greater than 0.08 to maintain the gradient of the experiment data and reach the next data point at 38.8%.

Iterative FCC

To improve on the FCC interpolation method, an iterative approach to generating the FCCs was proposed (Figure 8) and is described as follows. Firstly, constant friction curves were created from the initial geometry up to the change in height recorded at the end of the first load step and the friction coefficient evaluated similarly to the interpolation method. New constant friction curves were then generated starting from the geometry at the end of the first load to the end of the second load step and the friction coefficient was again evaluated for this second load step.

This is repeated across all load steps to produce a relationship between the contact pressure and the coefficient of friction. Figure 9 shows the results of this method. Because the friction coefficient was modelled as a constant throughout each load step, a final "smoothed" pressure-friction relationship was obtained by using the average pressure for each load step as shown in Figure 9.

When compared to FCC interpolation, the iterative FCC method produces a better prediction for the ring compression test and remains within the 95% confidence interval of the experiment data across its entire test range (Figure 10). A comparison of both contact pressure-coefficient of friction relationships is shown in Figure 11.

The relationship generated by the Iterative FCC method saw a rise in the friction coefficient from 0.064 to 0.115 at a contact pressure of 1334 MPa before decreasing to 0.085. The initial rise in the friction coefficient is likely attributed to the breakdown of the lubricant as the load-bearing capacity is exceeded and is spread thinner as the surface area of the test specimens increases with forming load. The peak friction coefficient at 1334 MPa was 1.35 times the yield strength of AMS5643 at 0.1 s^{-1} (985 MPa). This result agrees with the predicted decrease in friction coefficient expected at 1.3-1.5 times the yield strength (22,36).

When viewed in a broader context, the significant improvements of the Iterative-FCC method does not completely diminish the usefulness of the standard Interpolation method if the coefficient of friction remains constant across the entire contact pressure range. Under these specific conditions the Interpolation method can still produce accurate results without the need for further computational modelling. However, small changes in the evolution of the coefficient of friction can have a significant impact on the forming loads experienced during a forging process. To demonstrate this, a finite element simulation was created to model the staking of a spherical-plain bearing (31) using the pressure-friction relationships derived from both analysis methods. As shown in Figure 12, the Iterative-FCC model was able to better predict the forming load across all ranges of anvil compression. At a peak anvil compression of 0.46mm, the error in the forming load of the Interpolation method was ~30% compared to only ~5% for the Iterative-FCC method.

Conclusions

Friction is one of the most important properties in metal forming operations and yet it is often neglected or simplified to a single constant value. Presented in this research is the evaluation of two different methods for determining the relationship between the contact pressure and coefficient of friction for steel AMS5643 via ring compression testing. The conventional method (FCC Interpolation) compares the deformation of the ring specimens against FCCs simulating the ring compression test at various constant friction coefficients. The new method proposed in this study (Iterative FCC) generates new FCCs for each load step that begins at the geometry of the last load step. The results from this research are summarised as follows:

- The FCC Interpolation method provides a good initial prediction of the experimental data but fails to follow the experiment data at height reductions greater than 30%. Interpolation between FCCs is not able to describe the changing friction coefficient at each load step and becomes less accurate the more the coefficient of friction changes.

- The Iterative FCC method was able to produce an accurate prediction of the experiment data, remaining within the 95% confidence interval across the entire test range.

- The Iterative FCC coefficient of friction decreased from its maximum value of 0.115 after exceeding a contact pressure of 1334 MPa. This matched the theoretical decrease in the coefficient of friction expected at 1.3 to 1.5 times the yield strength of AMS5643.

The iterative FCC analysis method developed in this research can be applied to any ring compression test condition and provides improvement over the conventional FCC interpolation method. This improvement is expected to increase in conditions with higher contact pressures or when the variability of the coefficient of friction increases.

Acknowledgements

Conflicts of Interest

The author declares no conflicts of interest.

References

[1]   Kobayashi, S., Altan, T. and Oh, S.I. (1989) *Metal Forming and the Finite Element Method*. 4th ed. Oxford: Oxford University Press.

[2]   Sofuoglu, H. and Rasty, J. (1999) On the measurement of friction coefficient utilizing the ring compression test. *Journal of Engineering Materials and Technology*. 123(3), pp. 338-348.

[3]   Sedlacek, M., Gregorcic, P. and Podgornik, B. (2017) Use of the Roughness Parameters Ssk and Sku to Control Friction—A Method for Designing Surface Texturing. *Tribology Transactions*. 60(2), pp. 260-266.

[4]   Menezes, P.L., Kishore and Kailas, S.V. (2009) Study of Friction and Transfer Layer Formation in Copper-Steel Tribo-System: Role of Surface Texture and Roughness Parameters. *Tribology Transactions*, 52(5), pp. 611-622.

[5]   Qin, W., Jin, X., Kirk, A., Shipway, P.H. and Sun, W. (2018) Effects of surface roughness on local friction and temperature distributions in a steel-on-steel fretting contact. *Tribology International*. 120(1), pp. 350–357.

[6]   Cristino, V.A.M., Rosa, P.A.R. and Martins, P.A.F. (2011) Surface roughness and material strength of tribo-pairs in ring compression tests. *Tribology International*. 44(2), pp. 134–143.

[7]   Tomota, T., Masuda, R., Kondoh, Y., Ohmori, T. and Yagi, K. (2021) Modeling Solid Contact between Rough Surfaces with Various Roughness Parameters. *Tribology Transactions*, 64(1), pp. 178-192.

[8]   He, X., Liu, Z., Ripley, L.B., Swensen, V.L., Griffin-Wiesner, I.J., Gulner, B.R., McAndrews, G.R., Weirser, J.R., Borovsky, B.P., Wang, Q.J. and Kim, S.H. (2021) Empirical relationship between interfacial shear stress and contact pressure in micro- and macro-scale friction. *Tribology International*. 155, pp. 1–8.

[9]   Fukagai, S., Marshall, M.B. and Lewis, R. (2022) Transition of the friction behaviour and contact stiffness due to repeated high-pressure contact and slip. *Tribology International*. 170, pp. 1–14.

[10]   Woodhead, J., Truman, C.E. and Booker, J.D. (2015) Modelling of dynamic friction in the cold forming of plain spherical bearings. *Contact and Surface 2015*. Valencia, 21-23 April 2015. Southampton: WIT Press, pp.141-152.

[11]   Hu, C., Chen, H., Zhang, W. and Ohshita, H. (2023) Enhancing the sensitivity of a tribological testing method to enable development of lubricants for cold forging. *Tribology International*. 179, pp. 1-10.

[12]   Pearson, S., Shipway, P.H., Abere, J.O. and Hewitt, R.A.A. (2013) The effect of temperature on wear and friction of a high strength steel in fretting. *Wear*. 303(2), pp. 622-631.

[13]   Zhu, K., Zeng, W., Ma, X., Tai, Q., Li, Z. and Li, X. (2011) Determination of the friction factor of Ti-6Al-4V titanium alloy in hot forging by means of ring-compression test using FEM. *Tribology International*. 44(12), pp. 2074–2080.

[14] Mirahmadi, S.J., Hamedi, M. and Cheraghzadeh, M. (2015) Investigating Friction Factor in Forging of Ti-6Al-4V through Isothermal Ring Compression Test. *Tribology Transactions*. 58, pp. 778-785.

[15] Kunogi, M. (1956) A New Method of Cold Extrusion. *Journal of Scientific Research Institute*. 50(1437), pp. 215–246.

[16] Male, A., and Cockcroft, M.G. (1964). A Method for the Determination of the Coefficient of Friction of Metals Under Conditions of Bulk Plastic Deformation. *Journal of the Institute of Metals*. 93(3), p.241.

[17] Sofuoglu, H., Gedilkli, H. and Rasty, J. (2001) Determination of friction coefficient by employing the ring compression test. *Journal of Engineering Materials and Technology*, *Transactions of the ASME*. 123(3), pp. 338-348

[18] Martin, F., Martin, M.J., Sevilla, L. and Sebastian, M.A. (2015) The ring compression test: Analysis of dimensions and canonical geometry. *Procedia Engineering*. 132(2015), pp. 326-333.

[19] Kahhal, P., Yeganehfar, M. and Kashfi, M. (2021): An Experimental and Numerical Evaluation of Steel A105 Friction Coefficient Using Different Lubricants at High Temperature. *Tribology Transactions*. 65(1), pp. 25-31.

[20] Kalpajian, S. and Schmid, S.R. (2008) *Manufacturing Processes for Engineering Materials*, 5th ed. California: Pearson Education.

[21] Kobayashi, S. (1982) A review on the finite-element method and metal forming process modeling. *Journal of Applied Metalworking*. 2(1), pp. 163-169.

[22] Cora, Ö.N., Akkök, M. and Darendelier, H. (2008) Modelling of Variable Friction in Cold Forging. *Engineering Tribology*. 222(1), pp. 899-908.

[23] Orsolini, A. and Booker, J.D. (2012) Modelling capabilities required for the double nosing process in the assembly of spherical plain bearings. *Journal of Engineering Manufacture*. 226(5), pp. 930-940.

[24] Han, H. (2002) *Determination of Flow Stress and Coefficient of Friction for Extruded Anisotropic Materials under Cold Forming Conditions*. Stockholm: Royal Institute of Technology.

[25] Lu, Y. (2005) Study of Preform and Loading Rate in the Tube Nosing Process by Spherical Die. *Journal of Computational Methods in Applied Mechanics and Engineering*. 194(25-26), pp. 2839–2858.

[26] Foster, A.D., Copeland, T.J., Cox, C.J., Hall, P.W., Watkins, M.A., Wright, R. and Lin, J. (2009) Error Analysis and Correction in the Slab Method for Determining Forming Forces. *International Journal of Mechanical Education*. 37(4), pp. 304-317.

[27] Gisbert, C., Bernal, C. and Camacho, A.M. (2015) Improved analytical model for the calculation of forging forces during compression of bimetallic axial assemblies. *Procedia Engineering*. Volume 132, pp. 298-305.

[28] Buschhausen, A., Weinmann, K., Altan, T. and Lee, J. (1992) Evaluation of Lubrication and Friction in Cold Forging using a Double Backward-Extrusion Process. *Journal of material processing technology*. 33(2), pp. 95–108.

[29] Kraus, M., Lenzen, M. and Marklien, M. (2021) Contact pressure-dependent friction characterization by using a single sheet metal compression test. *Wear*. 476(1).

[30] Bialas, M., Maciejewski, J. and Kucharski, S. (2021) Friction coefficient of solid lubricating coating as a function of contact pressure: experimental results and

microscale modeling. *Continuum Mechanics and Thermodynamics*. 33(1), pp. 1733-1745.

[31] Hatherell, J., Marmier, A., Dennis, G., Curry, W. and Matthews, J. (2023) Exploring the potential for a FEA-based Design of Experiments to develop design tools for bulk-metal joining processes. *International Conference on Engineering Design* (ICED), Bordeaux, France, 24-28 July 2023.

[32] Sofuoglu, H. Gedikli, H. (2002) "Determination of Friction Coefficient Encountered in Large Deformation Processes," *Tribology International*. 35(1), pp. 27–34.

[33] Bridgman, P.W. (1952) *Studies in Large Plastic Flow and Fracture*. McGraw-Hill: New York.

[34] Ettouney, O. and Hardt, D.E. (1983) A method for in-process failure prediction in cold upset forging, *ASME Journal of manufacturing science and engineering*. 105(1), pp. 161–167.

[35] Mielnik, E.M. (1991) Metalworking Science and Engineering. New York: McGraw-Hill.

[36] Fereshteh-Saniee, F., Fallah-Nejad, K., Beheshtiha, A. S. and Badnava, H. (2013) Investigation of Tension and Compression Behavior of AZ80 Magnesium Alloy. *Materials and Design*. 50(1), pp. 702–712.

Tables

Table 1: Chemical Composition of AMS5643.

Element	C	Mn	P	S	Si	Cr	Ni	Cu	Mo	Nb
Content (%)	0.07	1	0.04	0.03	1	17.5	5	5	0.5	0.45

Figures

Figure 1
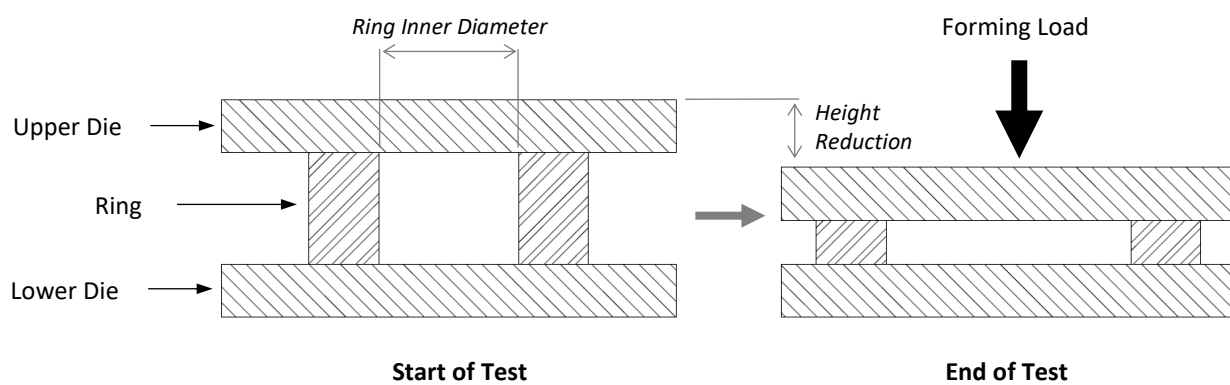
Figure 2
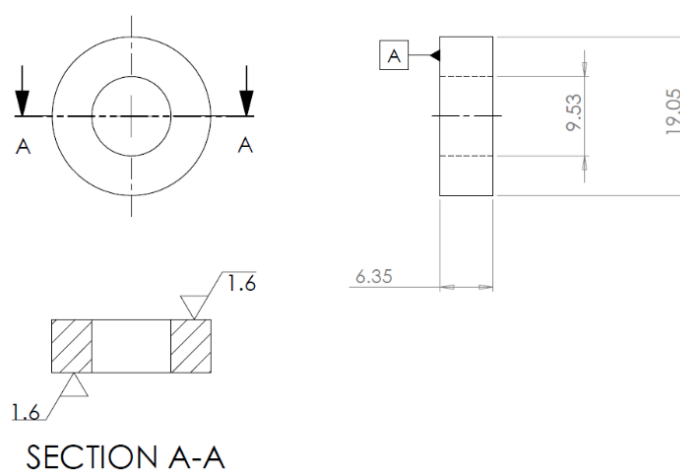
Figure 3
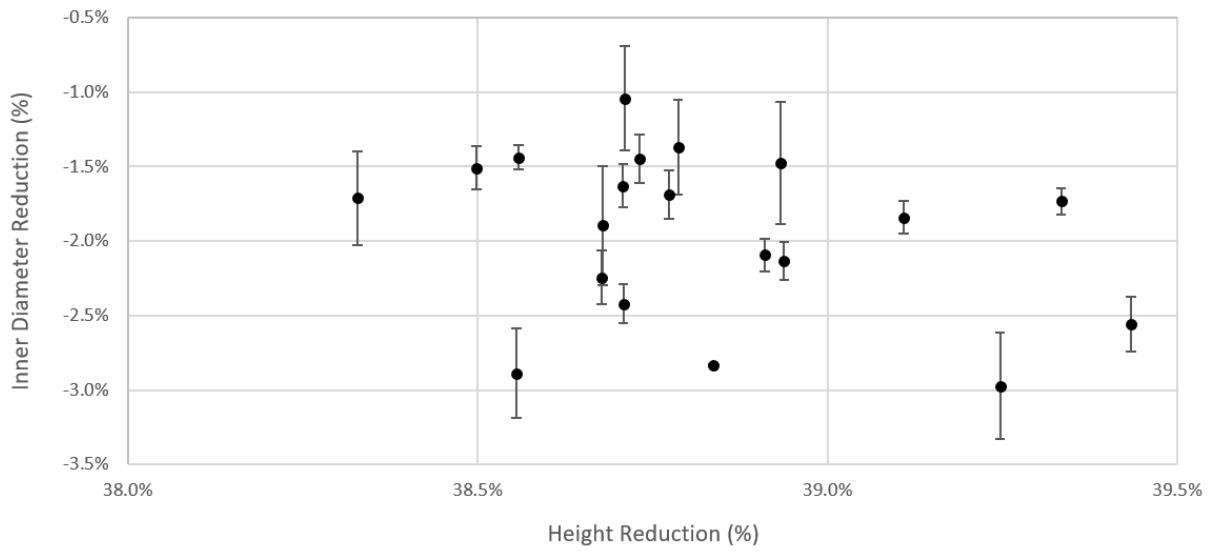
Figure 4
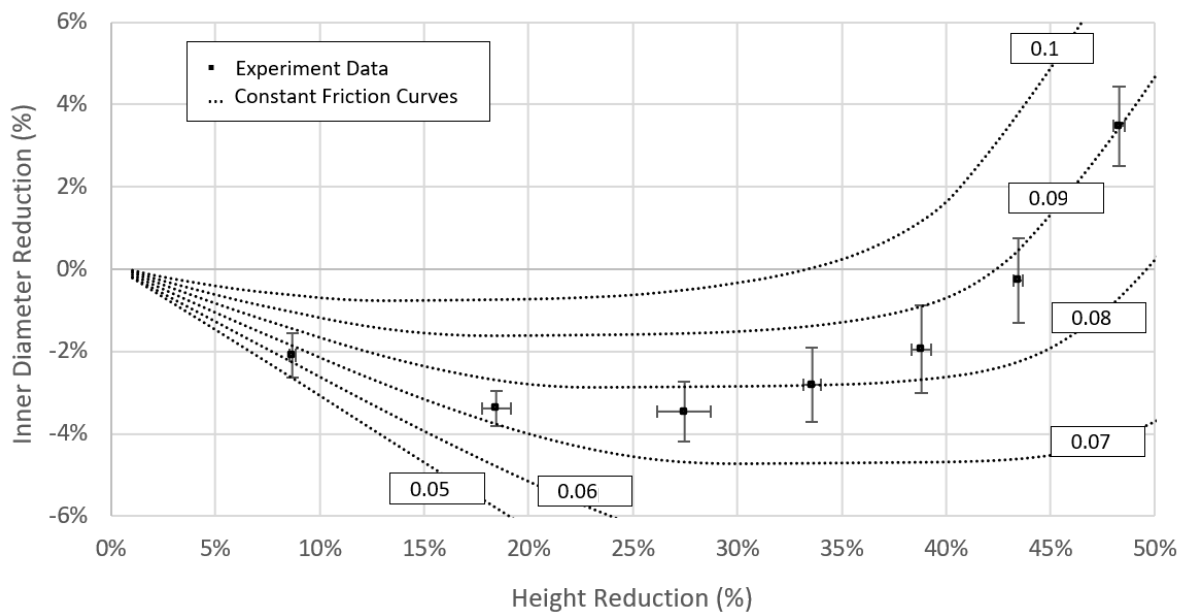
Figure 5
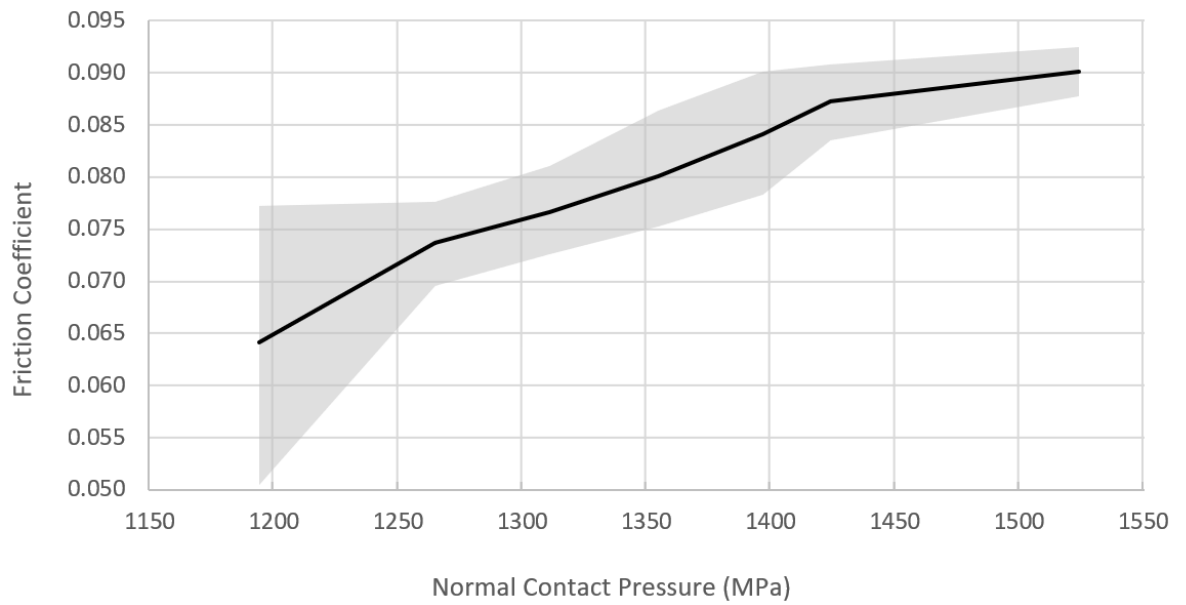
Figure 6
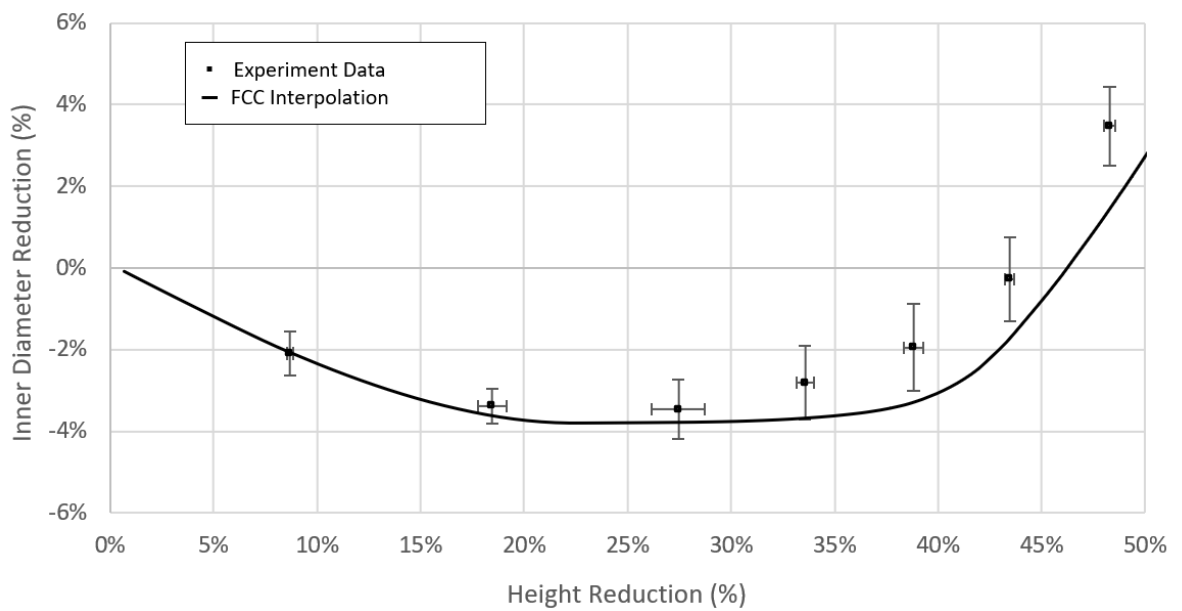
Figure 7
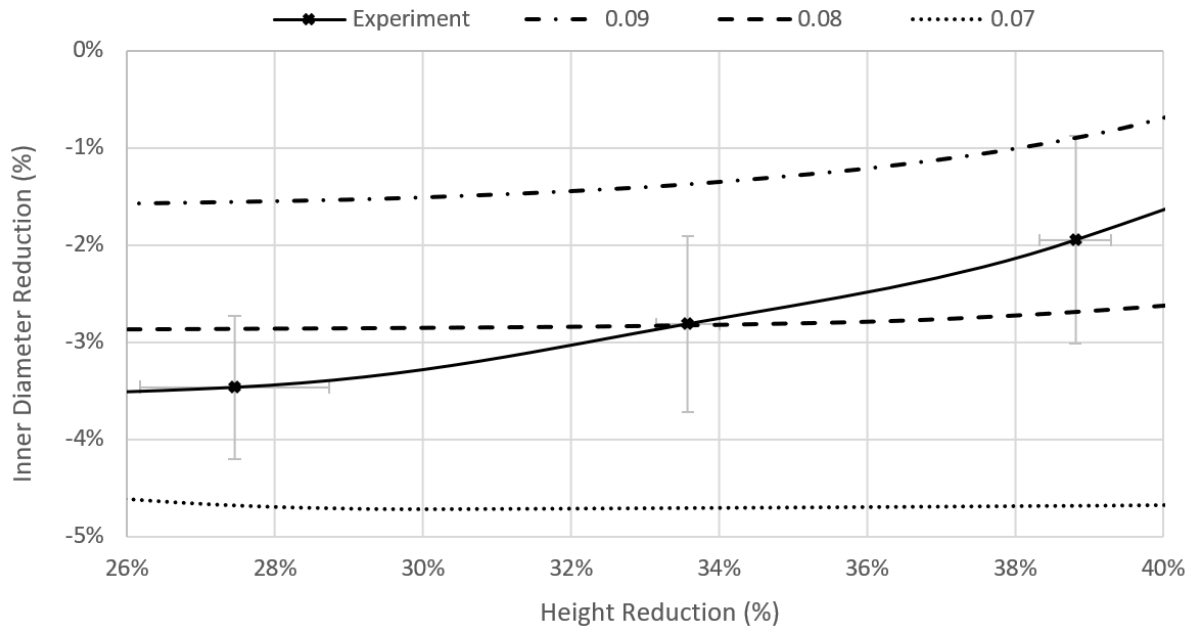
Figure 8
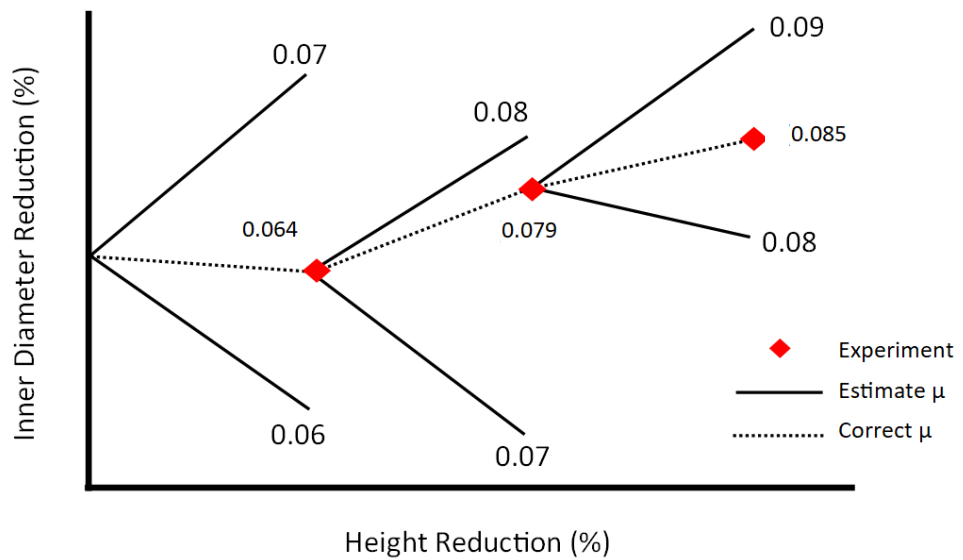
Figure 9
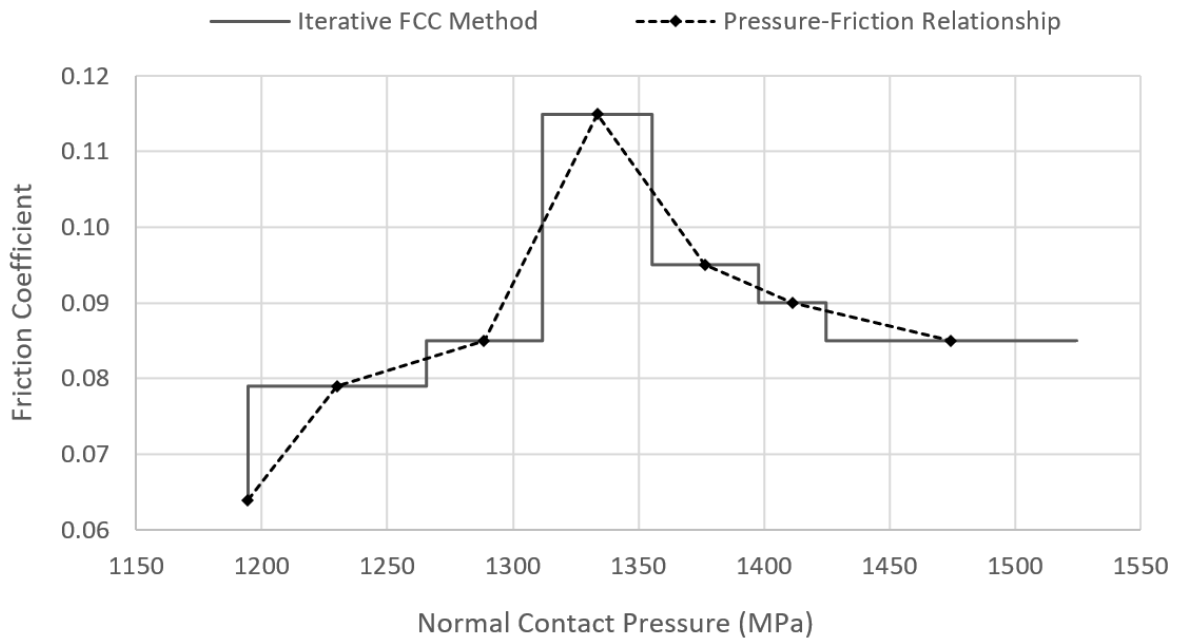
Figure 10
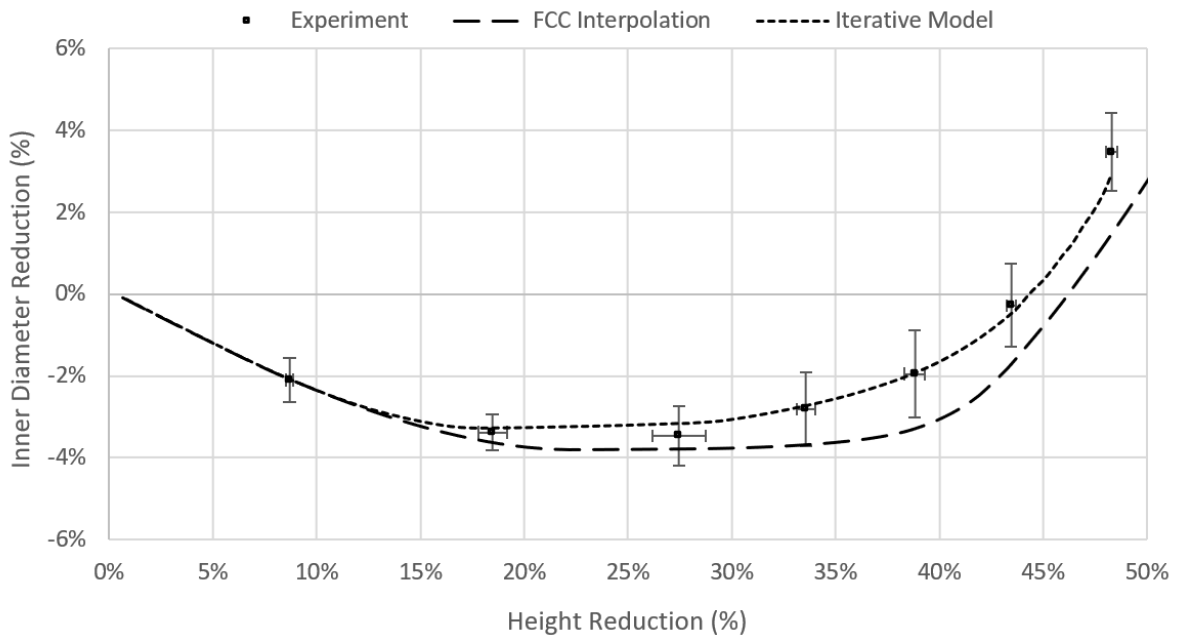
Figure 11
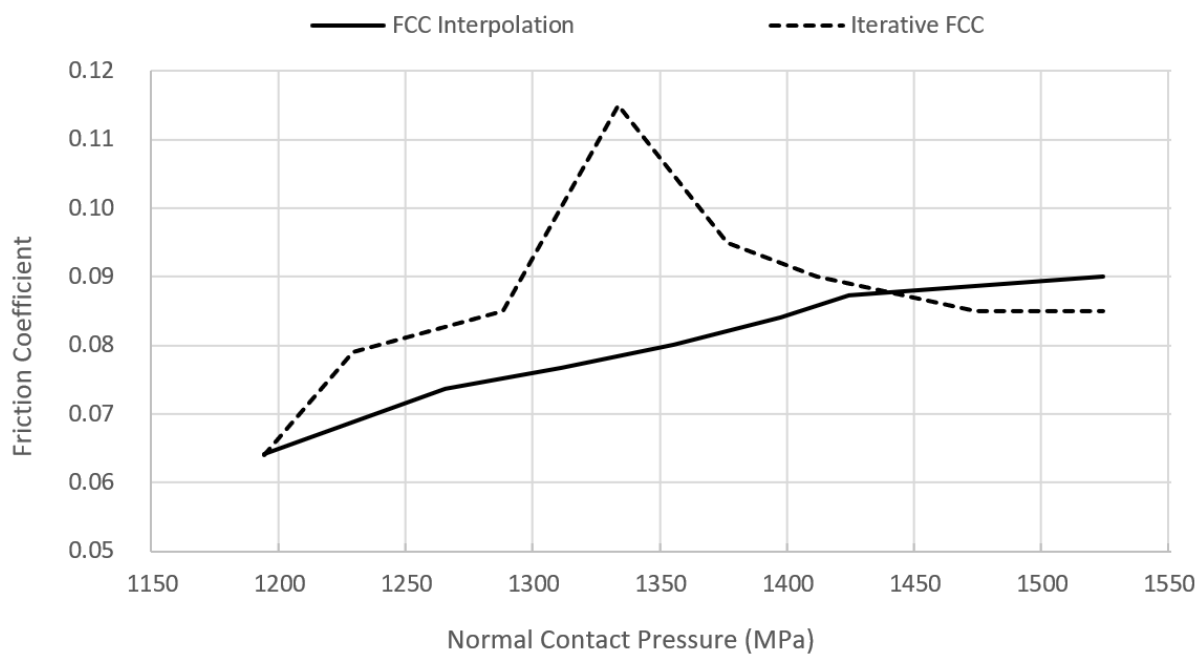
Figure 12
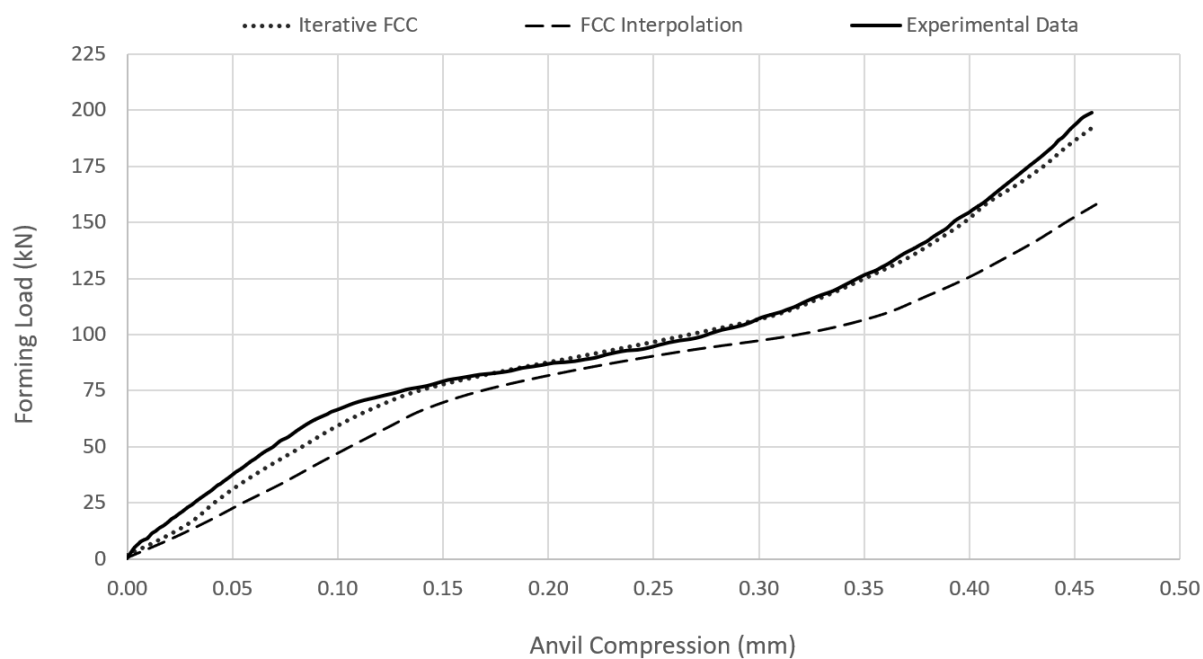
Figure Captions

Figure 1: Ring compression test schematic.

Figure 2: Ring compression test specimen drawing. All dimensions in mm and surface roughness (Ra) in micrometres.

Figure 3: Variation of the inner diameter reduction percentage caused by the ovality of the test specimens for the 50 kN load condition. Larger error bars represent greater ovality.

Figure 4: Ring compression test data for AMS5643 with a G-n Plus lubricant and FCCs ranging from a coefficient of friction of 0.05 - 0.1. Experiment error bars represent a 95% confidence interval.

Figure 5: Variation in the coefficient of friction against contact pressure for Steel AMS5643 with a G-n Plus lubricant. (Shaded region) 95% confidence interval for the friction coefficient.

Figure 6: Comparison of the ring compression test data and the prediction using the FCC interpolation method.

Figure 7: Detailed view from the FCCs in Figure 3

Figure 8: Schematic for the Iterative FCC methodology to evaluate the coefficient of friction (μ).

Figure 9: Pressure-friction relationship derived via the iterative FCC method.

Figure 10: Comparison of the interpolation and Iterative friction models to the ring compression experiment data.

Figure 11: Friction-Pressure relationship comparison.

Figure 12: Performance of the two ring compression analysis methods compared to the forming loads experienced during the staking of a production spherical-plain bearing.